



# Model and quality assessment of single image dehazing

Jessica Khoury

## ► To cite this version:

Jessica Khoury. Model and quality assessment of single image dehazing. Signal and Image processing. Université de Bourgogne Franche-Comté, 2016. English. <tel-01731624>

**HAL Id: tel-01731624**

**<https://hal.archives-ouvertes.fr/tel-01731624>**

Submitted on 14 Mar 2018

**HAL** is a multi-disciplinary open access archive for the deposit and dissemination of scientific research documents, whether they are published or not. The documents may come from teaching and research institutions in France or abroad, or from public or private research centers.

L'archive ouverte pluridisciplinaire **HAL**, est destinée au dépôt et à la diffusion de documents scientifiques de niveau recherche, publiés ou non, émanant des établissements d'enseignement et de recherche français ou étrangers, des laboratoires publics ou privés.

# SPIM

## Thèse de Doctorat



école doctorale sciences pour l'ingénieur et microtechniques  
UNIVERSITÉ DE BOURGOGNE

# Model and quality assessment of single image dehazing

■ JESSICA EL KHOURY





# SPIM

## Thèse de Doctorat



école doctorale **sciences pour l'ingénieur et microtechniques**  
U N I V E R S I T É D E B O U R G O G N E

N° X X X

THÈSE présentée par

JESSICA EL KHOURY

pour obtenir le

Grade de Docteur de  
l'Université de Bourgogne

Spécialité : **Instrumentation et Informatique de l'Image**

## Model and quality assessment of single image dehazing

Soutenue publiquement le 5 Décembre 2016 devant le Jury composé de :

ABDERRAHIM ELMOATAZ	Président du jury	Professeur à l'Université de Caen Basse-Normandie
SABINE SÜSSTRUNK	Rapporteur	Professeur à l'École Polytechnique Fédérale de Lausanne
PATRICK LAMBERT	Rapporteur	Professeur à Polytech Annecy-Chambéry
PIERRE GOUTON	Examineur	Professeur à l'Université de Bourgogne
ALAMIN MANSOURI	Directeur de thèse	Professeur à l'Université de Bourgogne
JEAN-BAPTISTE THOMAS	Co-encadrant	Maitre de conférences à l'Université de Bourgogne

"We lay there and looked up at the night sky and she told me about stars called blue squares and red swirls and I told her I'd never heard of them. Of course not, she said, the really important stuff they never tell you. You have to imagine it on your own."

-Brian Andreas-

# ACKNOWLEDGMENTS

First of all, I am grateful to God for the good health and will that were necessary to make this thesis a reality.

I would like to express my sincere thanks to my supervisors, Jean-Baptiste Thomas and Alamin Mansouri for the precious professional advice all along these three years, for their support and for providing me all the necessary facilities for the research.

As well, I would like to thank Pierre Gouton who was always there to give me some of his knowledge and expertise. I will never forget that because of you I had the opportunity to have a place in vision department at LE2I.

A special thought to the Norwegian Color Lab presented by Jon Hardeberg, who afforded me the opportunity of an internship in The Norwegian Colour and Visual Computing Laboratory, NTNU in Gjøvik – Norway, for four months. I appreciate the professional help of Steven Le Moan, who shared with me some of his knowledge and experiences in the image quality field.

I cannot imagine how these years would have been passed without the great moments that I have shared along with my colleagues in vision, computer science and electronics departments. I cannot forget the secretariat staff of SPIM and LE2I, who have been always ready to take charge of our professional missions and administrative papers.

I thank the jury members, Sabine Süssstrunk, Patrick Lambert and Abderrahim Elmoataz for the attention given to this thesis, for their comments and valuable suggestions.

This work is a part of a national project Open Food System, which was supported by Vitagora, Cap Digital, Imaginove, Aquimer, Microtechnique and Agrimip, and funded by the French State and the Franche-Comté Region as part of The Investments for the Future Programme managed by Bpifrance.

Finally, I want to thank my family, especially my parents who have endured the pain of distance, and all my uncles, my aunts, my cousins and my friends in Lebanon and abroad, for standing by me through these years and encouraging me to move forward.



# CONTENTS

<b>1</b>	<b>Introduction</b>	<b>1</b>
1.1	Color image . . . . .	1
1.2	Motivations . . . . .	2
1.3	Contributions . . . . .	3
1.4	Dissertation outlines . . . . .	4
<b>I</b>	<b>Haze in imaging model</b>	<b>6</b>
<b>2</b>	<b>Vision in bad environment</b>	<b>8</b>
2.1	Introduction . . . . .	8
2.2	Bad environment . . . . .	9
2.3	Vision in the atmosphere . . . . .	10
2.3.1	Composition of the air . . . . .	10
2.3.2	Atmospheric light . . . . .	13
2.3.2.1	Attenuation . . . . .	15
2.3.2.2	Airlight . . . . .	16
2.3.3	Haze and dehazing: definition and usefulness . . . . .	17
2.3.4	Visibility and visual range . . . . .	20
2.3.5	Beyond the visible range . . . . .	21
2.4	Conclusion . . . . .	22
<b>3</b>	<b>Dehazing</b>	<b>23</b>
3.1	Introduction . . . . .	24
3.2	Dehazing methods: state of the art . . . . .	24
3.2.1	Overview . . . . .	24
3.2.2	Single image dehazing . . . . .	25
3.2.2.1	Physics model based methods . . . . .	26
3.2.2.2	Image enhancement methods . . . . .	34
3.2.3	Multiple images dehazing . . . . .	35



3.2.4	Depth map dehazing . . . . .	40
3.2.5	Haze and noise removal . . . . .	40
3.2.6	Nighttime haze removal and multiple light colors . . . . .	42
3.2.7	Video haze removal . . . . .	43
3.2.8	Detection and classification of hazy images . . . . .	44
3.2.8.1	Detection of hazy areas in images . . . . .	45
3.2.8.2	Classification of hazy images . . . . .	46
3.3	Gaps in the literature . . . . .	46
3.3.1	Background . . . . .	46
3.3.2	Color fidelity . . . . .	47
3.3.3	Evaluation of the color shift . . . . .	47
3.3.3.1	Color spaces . . . . .	47
3.3.3.2	Real hazy images . . . . .	50
3.3.3.3	Color transparency model . . . . .	51
3.3.3.4	Simulation . . . . .	52
3.3.3.5	Discussion . . . . .	57
3.3.4	Quality evaluation . . . . .	57
3.4	Conclusion . . . . .	58
<b>II</b>	<b>Haze model and quality evaluation</b>	<b>59</b>
<b>4</b>	<b>Hazy image databases</b>	<b>61</b>
4.1	Introduction . . . . .	62
4.2	Required tools . . . . .	62
4.3	Color hazy images . . . . .	63
4.3.1	Existing databases . . . . .	63
4.3.2	CHIC . . . . .	64
4.3.2.1	Material and Setup . . . . .	64
4.3.2.2	Scenes . . . . .	65
4.4	Multispectral hazy images . . . . .	69
4.4.1	MHIA . . . . .	70
4.4.1.1	Material and setup . . . . .	70
4.4.1.2	Scenes . . . . .	72
4.4.1.3	Preprocessing . . . . .	73
4.5	Conclusion . . . . .	75

<b>5</b>	<b>Haze model evaluation</b>	<b>82</b>
5.1	Introduction . . . . .	82
5.2	Haze model vs haze density . . . . .	83
5.2.1	Real data . . . . .	83
5.2.1.1	Fog levels characterization . . . . .	83
5.2.1.2	Analysis . . . . .	86
5.2.2	Real world vs Simulation . . . . .	87
5.3	Geometric model . . . . .	93
5.3.1	Atmospheric light calculation . . . . .	94
5.3.2	Impact of the number of samples . . . . .	96
5.4	Haze model vs Spectral dependence . . . . .	98
5.5	Conclusion . . . . .	101
<b>6</b>	<b>Quality assessment of single image dehazing</b>	<b>102</b>
6.1	Introduction . . . . .	103
6.2	Quality of color dehazed images . . . . .	103
6.2.1	Background and motivation . . . . .	104
6.2.2	Subjective quality assessment . . . . .	108
6.2.3	Objective quality assessment . . . . .	109
6.2.3.1	General quality metrics . . . . .	111
6.2.3.2	Dehazing dedicated quality metrics . . . . .	115
6.3	Experiment . . . . .	118
6.3.1	Description . . . . .	121
6.3.2	Subjective evaluation of dehazing algorithms . . . . .	125
6.3.3	Subjective evaluation of image quality metrics . . . . .	125
6.3.4	Objective evaluation of dehazing algorithms . . . . .	129
6.3.5	Computational time . . . . .	131
6.3.6	Denoising . . . . .	132
6.3.7	Discussion . . . . .	135
6.4	Conclusion . . . . .	136
<b>7</b>	<b>General conclusion</b>	<b>137</b>
7.1	Summary . . . . .	137
7.2	Perspectives . . . . .	139
7.3	Closing . . . . .	141

<b>References</b>	<b>142</b>
<b>A Transmission refinement algorithms</b>	<b>166</b>
A.1 Soft matting . . . . .	167
A.2 Gaussian filter . . . . .	168
A.3 Bilateral filter . . . . .	168
A.4 Guided filter . . . . .	169
<b>B Airlight and transmission curves of MHIA images</b>	<b>170</b>
<b>C Link between image enhancement inside oven and this thesis</b>	<b>183</b>
C.1 Visibility disturbance . . . . .	184
C.2 Proposed solutions . . . . .	189
C.2.1 Hardware solution . . . . .	189
C.2.2 Software solution . . . . .	189

# INTRODUCTION

*"In visual perception a color is almost never seen as it really is - as it physically is. This fact makes color the most relative medium in art."*

*-Josef Albers-*

*This first chapter includes general outlines of thesis context. We first single out the role that color images play in most aspects of our daily life. In a second part, we provide the motivating factors as well as the main contributions of this work and the dissertation outlines.*

---

1.1	Color image . . . . .	1
1.2	Motivations . . . . .	2
1.3	Contributions . . . . .	3
1.4	Dissertation outlines . . . . .	4

---

## 1.1/ COLOR IMAGE

Our life is full of colors. Wherever we look we see colors. They are all around us in everyday life, and yet we rarely stop to give them a second thought, because we used to live in a colorful world. However, when they are strikingly combined with each others forming an unaccustomed scene that may please or dismay us, colors do not stay unremarkable anymore. We often notice the importance of colors in the dark when all colors look alike. Color perception is widely dependent on light. In images, color is the principal element of visual language. It is the first element which pops out at observers and being processed. Colors are not only used to beautify our images, they have serious effects on our psychic and physical behavior, and they have as well an important role in providing useful indications for subsequent actions.

Let us imagine that images, which are the medium of visual communication, are colorless. Would images be appreciated as much as they are colored? Would it be possible to get the same messages through? Would images impress the viewers? Would there be masterpiece paintings?

Colors in images often speed up visual search. For instance, if Paris metro map is without colors, we would spend a few minutes to locate a specific location or to follow the path of a rail line. The search process would be longer and tricky. When it comes to object recognition, we recognize objects more quickly when they have the same colors as in the real world.

In the art of painting, colors are used to express moods, metaphors and for symbolism. If we consider two paintings of the same sea scene. The first shows light and saturated colors and the second shows dark colors. The first one is more likely to give positive effect and the second one creates a negative one. Thus, painters and photographers exploit color value to communicate a particular mood.

In addition, colors have been always used to symbolize emblems, brands, psychological state, etc. And this may be different from culture to another.

Colors can lead to a better human memory performance. A large number of studies have been conducted to investigate the relation between color and memory performance [42].

In the marketing field, color concept is located on the boundary between art and science. A psychophysical experiment was carried out to estimate which hues attract more human attention [59]. According to color saliency, a ranking of twelve colors selected in the CIE LAB color space has been done. The results showed that red is the most salient color, followed by yellow and green. Many of the most recognizable brands in the world rely on color as a key factor in their instant recognition.

In the industrial sector, automation is one of the main manufacturing requirements. Since manual sorting is time and effort consuming, and misses sometimes reliability, thus, some computer vision color image based applications have replaced Humans in many manufacturing processes such as fish sorting [120], date fruit sorting [9], a real-time color-based counting system [163], etc.

In the cooking field, color plays an important role to recognize the different degrees of doneness.

## 1.2/ MOTIVATIONS

Recorded color images taken in bad environments exhibit problems such as low visibility, reduced contrast and generally bad "quality". For this reason, many methods known as *dehazing* methods have been designed to improve the perceived image quality in order to be used later in Computer Vision applications, which require images of high quality. Unlike computational photography, image usability and fidelity may be promoted over preference in computer vision. Amongst these two aspects, we consider particularly the fidelity.

One motivation of this work is related to the Open Food System (OFS), which is a research project that gathers 25 public and private partners all over France. This project aims to build an ecosystem to facilitate the preparation of meals by developing new appliances functionalities and innovative services. Indeed, taking accurate color images of food into an oven during their cooking and either getting information on their cooking status allow the user to follow the cooking process at distance on a connected tablet or phone. The potential link between this thesis and this project is described in Appendix C.

The rapid increase of the number of dehazing methods as well as their varieties, require

some common tools that allow to evaluate and compare all of these algorithms performance in a reliable way.

Amongst the numerous methods, which often provide no matching results, none has been commonly accepted as the best. In general, the evaluation of dehazing methods is not obvious and usually very limited. This is mainly due to some major shortcomings:

- The physical model of visibility degradation is completely ignored in some image enhancement methods. And it is blindly used in some others.
- Owing to deficient complementary subjective and objective quality assessment, there is a lack of accepted image quality metrics.
- Quality assessment of dehazing algorithms is a challenging problem since a perfect quality image is not available as a reference.

### 1.3/ CONTRIBUTIONS

The aim of this research is to investigate the evaluation of dehazing methods as well as the haze model. This can be done by defining some procedures and some suitable tools.

The evaluation of dehazing methods refers to:

- *Goal 1:* developing new tools to measure and monitor the evolution of colors with the haze density, before and after processing.
- *Goal 2:* evaluating dehazing quality metrics as well as dehazing methods while considering the haze-free reference image in terms of quantitative and qualitative ways.

The evaluation of the haze model refers to:

- *Goal 3:* comparing the simulated hazy images formed by the haze model to the real hazy images in terms of accurate representation of haze effects and the behavior of dehazing against real and simulated haze. In other words, this means to show when the haze model fails to represent the reality.
- *Goal 4:* marking out the limitations of the haze model when it comes to distance, haze density and spectral characteristics.

Indeed, we have contributed, either partially or fully to the overall goals. With regard to goal 1, we have designed an original color hazy image database of real fog including the haze-free image and some physically measured parameters. This database has been used to compare a number of dehazing methods that perform dehazing differently. The description of this database submitted to a Journal for publication [49] and benchmarked in a conference paper [48]. The images are also freely available at <http://chic.u-bourgogne.fr/>.

This database has allowed us to achieve partially the goal 2 by tackling the full-reference quality assessment issue and to understand better what a dehazed image quality means

and the best metric to be used. The subjective and objective experiments have been described and discussed in [45], which has been submitted to a Journal for publication.

On the other hand, concerning the goal 3, we could understand better how the simulated fog differs from the real fog, and how this impacts dehazing as well as the accuracy of color recovery. These points, in addition to the limitation of simulation comparing to the real-world, were singled out in two conference papers [46, 47].

Using again our color database, we fulfilled goal 4 by marking out the threshold from which the inversion of the haze model is no more possible. For this purpose, we have addressed also the multispectral aspect, which it was not basically supposed to be in the scope of this thesis (This material will be made available through a scientific communication). The validation of color database against the fog density is publicly communicated through a conference paper [48].

## 1.4/ DISSERTATION OUTLINES

This dissertation is structured as a series of interlinked points from having a light signal going through heterogeneous atmosphere until getting a processed image associated to a quality grade. It consists of two main parts including 7 chapters. The first part includes 2 chapters, which focus on the factors that lead to visibility deterioration and the adopted procedures to restore it. Part I closes with highlighting some incompletenesses present in the literature that we tried to address in Part II, which includes 3 chapters. They provide a description of the conceived hazy image databases, the haze model evaluation and the dehazed image quality assessment. This manuscript ends with a global conclusion.

The chapters are organized as follows.

**Chapter 2** provides a global description of the outdoor environments and its constituents that hamper clear light transmission, as well as the image formation. Image acquisition in bad environment requires specific colorimetric calibration taking into account the presence of the degradation factors. This chapter ends with the formation of visibility degradation model, which will be considered for image recovery and evaluation.

**Chapter 3** reviews the categories of dehazing methods. Since image dehazing is an active international research domain, there is a rapidly growing number of approaches. We only explain in this study some of them that we consider representatives of the state of the art. Single image dehazing approaches have been mainly considered, since they meet the needs arising from the real-world computer vision applications. At the end of this chapter, we describe the identified gaps as an introduction to the next chapters.

Based on the formation scenario of degraded images caused by atmospheric particles, we detail in **Chapter 4** the setup of CHIC (Color Hazy Image for Comparison), an original semi-indoor image database of different fog levels, with associated parameters that we will show how they have been used to compare some dehazing methods, to characterize the quality of dehazed images and to evaluate visibility degradation model. We describe as well the Multispectral Hazy Image Database (MHIA) associated to a depth map constructed with a Kinect device.

Using CHIC images, and simulated hazy images, we studied to which extent the degradation model succeeds to get similar outputs as real world in both ways: hazing and dehazing. The inaccuracies, which are introduced through hazing and dehazing are widely

discussed in **Chapter 5**. This has a twofold benefit: one is to define the maximal accuracy a single color image dehazing methods can effectively reach. The other is to show how this is strongly related to the Koschmieder model of visibility degradation, in terms of the density of fog and the spectral dependence.

After obtaining a more complete understanding of the nature of haze removal and the resulting inaccuracies, we are able to define the quality of dehazed images. In order to see what people perceive as good quality in terms of color and sharpness fidelity, a psychometric experiment has been carried out using images from CHIC database. Subjective judgments have been compared with a set of IQA (Image Quality Assessment) metrics, showing the evolution across scenes and haze levels. Thus, a set of guidelines for designing an efficient index dedicated to image dehazing is provided in **Chapter 6**.

Finally, **Chapter 7** is divided into three parts. The first one provides concluding remarks based on the results reported here. The second one gives a few perspectives on ways to think and to proceed to fill up the identified gaps and to improve what has been done. And the closing paragraph, which points out the potential utility of this study.





## HAZE IN IMAGING MODEL



## VISION IN BAD ENVIRONMENT

*"We don't see things as they are, we see them as we are."*

*-Anais Nin-*

*This chapter proposes a global description of the vision in bad weather. We first define what a challenging environment is. We describe the properties of particles that constitute our atmosphere and the related extinction phenomena, as well as the resulting visibility degradation model.*

---

2.1	Introduction . . . . .	8
2.2	Bad environment . . . . .	9
2.3	Vision in the atmosphere . . . . .	10
2.3.1	Composition of the air . . . . .	10
2.3.2	Atmospheric light . . . . .	13
2.3.2.1	Attenuation . . . . .	15
2.3.2.2	Airlight . . . . .	16
2.3.3	Haze and dehazing: definition and usefulness . . . . .	17
2.3.4	Visibility and visual range . . . . .	20
2.3.5	Beyond the visible range . . . . .	21
2.4	Conclusion . . . . .	22

---

### 2.1/ INTRODUCTION

Different natural environments around the world experience different levels of perturbation. This is simultaneously related to the physical composition of the environment and the interaction with external elements. This leads to visibility degradation that could lead to serious consequences. For instance, the pollution in developing countries such as China has become a serious threat the last few years. It has been estimated that the air pollution in China contributes to 1.2 to 2 million deaths annually and it is believed that

it kills more people worldwide than AIDS, malaria, breast cancer, or tuberculosis [150]. Moreover, the pollution prevents people from their daily life activities and it blocks some services that may have a negative impact on the international economy and trade. On Christmas 2015, the chinese authorities canceled more than 200 flights from Beijing due to limited visibility caused by the air pollution [85].

Generally, it is in our interest to have a clear visibility, no matter where we are. For security reasons: in the presence of fog, the risk of road accidents increases; in a not clear area, security cameras are not efficient. When visibility is good, even the most boring site seems somehow magical; when visibility is poor, even the best reef or the most spectacular sunset view seem dull. A bad visibility encumbers greatly a maritime search or a rescue mission.

When it comes to photography, atmospheric conditions such as fog and haze, are sometimes considered as useful tools of artistic expression. However, they are deemed as disruptive phenomena for other outdoor capturing applications, and some processing are therefore required.

Degraded visibility occurs not only in natural environments. Other artificial environments provide similar characteristics and cause therefore the deterioration of visibility. In a complementary work of this thesis, the oven cavity and all what goes on during cooking, represented to us a bad environment that obstructs spectral measurements and the capture of images (see Appendix C).

## 2.2/ BAD ENVIRONMENT

From an optical point of view, a bad environment groups a set of factors that interact with each other leading to a bad visibility.

Bad environments and their contents can be broken into two main groups. Underwater and atmospheric environments (Figure 2.1). Both of them are heterogeneous mediums. They are particularly prone to visibility degradation, which is mainly caused by the obstacles that break light transmission. In underwater areas, three main factors affect visibility: suspended particulate matter, biological species and light penetration. As regards the atmosphere, although their impacts are different (cf. section 2.3.1), the presence of haze, fog, mist and other aerosols reduces the visibility and the clarity of the scenes.

The presence of these particles in both environments decreases the contrast and deteriorates the original colors. This creates therefore annoying problems for computer vision applications. When these particles are abundant, the visibility is dramatically degraded and it leads to serious issues of individuals' safety. For instance, the risk of road accidents is higher in a foggy day than in a clear day.

Various degrading scenarios can be identified. We show in Figure 2.1 the most common and encountered ones. Underwater images (a); an outdoor image where fog covers uniformly objects that have colors not only similar to fog (b, c); an outdoor image where fog covers uniformly snow that is similar to fog (d); an image captured in a polluted area (e); a satellite image degraded with a non-uniform veil of fog (f); a nighttime foggy image with some light sources (g); an indoor smoky image (h).



Figure 2.1: Images captured in bad environments. (a) underwater image; (b) foggy road image; (c) landscape foggy image; (d) fog over snow image; (e) air pollution image; (f) satellite image; (g) nighttime foggy image; (h) indoor smoky image.

## 2.3/ VISION IN THE ATMOSPHERE

Imagine that you are standing on the roof of your house, and you are gazing something far away at the distant horizon. This scene may bring up many questions: what is the object that we see? How much is it easy to distinguish it from its background? What color does it have? How far it should be located to be easily perceived?

To find answers, we describe and define some concepts related to the particles forming the atmosphere, their optical characteristics and the modeling of the resulting image formation.

### 2.3.1/ COMPOSITION OF THE AIR

Our atmosphere is full of particles that cause the occurrence of several phenomena that lead to visibility degradation and make the detection of scenes' objects more difficult. We present a quick overview of the composition of the dry clear air and the aerosols caused by bad weather conditions or the human activities that affect the ecosystem.

The dry clear air is composed of gases, primarily nitrogen and oxygen with a small amount of argon, carbon dioxide, and very small amounts of other gases (see Table 2.1). Air molecules are inefficient scatterers because their sizes are smaller than the wavelengths of visible radiation (see Table 2.2).

In addition to gases, the atmosphere contains solid and liquid particles that are suspended in the air. Major components of fine aerosols are sulfate, nitrate, organic carbon, and elemental carbon. These particles have various sources such as volcanic ashes, foliage exudations, combustion products, and sea salt. In contrast to the air molecules, aerosols have important radiative effects in the atmosphere. Indeed, they cause the scat-

Table 2.1: The constituents of the dry air [38].

Constituent	Mole percent
Nitrogen	78.084
Oxygen	20.947
Argon	0.934
Carbon dioxide	0.0350
Neon	0.001818
Helium	0.00052
Methane	0.00017
Krypton	0.000114
Hydrogen	0.000053
Nitrous oxide	0.000031
Xenon	0.0000087
Ozone	trace to 0.0008
Carbon monoxide	trace to 0.000025
Sulfur dioxide	trace to 0.00001
Nitrogen dioxide	trace to 0.000002
Ammonia	trace to 0.0000003

Table 2.2: Weather conditions and associated particle types, sizes and concentrations [115].

Weather condition	Particle type	Radius ( $\mu m$ )	Concentration ( $cm^{-3}$ )
Air	Molecule	$10^{-4}$	$10^{19}$
Haze	Aerosol	$10^{-2} - 1$	$10^3 - 10$
Fog	Water droplet	$1 - 10$	$100 - 10$
Cloud	Water droplet	$1 - 10$	$300 - 10$
Rain	Water drop	$10^2 - 10^4$	$10^{-2} - 10^{-5}$

tering of light and absorb its radiation. The severity of these phenomena is directly related to the size of particles and to their concentrations. All of this leads subsequently to different visual effects. The size of aerosols typically varies between 0.01 and 1  $\mu m$  in radius. Most aerosols are found in the lower troposphere, where they usually stay a few days. They are usually carried out the atmosphere by rain and snow. During their residence time in the atmosphere, they form the haze.

The haze is mainly formed by aerosol particles, that have a larger size than air molecules and a smaller size than water droplets. Haze produces a distinctive gray hue and it is certain to affect visibility [132]. Haze appears in three main forms: a uniform haze, a layered haze and plumes [1] (see Figure 2.2). Referring to Table 2.3 the daylight visual range of the thin haze is between 4 and 10  $km$  and between 2 and 4  $km$  for the haze.

When aerosol's particles and air molecules are associated with some amount of humidity, they turn into water droplets. Water droplets have more severe action on the propagating light than aerosol particles. The daylight visual range varies from 1 – 2  $km$  for the thin fog up to 50  $m$  for the dense fog. Fog tends to produce a white hue. There are many types of fog which differ from each other in their formation processes, including radiation fog and

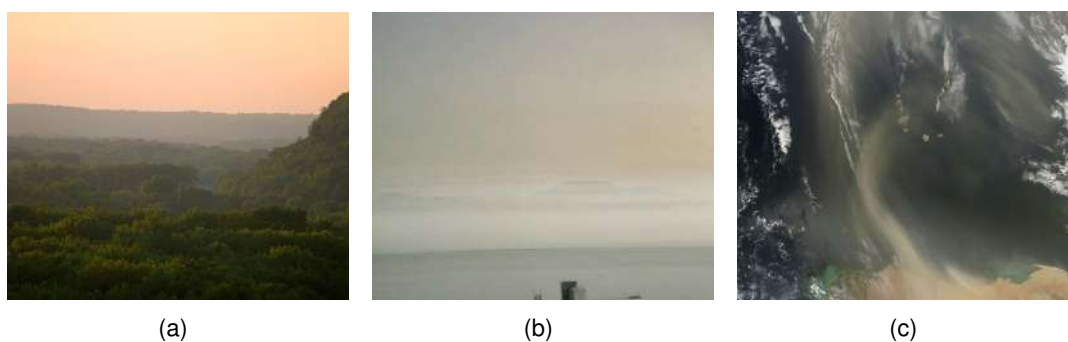


Figure 2.2: Hazy images with different haze types. (a) Uniform haze; (b) Layered haze; (c) ; (d) Plumes.

Table 2.3: Atmospheric attenuation and visual range of atmospheric conditions [75].

Atmospheric condition	Daylight visual range	Attenuation coefficient ( $km^{-1}$ )
Exceptionally clear	$>50km$	0.0427
Very clear	20 - 50 $km$	0.0713
Clear	10 - 20 $km$	0.214
Light haze	4 - 10 $km$	0.354
Haze	2 - 4 $km$	0.533
Thin fog	1 - 2 $km$	1.22
Light fog	500 - 1000 $m$	1.42
Moderate fog	200 - 500 $m$	7.13
Thick fog	50 - 200 $m$	21.3
Dense fog	$<50m$	42.6

advection fog [4] (see Figure 2.3).

The main two differences between the fog and the cloud is the concentration of water droplets and the altitude of the formation of these two phenomena. The cloud is located at high altitudes, rather than sitting at ground level as the fog.

Unlike all above weather conditions, the rain causes random spatial and temporal variations at the ground level.

Clouds and rain, as well as the particularities of the haze and the fog types above the ground level are out of scope for this thesis. Our study is restricted to vision at ground level, and to variations, which are steady over a period of time. Thus, it is assumed that, over horizontal paths, the scattering coefficient  $\beta$  is constant [132].

Human activities represent the main causes of the atmospheric pollution, which does not only affect the human health and the environment, but also the outdoor visibility. The contaminants which are emitted from many different sources, especially, in industrial areas, interact with the air particles to form new compounds, and degrade therefore the quality of the air. The air pollution that reduces visibility is often called haze or smog. Smog refers to any mixture of air pollutants and it can change the climate [135].

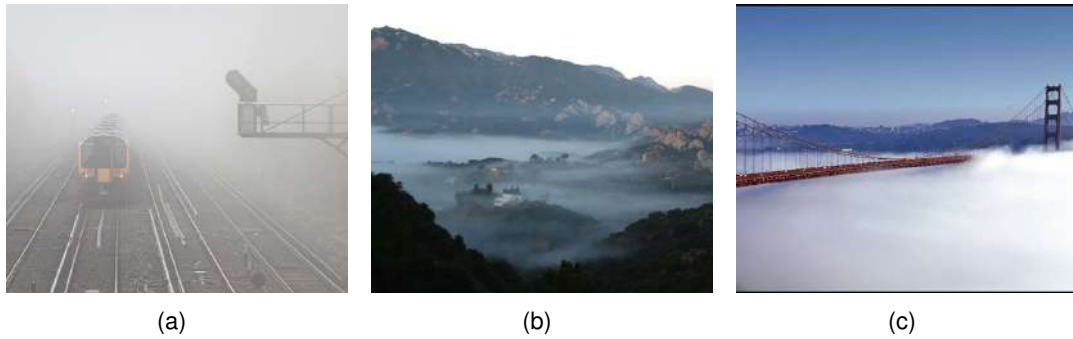


Figure 2.3: Foggy images with different fog types. (a) Uniform fog; (b) Radiation fog; (c) Advection fog.

### 2.3.2/ ATMOSPHERIC LIGHT

As light is crossing the atmosphere, it undergoes **attenuation** caused by solid and liquid particles that form the air, and it is therefore redirected out of the original direction of propagation. **The attenuation (extinction) is caused primarily by scattering rather than by absorption of the light.** The interaction of light (an electromagnetic wave) with matter can provide important information about the structure and dynamics of the material being examined. For instance, if the scattering particles are in motion, the scattered radiation is Doppler shifted [55].

Similarly, the structure and the size of the particle define the scattering properties and the law describing its mechanism and effects. In this regard, two scattering categories are evoked, Rayleigh and Mie scattering, which are detailed in the following paragraphs.

When we look for some information about Rayleigh scattering theory, we are more likely to come across the blue color of the sky, which is the result of the scattering of the sun light caused by the particles forming the atmosphere. **Rayleigh scattering is more effective at short wavelengths in the visible range (blue). Since short wavelengths are the most affected, scattered light comes down to earth with predominant blue cast.**

Considering an atmospheric particle of volume  $V$ , Rayleigh scattering is given by Equation 2.1:

$$I_r(\theta) = I_0 \frac{V^2}{\lambda^4 d^2} (1 + \cos^2 \theta) \quad (2.1)$$

$d$  is the distance between the scattering particle and the observer.  $\theta$  is the scattering angle formed between the incident light  $I_0$  and the scattered light  $I_r$ . Since Rayleigh scattering is proportional to  $\frac{1}{\lambda^4}$ , **the scattering is larger for blue light than for red light.** For a given angle of scattering the blue light will be scattered 16 times as much as the red (Figure 2.4).

Rayleigh scattering is mainly applicable to small, dielectric (non-absorbing), spherical particles. According to the ratio describing the relation between the particle size and the wavelength, we delimit the transition between Rayleigh scattering, which is wavelength dependent and Mie scattering, which is non-wavelength dependent, by Ratio 2.2:

$$x = \frac{2\pi r}{\lambda} \quad (2.2)$$

where  $r$  is the particle radius,  $\lambda$  is the wavelength of light.



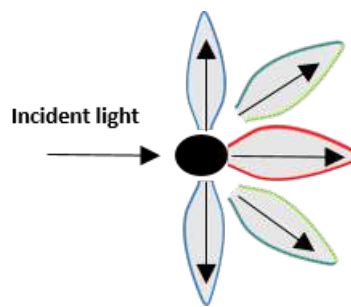


Figure 2.4: The intensity of the forward scattered light by a single atmospheric particle. According to Rayleigh scattering, with the angular increase from  $0^\circ$  (red) to  $90^\circ$  (blue), the intensity decreases.

In Figure 2.5 we see that the intensity and the form of the scattering light varies with the size of the scattering particle. Rayleigh scattering is applied when the size of the scattering particle is relatively small,  $x \ll 1$ , the light beam is equally scattered in all directions on the forward and the backward sides, thus the intensity is distributed in all directions. Otherwise, Mie scattering is considered. For a medium size of the particle,  $x \sim 1$ , the largest part of the beam is scattered in the forward direction. For a large size of the particle when it is larger than  $\lambda$ ,  $x \gg 1$ , the entire beam is scattered forward. This directive scattering has a high intensity.

The theory of Mie scattering [122], encompasses without particular attention to the particle size, all spherical, absorbing and non-absorbing particles. However, since its formulation is somehow complicated, Rayleigh scattering is preferred when it is applicable.

Scattering particles are numerous in the atmosphere. Hence, the incident light undergoes a multiple scattering (see Figure 2.6). A given particle is not only hit by the incident light, but also by the light scattered by other particles.

Atmospheric light scattering varies by time of day, weather and pollution. During the day, the amount of solar radiation reaching the earth's surface changes greatly because of the changing position of the sun. At midday, for example, the sun is positioned high in the sky and the path of the sun's rays through the earth's atmosphere is shortened. Consequently, less solar radiation is scattered or absorbed, and more solar radiation reaches the surface of the Earth. During sunset and sunrise, as the path that sunlight takes through our atmosphere increases in length, an increased amount of violet and blue light being scattered out of the beam by the nearly infinite number of scattering particles that occur along the way, the light that reaches an observer early or late in the day is noticeably reddened, since longer wavelengths have a higher penetration power and resist consequently more to scattering (Mie scattering). The effect of a red sunset becomes more pronounced if the atmosphere contains more and more particles. This increasing number of particles may be due to weather conditions or pollution (cf. Section 2.3.1).

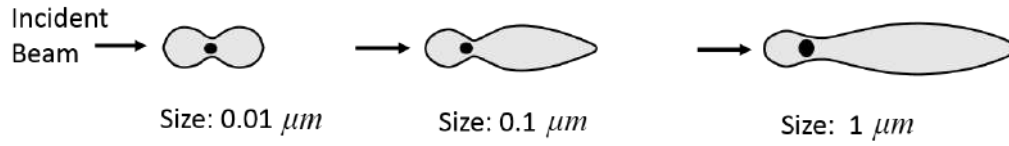


Figure 2.5: The variation of the scattering properties (intensity, type and form) with the ratio of the particle size to the incident light wavelength. Rayleigh scattering is applied when the size of the scattering particle is lower than  $\frac{\lambda}{10}$ . For particles with a larger size than the light wavelength  $\lambda$ , Mie scattering is applied. This figure is reproduced here from the Figure 1 of the paper of Nayar *et al.* [132]

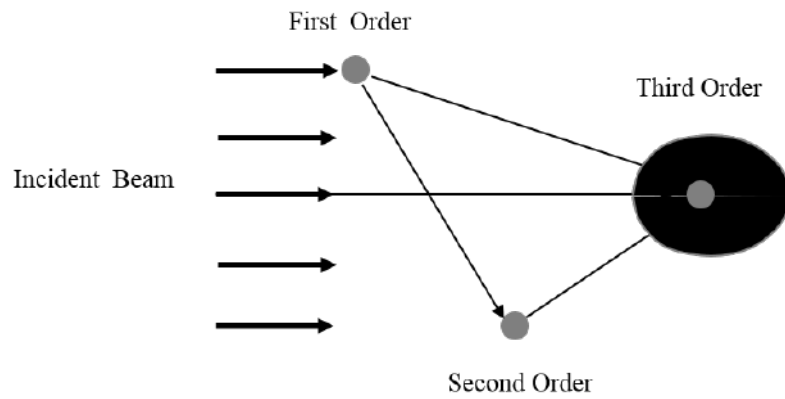


Figure 2.6: Atmospheric multiple scattering. This figure is reproduced here from the presentation of the paper of Nayar *et al.* [132].

### 2.3.2.1/ ATTENUATION

The light reflected by the scene's objects is partially attenuated before reaching the camera. More the distance from the observer to object increases, the radiance emitted from the object decreases.

The attenuation is caused by two main phenomena: scattering and absorption. The attenuation coefficient given in Equation 2.3, is the sum of the scattering coefficient  $\beta_s$  and the absorption coefficient  $\beta_a$ :

$$\beta = \beta_s + \beta_a \quad (2.3)$$

In Figure 2.7, we consider a unit volume (scattering particle) illuminated by a spectral irradiance  $E(\lambda)$  and observed at angle  $\theta$  as a radiant intensity  $I(\theta, \lambda)$ , as given in Equation 2.4:

$$I(\theta, \lambda) = \beta(\theta, \lambda)E(\lambda) \quad (2.4)$$

where  $\beta(\theta, \lambda)$  is the angular attenuation coefficient.  $I(\theta, \lambda)$  is the radiant intensity (flux radiated) per unit solid angle per unit volume of the surrounding medium.

The total flux scattered in all directions is independent of  $\theta$  (Equation 2.5), but it is still dependent on wavelength, since Bouguer's law is valid only for monochromatic light:

$$\Phi(\lambda) = \beta(\lambda)E(\lambda)dx \quad (2.5)$$

The fractional change in irradiance at location  $x$  from the camera can be written as Equation 2.6:

$$\frac{dE(x)}{E(x)} = -\beta(\lambda)dx \quad (2.6)$$

By integrating both sides between  $x = 0$  and  $x = d$ , we get the Equation 2.7 :

$$E(d, \lambda) = E_0(\lambda)e^{-\beta(\lambda)d} \quad (2.7)$$

If we assume that the camera has a linear radiometric response denoted by  $u$ , the horizon irradiance becomes linked to the horizon radiance as:

$$E_\infty(\lambda) = uL_\infty(\lambda) \quad (2.8)$$

Thus, Equation 2.8 becomes:

$$E(d, \lambda) = uL_0(\lambda)e^{-\beta(\lambda)d} \quad (2.9)$$

This is Bouguer's exponential law for attenuation. Based on Allard's law [10],  $L_0$  is replaced by  $\frac{I_0}{d^2}$ , where  $I_0$  is the radiant intensity of a scene point. Along this operation,  $\beta(\lambda)$  is assumed to be constant, since the medium is supposed to be homogeneous; all scattered flux are assumed to be removed from the incident energy. The fraction of energy that remains is the direct transmission. Thus, Equation 2.9 becomes:

$$E(d, \lambda) = u \frac{I_0(\lambda)e^{-\beta(\lambda)d}}{d^2} \quad (2.10)$$

According to Narasimhan *et al.* [125],  $I_0(\lambda) = L_\infty(\lambda)r$ , where  $L_\infty(\lambda)$  denotes the horizon radiance and  $r$  denotes the sky aperture (the cone of the sky visible from a scene point).

Thus, Equation 2.10 becomes:

$$E(d, \lambda) = \frac{E_\infty(\lambda)re^{-\beta(\lambda)d}}{d^2} \quad (2.11)$$

### 2.3.2.2/ AIRLIGHT

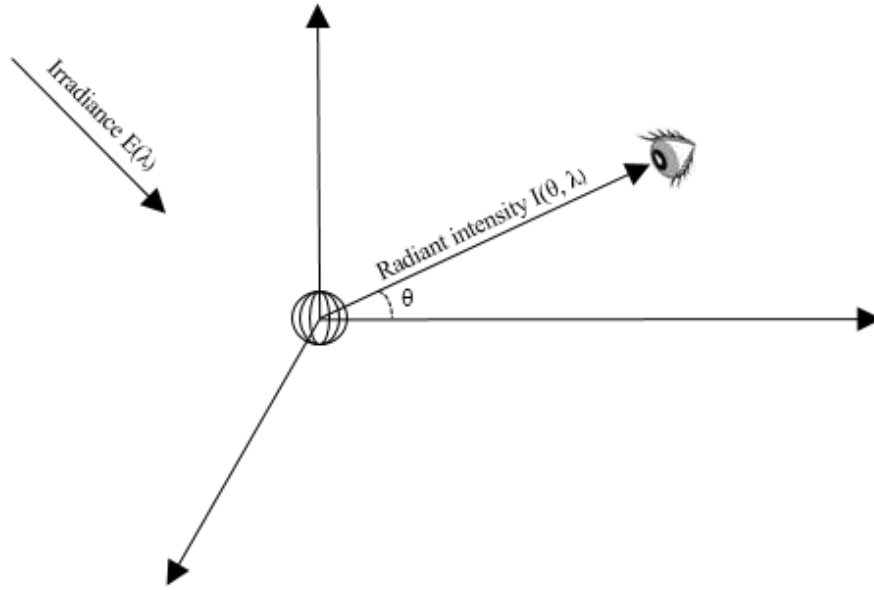
Airlight definition first appeared in 1924, by Koschmieder [87]. The airlight is caused by the scattering of the environmental light by the particles suspended in the atmosphere. It causes the atmosphere to act like a source of light. The airlight is added to the attenuated transmitted light coming from the scene, to thereby form the hazy scene [132].

There is a contradictory relationship between the airlight-depth and the attenuation-depth: the attenuation causes the decreasing of the light intensity of the scene radiance while the airlight increases the light intensity and the global chromaticity turns towards the ambient light color.

Let us consider the atmospheric particle with no defined geometrical shape shown in Figure 2.8 with a light source placed at a finite distance  $x$  from the observer.

The light coming from the object is scattered by the atmospheric particle  $d\nu$  and redirected toward the observer with an intensity (Equation 2.12):

$$dI(x, \lambda) = d\nu k\beta(\lambda) = dwx^2 dx k\beta(\lambda) \quad (2.12)$$

Figure 2.7: An illuminated unit volume observed at angle  $\theta$ .

where  $x$  is the distance from the scattering particle to the observer,  $dw$  is the solid angle of the cone formed by the observer and the scattering particle and  $k$  is a constant value defined by the global illumination.

We calculate the radiance from the irradiance given by Equation 2.11:

$$\begin{aligned} dL(x, \lambda) &= \frac{dE(x, \lambda)}{dw} \\ &= \frac{dI(x, \lambda)e^{-\beta(\lambda)x}}{dw x^2} \\ &= k\beta(\lambda)e^{-\beta(\lambda)x} dx \end{aligned} \quad (2.13)$$

The total radiance along the path  $d$  between the object and the observer is obtained by integrating  $dL(x, \lambda)$  in Equation 2.13 between  $x = 0$  and  $x = d$ :

$$L(d, \lambda) = k(1 - e^{-\beta(\lambda)d}) \quad (2.14)$$

The radiance of the airlight for an object placed at a distance  $d$  from the observer is given by Equation 2.15:

$$L(d, \lambda) = L_h(\infty, \lambda)(1 - e^{-\beta(\lambda)d}) \quad (2.15)$$

where  $k$  is replaced by  $L_h(\infty, \lambda)$ , the airlight radiance at the horizon at  $d = \infty$ . This shows that the airlight radiance increases with the distance between the object and the observer. When  $d = 0$ ,  $L(d, \lambda)$  equals zero and when  $d = \infty$ , the object is no more observable, thus,  $L(d, \lambda)$  equals the sky radiance.

### 2.3.3/ HAZE AND DEHAZING: DEFINITION AND USEFULNESS

The apparent luminance of any distant object is controlled by two processes that occur concurrently. The light emanating from the object is gradually attenuated by scattering

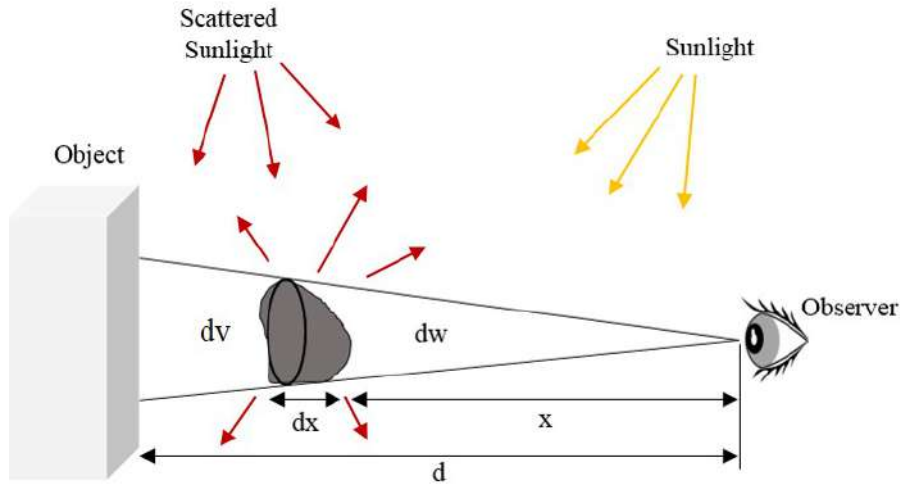


Figure 2.8: An atmospheric particle placed on the line of sight between the observer and the object with no defined geometrical shape plays the role of a light source by scattering the light coming either from other scattering particles or from the sun.

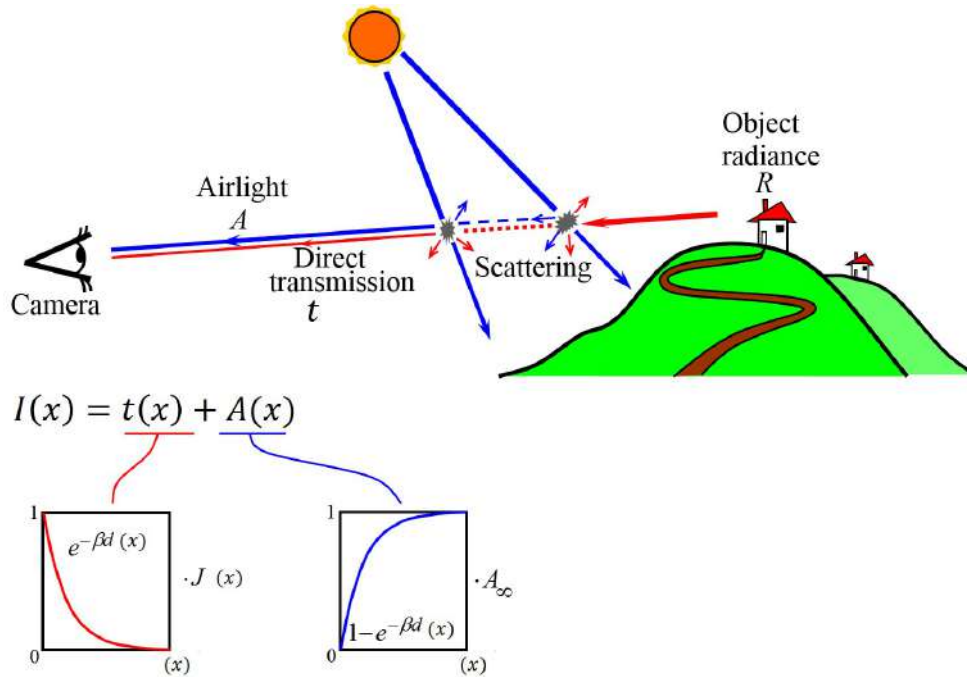


Figure 2.9: Imaging through haze. The apparent luminance  $I$  of an object placed at distance  $d$  is controlled by two processes that occur concurrently: the transmitted light denoted by  $t$ , which emanates from the object and it is attenuated by scattering and absorption along the line of sight. The airlight  $A$ , which comes from a light source (*i.e.* Sun) and scattered by the haze particles toward the observer before reaching the object. This figure is reproduced here from the Figure 1 of the paper of Schechner *et al.* [156].

and absorption. It is denoted by  $t$ . The airlight  $A$  coming from a light source (*i.e.* Sun) and it is scattered by the haze particles toward the observer all along the line of sight [39].

The formation of hazy images represented in Equation 2.16, can be modeled as the sum of the scene's radiance  $J(x)$  and the atmospheric light  $A_\infty$ , weighted by a transmission factor  $t(x)$ . The  $A_\infty$  is the airlight scattered by an object located at infinity with respect to the observer.

$$I(x) = J(x)t(x) + A_\infty(1 - t(x)) \quad (2.16)$$

where  $I(x)$  is the image formed on the camera's sensor. The transmission factor  $t(x)$  depends on scene depth  $d$  (distance to the sensor) and on the scattering coefficient  $\beta$  of the haze, such that  $t(x) = e^{-\beta \cdot d(x)}$  [87]. Unlike other traditional image degradations, haze/fog has some degrading particularities (Table 2.4). It is a natural, depth-dependent perturbation that spans non-uniformly over the whole image. The degradation and the loss of information increases with depth, as the amount of fog between the imaged surface and the sensor increases. Hazy and foggy images have also different prevailing colors, which depend on the density of the scattering particles and the ambient light. The process to recover  $I(x)$  from  $J(x)$  is known as **dehazing** or **defogging**.

Table 2.4: The characteristics of Hazy/foggy image degradation.

<b>Hazy/foggy image degradation</b>
Distance-dependent degradation
Fog density-dependent degradation
Chromatic degradation
Degradation leads to contrast reduction and color shift
Fog is a continuous uniform/non-uniform layer across the image
Classical enhancement algorithms are not efficient to deal with these degradation characteristics

According to Narasimhan and Nayar [127], the haze model assumes a single scattering and a homogeneous atmosphere. Thus, this model is not valid for depths that are more than a few kilometers, nor for high densities of fog (cf. Section 5). Referring to section 2.3.2, the size of haze aerosols and water droplets forming the fog is larger than the wavelength of light. Hence, the scattering coefficient does not depend on wavelength. Thus, in a foggy weather all wavelengths are assumed to be scattered equally. Thus, we see white or grayish fog and the haze model (Equation 2.16) does not include  $\lambda$  parameter.

Although weather conditions differ in particle types, sizes, concentrations and the resulting veil hue and visibility (Table 2.2), the same methods are used indiscriminately for all aerosols, since the haze model is a good approximation for a wide range of weather conditions and for several situations.

For the sake of transparency, in this manuscript, we use indiscriminately the terms of **haze-free image**, **hazy image** and **dehazing** for both haze or fog degrading visibility layers.

A common question may be asked: **how dehazing should be defined? Is it an enhancement or a restoration technique?**

Before providing an answer, we define each of enhancement and restoration techniques.

Enhancement techniques are essentially used in order to get a resulting image of better quality than the degraded one, and not necessarily the same properties as an image of the same scene, taken in the same conditions, but without any visible haze. While restoration techniques aims at reconstructing back the original image.

While the majority of researchers working in this area define dehazing as being an enhancement technique, we investigated in this project the circumstances, within which a dehazing method is considered as a restoration processing. This has been reflected, first, through our CHIC database that provides the haze-free image (refer to Section 4), the quality assessment that considers in a good part the similarity with this image and the haze model evaluation.

The principal aim of any dehazing method is to improve the visual quality and fidelity of a hazy image. When developing a new dehazing method, there is often a need to compare the results with the state-of-the-art methods in order to evaluate their performances or to rate them.

If we consider dehazing as an enhancing visibility procedure, it is therefore necessary to rate the improvement level by evaluating how a given method succeeds simultaneously to improve the hazy image visibility and to preserve the original features of the ground-truth image like colors and structure data. Thus, a measuring methodology of the image quality is needed. A number of image quality assessment indexes were proposed to automatically evaluate the quality of images in agreement with human visual perception.

#### 2.3.4/ VISIBILITY AND VISUAL RANGE

Meteorological visibility is defined as the greatest distance at which a black object of adequate dimensions (located on the ground) can be seen and recognized when observed against the horizon sky during daylight or could be seen and recognized during the night if the general illumination was raised to the normal daylight level [118].

The visual range of a specific target under given meteorological conditions is defined as that distance from the observer at which the specific target could just be detected by the human eye (Equation 2.17). That means that the apparent brightness contrast of the target against the background, has decreased to the contrast threshold of the human eye. The maximal distance one can see through the air is the meteorological range defined by Middleton [119]:

$$D = \frac{-\ln(0.02)}{\beta} \quad (2.17)$$

where  $\beta$  is the scattering coefficient. At  $\lambda = 555nm$ , the sensitivity of the human eye has its maximal value.  $D$  depends on the threshold contrast, which represents the minimal brightness contrast from which a person can see. It is commonly assumed to be equal to 0.02 although it varies from individual to another. Visual range varies enormously from several meters in a dense fog to several hundred kilometers in a clear air [143].

The visibility in the atmosphere is degraded through the scattering and the absorption of light by the particles and gases. Both of these phenomena reduce the amount of the transmitted light along its path, from the object located at some distance to the camera. Many factors impact visibility degradation such as the particles size, the particles concentration, the object physical characteristics, the characteristics of the observer or the camera, the ambient illuminant and the distance from the object to the camera.



A change in contrast with viewing distance occurs for dark and bright objects. In case of dark objects, under the action of the airlight, the dark objects appear lighter with distance. With bright objects, light is lost from the line of sight with increasing distance. In both cases, the contrast between the object and the background decreases. The light reaching the target is close to the light intensity of the background. When the eye is no longer able to discern the object from its background, we say that the object is beyond the limit of visibility.

The reduction of the contrast is due to the scattering and the absorption of light caused by the atmospheric particles along the viewing distance. The decreasing of the light intensity emanating from object is represented as follows:

$$dI = -\beta I dx \quad (2.18)$$

The intensity  $dI$  is proportional to the initial intensity  $I$ , which is reduced when the attenuation coefficient  $\beta$  increases with the infinitesimal distance step  $dx$ .

By integrating over the path, Equation 2.18 becomes:

$$I = I_0 e^{-\beta x} \quad (2.19)$$

The relation between the apparent contrast  $C$  at a distance  $x$  and the actual contrast  $C_0$  can be expressed in a similar manner in Equation 2.20:

$$C = C_0 e^{-\beta x} \quad (2.20)$$

### 2.3.5/ BEYOND THE VISIBLE RANGE

In looking at visibility as being a complex psycho-physical phenomenon, this gives rise to the question of whether we would see farther with other imaging techniques in the same foggy and rainy conditions. For instance, we may ask how much we would push the limitations of the visible range by navigating toward the infrared range and how this would change with atmospheric conditions.

Like visible light, infrared radiation fades out due to scattering and absorption caused by aerosols and water droplets. The bigger the droplets' size is and the higher their concentration is, the more the infrared signal is lost. However, visible and infrared signals have distinct characteristics that make infrared more useful in only some situations (see Equation 2.11, where attenuation depends on the wavelength). In other words, the transmission characteristics alone of both bands do not determine the detection ranges, but there is a need to consider also the physical properties of the atmosphere. Both of them determine whether we can take advantage or not of this discrimination.

Infrared range encompasses a large number of wavelengths, beginning at the top end of the visible range (red) and extending up to the microwave portion of the electromagnetic spectrum. Thus, the infrared range is from  $750nm$  to  $1mm$ . Infrared spectrum can be broken down into five wavelength ranges: Near-infrared (NIR) is from  $0.75$  to  $1.4\mu m$ ; Short-Wavelength infrared (SWIR) is from  $1.4$  to  $3\mu m$ ; Mid-Wavelength infrared (MWIR) is from  $3$  to  $8\mu m$ ; Long-Wavelength infrared (LWIR) is from  $8$  to  $15\mu m$ ; Far-infrared (FIR) is from  $15\mu m$  to  $1mm$  [6].

In his report prepared for the United States Air Force, Chen [29] describes attenuation caused by haze, fog, clouds and rain through visible, infrared and radio ( $\lambda > 1mm$ ) frequencies. This report is considered as a handbook that provides a quick estimate of the



effects that different weather conditions induce on the sensors. It helps to examine implications of the development of precision-guided munitions. We only consider the haze and the fog (clouds and fog have similar properties (Table 2.2) except that clouds do not contact the ground and do not therefore trouble ground-level vision applications). Rain is out of scope in this thesis.

Because of the smallness of the haze particles (Table 2.2), the transmission through haze keeps on increasing with the wavelength from 350 nm to 10  $\mu\text{m}$ . Haze is almost invisible for higher wavelengths. Thus, infrared sensors improve markedly the visibility in hazy weather.

However, this is not the same for the fog. Since fog has a higher concentration and bigger particles' size (Table 2.2), besides scattering it causes absorption at infrared wavelength because of its humid nature. Thus, a severe extinction is caused by fog. The severity level depends strongly on the fog characteristics. Referring to [134], considering the four different fog types shown in Table 2.3 (thin fog, light fog, moderate fog and thick fog), the exploitation of the infrared ranges is not always better comparing to the visual band. Considering the thin fog, the wavebands MWIR and LWIR are 2.5 and almost 4 times better than visible, respectively. For the light fog, LWIR is also 4 times better than visible, while MWIR does not show any performance improvement. In the atmospheric conditions, moderate fog and thick fog, neither MWIR nor LWIR improve the imaging performance. These fog categories are opaque to visible and infrared. This is due to the atmosphere, which represents a limiting factor.

## 2.4/ CONCLUSION

In this chapter we have first defined from an optical and physical point of view what a hazy environment is. Visibility degrading environments are various. The optical effects generated by each of them is differently modeled according to the nature of present particles. They also have different impacts on the global quality of the perceived image.

Special attention has been given to outdoor images taken in bad weather. A global description of the particles contained in the atmosphere and the interaction they have with light. Visibility is considered as being a complex psycho-physical phenomenon. From one side, the deterioration of visibility is basically caused by bad atmospheric conditions and the type of degrading layer. The interpretation of this degradation is not a constant function. It depends on the vision system characteristics, as well as the properties of the target object, such as its size and the temperature difference of the target and background when we deal with infrared signal [19]. This is why it is important to specify a frame of reference when we want to interpret hazing or dehazing behavior.

Since the perceived apparent luminance of a hazy scene is controlled by two factors, the direct transmission and the airlight, we are exposed to two main inaccuracies: if  $A_\infty$  is not accurately estimated, the recovered colors are shifted from their original values. If  $t$  is wrongly calculated, the haze is not effectively removed. These inaccuracies are differently handled by dehazing approaches. In the next chapters we will mark the boundaries between the haze model validation and the dehazing approaches accuracy.

*"Vision is the art of seeing what is invisible to others."*

*-Jonathan Swift-*

*In this chapter we first review dehazing methods that have been proposed over the last several years. We break them down into separate categories. We focus on those that have been widely adopted and often used to evaluate the performance of new methods through comparison. We shed the light on single color image dehazing. The last part of this chapter is dedicated to identify some literature gaps that we show how we proceeded to address in part II.*

---

3.1	Introduction . . . . .	24
3.2	Dehazing methods: state of the art . . . . .	24
3.2.1	Overview . . . . .	24
3.2.2	Single image dehazing . . . . .	25
3.2.2.1	Physics model based methods . . . . .	26
3.2.2.2	Image enhancement methods . . . . .	34
3.2.3	Multiple images dehazing . . . . .	35
3.2.4	Depth map dehazing . . . . .	40
3.2.5	Haze and noise removal . . . . .	40
3.2.6	Nighttime haze removal and multiple light colors . . . . .	42
3.2.7	Video haze removal . . . . .	43
3.2.8	Detection and classification of hazy images . . . . .	44
3.2.8.1	Detection of hazy areas in images . . . . .	45
3.2.8.2	Classification of hazy images . . . . .	46
3.3	Gaps in the literature . . . . .	46
3.3.1	Background . . . . .	46
3.3.2	Color fidelity . . . . .	47
3.3.3	Evaluation of the color shift . . . . .	47

3.3.3.1	Color spaces . . . . .	47
3.3.3.2	Real hazy images . . . . .	50
3.3.3.3	Color transparency model . . . . .	51
3.3.3.4	Simulation . . . . .	52
3.3.3.5	Discussion . . . . .	57
3.3.4	Quality evaluation . . . . .	57
3.4	Conclusion . . . . .	58

---

### 3.1/ INTRODUCTION

A number of developments in computer vision are there to enhance the visibility of outdoor images by reducing the undesirable effects due to scattering and absorption caused by the atmospheric particles. This could be a pre-step of other applications, which assume that input is exactly the scene radiance. Otherwise, these algorithms would generate inaccurate results.

Dehazing is needed for human activities and in many algorithms like recognition, tracking and remote sensing [105, 176] and sometimes in computational photography [147]. Applications that are of interest in this scope: fully autonomous vehicles typically use computer vision for land or air navigation, monitored driving [54, 168, 133], outdoor security systems [141], or remote surveillance systems [14]. In bad visibility environments (cf. Section 2.2), such applications no longer function efficiently. An extra layer of processing should be added.

Image dehazing is a transdisciplinary challenge, as it requires knowledge from different fields: meteorology to model the haze, optical physics to understand how light is affected by this haze and computer vision as well as image and signal processing to recover the parameters of the scene. Researchers have been always searching for an optimal method to get rid of degradation by light scattering along aerosols. Many methods have been proposed and compared to each other. Although today we have a varied collection of approaches, they are limited and they do not meet efficient recovery requirements.

Throughout dehazing process, many modifications are introduced, affecting the image features. These modifications might lead to have a better or a worse rendering to the whole image, while knowing that image features are affected differently. The rendering level depends directly on the method hypothesis and the distortions introduced by the viewing and capture conditions.

### 3.2/ DEHAZING METHODS: STATE OF THE ART

#### 3.2.1/ OVERVIEW

The main objective of haze/fog removal, defogging or dehazing is to recover the attenuated light of the scene (*i.e.* scene radiance). This problem is mathematically ill-posed

since the number of unknown parameters is bigger than the number of equations. This explains the great attention given to this research domain and the variety of approaches, which are reflected by a dramatically increasing in the number of publications over the past few years (see Figure 3.1).

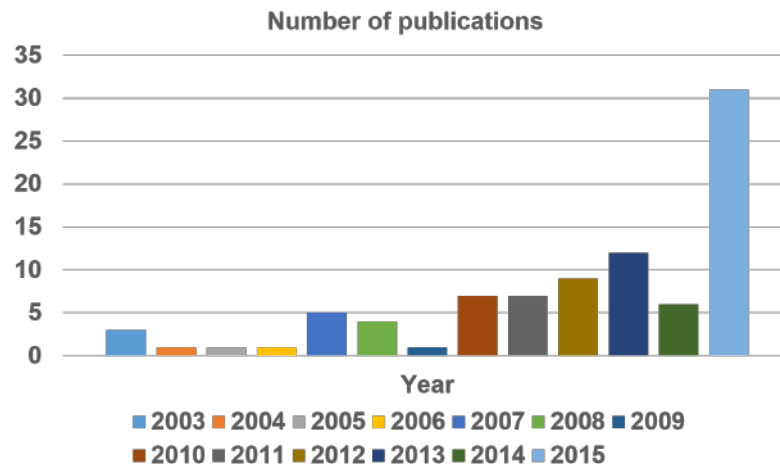


Figure 3.1: Number of publications describing new dehazing approaches over 13 years. This figure has modified from Figure 1 of the paper of Liu *et al.* [103].

As shown in Figure 3.2, dehazing methods can be classified into two main categories:

1. **Single image methods:** these methods can be whether physics-based and image enhancement methods (cf. Section 3.2.2). This category has had a lot of success and popularity. It represents a very active domain of research, since approaches do not require user interaction nor additional information (the vast majority of recently proposed dehazing methods belong to this category). Considering a single degraded image, these color-based methods provide results as good as other categories' results. They are used for a variety of applications ranging from simple visualization to e.g. monitored driving [54], outdoor security systems [141], or remote surveillance systems [14].
2. **Multiple image methods:** unlike single image methods, these methods suffer from additional cost. Some of them cannot be performed without user interaction. Moreover, special equipment are usually required, such as polarizers [158], [157], [162]. Different images may be used, such as images taken for the same scene under different weather conditions [127], [127] or images of different types (RGB and NIR). Thus, they are less prone to be used into real time applications. Sometimes, besides the degraded image, additional information are required, such as the scene depth map [86]. These methods, like multiple image methods, have not raised yet a lot of interest.

### 3.2.2/ SINGLE IMAGE DEHAZING

Much work has been carried out on single image dehazing. However, further research is still needed to overcome existing shortcomings. Some of them have been widely addressed in this thesis (cf. Chapters 4 and 5).

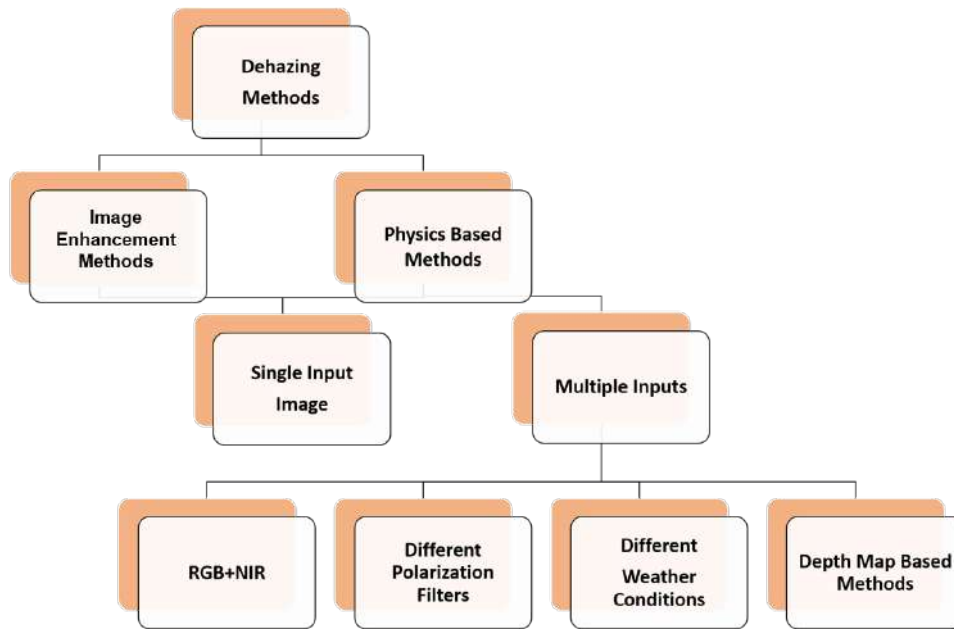


Figure 3.2: The family of dehazing methods.

Single image dehazing approaches can be divided into two groups: physics-based and image enhancement methods. Methods in the first group are based on the inversion of the visibility degradation model (Equation 2.16). The challenge is to evaluate the model parameters, and for that, prior assumptions and constraints have to be taken. The key point is then to find the most suitable hypothesis which leads to the best parameter estimates. Such methods are known by image restoration methods.

Methods in the latter category do not consider the physical causes of image degradation caused by weather conditions, but rely on observers preferences that are known to improve the image quality. In particular, contrast enhancement is the major general concept. They include image enhancing techniques such as the applying of bilateral and guided filter [17], [172], [71] for image smoothing or the histogram equalization for contrast adjustment, etc. They suffer from less effectiveness on maintaining color fidelity. Since they aim to improve the quality of images, no matter if the features of images are accurately recovered or not, they are called image enhancement methods.

### 3.2.2.1/ PHYSICS MODEL BASED METHODS

Although physics model based methods have been judged as good in handling original information fidelity [193], they suffer from some practical limitations. Since they are based on the haze model (Equation 2.16), they fail as soon as it is physically invalid. When the airlight is not uniformly applied on the whole image, the constant-airlight assumption will be violated. If the haze is not uniformly distributed on the image, the single scattering coefficient hypothesis will be no more true. If the transmission is not the same for R, G and B channels, a color distortion is generated. They usually fail in the dense haze condition, or in particular zones where the scene objects are similar to the atmospheric light and no shadow casts on them.

As we pointed out that the number of dehazing methods is increasing very fast, it would be nearly impossible and tedious to describe all of them in this manuscript. We will only

detail representatives of each of the dominant methods and assumptions, which we used in the quality evaluation section 6.2.

**Dark Channel Prior** In 2009, the Dark Channel Prior (DCP) was first introduced by He *et al.* [70]. It was inspired from an earlier haze removal method known as dark object subtraction technique [28]. Based on the observations provided in the paper, the intensity of one of the channels in a typical color image pixel is low and tends to be zero (5000 outdoor and daytime images have been chosen from flickr.com, they cut out the sky region, they calculated the dark channel prior: 75 % of the pixels in the dark channel have zero values, and the intensity of 90 % of the pixels is below 25). This technique has been used to remove spatially homogeneous haze. This is done by subtracting a constant value corresponding to the darkest object in the scene.

Using DCP, dehazing is done through five steps (Figure 3.3). Step 1: dark channel construction, Step 2: atmospheric light estimation, Step 3: transmission estimation, Step 4: transmission refinement, Step 5: scene radiance recovery.

**Step 1. Dark channel restoration** It relies on the assumption that, for a given pixel in a color image of a natural scene, one channel (red, green or blue) is usually very dark, except for the sky. The airlight tends to brighten these dark pixels, and therefore it is estimated from the darkest pixels in the scene. This observation is inspired from [28], and it is known as *dark channel prior*. For a hazy image  $J(x)$ , the dark channel  $J^{dark}(x)$  is given by Equation 3.1:

$$J^{dark}(x) = \min_{c \in \{r, g, b\}} (\min_{y \in \Omega(x)} (J^c(y))) \quad (3.1)$$

$J^c$  is a color channel of  $J$  and  $\Omega(x)$  is a local patch centered at  $x$ .

In [72], dark channels are computed using a patch size  $15 \times 15$ . Few hints are provided to define the patch size: larger size increases the probability that a patch contains dark pixels. Thus, dark channel could be accurately estimated. However, with a large patch, the assumption that the transmission is constant in a patch becomes less appropriate and the halo artifacts near depth edges become stronger. According to Lee *et al.* [91], with a minimum possible patch size, we avoid the heterogeneous textures and the selection of a patch containing parts of two objects with different distances to the camera.

**Step 2. Atmospheric light estimation** The brightest pixels in the hazy image are considered to be the most haze-opaque, if and only if, the weather is overcast and the sunlight denoted by  $S$  is ignored and only the atmospheric light  $A_\infty$  is considered:

**if it is the case then**

$$J(x) = R(x)A_\infty \text{ where image intensity without hazy is } 0 \leq R \leq 1$$

$$I(x) = R(x)A_\infty t(x) + (1 - t(x))A_\infty \leq A_\infty$$

**else**

$$J(x) = R(x)(S + A_\infty)$$

$$I(x) = R(x)S t(x) + R(x)A_\infty t(x) + (1 - t(x))A_\infty \geq A_\infty$$

Thus, the brightest pixel can be brighter than the atmospheric light.

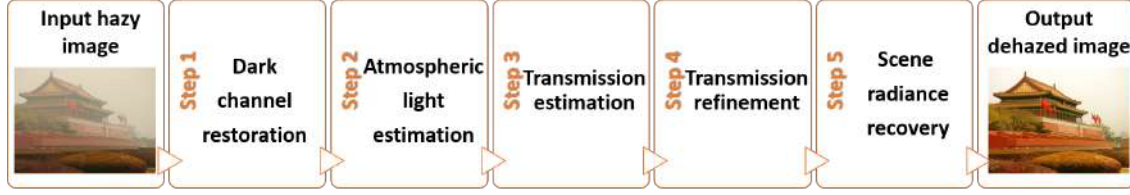


Figure 3.3: Flowchart of DCP showing its main steps.

To resolve this problem, the dark channel is used: we pick the top 0.1% brightest pixels in the dark channel. Then, among these pixels, the pixels with highest intensity in the input image  $I$  are selected as the atmospheric light.

**Step 3. Transmission estimation** After estimating atmospheric light, transmission is estimated as follows:

$$t(x) = 1 - \omega \min_{y \in \Omega(x)} \left( \min_c \left( \frac{I^c(y)}{A_\infty^c} \right) \right) \quad (3.2)$$

where  $\omega$  is the amount of haze kept in the image to avoid unnatural scenes ( $\omega = 0.95$ ).

**Step 4. Transmission refinement** In order to refine the transmission map, soft matting Laplacian is applied to smooth artifacts along edges. However, it increases dramatically the computational time. For more details on the soft matting, readers may refer to Appendix A.

**Step 5. Scene radiance recovery** Referring to Equation 2.16, we can deduce:

$$J(x) = \left( \frac{I(x) - A_\infty}{\max(t(x), t_0)} \right) + A_\infty \quad (3.3)$$

$t_0 = 0.1$ . It avoids to obtain a dim enhanced image.

DCP, like any other dehazing method, has also some drawbacks. Some of them have been addressed in the following-up DCP-based methods explained later in this section:

- DCP fails to estimate the transmission when the objects are inherently similar to the atmospheric light and not covered by shadows. It fails to restore the image with a large sky area or a large white area, as well.
- Since DCP is a physics-based method, it fails when the haze model (Equation 2.16) is physically not valid.
- DCP fails to recover the image under non-homogeneous haze.



- The soft matting used for transmission map refinement is time consuming. Thus, it is not suitable for real time applications.
- The color distortion phenomenon will occur when the transmission is not accurately estimated and it is different among three color channels.
- Like any other color-based dehazing methods, DCP fails when the fog is dense.

**DCP derivatives** Later on, various derivative versions of DCP have been released. Some of them proposed an improvement in one or more steps [91]. Some others were adjusted to be used in other applications. We list some derivative methods according to the step in which the change was occurred.

**Step 1** Most DCP-based dehazing methods calculate the dark channel by simply using a local patch with a fixed size to basically reduce the calculation time. Some of the DCP-based following up methods consider a patch with a different size from  $15 \times 15$ , which was basically used. The patch size can be more adapted based on the image content (cf. Section 3.2.2.1). Some of them used a patch size of  $11 \times 11$  to reduce time complexity [106]. In [31], authors considered that serious over-saturation effects occur in the recovered scene radiance when a small patch size is used in the original hazy image featuring localized light. This leads to a failure in the identification of the atmospheric light source. Larger size can resolve this problem, but it leads to halo effects and block artifacts, especially along edges (see Figure 3.4). Therefore, two patch sizes of  $3 \times 3$  and  $45 \times 45$ , which are experimentally identified, have been used in a hybrid process of DCP.

Apart from the size of the patch, unlike the majority of DCP-based methods, Zhang *et al.* [197] replaced the minimum operator by the median operator:

$$J^{dark}(x) = \underset{c \in \{r, g, b\}}{\text{median}}(\min_{y \in \Omega(x)} (J^c(y))) \quad (3.4)$$

This replacement leads to a less blurry dark channel on one side and to a higher computational time on the other.

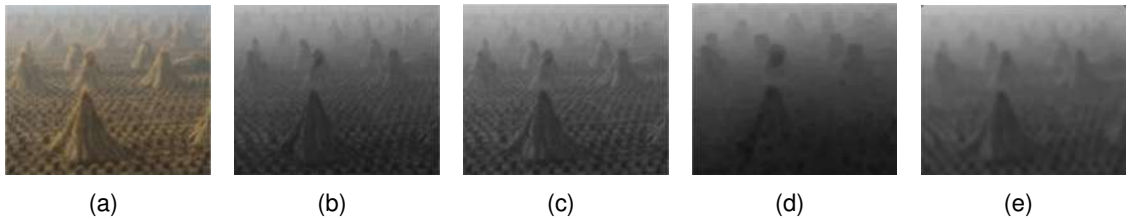


Figure 3.4: (a) Hazy image. (b) Dark channel obtained by Equation 3.2 ( $3 \times 3$ ). (c) Dark channel obtained by Equation 3.4 ( $3 \times 3$ ). (d) Dark channel obtained by Equation 3.2 ( $15 \times 15$ ). (e) Dark channel obtained by Equation 3.4 ( $15 \times 15$ ). This figure is reproduced here from Figure 6 of the paper of Lee *et al.* [91].

**Step 2** The majority of DCP-based dehazing methods estimate the atmospheric light as it is described in the original method [74, 100, 184, 166, 188, 153, 79, 197]. In [182],  $A$  is



the highest intensity value among the 0.2% instead of the 0.1% of the brightest pixels of the dark channel.

There are others, who assumed that  $A$  is the highest dark channel intensity value and it should be calculated as follows:

$$A = I(\operatorname{argmax}_x(I^{\text{dark}}(x))) \quad (3.5)$$

In later works, researchers assumed that this estimation is inaccurate, especially when the scene contains many bright pixels. Thus, a third form has been released [79] to exclude the bright pixels from the estimation of  $A$  by calculating the local entropy:

$$E(x) = \sum_{i=0}^N (p_x(i) \times \log_2(p_x(i))) \quad (3.6)$$

where  $p_x(i)$  is the probability of a pixel value  $i$  in a local patch centered at  $x$ .  $N$  is the maximum pixel value. The local entropy value is high for regions with sharp variations and it is low for regions with smooth variations. Thus,  $A$  is the lowest local entropy value, since the variations over an opaque layer of fog are smooth.

**Step 3** Two equations have been mostly used to calculate the transmission map. The first one was mainly used by the original DCP (Equation 3.2). And it was later used in many following-up methods described in [74], [100], [166], [182], [188], [153], [105], [106], [99], [197] and [191].

Xu *et al.* [184] have addressed the under-estimation problem of the transmission map. To resolve this, they added a positive value  $\rho \in [0.08, 0.25]$  to the transmission map:

$$t(x) = 1 - \min_{y \in \Omega(x)} \left( \min_c \left( \frac{I^c(y)}{A^c} \right) \right) + \rho \quad (3.7)$$

Indeed, the addition of  $\rho$  in Equation 3.7 or  $\omega$  in Equation 3.2 resolves partly the problem. According to [91], where RMSE (Root Mean Square Error) values were calculated between the ground-truth and the estimated transmission map using 66 synthetic images from FRIDA database,  $\omega$  should be around 0.9 and  $\rho$  around 0.12.

**Step 4** Inaccurate estimation of the transmission map may lead to some distortions such as block artifacts. The patch-based dark channel calculation, leads to a blurry transmission map. This is mainly due to the assumption that  $t$  is a constant value in a local patch. This is not always true, especially when the patch contains a sharp edge. This wrong assumption leads to clear edge artifacts. In order to get a refined map, many methods have been used. The reader may refer to the Appendix A for more information about the transmission refinement algorithms.

Some dehazing methods have used gaussian filter to smooth the map [188, 153, 105]. Some others [184, 191] have used instead the bilateral filter [172], which is very similar to Gaussian convolution, but pixels are treated based on nearby location and similar values. It is a smoothing filter with edge-preserving [191, 184]. The guided filter can perform edge-preserving like bilateral filter, but it has a better action near edges [71]. Since the application of the soft matting [93], which has been used in the original DCP method [70, 72] was extremely slow, the authors of this method replaced it by the guided filter to

speed up the transmission refinement map. For this reason, the soft matting has never been used later in any other dehazing method. Contrariwise, the guided filter has been used later in other methods [100, 153, 99].

The main difference point between these refinement algorithms, that unlike the Gaussian and the Bilateral filters, the soft matting, the Cross-bilateral filter and the Guided filter consider the color hazy image and not only the gray image of the transmission map. This helps to remove the erroneous textures based on the real colors and to keep a similar sharpness to the original color hazy image. For more information about the transmission refinement algorithms, the reader may refer to Appendix A.

All of these enhancing algorithms have been applied directly on the transmission map. However, other algorithms apply a pre-processing enhancing algorithm to the hazy image in order to prevent the transmission map from blur and erroneous textures. In [95], a morphological filtering process is applied on the grayscale hazy image in order to reduce the block artifacts in the transmission map.

In [200], the edge-guided interpolated filter is applied on the hazy image, which is used as a guidance image in the guided interpolated filter applied on the transmission map, in order to sharpen the fine details in the final dehazed image such as edges.

In other works, a focus has been placed on the amelioration of the transmission estimation in such a way to overcome the refinement step. Fang *et al.* [50] presented a windowed adaptive method to estimate the transmission. Within the local patch, for each pixel, the intensity difference between it and the other pixels is calculated. The pixels which have the minimal distances are retained as having the same transmission value.

**Step 5** After the estimation of  $A$  and  $t$ , the clear image is usually recovered using Equation 3.3.  $t_0$  is introduced in the denominator to avoid zero values and to maintain a natural image with some amount of haze. The majority of the following up DCP-based methods use the same equation. However, in their paper that considers sandstorm images, Huang *et al.* [74], the atmospheric light is no more achromatic, thus, at the final step of dehazing, a color correction is needed. The clear image  $J$  is calculated as follows for each pixel  $x$ :

$$J^c(x) = \frac{I^c(x) - (A^c - d^c)}{\max(t(x), t_0)} + (A^c - d^c) \quad (3.8)$$

where  $c$  denotes the color channels R, G and B.  $d^c$  denotes the difference between the average values of the red and  $c$  channels of the image  $I$ .

**Applications using DCP and its derivatives** Besides the outdoor applications used in bad atmospheric conditions, DCP is used and adapted in a wider range of applications. For instance, there are common features and mechanisms within the underwater and outdoor environments. Underwater images, like images captured in bad weather, have a weak quality, which is caused by the scattering and the absorption of light by the particles suspended in water, with significant size and density. All of these mechanisms reduce the overall image quality and turn underwater photography into a challenging task [15]. These images usually suffer from poor visibility, low contrast, blur, non uniform lighting and color distortions.

Scattering and absorption, which are assumed to be wavelength-independent in a foggy day, they are not in underwater environment [40].

**How did DCP gain this popularity?** Despite its drawbacks, there are few reasons lying behind its success over its contemporary methods.

- It is based on a simple, logical, robust and real assumption derived from a statistical characteristic of outdoor natural images.
- It does not introduce any pre-processing adjustment to dehazing. Parameters are estimated from the original values.
- From the marketing side, unlike its contemporary methods, especially Fattal and Tan approaches, He *et al.* succeeded to attract the interest of researchers by providing the whole code of their algorithms.

During the same period, two single dehazing approaches have been released: Fattal and Tan approaches [52], [165].

**Fattal's approach** In his work [52], Fattal decomposed the unknown radiance image  $J$  as a pixelwise product of surface albedo coefficients  $R$  and shading factor  $I$ , that he assumed to be locally uncorrelated. Then, he broke  $R$  into two components. One parallel to the airlight and a residual vector which is orthogonal to it.

Based on the above assumption, the atmospheric light  $A_\infty$  is estimated using the Independent Component Analysis (ICA) algorithm [76]. Likewise, the transmission  $t$  is calculated using ICA and the Gauss-Markov random field model [140].

Like DCP, Fattal's approach is based on a statistical assumption. So, it greatly depends on the input image. Moreover, it seems to be not effective at dense fog.

**Tan's approach** Tan *et al.* [165] proposed a method based on two basic observations. The clear-day images have more contrast than images in bad weather. Second, airlight with the variation depends mainly on the distance of objects to the viewer, tends to change smoothly in small local areas.

After applying the white balance operation to transform the input image into white color, the atmospheric light is estimated as the highest intensity of the image. The atmospheric light, like the many other methods, is estimated by the highest intensity of the input image. Afterwards, the airlight is modeled using the Markov Random Field (MRF) by maximizing the local contrast of the image. The main purpose of this algorithm is not to recover the original color or reflectance of the images, but to enhance the visibility of scenes in bad weather with some degree of accuracy on the scene colors.

The main drawback of this method is the over-saturation of images' pixels. Thus, dehazed images seem unnatural (see Figure 3.5). Moreover, some halo artifacts caused by the patch-based operations, especially on depth discontinuities, may also appear on the final result.

**Fast visibility restoration** Considering the intensity of the airlight at location  $x$  in the scene as:  $V(x) = I_s(1 - e^{-kd(x)})$ , the hazy image is represented by an alternative equation of the Equation 2.16 [167]:

$$I(x) = R(x)(1 - \frac{V(x)}{I_s}) + V(x) \quad (3.9)$$

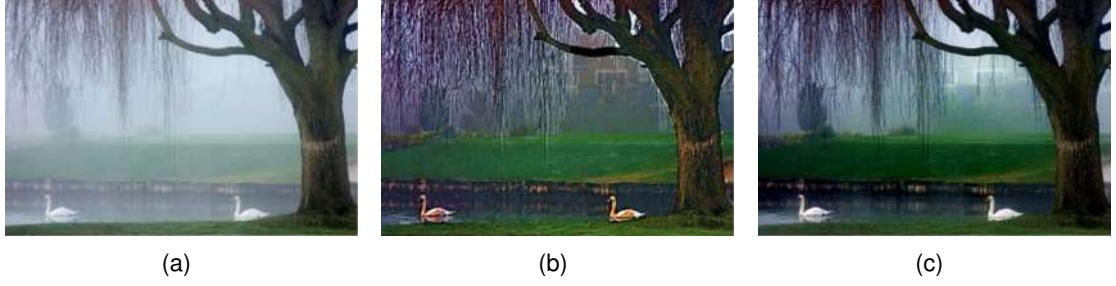


Figure 3.5: (a) Hazy image. (b) Tan's result. (c) DCP's result. Images are borrowed from the Figure 8 of the paper of He *et al.* [70].

where  $I(x)$  is the observed image intensity;  $R(x)$  is the image intensity without haze;  $I_s$  is the intensity of the atmospheric light;  $V(x)$  is the atmospheric veil, which is calculated instead of the depth map.

Considering the haze model, the processing consists of the following steps:

1. **Estimation of the atmospheric light:** it is done by applying a local white balance prior to dehazing. Thus, atmospheric light is set to  $(1, 1, 1)$ . A local white balance performs better when the light color changes along the image.
2. **Inference of the atmospheric veil:** Atmospheric veil is subject to the constraint:  $0 \leq V(x) \leq W(x)$ , where  $W(x) = \min(I(x))$  is the whiteness image. In his paper [165], Tan considered that restoration is an ill-posed problem and the solution can be obtained by maximizing the contrast of the image while assuming that the depth-map must be smooth except along edges with large depth jumps. Here, the same problem is reformulated as maximizing  $V(x)$  and assuming that  $V(x)$  is smooth most of the time.  $V(x)$  is optimized as follows:

$$\underset{V}{\operatorname{argmax}} \int_{(x)} V(x) - \lambda \Phi(\|\nabla V(x)\|^2) \quad (3.10)$$

$\lambda$  controls the smoothness of the solution,  $\Phi$  is an increasing concave function allowing large jumps. Indeed, when the atmospheric veil  $V(x)$  does not show clearly the edges, an incorrect halo appears when complete smoothness is enforced. This implies that the local average of  $W(x)$  must be performed using a smoothing algorithm which preserves large jumps along edges. Thus, bilateral filter or fast median filter could be applied:

1. The local average of filter of  $W$  is computed as:  $A(x) = \operatorname{median}_{s_v}(W(x))$  where  $s_v$  is the size of the filter window.
2. Then, to take into account that areas with contrasted texture are probably not hazy, the local std of  $W(x)$  is subtracted from  $A(x)$ . Again, to be robust to outliers, this std must be estimated in a robust way by applying the median filter on  $|W(x) - A(x)|$ :

$$B(x) = A(x) - \operatorname{median}_{s_v}(|W - A|)(x) \quad (3.11)$$

3. The last step consists on multiplying  $B(x)$  by  $p \in ]0, 1[$  to control the strength of the visibility restoration. The values of  $pB(x)$  do not necessarily respect the constraints on  $V$  and thus are thresholded:  $V(x) = \max(\min(pB(x), W(x)), 0)$ .

In order to preserve edges as well as corners with obtuse angles, an original filter named Median of Median Along Lines is introduced [167].

- 3. Estimation of the radiance:** Based on the Equation 3.9, when  $V$  is calculated, image radiance is deduced as follows:

$$R(x) = \frac{I(x) - V(x)}{1 - \frac{V(x)}{I_s}} \quad (3.12)$$

- 4. Post processing enhancement** The recovered radiance usually suffers from compression artifacts and noise, which is amplified through inversion process (see Section 3.2.5) and it has as well a higher dynamic than the original hazy image.

In order to soften the noise and artifacts issue, a local smoothing is applied to the image. For better comparison between the input and the output image and between the output images of different algorithms, it is important to always apply tone mapping.

**Fusion strategy** The fusion strategy denotes here the fusion of several images derived from the same hazy image. The fusion technique (FUSION) introduced by [13, 11] consists in combining white balancing and contrast enhancement via a linear transformation. The two images are then weighted by multiplying three weight maps: luminance, chromatic and saliency weight maps. The image is then smoothed by Laplacian and Gaussian pyramid to reduce artifacts introduced due to the weight maps. According to Sahu [152], the fusion based image dehazing leads to better results than any other techniques. This method considers visual informations: saliency and specifically color and chromatic effect of airlight. Such method is not suitable for inhomogeneous fog, since it does not consider depth information.

### 3.2.2.2/ IMAGE ENHANCEMENT METHODS

Image enhancement methods consider mostly the subjective judgment of humans. They mainly aim to improve the image contrast by local histogram equalization and to adjust the colors of the image in order to make an image look better with vivid colors.

**Dehazing using CLAHE** Xu *et al.* [187] presented a CLAHE-based method to restore fog degraded color images. Unlike the ordinary histogram equalization, in CLAHE method (Contrast Limited Adaptive Histogram Equalization) [142], we determine a maximum value to clip the histogram and redistribute the clipped pixels equally to each gray-level. This prevents as well the over-amplification of noise through image restoration.

In this method, RGB image is first converted into HIS color space, to handle lightness separately from hue and saturation. The reason of conversion is that, the HSI represents color similarly to how the human eye senses colors. Second, the intensity component of the image is processed by CLAHE. Hue and saturation are unchanged. Finally the processed image is converted back to RGB.

**Variational approach** Galdran *et al.* [56] assumed that the physical model is too simple to be able to model the real situation, and it fails to handle the change of the size of atmospheric particles and the non-uniformity of the illuminant as the brightness of the atmosphere is spatially variant. They proposed, a variational framework (VAR) for image dehazing that deals with spatially-variant features. It performs contrast enhancement on hazy regions of the image throughout an iterative procedure allowing to control the degree of restoration of the visibility in the scene, while considering white patch assumption adapted to haze-free images, thus respecting the colors of the haze-free image. In a further work [57], an additional energy term was added to control the degree of saturation of the processed image. This term avoids obtaining over-saturated results. This method is selected as an iterative enhancement representative.

This method is not dedicated to image dehazing, it can be applied on any other image for contrast enhancing purpose. This is due to the fact that the contrast is enhanced no matter how it has been degraded. While contrast improvement through dehazing consists in estimating the scene transmission which is depth-dependent. Once physical characteristics of the hazy scene formation is respected, dehazing process would maintain better original features.

### 3.2.3/ MULTIPLE IMAGES DEHAZING

More than a single image imply the use of a special equipment, such as polarizers are required, or some scenes taken under different weather conditions, or maybe various image types. In this section, methods dealing with two input images are presented: first, a method that considers images taken under different weather conditions. Second, a method that uses the dissimilarity between RGB and infrared images, which may be acquired by a single sensor [170], [88]. Third, a method that manipulates images with different polarizing angles [158], [162], [156]. Perhaps these methods are not suitable for many applications since they require a considerable effort and cost in terms of user interaction, time and complexity. In light of this, methods of this category cannot be used in applications requiring autonomous control. Thus, little work exists in this domain, since in addition to what is mentioned before, they do not provide more enhanced results comparing to single image dehazing methods.

**Contrast restoration from two or more weather conditions** Narasimhan *et al.* studied widely the dehazing from various images taken under different weather conditions [125, 127, 128]. For this purpose, they created as well a database of real images of different conditions of the same outdoor scenes [130] (see Section 4.3.1).

Considering the mechanisms of atmospheric scattering, the attenuation and the airlight (cf. Section 2.3.2), Nayar and Narasimhan presented a color model called dichromatic model, which represents the color of a scene point  $C$  as the vector sum of the color of the direct transmission  $\hat{A}$  and the airlight color  $\hat{B}$ :

$$\begin{aligned} C &= p\hat{A} + q\hat{B} \\ &= \frac{E_{\infty}re^{-\beta d}}{d^2}\hat{A} + E_{\infty}(1 - e^{-\beta d})\hat{B} \end{aligned} \quad (3.13)$$

This linear relation between  $C$ ,  $\hat{A}$  and  $\hat{B}$  leads to plot these points on the same dichromatic plane of the color space RGB. Since the units of  $\hat{A}$  and  $\hat{B}$  of a given scene point do



not change between different weather conditions,  $C_i$  and  $C_j$  taken under the weather conditions  $i$  and  $j$  can be plotted as in Figure 3.6.

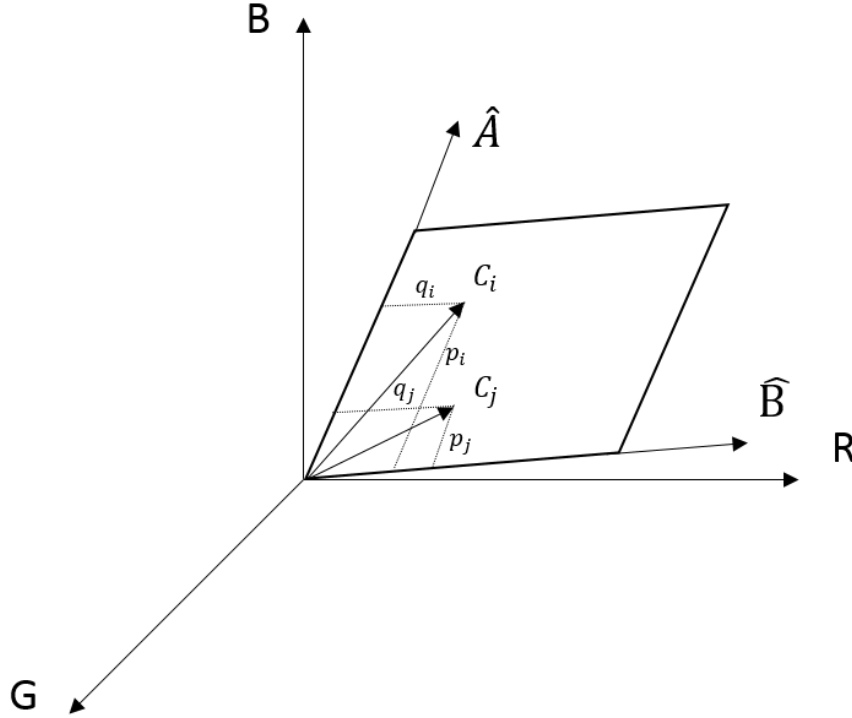


Figure 3.6: The estimated color coordinates of the same scene point taken under two different weather conditions  $i$  and  $j$  are plot on the same plane in the RGB color space. These coordinates differ from each other by the magnitudes of  $\hat{A}$  and  $\hat{B}$ . This figure has been modified from Figure 1 of the paper of Narasimhan *et al.* [128].

Considering two points of the same scene  $P^1$  and  $P^2$ , the color of each one of them lies on its own plane. These planes share the same airlight color with different magnitudes. Thus, the airlight color vector  $\hat{B}$  represents their intersection (see Figure 3.7).

Based on this chromatic framework and these assumptions, through a geometrical way, for every point in the scene we compute the brightness in both weather conditions from non-sky regions only, and we deduce therefore the structure of the whole scene.

**Dehazing using near infrared** Near-infrared light has stronger penetration capability than visible light due to its long wavelength. So, this light is less scattered by particles in the air. The advantage of deep penetration of NIR makes it possible to unveil the details, which could be completely lost in the visible band. The dissimilarity between RGB and NIR can be exploited to estimate the airlight color. A key step in such a scene recovery is subtraction of the airlight.

The hybrid VIS-NIR dehazing method proposed in [53], consists of two main steps:

- Airlight color is estimated by the dissimilarity between RGB and NIR:
  - Considering that  $t(x)$  depends on the scene depth  $d$  and the density of haze  $\beta$ ;

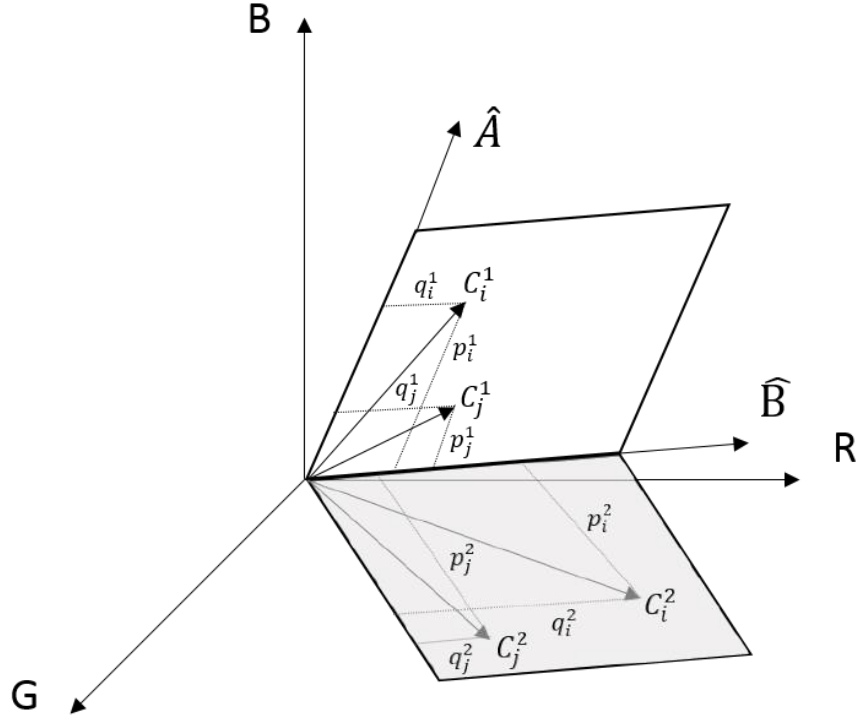


Figure 3.7: The estimated color coordinates of two points  $P^1$  and  $P^2$  of the same scene are plot on two different planes in the RGB color space.

- $J$  depends on the illumination of the scene and the surface reflectance.
- Thus, it can be assumed that  $J$  and  $t$  are not correlated within a local patch. The idea proposed here consists in finding a local patch with pixels having large similarities, followed by searching an airlight color that leads to the smallest correlation between  $t$  and  $J$ .

Thus, two criteria should be fulfilled:

- \* C1: pixels within the patch should have intermediate level of haze, so that both  $J$  and  $A$  contribute to the observed intensity values  $I$  in the equation.
- \* C2: pixels within the patch should have similar properties such as surface reflectance.
- A haze map is generated first to find pixels that satisfy C1 and then adopt RGB-NIR relationship to meet C2.
  - \* Haze increases the intensity value over all R, G, and B channels and this reduces the image contrast. The smallest intensity value over the three color channels infers the density of the haze.
  - \* In order to refine the density of the haze, the difference between NIR and RGB is calculated.

$$H = \min\left\{ \min_{K \in \{R, G, B\}} (I^K), D \right\}, D = N\{|I^B - I^{NIR}|\} \quad (3.14)$$

- \* In order to meet the criterion which consists of having a patch that contains an intermediate level of haze. Therefore, the image histogram of  $H$  is



generated, and the first valley  $h$  of the histogram is used as a reference to select a coarse patch region  $\Omega_c$ . Pixels within  $\Omega_c$  should have similar haze density, and the similarity is defined by  $\gamma$ :

$$\Omega_c = x : |H(x) - h| \leq \gamma \quad (3.15)$$

Within these patches, a searching process is made for an airlight color  $A$  that leads to the smallest correlation between  $J$  and  $t$ .

$$A = \arg \min_{\forall(x) \in \Omega} C(J, t)^2 \quad (3.16)$$

C: Pearson's correlation coefficient

- Enforcing the NIR gradient constraint through an optimization framework:
  - The initial transmission map is defined as follows:

$$t_i = 1 - \min_{k \in \{R, G, B\}} \left( \frac{I^k}{A} \right) \quad (3.17)$$

- The initial haze-free image:

$$J_i = \frac{I - A}{\max(t, \epsilon)} + A; \epsilon = 0.1; \quad (3.18)$$

Based on the Baye's theorem, the optimal solution for  $J$  and  $t$  is found by solving the following optimization problem:

$$\begin{aligned} (J, t) = \operatorname{argmin} \bigg\| & tJ + (1 - t)A - I^{RGB} \bigg\|^2 \\ & + \lambda_1 \omega \left| \nabla J - \nabla I^{NIR} \right|^\alpha \\ & + \lambda_2 \left| \nabla J \right|^\beta + \lambda_3 \left| \nabla t \right|^2 \end{aligned} \quad (3.19)$$

By solving the optimization problem stated in Equation 3.19 using Iteratively Reweighted Least Squares (IRLS) with initialized  $J_0$  and  $t_0$  derived from Equation 3.17 and Equation 3.18, the haze-free image  $J$  and the transmission map  $t$  simultaneously recovered.

**Dehazing using polarizing** Here, we find another way to enhance a dehazed image issued from two images differently polarized. Polarization angles are:  $\theta_1 = 0^\circ$  and  $\theta_2 = 90^\circ$ . One of the causes of light polarization is the scattering. Scattered airlight intensity is divided into two components:  $A^\perp$  and  $A^\parallel$  that are parallel and perpendicular to the plane of incidence, which is defined by the camera, the scattering particle and the sun. The degree of polarization is defined as follows:

$$P \equiv \frac{A^\perp - A^\parallel}{A} \quad (3.20)$$

where the airlight  $A$  is formed as:

$$A = A^\perp + A^\parallel \quad (3.21)$$

Only when the light source is normal to the viewing direction, the airlight is totally polarized ( $P = 1$ ). In other words, the airlight is totally perpendicular to the plane of incidence. It

can be eliminated if the image is captured through a polarizing filter oriented parallel to this plane. The polarization decreases as the direction of illumination deviates from  $90^\circ$ . So, the degree of polarization decreases by depolarization. Since that, the scattering of the directly transmitted  $t$  light does not change the polarization state of the incident light. The polarization of the direct transmission is insignificant.

$P$  does not depend on the distance, since polarization degree does not change along the line of sight.

**Image Formation** The intensity which hits the sensor without polarizer is defined as:

$$I^{total} = t + A; \quad (3.22)$$

When a polarizer is mounted, the captured intensity changes with the polarizer orientation angle  $\theta$ :

$$I = I_{max} \cos^2(\theta) \quad (3.23)$$

As stated above, an intensity variation is only due to the airlight:

$$I^\perp = \frac{t}{2} + A^\perp \quad (3.24)$$

$$I^\parallel = \frac{t}{2} + A^\parallel \quad (3.25)$$

The best state is to have  $I^\parallel$ , because the captured intensity is the closest to the direct transmission. Thus, in order to recover  $t$ , we have to compare two images taken with two different polarizer's orientations, and then we remove the airlight. Comparison process starts by removing the airlight. In order to do so, we estimate  $P$ :

when the scene's depth  $d \rightarrow \infty \Rightarrow I^{total} \rightarrow A_\infty$ :  $P = \frac{I^\perp - I^\parallel}{I^\perp + I^\parallel} \Rightarrow P = \frac{A_\infty^\perp - A_\infty^\parallel}{A_\infty^\perp + A_\infty^\parallel}$ .  $A_\infty$  is the highest intensity value of the image. It is usually estimated by measuring a patch of the sky at the horizon.

Once the parameters  $A_\infty$  and  $P$  are estimated, the remaining parameters are calculated as follows:

Airlight  $A$ :

$$A = \frac{I^\perp - I^\parallel}{P} \quad (3.26)$$

Transmission  $t$ :

$$t = I^{total} - A \quad (3.27)$$

Attenuation factor:

$$e^{-\beta d} = 1 - \frac{A}{A_\infty} \quad (3.28)$$

And finally, the scene radiance:

$$J = \frac{t}{e^{-\beta z}} \quad (3.29)$$

Although we are mainly concerned with the single RGB image dehazing, this does not mean that these methods are useless. In this study there is a preference for methods, which require all minimal data of the same nature. Otherwise, the comparison is no more

fair. A method that estimates parameters based on assumptions is not equal to a method that handle provided parameters.

Dehazing being an image processing mostly needed for real time applications, it does not tolerate a long processing time. The aforementioned methods, in their current forms, they can serve the research interests in seeking potential development paths. They serve also to point out the efficiency of an acquired parameter, that initiates the researches to find a way to estimate it automatically.

### 3.2.4/ DEPTH MAP DEHAZING

An accurate dehazing logically requires precise weather and depth information. For their part, Srinivasa *et al.* [128] assumed that a good dehazing could be performed without precise depth information. One argument was that, within small depth ranges, using a camera with limited dynamic range does not capture subtle effects created by bad weather. Thus, they proposed a single image dehazing based on depth approximation provided by the user, who selects a minimum distance (good color region) and a maximum distance (airligh color). The distances in between are calculated trough interpolation. This method is not suitable for images with depth discontinuities such as urban scenes. Since planar surfaces in such scenes are assumed to have similar brightness, using urban scenes from WILD database (refer to Section 4.3.1), planes of depth are derived from satellite orthophotos.

Later on, Kopf *et al.* [86] assume that a simple user interaction aiming to align a photograph with a georeferenced digital terrain and urban models such as Google Earth and Microsoft's Visual Earth feeds the haze model by useful data such as depth and texture information. Once the depth is known, haze can be removed accurately.

Although this strategy achieves dehazing with competitive results with no additional equipment, it is not automatic and it needs the estimation of some parameters.

### 3.2.5/ HAZE AND NOISE REMOVAL

Hazy and dehazed images usually contain some noise. This is mainly due to the environment (extrinsic noise) and the sensor (intrinsic noise) and it is remarkably amplified by dehazing (Equation 3.31). Accordingly, since the exponential attenuation comes quickly down to zero, the noise is greatly amplified for high fog densities and long distances [86, 48].

While the majority of dehazing methods ignored the noise and its effects, some researchers have addressed simultaneously haze and noise issues. Let us explain the importance of such enhancement approaches.

A hazy image containing an amount of noise that comes from the environment and the sensor is modeled as follows:

$$I(x) = J(x)t(x) + A_{\infty}(1 - t(x)) + n(x) \quad (3.30)$$

where  $n(x)$  denotes zero-mean Gaussian noise having variance  $\sigma^2$ .

The estimation of the scene radiance, by simply inverting Equation 3.30 gives the follow-

ing equation:

$$\hat{J}(x) = A_{\infty} + \frac{I(x) - A_{\infty}}{t(x)} - \frac{n(x)}{t(x)} \quad (3.31)$$

where  $t(x) \in [0, 1]$ . In the best case, for an image without haze,  $t(x) = 1$ , the noise remains the same after dehazing if it is not removed before. When the  $t(x)$  has a lower value, the noise is amplified. It dramatically increases in very hazy regions or for very far objects, where  $t(x)$  is close to zero.

There are two main approaches to deal with haze and noise. The first one is to dehaze and to denoise in a step by step manner (denoising followed by dehazing and vice versa). The second one is to dehaze and denoise at the same time.

According to Equation 3.31, when denoising is performed after dehazing, the noise is no more uniform through the image, since it is exponentially amplified with the fog density. Thus, a standard space-invariant denoising method is not efficient. In an outdoor image, it might over-smooth the objects near to the camera, which have a low noise and smooth insufficiently the distant objects, which are very noisy. To avoid this problem, Kaftory *et al.* [81] presented a variational denoising method based on a regularization operator, which is distance dependent. Comparing to the Non-Local Means filter [26], the variational approach achieves the denoising of the variant noise with more accuracy.

Matlin and Milanfar [113] proposed two dehazing algorithms associated to denoising in two ways. In the first one, to avoid the amplification of noise generated as a result of Equation 3.31, the denoising is first applied to the hazy image using the color image denoising method BM3D [36] (refer to Section 6.3.6) to lower the noise factor  $n(x)$  in the hazy image (Equation 3.30). Any other linear denoising method can be applied, since the noise in hazy images is spatially no variant, unlike the dehazed images when the noise is exponentially amplified with the fog level. The DCP is then applied. This method produces an improved dehazed image against dehazing without denoising, if and only if the variance of noise is accurately known and used as a parameter for denoising. In practical cases, it is highly likely that the variance is not exactly estimated, thus this approach does not bring any particular benefit for outdoor and real-world applications, where the original haze-free image is not available.

In the second one, dehazing and denoising are performed simultaneously through an iterative process using non-parametric regression method, which is tuned by the Mean Squared Error (MSE) results. This approach overcomes the first one when the noise is not known, thanks to the iterative process.

Based on the conclusions of the previous works and the fact that when denoising is applied prior to dehazing, this may cause a loss of information on image fine details, Nan *et al.* [124] proposed a simultaneous dehazing and denoising processing based on a bayesian iterative approach tied to statistical prior, by considering that the signal and the noise are uncorrelated. It is tied also to objective assumptions by considering that the distribution of the chromaticity gradient histograms of the hazy and the haze-free images are the same, and according to the green sensitivity in the human visual system, the transmission is accurately estimated from the green wavelength. A factor is defined to ensure through an iterative way the balance between the amount of removed noise and the edge information in the transmission map.

The variational dehazing method presented in [56] does not deal with the noise and it is a general contrast enhancement method, which can be applied for dehazing and other enhancement purposes. Unlike this method, Fang *et al.* [50] dealt simultaneously with

haze and noise through a variational approach consisting of two steps. The estimation of the transmission  $t$  is done using windows adaptive method that only considers patches with no large differences in intensities, since the presence of an edge within the local patch makes the constant assumption of  $t$  no more correct. The estimated transmission is then converted into a depth map. The energy functional includes dehazing and denoising, simultaneously. The minimization of this function is based on the assumption that the radiance and the depth are piecewise constant.

### 3.2.6/ NIGHTTIME HAZE REMOVAL AND MULTIPLE LIGHT COLORS

Nighttime dehazing is important for the same applications as daytime dehazing (cf. Section 3.1) when they are used over night. The dehazing methods that have been proposed to deal with the daytime hazy images are not efficient for nighttime hazy images. This is due to the large dissimilarities between them (see Table 3.1).

When there is no haze, clear nighttime images comparing to daylight images, they suffer from low overall contrast, low overall brightness, desaturation, loss of acuity, visible noise and "blue shift" airlight color [171].

Therefore, the nighttime dehazing is more challenging than the daytime dehazing.

Table 3.1: Nighttime vs daytime hazy images

Nighttime hazy image	Daytime hazy image
Artificial light source	Natural light source
Non-uniform illumination from the artificial light sources	A uniform illumination usually covers the image
Blow effect	No blow effect
Low overall brightness	High overall brightness
Low contrast	Low contrast
Chromatic atmospheric light	Achromatic atmospheric light

A few dehazing methods dealing with nighttime images have been proposed. In this scenario, DCP finds again a place. Pei *et al.* [139] proposed a nighttime dehazing method based on the refined DCP. This means that, the original image is first transferred into a grayish one by applying the color transfer method [148]. This transformation has been done to fulfill the hypothesis of the DCP, which is then applied with the guided filter to the transferred image. After this operation, the contrast of the processed image still seems dim and unclear. Therefore, the Bilateral Filter in Local Contrast Correction (BFLCC) [159] is applied as a post-processing to improve the overall dehazed image quality.

A little later, Zhang *et al.* [194] have proposed another method based on a new imaging model for nighttime haze condition, that takes into account in addition to the haze effects, the non-uniform light and the color feature of artificial light source. And they assumed that the color transfer applied to the input image in [139], changes in a remarkable way the original colors and it provides unrealistic dehazed images.

The nighttime haze condition is modeled as Equation 3.32:

$$I_i^c = L_i t_i^c R_i^c t_i + L_i t_i^c (1 - t_i) \quad (3.32)$$

where  $I_i^c$  is the captured hazy image,  $c$  denotes one of the channels R, G and B,  $t_i$  and  $R_i^c$  are the transmission and the reflectance at location  $i$ .  $L_i$  and  $t_i^c$  are scalars that represent the intensity and the quantity accounts for the color characteristic of the incident light at location  $i$ , respectively.

Three main steps are performed in this method. The first one is the light compensation, which aims at removing the color casts and obtaining an image with adjusted illumination. The second one is the color correction that is done by removing the color characteristics of the incident light. The third one is the dehazing process through the DCP method, however the atmospheric light is estimated as being a local variable and it is not achromatic as in daytime dehazing. This is mainly due to the colors caused by the active sources of light.

Recently, Li *et al.* [97] proposed a new nighttime dehazing method based on a new model to override the previous one presented in [194] by considering the glow of active light sources and their light colors:

$$I(x) = J(x)t(x) + A(x)(1 - t(x)) + A_a(x) * K \quad (3.33)$$

In addition to the parameters that form the daytime hazy image model (Equation 3.33), the glow effect is modeled by a convolution between the active light sources  $A_a$  and the atmospheric point spread function  $K$  [129].

Considering this model, the glow image is first separated from the nighttime hazy image before being dehazed. The separation is based on the smoothness property of the glow layer, which decreases smoothly away from the active light. While the hazy image layer is less smooth [96]. The DCP is then applied to the hazy image with a simple adjustment, by estimating locally the atmospheric light as being the brightest intensity of each local patch in the image.

### 3.2.7/ VIDEO HAZE REMOVAL

As we have seen earlier in this dissertation, a good number of image dehazing algorithms have been proposed. In real-world applications, two inseparable constraints are imposed: the good performance and the real-time of visibility enhancement. Video can be defined as a group of frames (images). Thus, dehazing should be applied consecutively on frames, which are combined later to form back the dehazed video. The time of this process depends directly on the frame size. Therefore, for video dehazing, in addition to the inaccuracies of image dehazing methods, the reduction of the process time remains an outstanding issue.

In contrast with image dehazing algorithms, only a few algorithms are proposed to deal with video visibility enhancement. However, such algorithms are more heavily utilized in daily activities. Most of video dehazing algorithms were proposed for video monitoring systems with a still background.

Let us have a look at what has been proposed for video dehazing. According to Xu *et al.* [185], video dehazing algorithms can be grouped into three categories: frame-based, fusion-based and universal component-based video dehazing. In the first one, dehazing is performed separately on each frame of the video. In the second one, for each frame, we merge the background and foreground images, which are separately enhanced. The

third one is characterized by the estimation of a universal component that can be used for all frames dehazing.

**Frame-based video dehazing** As an example of this category, Archa and Abdul [16] applied consecutively the FUSION algorithm explained above to each of the video frame. Such implementations are usually time consuming, especially when the video duration is long. They neglect both content and context interaction between adjacent frames that may lead to perceived discontinuities between the recovered data such as the color and the brightness of successive frames.

**Fusion-based video dehazing** Since the separation of the background and the foreground is done on each frame and they are singly dehazed, we come to the same problems evoked in the first category. In this category both physics-based and image enhancement methods have been used.

Referring to [186, 146], a separation of the background and the foreground is first done through the moving objects detection. CLAHE algorithm is applied to both of them and they are merged back to form the dehazed frame. CLAHE, which is based on histogram equalization, is fast, but it suffers from some inefficiencies (refer to Section 3.2.2.2).

In their turn, considering the haze model, John and Wilsby [80] estimated the global lightness once for the background image as well as the local lightness parameters of each foreground image. They are both used for contrast enhancement. The global enhancement is done through a wavelet fusion method before merging back the image parts.

Yoon *et al.* [190] considered also the haze model by estimating the transmission map through the multiphase level set formulated from the intensity channel and the atmospheric light as the pixel of the highest intensity value in the HSV color space. In order to overcome the issues generated by the separate processing of the consecutive frames, without considering the temporal correlation between them, they applied a color correction through the adjacent frames.

**Universal component-based video dehazing** Since the consideration of the correlation between the properties of the consecutive frames such as color and brightness, is of great importance, a global component of the video sequence is estimated. This reduces the long computation issues. However, when the estimated transmission from the background is used as universal component, this may induce edge degradation and halo artifacts when there is a large difference with the background [185].

From the background image, Xie *et al.* [183] estimated the atmospheric light using DCP. The map transmission is estimated through a process of multiscale retinex (MSR), refined by a bilateral filter and denoised by total variation denoising filter. The final dehazed video is obtained after inverting the haze model.

### 3.2.8/ DETECTION AND CLASSIFICATION OF HAZY IMAGES

When we look at an image, we automatically recognize if it is hazy or not. We usually apply dehazing on these images to make them clearer. And we do not do so with haze-free



images, since we consider it of good quality. But, when it comes to real-world applications, there is a need to know if the captured image is covered by haze or not. Since the application of dehazing on clear images produces some adverse effects. It may produce an image of worse quality than the original clear one. It is likely to lost the original raw data acquired from the vision system. Dehazing is a time consuming process. Its application delays the following-up processing.

Few algorithms have been proposed whether to detect the hazy areas in a clear image, or to detect the presence of haze all over the image and to classify it later as hazy image.

### 3.2.8.1/ DETECTION OF HAZY AREAS IN IMAGES

Ancuti *et al.* [12] were the first to introduce an algorithm that allows the identification of hazy regions. It is based on the dissimilarity between the original hazy image and the semi-inverse hazy image, which is, for each channel, calculated as given in Equation 3.34:

$$I_{si}^c(x) = \max_{x \in I} [I^c(x), 1 - I^c(x)] \quad (3.34)$$

where  $c$  denotes one of the channels R, G and B.  $I$  is the original image and  $1 - I$  is its inverse image. This detection is based on the observations related to the image characteristics. The intensity values of pixels in sky and hazy regions are higher than those in haze-free and non-sky regions. Thus, in the inverse-image the hazy images keep the same appearance with enhanced contrast, while the clear regions appear as the inverse of the original image.

Therefore, after the renormalization of the inverse-image, the hazy regions are detected in the hue channel of CIE  $L^*c^*h^*$  color space. The clear pixels are those which have a large dissimilarity between the semi-inverse image and the original hazy image.

Although, this algorithm showed an acceptable precision on a large number of images, it fails to judge if the detected area was a hazy region, a white area or a sky region.

Another category of hazy area detection is based on the meteorological visibility distance. It is a measure defined by the International Commission on Illumination (CIE) as the distance beyond which a black object of an appropriate dimension is perceived with a contrast of less than 5% [33]. Hautière *et al.* proposed a daytime foggy area detection method used for on-board visual systems [69], [67]. Gallen *et al.* [58] addressed this issue that occurs overnight in two ways. The first is done by the detection of the back-scattered light from the headlights is toward the driver, when the vehicle is alone on the road and no other external light sources exist. Here, the detection is performed through the calculation of a correlation score between the captured image and the reference image that could be real or synthetic, sharing similar position, field of view and resolution. As soon as other light sources appear in the image, because of the low dynamic range of the camera the back-scattered light is no more detectable. Thus, the second way is done by the detection of halos around the sources of light within the vehicle's surrounding environment. Based on the intensity evolution of a halo, the light sources are detected, segmented and selected according to the halos directions and the distance between adjacent sources.



### 3.2.8.2/ CLASSIFICATION OF HAZY IMAGES

In order to determine whether an image is hazy or not and the level of haze present in it, we need to extract some effective features, which are widely different between clear and hazy images. An adequate classifier should be trained on these features using a large set of images different in context and content.

#### ***Which features are the most efficient for a reliable classification?***

Let us try to define what an efficient feature for hazy image recognition is. A good feature is able to judge efficiently the image category with a minimum doubt, whether it was single or associated to another feature. This feature should be extracted fastly to not delay the prospective post-processing.

This feature could be a quality metric for dehazing evaluation. However, the quality of dehazed images still need more investigation to be clearly defined and the quality indexes seem weak to provide an accurate judgment for various haze conditions (see Section 6.2).

Some previous works have used various characteristics that are supposed to recognize the hazy images. Yu *et al.* [192] extracted three main features by defining a threshold separating hazy and clear images. The threshold of these features was calculated from a large set of images. The image visibility measured by the number of visual edges, which is higher in clear images than hazy images. The global intensity of dark channel [70], which is higher in hazy images than clear images. The global image contrast, which is calculated through the variance over the patches of the image.

A number of hazy images and clear images have been used as training and test samples using Support Vector Machine (SVM). The classification showed a high accuracy.

In [198], the supervised learning model SVM has been also used for hazy image classification. Based on the fact that HSI represents more accurately the human perception than RGB, the variance over the image that denotes the contrast is analyzed through its three channels. Another feature considers the dichromatic atmospheric scattering model [132, 126] by calculating the angular deviation of the intensity of a pixel between the hazy image and the clear image of the same scene. This condition is usually not fulfilled, since the haze-free image is often not available.

Instead of considering local features such as lane markings, traffic signs and back lights of vehicles to detect the presence of fog on road images of on-board cameras, Pavlić *et al.* [137] considered global features deduced from the power spectrum of Fourier transform, which varies in shape between hazy and haze-free images, due to the contrast attenuation and blurring increasing caused by the haze.

## 3.3/ GAPS IN THE LITERATURE

### 3.3.1/ BACKGROUND

Dehazing methods are numerous. They handle haze removal in different manners, providing then no matching results (see Figure 3.8). If we consider a set of dehazed images of the same hazy image processed by different methods, we may come across a lot of questions concerning the method that provides the result of the highest quality. We may

wonder about the definition of the quality. If this means the best matching with the clear image. If this true, there is a need to have this image, which is not available in real situations.

Once we are able to deal with these points for a given fog density, we should seek this for other fog densities. Considering the simulated hazy images, which seem as a simple solution to overcome the aforementioned points, there is a need to see to which extent do we really achieve a good simulation of the real situation by creating synthetic hazy images using the visibility degradation model.

### 3.3.2/ COLOR FIDELITY

Today, many application domains require to maintain color fidelity, where a real color represents a fundamental property of objects as mentioned by Helmholtz: "Colors have their greatest significance for us in so far as they are properties of bodies and can be used as marks of identification of bodies." [73].

Considering Figure 3.9, several questions come to mind. Dehazing enhances scene visibility by increasing contrast and saturating pixels. Does dehazing only saturate colors without affecting hue? How far color fidelity is maintained when haze increases? If the color is critically modified, how such shift could be quantified and adjusted, especially when original clear image is not available?

To deal with the color recovery, we selected the popular DCP approach and applied it in order to calculate the elements we need to calculate: airlight, transmission and image radiance. A colorimetric comparison study is conducted between the original clear image and the enhanced image.

According to Mie scattering, which is non-wavelength dependent, all light wavelengths are identically scattered. Unlike underwater degradation, where colors fade proportionally throughout distance [155]. Therefore, haze model is not dependent on wavelength. It is only dependent on the distance between object and camera, and the amount of haze covering the scene. This means also, that there is no shift in hue of the original color of a scene point when it is covered by haze. Therefore, we try to address this topic from the perceptual side. The perceptual hue could be differently interpreted even if the hue does not physically change when a scattering layer is applied.

According to [108], besides luminance contrast reduction, haze displaces chromaticities towards the white point. Consequently, it reduces the purity and the colorfulness of the scene. Because of chromatic adaptation, this effect is independent of the color of haze. It depends on the amount and depth of the haze. The reduction fraction of luminance contrast is approximately the same of purity reduction.

### 3.3.3/ EVALUATION OF THE COLOR SHIFT

#### 3.3.3.1/ COLOR SPACES

It is widely important to choose the adequate color space for a given processing and the suitable model to represent correspondent colors. Although the majority of dehazing methods use RGB color space, maybe the performance of dehazing will be better when



Figure 3.8: A hazy scene taken from CHIC database processed by five different dehazing methods: (a) CLAHE; (b) DCP; (c) FAST; (d) FUSION; (e) VAR. Dehazed colors are differently perceived across images.

using another color space. In this work, we use CIE XYZ to embed haze into image via convergence model (cf. Section 3.3.3.3). CIE LUV is used to evaluate saturation evolution



Figure 3.9: The color recovery of a hazy image treated by Tan's dehazing method. These images have been borrowed and modified from the Figure 10 of the paper of Tan [165].

with dehazing process, and IPT color space to assess hue shift.

CIE XYZ is a metrological color space and CIE LAB is a color appearance space dedicated to the evaluation of small color differences. Similarly, CIE LUV is conceived for the same goal, but embeds an analytical expression of color saturation, which is very convenient here. This is due to the fact that while CIE LAB performs the chromatic adaptation by dividing by the illuminant, CIE LUV rather performs a subtraction of the illuminant. Both of these spaces have the major limit of curved constant hue lines, thus they are not suitable for the part of our analysis which considers hue. Therefore, we used the IPT color space for this aspect.

Many papers reported that dehazing methods suffer from a common weakness: color fidelity deficiency [193, 62]. But this deficiency has never been clearly defined. This ambiguity pushes us to split up color components in order to precise how and how much each one is affected.

The perceptually uniform color space CIELUV clearly defines saturation [114]. This helps to point out through Equation 3.35 how far saturation is affected with dehazing algorithms:

$$s_{u,v} = 13[(u' - u'_n)^2 + (v' - v'_n)^2]^{1/2} \quad (3.35)$$

$u'$  and  $v'$  are the chrominance coordinates.  $u'_n$  and  $v'_n$  are the coordinates of the white point. The white point is the airlight color components. In synthetic image, airlight is the haze veil embed via convergence equation, and in real image it is the atmospheric light estimated by Dark Channel Prior (pixels with highest intensity of the hazy image among the top 0.1% brightest pixels in the dark channel).

The IPT space was designed to be a simple approximation of color appearance specifically designed for image processing and gamut mapping [43]. It is designed with fixing the hue nonlinearity of CIE LAB. It consists on a linear transformations, along with some non linear processing. The second linear transformation goes from non linear cone sensitivities to an opponent color representation. Unlike other color spaces, such as CIE XYZ, IPT is characterized by having a very well aligned axis for constant hue. It has a simple formulation and a hue-angle component with good prediction of constant perceived hue. I, P and T coordinates represent the lightness dimension, the red-green dimension and



Figure 3.10: Hazy input image and dehazed output image obtained by DCP. In order to investigate the influence of dehazing with depth on both saturation and hue, we select pixels at red and green points, which are supposed to have the same initial color, located at different depths and covered by a uniform haze veil. These images have been borrowed and modified from the Figure 7 of the paper of Tan [72].

the yellow-blue dimension, respectively. Using a converting  $3 \times 3$  matrix, when  $I$ ,  $P$  and  $T$  are computed from LMS, which is a color space representing the sensitivities of the human eye cones at long, medium and short wavelengths. The hue angle can then be computed through Equation 3.36 by inverting the tangent of the ratio of  $T$  to  $P$ :

$$h_{IPT} = \tan^{-1}\left(\frac{T}{P}\right) \quad (3.36)$$

### 3.3.3.2/ REAL HAZY IMAGES

In Figure 3.10, we consider a real hazy image and its correspondent dehazed image obtained by the dehazing method DCP (intentionally selected since it is a physical-based method (see Section 3.2.2.1), saturation and hue are evaluated on a real image, where unlike synthetic image, transmission light emanating from far objects undergoes a severe attenuation. We chose two points, red and green, which are supposed to have the same initial color, located at different depths and covered by a uniform haze veil.

According to Figure 3.11 that shows the quantitative variation at both locations in terms of saturation and hue through dehazing process, there is a noticeable difference, which is higher for saturation.

Considering the saturation rate, dehazing is more efficient at scene's points, which are near to the camera and covered therefore by less haze. This is shown by the saturation value at the red point after dehazing, which is significantly higher than the correspondent value at the green point. Moreover, the difference between the saturation values before and after dehazing is greater at the red point. This reflects a good efficiency in the color recovery for near objects and light haze as well.

When it comes to the hue evolution through dehazing, considering the difference rate at both points, dehazing maintains the hue information at red point better than at the green one. Although, there is a difference in both components, the dehazing acts much more on the saturation than the hue.

Globally, DCP enhance the saturation and maintain the hue information at near objects,



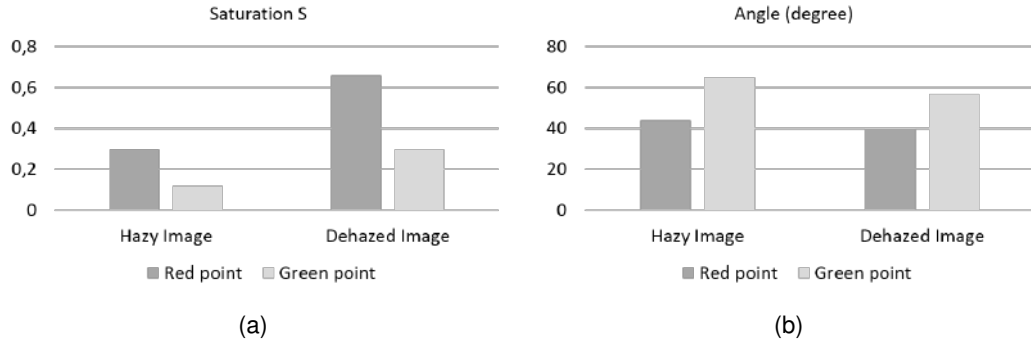


Figure 3.11: (a) Saturation difference and (b) IPT angle difference at red and green dots in hazy and dehazed images. When dehazing is applied, both points are saturated. The green point, which is covered with much haze is less saturated. The difference of hue angle at the green point is larger. This reflects the failure of dehazing to provide accurate recovery of colors hue at far objects and high haze density as well.

which are covered by less haze, better than at far objects, which are basically covered by more haze.

### 3.3.3.3/ COLOR TRANSPARENCY MODEL

When a colored object is viewed simultaneously partly directly and partly through a transparent filter but still perceived as the same surface, we talk about color transparency. Translation and convergence in a linear trichromatic color space are supposed to lead to transparency perception. Humans are naturally able to separate chromatic properties of the transparent filter and the seen surface. Referring to [116], with overlapping surfaces, three conditions are needed to perceive transparency: the uniformity of the transparent filter, the continuity of its boundaries and an adequate stratification.

The effects created by the haze in the images depend on the scene depth and the haze density. The attenuation rate of the transmitted light increases exponentially when the scene depth and/or the haze intensity increases ( $t(x) = e^{-\beta \cdot d(x)}$ ). However, convergence model handles transparent filter without depth dimension.

According to [41], translation and convergence in CIE xy lead to the perception of transparency. It has been revealed that in presence of fog, color constancy can be modelled by convergence model while taking into consideration shift in color and contrast. This was confirmed with asymmetric matching task described in [64].

Fog is simulated with convergence model as follows:

$$b = (1 - \alpha)a + \alpha f \quad (3.37)$$

where  $a = (X_a Y_a Z_a)$  represents the tristimulus values of a surface, a convergence application leads to new tristimulus values  $b = (X_b Y_b Z_b)$ .  $f = (X_f Y_f Z_f)$  is the target of convergence.  $\alpha$  represents the amount of fog covering the surface: no fog when  $\alpha = 0$  and opaque fog when  $(\alpha = 1)$ .

Fog differs from a transparent filter because chromatic effects of fog increase with depth, as the amount of fog intervening between surface and viewer increases. Unlike the transparent filter, fog imposes a chromatic shift on underlying surfaces that depends strongly

on the depth of a surface behind the filter. Referring to Hagedorn *et. al* [64], observers discount two aspects of the chromatic properties of fog: reduction in contrast and shift in the colors of lights from surfaces. Convergence model allows us to recover this shift. How does haze model meet this consideration?. As we mentioned above,  $\alpha$  includes simultaneously the haze intensity and the scene depth.

### 3.3.3.4/ SIMULATION

According to the convergence model, the simulation consists on embedding haze in CIE XYZ image. We applied the same model to RGB image in order to perform a cross validation with two different space basis. As it is shown in Figure 3.12, the original haze-free image is initiated as RGB and XYZ images. Haze was by R, G and B coordinates and the equivalent X, Y and Z were then calculated. It was added to both images through the convergence model. DCP is then applied to  $RGB_{RGB}^H$  and to  $XYZ_{RGB}^H$  hazy images, which are converted from  $RGB^H$ . It is applied also to  $XYZ_{XYZ}^H$  and to  $RGB_{XYZ}^H$ , which are converted from  $XYZ^H$ .

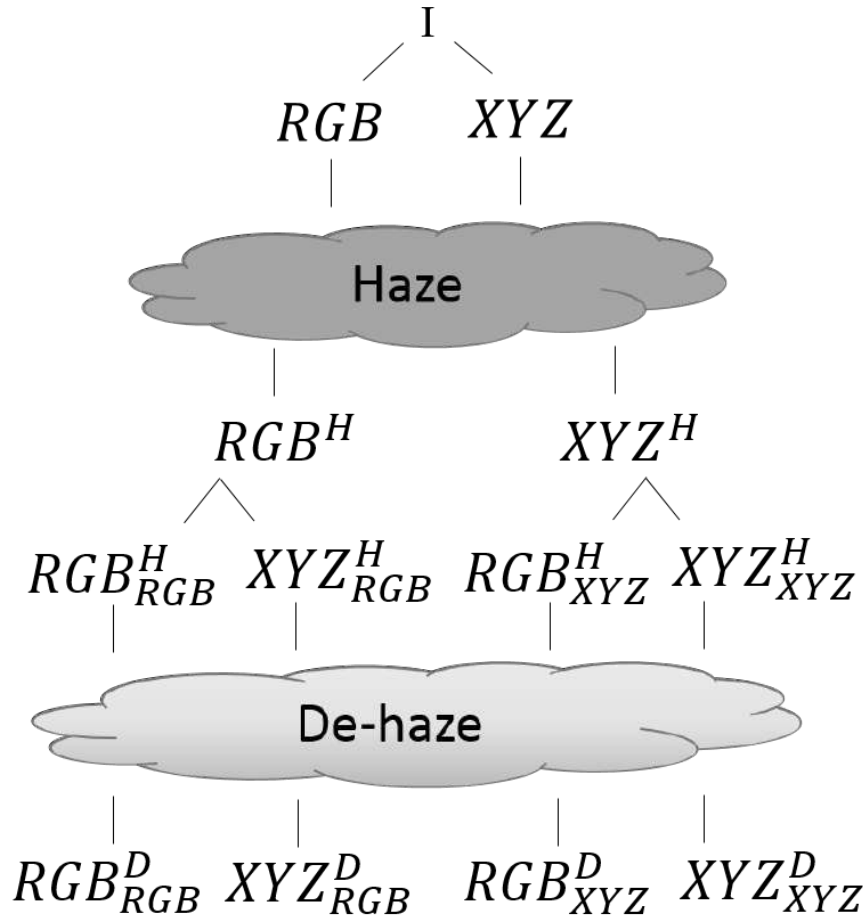


Figure 3.12: Flowchart of the synthetic formation of analyzed images

Four enhanced images are obtained for different values of  $\alpha$ . Three values were assigned to  $\alpha$ : 0.5, 0.7 and 0.9. These values  $(X_f Y_f Z_f) = (0.8 \ 0.8 \ 0.8)$  were randomly assigned to haze layer along this simulation to represent a transparent gray veil. Although the same

process may be used for a chromatic veil.

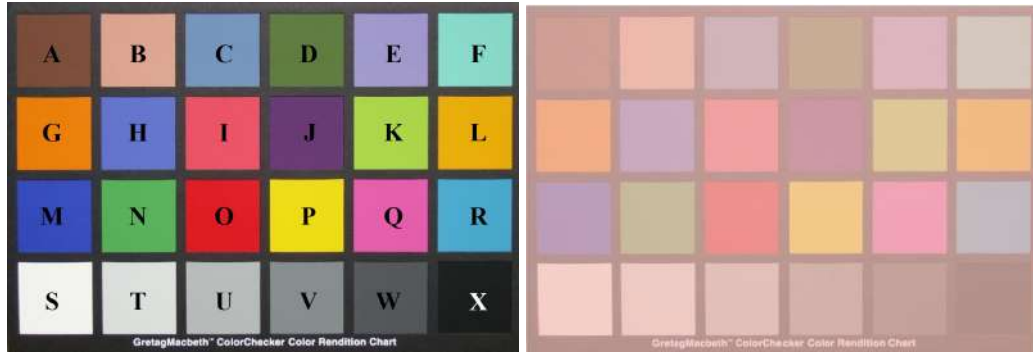


Figure 3.13: Original and hazy images

Resulting images (Figure 3.14) were converted to IPT images to evaluate hue changes by calculating the angle between the hue of the patch before and after dehazing, and to CIE LUV for saturation estimation.

Comparison was done between corrected images derived from the same original image type ( $(RGB_{XYZ}^D$  and  $XYZ_{XYZ}^D)$ ,  $(RGB_{RGB}^D$  and  $XYZ_{RGB}^D)$ ), and between the correspondent images derived from RGB and XYZ ( $(RGB_{XYZ}^D$  and  $RGB_{RGB}^D)$ ,  $(XYZ_{XYZ}^D$  and  $XYZ_{RGB}^D)$ ). Curves that are shown in Figures 3.15 and 3.17, are resulting from hazy image where  $\alpha = 0.5$ . The impact of haze intensity on saturation is shown in Figure 3.16.

We used the Macbeth Color Checker [114] to simulate a flat object with no distance dimension to the camera. A synthetic fog image is composed of Macbeth Color Checker image and haze layer introduced by  $f$  in Equation 3.37 (see Figure 3.13). Haze layer thickness is modified with the parameter  $\alpha$ . Distance and fog intensity are implicitly correlated: when fog intensity rises, it gives the same effect as if distance increases. Saturation and hue evolution are calculated for each patch within three different values of  $\alpha$ . When  $\alpha$  increases, it brings the apparent color toward veil color, such as far objects, which are almost indistinguishable from haze.

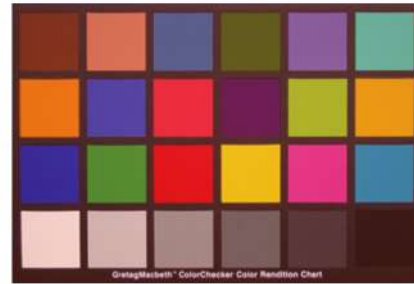




(a)



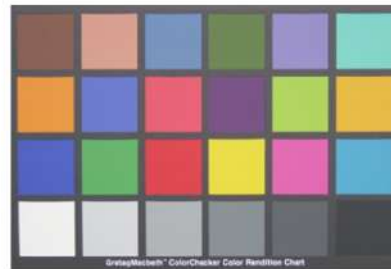
(b)



(c)



(d)



(e)

Figure 3.14: Original RGB image and corrected images. (b):  $\text{RGB}_{XYZ}^D$   $\alpha = 0.5$ , (c):  $\text{RGB}_{XYZ}^D$   $\alpha = 0.7$ , (d):  $\text{RGB}_{XYZ}^D$   $\alpha = 0.9$ , (e):  $\text{RGB}_{RGB}^D$   $\alpha = 0.9$ .

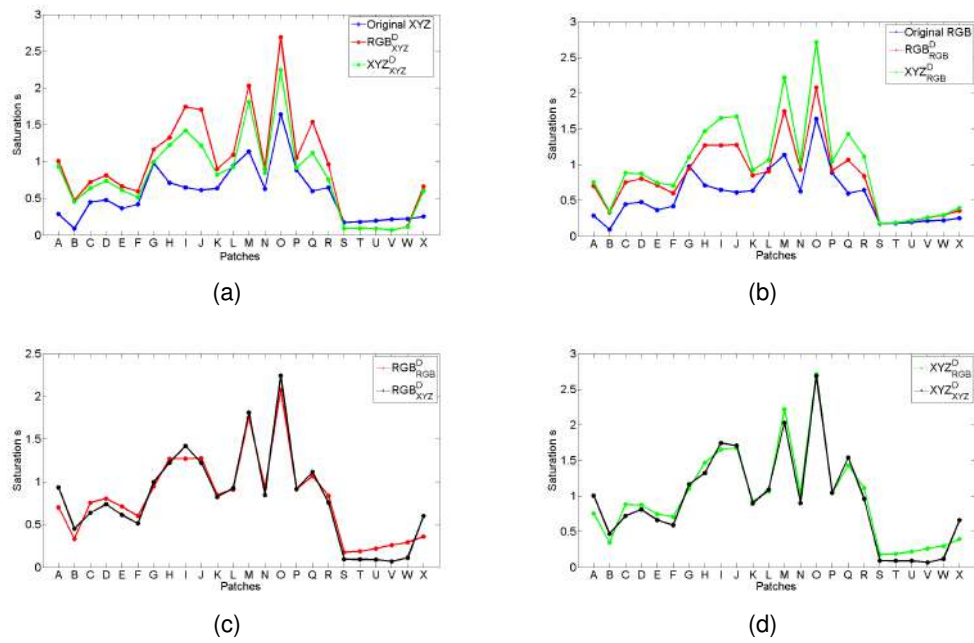


Figure 3.15: Saturation evolution curves of the patches recovered from hazy image when  $\alpha = 0.5$  in comparison with original clear images and other rectified images (normalized images).

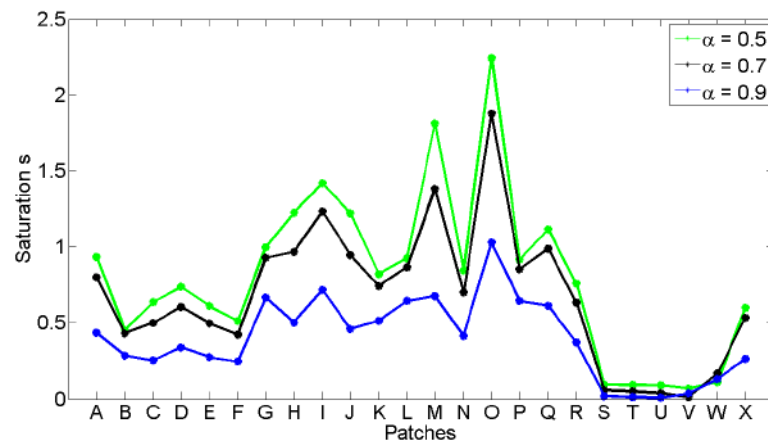
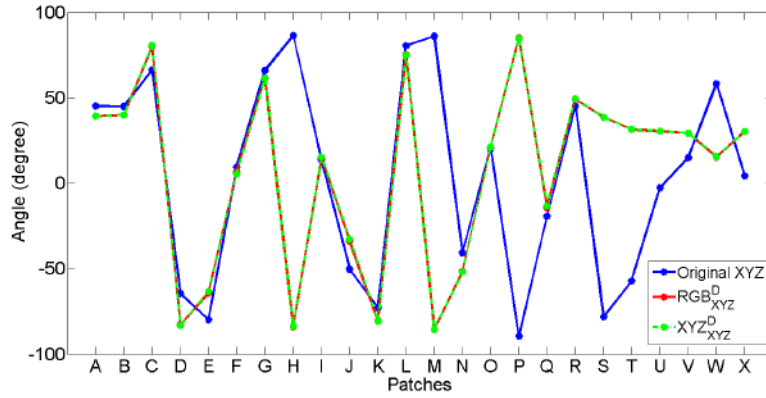
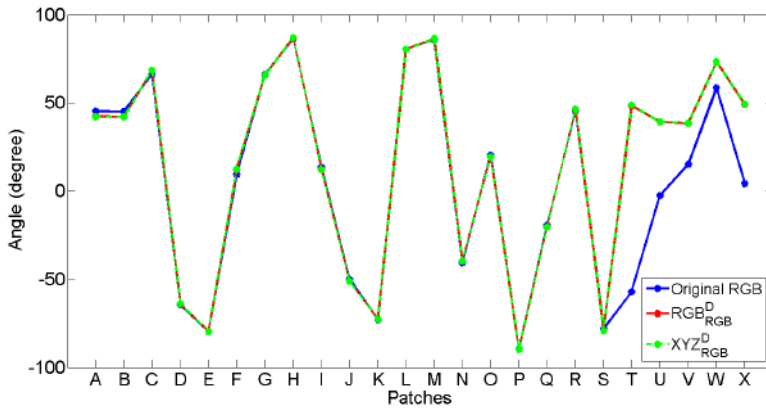


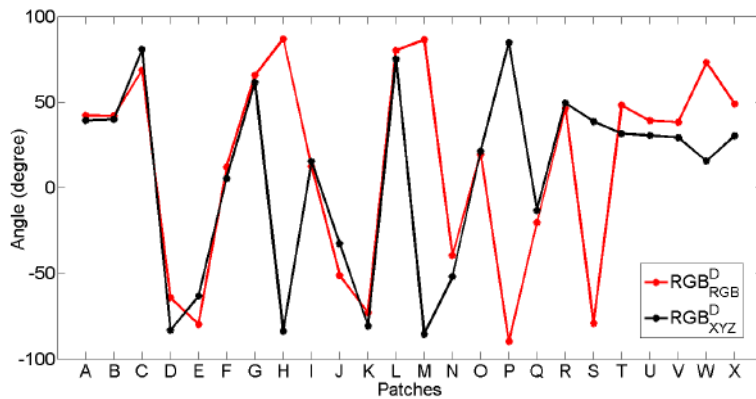
Figure 3.16: Saturation evolution with  $\alpha$  ( $\text{RGB}^D_{XYZ}$  image)



(a)



(b)



(c)

Figure 3.17: Hue evolution curves of the patches recovered from hazy image when  $\alpha = 0.5$  in comparison with original clear images and other rectified images (normalized images).

Dehazing generally saturates pixels, whether it was applied to  $XYZ_{RGB}^H$  or  $RGB_{XYZ}^H$ . However, excluding black patch, achromatic patches (S, T, U, V, W) are desaturated when original image is XYZ and they are slightly saturated when original image is RGB (Figure 3.15).

When RGB and XYZ are dehazed, if the original image is XYZ,  $RGB_{XYZ}^D$  will be more saturated (Figure 3.15(a)). On the other side, if the original image is RGB,  $XYZ_{RGB}^H$  will be more saturated (Figure 3.15 (b)).

When the amount of haze increases, dehazing algorithms fail to retrieve accurately the original information. This reflects a lesser capability to radically get rid of the veil and to consequently saturate objects color. Referring to Figure 3.16, when  $\alpha$  increases, saturation values decrease with a non proportional manner.

Unlike saturation, recovered hue of  $RGB_{XYZ}^D$  and  $RGB_{RGB}^D$  fit the recovered hues of  $XYZ_{XYZ}^D$  and  $XYZ_{RGB}^D$ , respectively (see Figure 3.17 (a) and (b)). Thus, regardless color space, hue is identically recovered. But, they do not fit the hue of original color, especially when original image is XYZ. In this case, the correspondent achromatic and blue/yellow hues (patches H, M and P) before and after dehazing are not placed on a constant hue line. However, when original image is RGB, hue difference is important only on achromatic colors, except white (see Figure 3.17(b)).

### 3.3.3.5/ DISCUSSION

Haze model tends to enhance significantly the saturation of colors and to maintain color hue unchanged. This is clearly reflected through the dissimilarities between the dehazing at high haze densities and/or relatively far objects and at low haze densities and/or near objects.

Although the hue seems to be robust to change for chromatic colors, especially at not very high haze density, it shows a noticeable shift for achromatic patches (S, T, U, V, W and X) that have basically a close perceptual appearance to the haze layer (Figure 3.17). This is further explained in the section 5.2.2.

According to Figure 3.17, the opposite values of hue angles at H, M and P patches corresponding to blue/yellow hue do not necessarily denote no matching hues. Referring to [43], the blue region adjoins the origin in IPT. In this small area, it is highly probable that two different angle values point toward the same hue.

The cross validation analysis done through the handling of two types of images, shows a consistent behavior of dehazing in terms of hue and saturation evolution.

### 3.3.4/ QUALITY EVALUATION

With the continuous increasing in the number of dehazing methods (Figure 3.1), it becomes pivotal to compare their performance, since they do not provide matching results for the same hazy image (see Figure 6.1). This will help to find new advancement directions.

The subjective evaluation of images processed by dehazing has been not much addressed. Generally, when a research aspect is overlooked, this may mean whether it does not represent an attractive research topic over a specific period of time, or there are missing prerequisites.

Regarding the first prospect, the emphasis was initially on the development of good dehazing methods by migrating from the multiple image dehazing methods, which they got a particular attention at the beginning of the 2000's [125, 156], toward the single image

dehazing methods that are more suitable to the real-time applications. Afterwards, especially from 2009 onwards, after the release of the most popular DCP dehazing method, which presented a pivotal point in this domain, the number of methods has undergone a rapid expansion (Figure 3.1). A strong competition took place to provide a method, which is based on a global robust assumption and provides a good perceived quality of the dehazed images with a minimal processing time. During that time, researchers did not give much attention to the features that define the quality of dehazed images nor to mathematical quality indices.

On the other hand, with regard to the prerequisites of subjective and objective quality assessment, evaluations are typically carried out in a qualitative way [199], [167], [164], and only a few recent studies have considered subjective experiments [107], [104], [30], [65]. However, the lack of a haze-free image in the assessment of dehazing quality is a considerable problem.

Because of the absence of the original haze-free image that would be considered as reference, objective quality evaluation has been always considered as a challenging task. Full-reference metrics that evaluate the similarity between the original haze-free and the dehazed images cannot be employed. Moreover, since emphasis is given to the fidelity criterion of dehazed features, this requires a comprehensive subjective study in the presence of the haze-free image. This gives later the possibility to quantitatively evaluate the performance of dehazing methods.

### 3.4/ CONCLUSION

We reviewed in this chapter the various dehazing approaches that have been proposed. Two main families have been identified for the single image case. The first one considers the haze model and besides the hazy image, some of these methods reduce the ill-posedness of the problem through strong assumptions to estimate unknown parameters. Some others use multiple data besides the hazy images. These approaches have been proposed or adapted for particular outdoor or indoor scenarios used in daytime or nighttime applications. The second one overlooks the physical model. Considering the human visual system, this methods' category aims at enhancing the quality of the hazy image no matter if the recovered image meets accurately the original one.

In this chapter we rather focused on the single image dehazing, which has been extensively investigated during the last few years, since it is performed automatically without any user interaction. The DCP hypothesis is the cornerstone of this category. It has been widely included in many dehazing methods and inspired a lot the conception of methods for other target application domains.

Color image dehazing methods are numerous and varied. However, they all suffer from some limitations when it comes to the efficient dehazing at high haze densities, and the accurate recovery of original features that would have been without haze. For a given hazy scene, different methods provide no matching results. In order to deal with these two issues, we present in the next chapters the developed tools responding to the above stated requirements, and the way in which they have been employed.



## HAZE MODEL AND QUALITY EVALUATION



# HAZY IMAGE DATABASES

*"In nature, light creates the colour. In the picture, colour creates the light."*

*-Hans Hofmann-*

*There is no easy way to have a haze-free image taken under the same conditions as hazy images. The availability of this image helps to investigate all aspects of dehazing methods' design and assessment. For these reasons, we have created two hazy image databases, Color Hazy Image for Comparison (CHIC) and Multispectral Hazy Image for Assessment (MHIA). In this chapter, we describe the databases setup and material, and single out their originality.*

---

4.1	Introduction . . . . .	62
4.2	Required tools . . . . .	62
4.3	Color hazy images . . . . .	63
4.3.1	Existing databases . . . . .	63
4.3.2	CHIC . . . . .	64
4.3.2.1	Material and Setup . . . . .	64
4.3.2.2	Scenes . . . . .	65
4.4	Multispectral hazy images . . . . .	69
4.4.1	MHIA . . . . .	70
4.4.1.1	Material and setup . . . . .	70
4.4.1.2	Scenes . . . . .	72
4.4.1.3	Preprocessing . . . . .	73
4.5	Conclusion . . . . .	75

---



## 4.1/ INTRODUCTION

The evaluation of the haze model and dehazing algorithms is a major challenge for ensuring the quality of processed images. The perceived color shift between original and recovered colors represents a crucial element in such evaluation. There is a need to identify the cause of this effect: the amount of haze as physical limiting factor or the spectral dependence of the haze effects. In this context, the lack of adequate tools makes this more complex. In a satisfactory database, besides some data, the haze-free reference image should be present in order to characterize the reasons and the extent of the color change.

Thus, two image databases have been proposed. Color Hazy Image for Comparison (CHIC), which is a color image database and Multispectral Hazy Image for Assessment (MHIA), which contains visible and near infrared discontinuous and narrow spectral images of hazy scenes. These databases share some characteristics such as the shooting environment, the haze-free image and different fog densities. Even if the number of scenes is limited, the several levels of fog and parameters make them valuable. All of these features make them original and favored over other existing hazy image databases.

CHIC database is basically conceived for image quality assessment in subjective and objective ways considering mainly the fidelity aspect of image quality. This database permits potential critics on the robustness of the model against haze density. On the other hand, MHIA is designed for fine analysis of fog parameters evolution over visible and near infrared bands.

## 4.2/ REQUIRED TOOLS

The evaluation of haze model and dehazing algorithms is a major challenge for ensuring the image quality of the processed image. In this context, the lack of haze-free reference image make the evaluation even more difficult. A number of requirements are needed to overcome these issues:

- Real hazy images: regarding the color shift introduced above, two possibilities suggest themselves: either the estimated haze model parameters  $A_\infty$  and  $t$  do not fit the real values or the haze model fails to represent the real situation. Thus, there is a need to collect real and not synthetic hazy images to deal with this issue.
- Clear image: in real-world dehazing applications, it is difficult, if not impossible to have the haze-free image. The presence of this image helps to deal with dehazed image quality that has been addressed in a limited manner. It helps as well to judge dehazing methods and to see to which extent they preserve original features.
- Different levels of fog: in outdoor environment, the fog level and the fog distribution are never predicted or controlled. Thus, the monitoring of the evolution of both elements mentioned earlier, image quality and dehazing methods performance across different fog densities are never ensured.

## 4.3/ COLOR HAZY IMAGES

### 4.3.1/ EXISTING DATABASES

A collection of single outdoor images taken in bad weather without any other consideration are widely used to evaluate visibility enhancement algorithms and for various methods comparative studies. The lack of common conditions of acquisition such as illuminant, viewing geometry and weather conditions may lead to wrong conclusions. Thus, we seek an original database representing a common tool to test the effectiveness and the deficiency of dehazing methods. It may allow developers and researchers, furthermore, to test their algorithms and to improve them to fit as close as possible the clear image by reducing undesirable effects.

There were many trials to experimentally evaluate the performance of methods aiming to improve the visibility and the contrast of unclear outdoor images, by creating some typical image databases.

For instance, FRIDA (Foggy Road Image DAtabase) [169], [77] and FRIDA2 [168], [77] that represent evaluation databases for visibility and contrast restoration algorithms. These databases comprise a number of synthetic images of urban road scenes and diverse road scenes, respectively. The view point is close to the one of the vehicles driver. The software SiVIC<sup>T</sup>M [61] was used to build physically-based road environments and to generate a moving vehicle with a physically-driven model of its movement, and to embed virtual sensors. Images are produced from a realistic complex urban model and a virtual camera inboard a simulated vehicle moving on a road path. To each image without fog, four foggy images and a depth map are associated. The depth map is required to be able to add fog consistently in the images. Different kinds of fog are added on each of the four associated images: uniform fog, heterogeneous fog, cloudy fog, and cloudy heterogeneous fog. These four types of fog were inserted by applying the Koschmieder's law [87] by weighting differently the attenuation coefficient and/or the atmospheric light with respect to the pixel position. Despite the different aspects that are addressed in this database, simulated images fail to represent accurately the natural phenomena effects. It also suggests a single type of images which have the same scene composition, the same fog distribution and similar background and foreground colors.

WILD (Weather and Illumination Database) [130], [131] is an outdoor urban scene database, acquired every hour over 5 months (January 2002 to June 2002). These images are taken under different weather and illumination conditions. Atmospheric conditions, scene distances and temporal data are also associated to images. Such database with uncontrolled illumination and regulated haze/fog densities remains far to evaluate correctly dehazing processes. This database suffers from the redundancy of images with the same conditions and from the drastic illumination change between scenes.

In addition to these databases, developers tend to use images which have usually a small size and an exponential haze density variation from the camera position until it gets the highest value at the back of the scene. Thereby, they can evaluate methods in a short time and with minimal resources [5], [8].

### 4.3.2/ CHIC

To overcome the previous limitations, we designed a setup allowing to acquire scenes with haze. We include in this section the description details of how the experiment was set up and run, the list of materials' properties and scenes arrangement.

#### 4.3.2.1/ MATERIAL AND SETUP

Several equipments were used in order to provide a full package of data that enables us to estimate haze model parameters, including depth, and to reconstruct images.

1. Color Camera Nikon D7100 [3]: this camera was used to get RGB images of the scenes when the fog density changes. As the white balance option cannot be disabled, "cloudy" option was selected. ISO sensitivity is remained tuned to the automatically chosen value 100. The autofocus was disabled. Two image formats are recorded: NEF (RAW) and fine-quality (Recorded JPEG images are compressed at a compression ratio of roughly 1:4) JPEG image, whose dimensions are  $6000 \times 4000$ . During the shoot session of each scene, the camera has been maintained at the same position with the same selected options. As the capture conditions such as the camera field of view, the illumination, the objects colors. Thus, the only variable element during time is the density of the fog layer. This allows us to follow the haze model parameters evolution according to it.
2. Spectro-radiometer Konica Minolta CS-2000 [2]: this spectro-radiometer was used to measure the transmission through fog on the white patch placed at the back of the scene for each fog density. It was calibrated focusing on the same patch without fog. The selected measuring angle was  $1^\circ$ . The  $2^\circ$  standard observer and the measurement illuminant D65 were chosen.
3. Fog machine: we used the FOGBURST 1500 with the flow rate  $566m^3/min$  and a spraying distance of  $12m$ , which emits a dense vapor that appears similar to fog. A large amount of fog is initially emitted until it is evenly distributed in the room and forms an opaque layer. Fog is then progressively evacuated by opening the window. Thereby, images of different levels of fog are captured.

This machine like most machines on the market, operates by evaporation. The vaporization of therein water-based liquid mixed with glycol, is done by heating. The difference is in the quality of the desired smoke. Fog is diffuse and not very dense. The smoke is more dense and less diffuse. The particles of the ejected fog are water droplets whose radius is close to the radius size of the atmospheric fog ( $1 - 10\mu m$ ). For more information about the properties of the emitted fog, the reader may refer to section 5.2.1.1.

4. Macbeth Color Checker (MCC): a number of MCCs was distributed in the scene in such a way as to cover different sides and distances to the camera. It is a color calibration target. The known values of the spectral reflectances of the 24 patches allow us to follow color visibility variation depending on distance and fog density parameters. Since patches are painted with matte colors, MCC can be captured with any orientation and line of sight [114].

Scenes were set up in a closed rectangular room, which is large enough to simulate the effect of the distance and the fog density on the objects radiance (length =  $6.35m$ , width =  $6.29m$ , height =  $3.20m$ , diagonal =  $8.93m$ ) with a large window (length =  $5.54m$ , height =  $1.5m$ ) that allows a large amount of outdoor light to get in, in a sunny day. The photo session of each scene lasted 20 minutes. This experiment was set up on February 2015, from 1:00 to 4:00 p.m. when sunlight was not directly coming in through the window (Figure 4.3). Thus, a uniform indirect light getting in, it is less prone to fast changes. Many MCCs are placed in the scene with different distances to the camera. The farthest one serves to estimate the atmospheric light. It is good to have the same shape and colors at different distances and different angles of view. This can be useful to follow up the color alteration when haze covers a scene, and how far it can be preserved when the haze model formula is simply reversed without considering any given hypothesis. For this reason, the scenes components present various colored surfaces types (reflective and glossy surfaces, rough surfaces, etc.). In these two scenes, the camera stayed fixed over the shoot session of each scene. The illuminant and the distance to the camera are not the same in both scenes.

#### 4.3.2.2/ SCENES

CHIC (Color Hazy Images for Comparison) is composed of static and dynamic scenes. In static scenes, the camera position remains fixed and only fog density changes. In contrast, distance lying between an outdoor scene captured through the window of a foggy room changes, while the fog density stays constant.

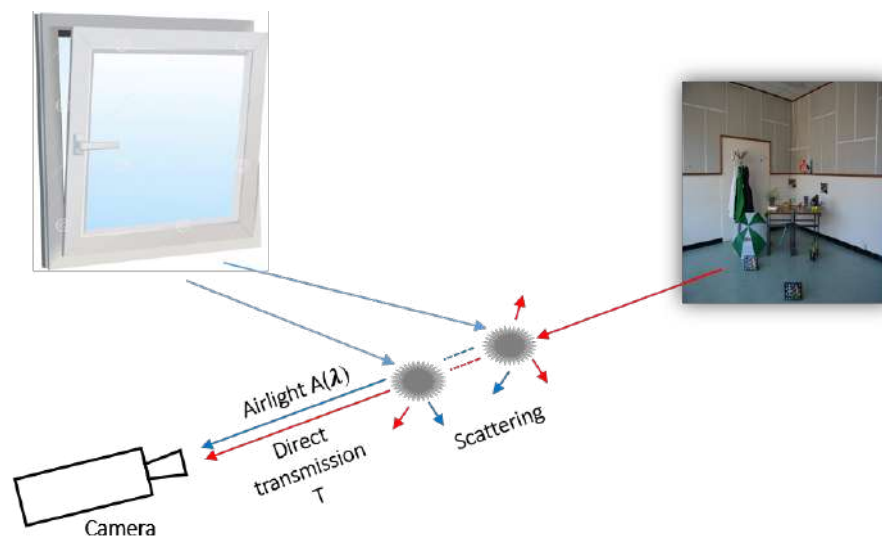


Figure 4.1: The light reaching the camera is the sum of the light coming from the object and attenuated by the scattering and the light coming from outside and scattered by fog particles towards the camera. The airlight component scattered by the fog particles depends on the wavelength.

#### Static scenes



Figure 4.2: Scene A (a) and Scene B (b). The distances of different MCCs to the camera are shown. The resolution of the image is 6000×4000.

1. Scene A: The shoot session of this scene was performed around 2:00 p.m. This scene shows a typical indoor view (see Figures 4.1 and 4.2 (a)). We put on the table that is placed in the middle, a number of items with different characteristics such as shapes, colors, positions, surface types (glossy or rough surfaces) and textures. The wall behind the scene is half white and the top half with the white lines and the black holes represent distinctive elements to study algorithms handling near edges.
2. Scene B: The shoot session of scene B was done two hours later. During this time the temperature of the illuminant significantly changes. The distance from the camera to the farthest scene point is smaller than in Scene A. It contains bigger geometric shapes. The fog densities which are randomly chosen are characterized by the transmittance spectrum of each fog level (see Figure 4.2 (b)).

In Table 4.1, the relative transmittance of fog is calculated in Equation 4.1 with respect to airlight at a given distance over the black patch of original hazy images, as follows:

$$t = 1 - \frac{S_{levelx} - S_{airlight}}{S_{haze-free} - S_{airlight}} \quad (4.1)$$

where  $S_{levelx}$ ,  $S_{airlight}$  and  $S_{haze-free}$  are the spectral values of green in images of different fog levels, of the airlight image of our database where the scene is completely covered by fog and the haze-free image. The relative transmittance is deduced from the green channel since the human visual system has the maximum sensitivity in the response to the green wavelength and the intensity of the scattered light (figure 2.4).

Table 4.1: Relative transmittance  $t$  of fog in original hazy images of scene A and scene B. Level 1: highest fog density. Level 9: lowest fog density.

$t$	Level 1	Level 2	Level 3	Level 4	Level 5	Level 6	Level 7	Level 8	Level 9
Scene A	100%	92%	91%	90%	84%	75%	71%	52%	28%
Scene B	100%	97%	91%	89%	74%	64%	55%	30%	15%

Comparing to outdoor scenes, the light source is located at infinity and the particles forming the synthetic fog are water particles fall in the same range of particles' size of

atmospheric conditions of thick and dense fog (see Figures 5.1 and 5.2), therefore the same scattering law is applied. Since the room where the shoot session was running is not an open place, the airlight color seems to be close to dark gray. According to Figure 5.3, the calculated values of  $A$  and  $t$  are almost the same over channels at all fog levels. All of these facts prove that, the outside conditions are almost fulfilled in our database. Moreover, having an indoor scene with a natural illuminant, we use the appellation *semi-indoor images*.

**Particular phenomena** Unlike the scene B, wherein the transmittance spectrum is less than 100 (in the absence of fog calibration) over wavelengths, in scene A the transmittance remarkably exceeds the calibration value (100) especially in short wavelengths within the visible spectrum (Figures 4.4 and 4.5). This is due to the influence of nearby particles from the light source can have on the beam. The light coming through the window (airlight) initially strikes the fog particles that reflect and redirect to the sensor before reaching the imaged object (Figure 4.1). Since longer wavelengths have a higher penetration capacity, we have an excess in small wavelengths.

**What makes this phenomenon arise?** The position of the window (a local light source) relative to the scene has indeed two main effects. The first one is related to the distance from the window to the fog and the second is related to the position of the window relative to the camera.

- The outdoor natural fog is spread over a large area, thus, the light coming from the Sun, travels a long distance through the fog, through which all wavelengths of visible light are scattered.

However, the distance traveled by the light through the fog is very small. Along this limited distance, the daylight having higher energy in short wavelengths, which are scattered in a pronounced manner comparing to longer wavelengths.

- The scattered light does not come to the camera from different directions as is the case outdoor. The camera being placed on the window side as it is shown in Figure 4.1, this boosts the capture of the first scattered beams before being attenuated through further multiple scatterings.

This phenomena is not accentuated in scene B because the light intensity is lower than in scene A and the camera have been moved away from the window toward the scene (Figures 4.7, 4.8 and 4.9).

**Dynamic scenes** In an approximately uniform smoke-filled closed room, we took photos of an outdoor landscape while moving toward the window separating hazy indoor and clear outdoor mediums. Nine levels of fog densities are considered by moving steps, each of 70cm. The image level 1 is 5.6m from the window and the image level 9 is taken when this distance is 0 (Figure 4.3). Both hazy and haze-free images that are taken at the same distance, are available. Despite uncommon settings, the transmission of these images varies exponentially with distance. Although two different mediums constitute the scene, the model outlines are maintained since the fog is here an actual veil of known thickness. Each medium has its own properties such as illuminant, objects nature and their arrangement, and depths. The camera stayed in place over shoot session of each



scene. However, the illuminant is not the same for both scenes, nor the distance to the camera and the density of fog for the correspondent levels (Table 4.1).

Unlike the static scenes, no particular measures were done on these images. Since these images provide a different scenario of haze and the haze model is violated, it would be of great use to see how a classic dehazing method would handle not classic situations.



Figure 4.3: Dynamic scene. The left column shows images with haze, with distances between the window and the camera: 0, 3.5, and 5.6m. The right column shows the free-haze images of the same distances.

**Originality and usefulness** CHIC database owes its originality to the haze-free image that is available under the same lighting conditions with the hazy ones, to the different levels of fog and to the parameters set including local scene depth, distance from the camera of known objects such as Macbeth color checkers, their radiance, and the fog properties (see Section 5.2.1.1). After all, CHIC provides not simulated but real fog on real scenes. Thus, a real interaction takes place between light and fog particles. All of these characteristics make our database original comparing to the existing image databases (Table 4.2).

All of these features give the possibility to do some investigations:

- Evaluate and compare dehazing methods regarding the haze-free image. This can be done in two ways. In a subjective way, by comparing visually the haze-free and the processed images. In an objective way, by using full-reference image quality metrics regarding the haze-free image (cf. Section 6.2).

Table 4.2: Requirements fulfilled by the hazy image databases: FRIDA, WILD and CHIC.

Requirements	FRIDA	WILD	CHIC
Real hazy images	×	✓	✓
Clear image	✓	×	✓
Different levels of fog	✓	×	✓
Haze model evaluation	×	×	✓
Pixel by pixel comparison	✓	×	✓

The majority of recently proposed methods, are usually evaluated by comparing their dehazed images to other methods' results, where the haze-free image is not available. This is not a reliable manner, since the visual comparison is not straightforward (see Section 6.3). On the other hand, so far, there are no reliable indices for dehazed images quality judgments.

- Evaluate the accuracy of the Koschmieder hazy image formation model through a good number of fog levels (cf. Section 5.2).

However, we have a number of criticisms to make at some points. Despite the fact that the several fog levels of each scene make it valuable, this database needs to be updated by the integration of more scenes with various natural contents. A special care was taken to make acquisitions in a clear day and to make all shoots of the same scene within a short time in order to maintain a stable natural light. For more accuracy, it is good to quantify the amount of outdoor lighting using a light meter.

#### 4.4/ MULTISPECTRAL HAZY IMAGES

Multispectral images are produced by sensors of different sensitivities, that measure the reflected energy within specific bands through the electromagnetic spectrum. The number of bands does not generally exceed 20. In hyperspectral images, this number becomes greater and the bands become narrower. Multispectral and hyperspectral images are indeed with better spectral resolution than color images. Since they contain more spectral information, they have greater potential to conduct studies on the spectral properties influence on haze and dehazing.

The earlier multispectral sensors appeared in the early 1970s. They were dedicated mainly to remote sensing and spatial fields [173]. Today, applications of multispectral imaging in the close field are varied. This is mainly due to recent technological advances in image sensors and spectral filtering. We may cite medicine and biology [92], military field [23], molecular imaging [110], cosmetics industry [84], underwater imaging, quality control of industrial products and food [145, 181], as well as the studies made on the art works and printing [34, 98].

Dehazing, which deals with images acquired with uncommon color camera has not been as widely addressed as the color-based dehazing. Typically, methods employed in ground applications such as driving assistance and surveillance, are applied to the visible range. This may due to the lack of outdoor multispectral images, the cost of required equipment and their complex usage.



Recently, there has been a noteworthy orientation towards the integration of advanced data such as multispectral data and the migration from visible to NIR-based dehazing [154], [53], [170]. As a first step, there is a tendency to extend color-based methods through considering non-visible or more than 3 channels.

The multispectral dehazing methods were mainly developed to deal with the degraded images taken from the space. Such images are usually multispectral and they suffer from visibility degradation. The number of these methods is still very limited.

In [176], DCP was again considered and it was extended to be applied to satellite images. The two main keys of extension consider the validity of Step 1 and Step 2 in section 3.2.2.1. Considering Step 1, DCP is valid for all image's spectral ranges. Thus, DCP is calculated through all image's channels. When it comes to atmospheric light calculation in Step 2, it is not correct anymore to consider it as being spatially invariant, since satellite images cover a large area with different types of aerosols. Thus, in order to deal with these non-uniformities, an atmospheric light distribution curved surface is proposed and the atmospheric light is locally estimated through patches, where it is assumed to be constant within a given patch.

Allmen *et al.* [175] modeled the hazy image by defining the surface reflectance of the objects in the scene and the scattering in the atmosphere. Using these model's parameters, the hazy image is calculated. These parameters are fitted to reproduce the measured image. They used their algorithm to handle images taken with Multi-angle Imaging Spectro-Radiometer (MISR) Instrument [37]. This instrument consists of nine cameras that obtain images at three visible and near-infrared wavelengths. Each of them has a different view direction. This helps to study the reflected sunlight through the angular variation, as well as the induced physical characteristics.

In all of this, there is a lack of multispectral hazy images that provide similar characteristics than CHIC database that allow to calculate haze model parameters and to assess it. It allows also to see if the spectral resolution had a particular influence on dehazing methods and to follow the behavior of haze/fog across wavelengths.

#### 4.4.1/ MHIA

In order to overcome the previously mentioned issues, we have constructed a new multispectral hazy image database. MHIA (Multispectral Hazy Image for Assessment) is an image database that comprises multispectral hazy images of  $n$  levels of fog of 2 scenes M1 and M2 ( $n = 13$  for M1 and  $n = 10$  for M2). In addition to  $n$  multispectral hazy images, we provide as in CHIC, the haze-free reference image. The construction procedure of MHIA is similar to the one of CHIC with some adjustments and the use of additional materials.

We describe below the additional materials that were not used for CHIC construction, the steps of the acquisition process, the scenes and the preprocessing stage of images.

##### 4.4.1.1/ MATERIAL AND SETUP

Some materials, which were used for CHIC construction, were used also for MHIA, such as Spectro-radiometer Konica Minolta CS-2000, fog machine and MCCs.

**Multispectral camera** The multispectral data was obtained using the Photon focus MV1-D1280I-120-CL camera based on e2v EV76C661 CMOS image sensor with  $1280 \times 1024$  pixel resolution [7].

A single filter cannot cover different wavelength ranges. Some characteristics such as glass, coating and polarizing material, are specific to the wavelength range. In order to acquire data in visible and Near-infrared (NIR) ranges, two models of VariSpec Liquid Crystal tunable filters (LCTF) have been used: VIS, visible-wavelength filters with a wavelength range going from 400 to 720 nm. NIR, near-infrared wavelength filter with a wavelength range going from 730 to 1100 nm (see Figure 4.12).

At each step of 10 nm from 400 to 720 nm in the VIS range and from 730 to 1100 nm in the NIR range (Figure 4.10), we captured a picture with a single integration time of 530 ms, which allows a sufficient light to limit the noise without producing saturated pixels over channels. This reduces as well the complexity of the preprocessing spectral calibration step (cf. Section 4.4.1.3).

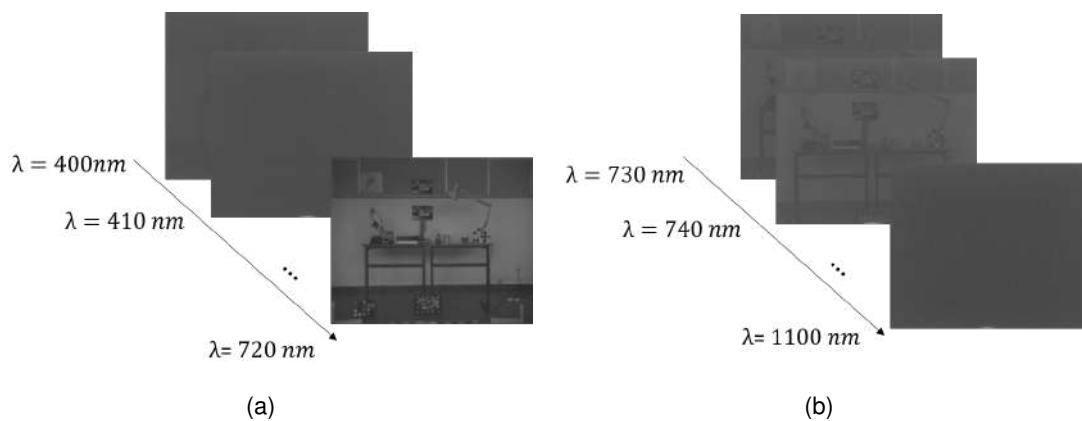


Figure 4.10: (a)Visible band, (b)NIR wavelength band.

#### ***Why the preference for a LCTF against other spectral cameras in such acquisition?***

In our study, LCTF was the most effective available way for such acquisition. On the one hand, its speed guarantees a short image acquisition time comparing to other cameras, such as filter wheel camera (The approximative time for the acquisition of one multispectral image is 40s when using VIS filter and 60s when using NIR filter). On the other hand, it reduces the chromatic aberration and minimizes the geometric distortions that usually increase the execution cost in other sensors [22].

**Kinect** The Kinect is initially an input device for the Xbox 360, that was basically conceived to control video games without using any gamepad [109]. But thanks to the depth map, it is used in many scientific applications. The Kinect measures the distance between itself and the objects within its field of view. It measures the distance by emitting a pattern of infrared dots toward the object and capturing the reflected signal by the IR camera. The pattern shape changes by expanding with the distance. The difference between the original known pattern and the detected one is used to construct the 3D depth map of the whole scene. It provides three outputs: infrared image, RGB image thanks to its RGB camera and the depth map. The Kinect can detect objects up to 10m but it shows some inaccuracies beyond 5m.

Scenes were set up again in the same room where the acquisition of the color images took place. The acquisition session was performed on a cloudy day of May 2016 from 11:00 a.m. to 4:00 p.m. For each of the scenes described later, we define a particular illuminant, since daylight illuminant changes over the daytime. This time, the scenes were placed in front of the large window, forming an angle of  $180^\circ$  with it. The sensors were placed by the window. Thus, the intensity is uniformly diffused on the scenes' objects.

For each scene, once it is installed, using the Kinect sensor, a depth image is captured. It is then removed to be replaced with the multispectral camera, which keeps the same place until the end of the given scene acquisition session. For the haze-free scene, a multispectral data acquisition is performed by the multispectral camera. The spectro-radiometer is once calibrated on the white patch placed at the back of the scene, than the measurement of the fog transmittance is done on the black patch. These two steps are repeated for each fog density.

In order to get different fog densities, in the closed room fog is emitted until we are not able to see anything than a uniform opaque layer of fog. Then, a part of it is evacuated consecutively through the window. The image of the setup is provided in Figure 4.11.



Figure 4.11: Image of the setup.

#### 4.4.1.2/ SCENES

1. Scene M1: The shoot session of this scene was performed at 11:00 a.m. It is similar to the scene A of CHIC. The distance from the camera to the color checker placed at the back of the scene is 4.5 m. In order to reduce the side effect induced by the position of the window relative to the camera (cf. Section 4.3.2.2), the window is intentionally kept behind the camera. We were just physically limited by that

distance, since the Kinect sensor does not provide accurate measurements beyond this value. Its measurement session lasted 40 min. This scene is only acquired by the visible filter. We denote it by  $M1_V$ .

2. Scene M2: This is almost the same as scene M1, but for this scene, two simultaneous images are captured for each fog level, one when the lamp is turned off and one it is lit. Two series of acquisitions were made. The first one using the VIS tunable filter, Scene  $M2_V$ , and the second one using the NIR tunable filter, Scene  $M2_{NIR}$ . Each acquisition series took 60 min.

The characteristics of the scenes containing in CHIC and MHIA databases are summarized in Table 4.3.

Table 4.3: The characteristics of CHIC and MHIA databases.

	CHIC	MHIA: Visible	MHIA: NIR
Image type	Color	Multispectral	Multispectral
Image resolution	$6000 \times 4000$	$1312 \times 1082$	$1312 \times 1082$
Wavelength band	380-730 nm	400-720 nm	730-1100 nm
Number of channels	3	33	38
Number of fog levels	9	10 ( $M1_V$ ), 13 ( $M2_V$ )	13
Width of bands	Large bands	10 nm (Figures 4.12, 4.10)	10 nm (Figures 4.12, 4.10)
Pixel coding	8 bits	16 bits	16 bits
Measured depth	Sampled depths	Depth map	Depth map
Acquisition time of a scene's levels	20 min	40 min	60 min
Maximum distance from the camera	4.25; 7 m	4.5 m	4.5 m

#### 4.4.1.3/ PREPROCESSING

We consider in this section the preprocessing stage, which includes a dark correction to get rid of the offset noise that appears all over the image, and a spectral calibration to deal with the spectral sensitivities of the sensor and the used filters.

**Dark Master** Dark Master or dark image correction is a standard processing, which is applied on images to eliminate offset noises [111]. It consists in taking several images in the dark at the same integration time. For each pixel, we calculate the median value over these images. Therefore, we obtain the dark image. We then subtract the dark image from the spectral images taken with this integration time. The negative values are set equal to zero.

**Spectral calibration** The relative spectral response of the camera and the filter being provided in the user manuals [7]. For each captured image at each wavelength band with an integration time of 530 ms, we divided by the maximum peak value of the spectral response of the sensor (Figure 4.13) and the filter (Figure 4.12).

These two steps have been performed for all spectral images before the construction of color images and the extraction of the haze model parameters (cf. section 5.4).

Since images contain Macbeth colorchecker, the color images have been constructed through a linear combination of the reflectance values of the 24 patches of the colorchecker, the standard illuminant D65 and the human color matching functions.

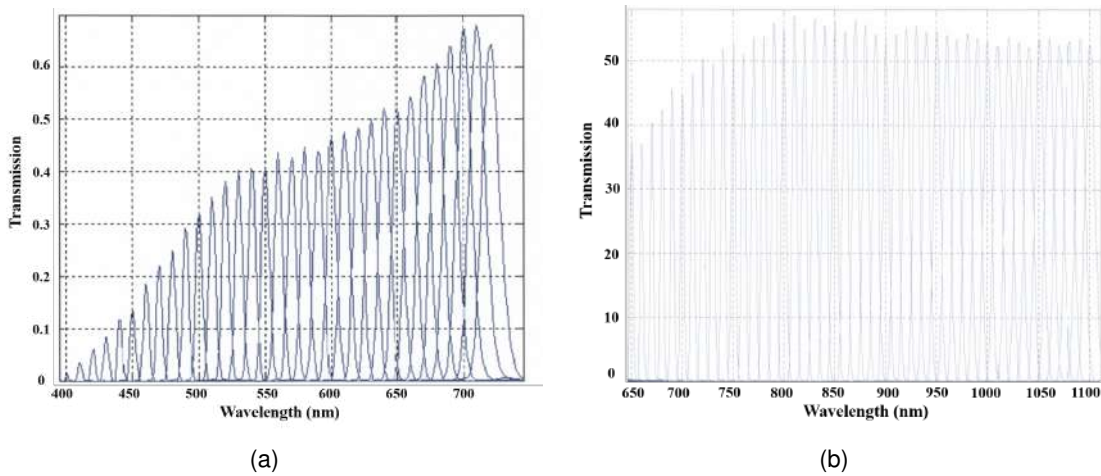


Figure 4.12: Transmission curves of LCTFs: (a) VIS and (b) NIR. These graphs have been scanned from the technical documentations of VariSpec Liquid Crystal tunable filters. Note that the transmission values are within the interval of  $[0,1]$  in the graph (a) and within the interval of  $[0,100]$  in the graph (b).

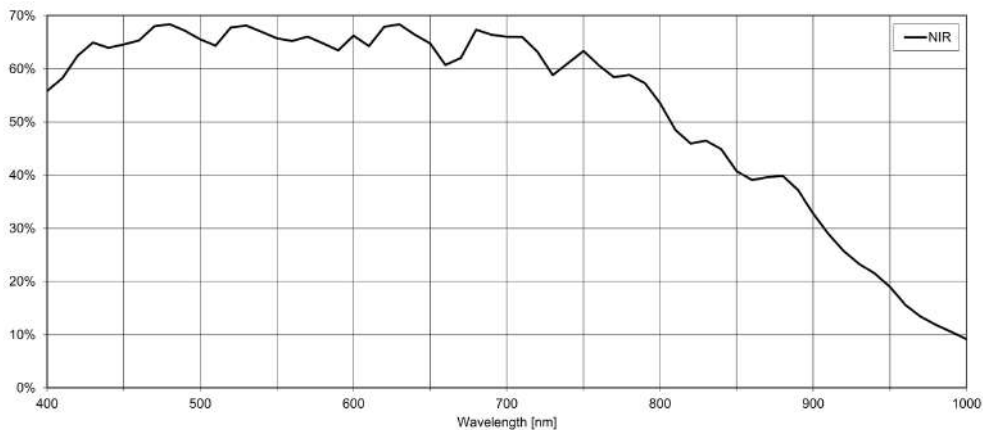


Figure 4.13: Transmission curve of the sensor Photon focus MV1-D1280I-120-CL camera based on e2v EV76C661 CMOS. This graph is borrowed from the correspondent technical documentation [7].

## 4.5/ CONCLUSION

In this chapter, we proposed and described a new color image database composed of static and dynamic scenes that we named CHIC (Color Hazy Images for Comparison). This database could be used for many purposes like haze model assessment or dehazing methods evaluation since the reference (haze-free image) is available. Unlike other existing databases used to enhancement visibility algorithms assessment, CHIC provides a set of metadata making it original and suitable for previous mentioned purposes. It is freely available for everyone to test a proposed algorithm, to compare it with other algorithms and to see its ability to meet the original image after recovering haze-free data.

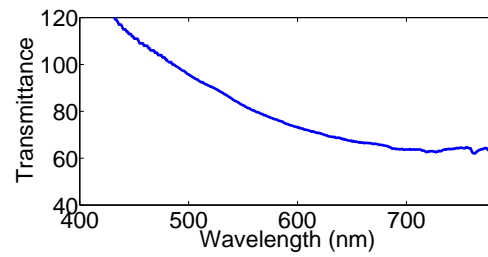
For a more refined analysis, following the same logic, a multispectral hazy image database MHIA has been also developed. Besides the narrow visible bands, we acquired images in the near infrared region.

Both of these databases do not offer a large number of varied scenes. However, general tendencies and conclusions could be drawn. More scenes, potentially related to given applications may be generated by following the same principles.

The remaining chapters consider the issues of haze model validation in terms of inversion accuracy through fog densities and imprecision of spectral dependence, by considering CHIC and MHIA databases, respectively. We consider also CHIC database to address the challenging image quality topic. CHIC database provided us the possibility to deal and to discuss for the first time the subjective and objective assessment of the fidelity of recovered original image features.



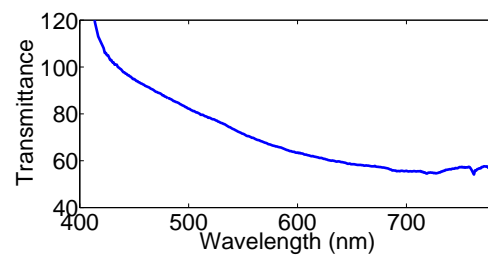
(a)



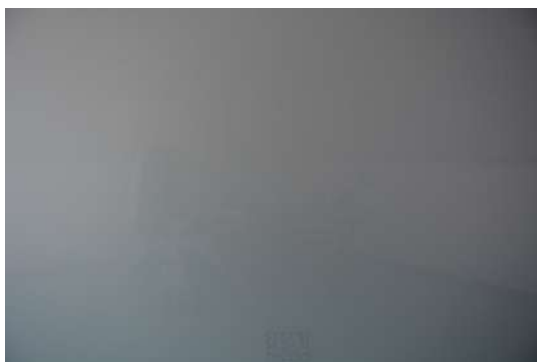
(b)



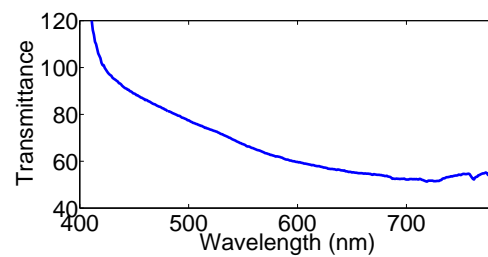
(c)



(d)



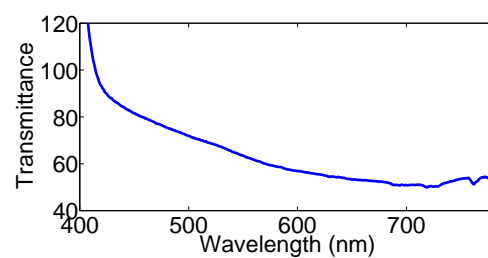
(e)



(f)



(g)



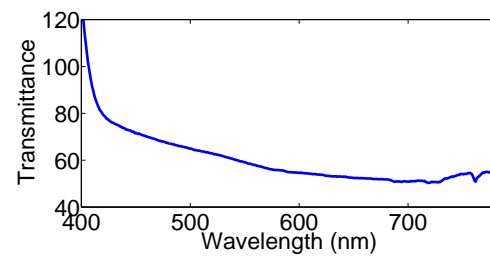
(h)

Figure 4.4: Scene A. Scene images taken under different fog levels and their correspondent transmission curves, which are measured over the farthest white patch from the camera. From top to bottom: level 1, level 2, level 3 and level 4.

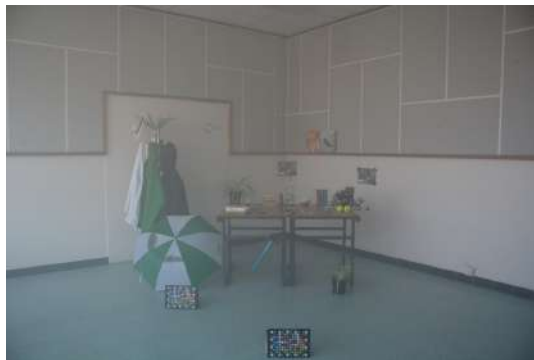




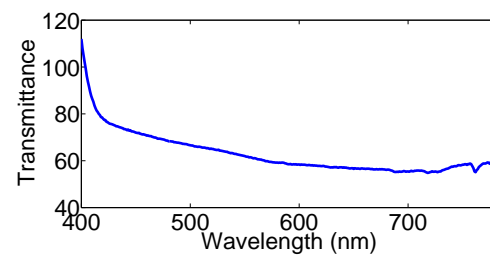
(a)



(b)



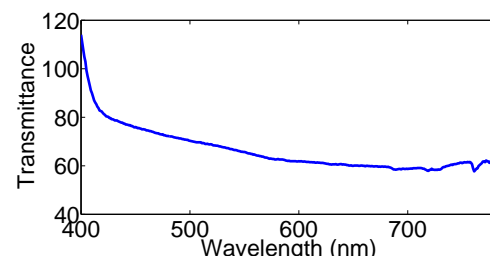
(c)



(d)



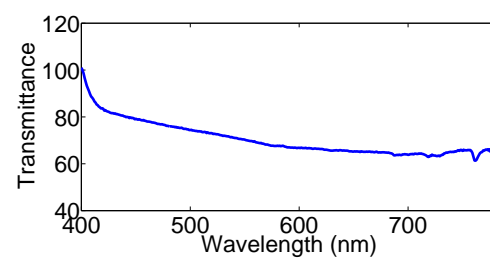
(e)



(f)



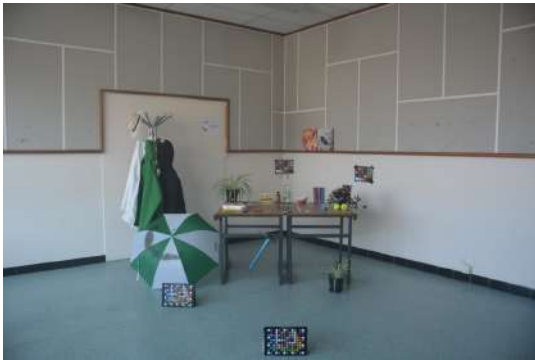
(g)



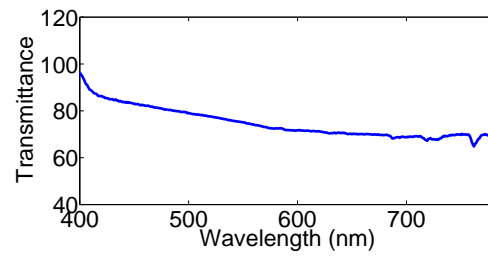
(h)

Figure 4.5: Scene A. Scene images taken under different fog levels and their correspondent transmission curves, which are measured over the farthest white patch from the camera. From top to bottom: level 5, level 6, level 7 and level 8.





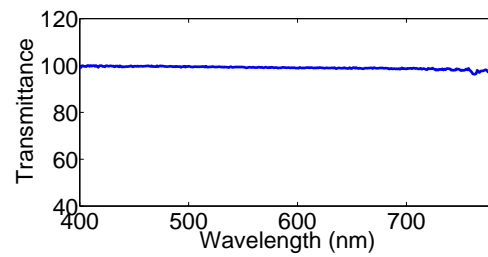
(a)



(b)



(c)

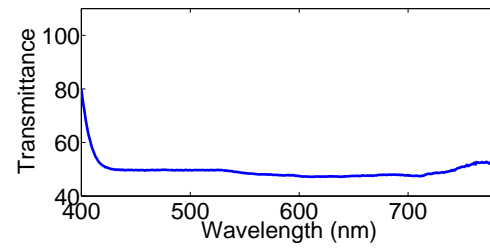


(d)

Figure 4.6: Scene A. Scene images taken under different fog levels and their correspondent transmission curves, which are measured over the farthest white patch from the camera. From top to bottom: level 9 and clear image.



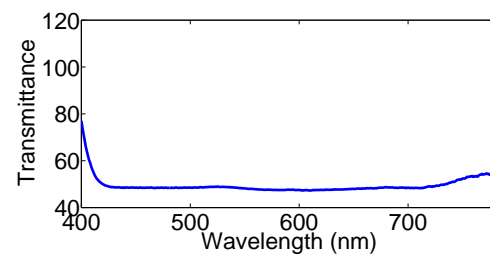
(a)



(b)



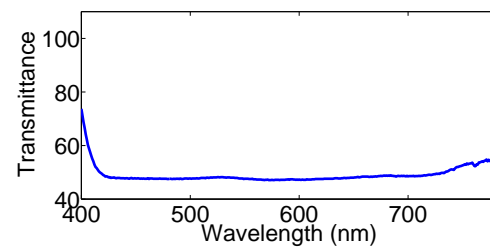
(c)



(d)



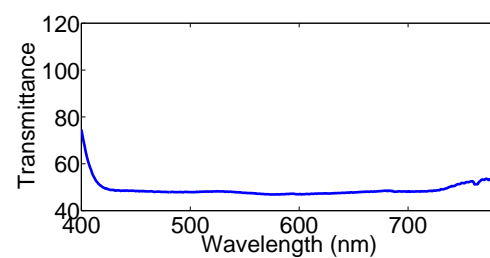
(e)



(f)



(g)

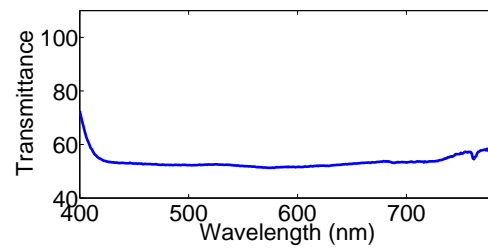


(h)

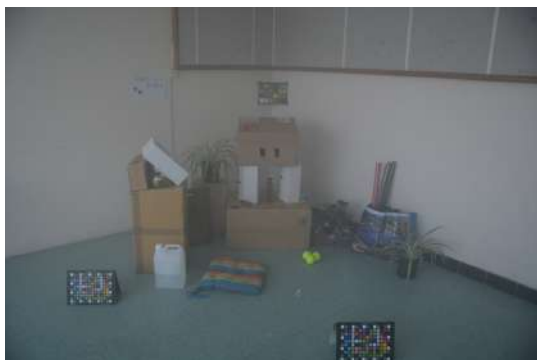
Figure 4.7: Scene B. Scene images taken under different fog levels and their correspondent transmission curves, which are measured over the farthest white patch from the camera. From top to bottom: level 1, level 2, level 3 and level 4.



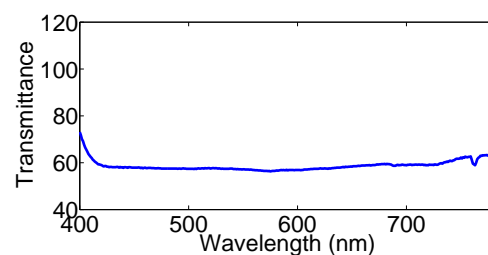
(a)



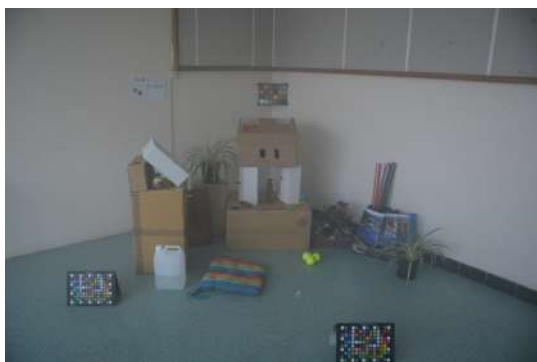
(b)



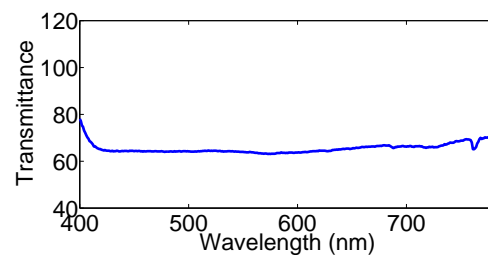
(c)



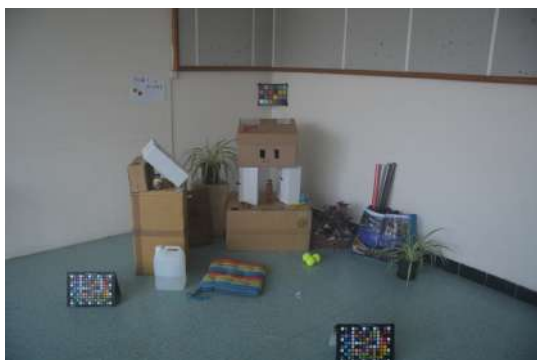
(d)



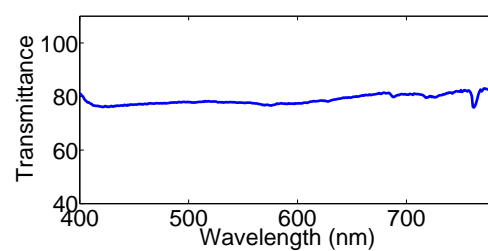
(e)



(f)



(g)

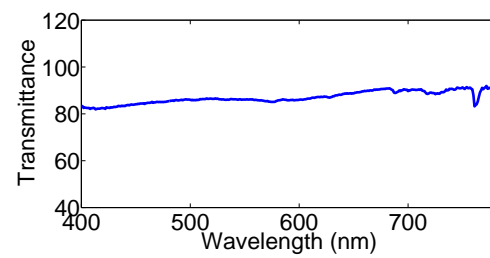


(h)

Figure 4.8: Scene B. Scene images taken under different fog levels and their correspondent transmission curves, which are measured over the farthest white patch from the camera. From top to bottom: level 5, level 6, level 7 and level 8.



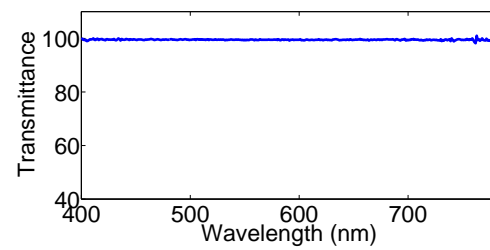
(a)



(b)



(c)



(d)

Figure 4.9: Scene B. Scene images taken under different fog levels and their correspondent transmission curves, which are measured over the farthest white patch from the camera. From top to bottom: level 9 and clear image.

## HAZE MODEL EVALUATION

*"It is not what you look at that matters, it is what you see."*

*-Henry David Thoreau-*

*This chapter considers the problem of achieving an accurate recovery of a color hazy scene. It first explains the aspects of color fidelity violation. An investigation of the performance of physics based dehazing approach on real hazy image and simulated one with the same fog density has been done. Using CHIC and MHIA data, we consider as well the inversion accuracy of the haze model through different fog densities as well as the spectral behavior of fog. These two aspects lead to mark out the limits of the haze model validation. Using our hazy images, we propose a geometrical way to calculate the atmospheric light.*

---

5.1	Introduction . . . . .	82
5.2	Haze model vs haze density . . . . .	83
5.2.1	Real data . . . . .	83
5.2.1.1	Fog levels characterization . . . . .	83
5.2.1.2	Analysis . . . . .	86
5.2.2	Real world vs Simulation . . . . .	87
5.3	Geometric model . . . . .	93
5.3.1	Atmospheric light calculation . . . . .	94
5.3.2	Impact of the number of samples . . . . .	96
5.4	Haze model vs Spectral dependence . . . . .	98
5.5	Conclusion . . . . .	101

---

### 5.1/ INTRODUCTION

Visibility through fog is a complex psycho-physical phenomenon. In some conditions, a vision system is able to handle atmospheric conditions and sometimes its performance is

restricted by the atmosphere, which represents a limiting factor. Dehazing methods are varied and numerous and they often provide dissimilar results. The recovered images of the same hazy image being different, we would logically refer this to the imprecision induced differently by the assumption on which each method is based. This is true. However, additional fundamental reasons related to the physical properties of fog and the vision system may lie behind color shift and dehazing inefficiency.

Away from any assumptions, the inversion of the haze model even when using accurate values shows some limitations. This is mainly due to the amount of fog, which represents a physical limiting factor that a near infrared sensor does not overcome. Light being uniformly scattered through fog, some imprecision due to sensor noise and filter sensitivities variations, lead to an inaccurate color recovery in light fog conditions.

Having generated images with different fog densities, we investigated the contradictory effects the high fog densities have. On one hand, a high density hampers dehazing process and, on the other hand, the calculated atmospheric light is closer to the real. Accordingly, we provide a mathematical characterization of the fog limitations with regard to colors.

## 5.2/ HAZE MODEL VS HAZE DENSITY

### 5.2.1/ REAL DATA

Single image dehazing methods, which consider the haze model given in Equation 2.16, are usually based on strong assumptions to estimate  $A_\infty$  and  $t(x)$  from the single RGB hazy image [72, 167]. Having access to the haze-free image permits to verify these assumptions and the model formulation.

Consequently,  $A_\infty$  is the R, G and B values of the fog layer calculated from image level 1, which is uniformly covered by fog. For each level, the airlight  $A(x) = A_\infty(1 - t(x))$  is similarly calculated over the black patch of MCC placed at the scene's back (color patch within the red surrounding in Figures 5.1 and 5.2). We subtracted from it the offset values of R, G, and B of a patch of  $20 \times 20$  pixels of the same black patch from the original image without fog.

Once  $A_\infty$  and  $A$  are estimated,  $t(x)$  of a given scene depth is deduced from the second part of Equation 2.16 over the same color chart. Since the distance of each chart is known, the scattering coefficient  $\beta$  is deduced and the transmission matrix is then calculated over the entire image, using approximative depths of secondary objects. Based on the known distances of MCCs, images have been split into four parts (see the green lines shown at Figures 5.1 and 5.2). Particular focus should be given to the color patch within the red surrounding, which has an accurate known distance to the camera, and has also the lowest object's transmission.

#### 5.2.1.1/ FOG LEVELS CHARACTERIZATION

The scattering coefficient  $\beta$  is already calculated as previously explained, it is constant all over the scene, since the fog is homogeneous. At each fog level, using  $\beta$ , we calculate the daylight visual range with Equation 2.17, which characterizes the fog categories shown in

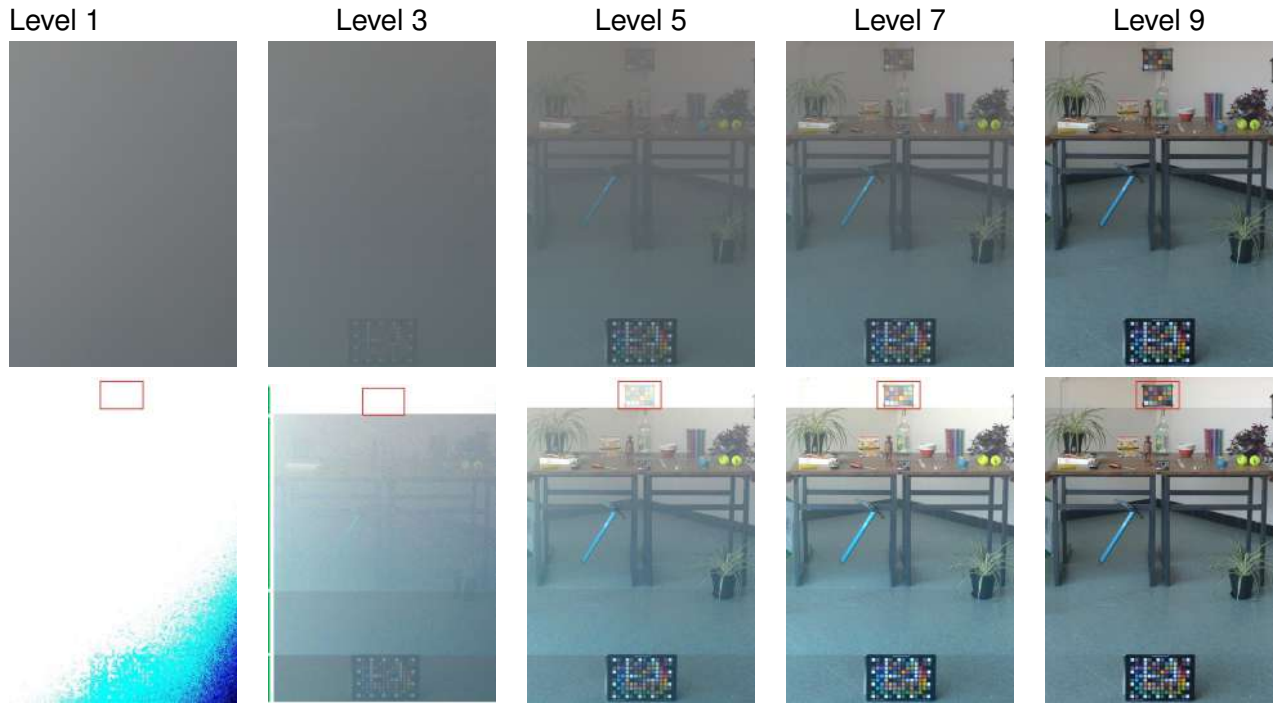


Figure 5.1: The original hazy (first row) and the reconstructed images of Scene A (second row).  $A$  and  $\tau$  are estimated on the surrounded red color patch. The distance between it and the camera is  $7m$ . First row: original hazy images, second row: reconstructed images. Cropped image size is  $1537 \times 2049$ .

Table 2.3.

Table 5.1: Atmospheric attenuation and visual range of the different fog levels of Scene A.

Fog level	Visual range	Attenuation coefficient ( $km^{-1}$ )
Level 1	$0 m$	$\infty$
Level 2	$< 24 m$	158.12
Level 3	$< 27m$	142.85
Level 4	$< 26m$	145.21
Level 5	$< 37m$	103.69
Level 6	$< 40m$	97.47
Level 7	$< 47m$	83.57
Level 8	$< 105m$	37.03
Level 9	$< 220m$	17.84

As stated earlier, the particles forming the fog emitted by the used fog machine are water-based and they have the same visual range as the moderate, thick and dense fog (see Tables 5.1, 5.2 and 2.3). Thus, they should have a similar radius as the natural fog (Table 2.2). In both scenes, from level 1 to level 7 the covering fog is considered as dense fog. The lightest layers, level 8 and level 9 are considered as thick fog and moderate fog,

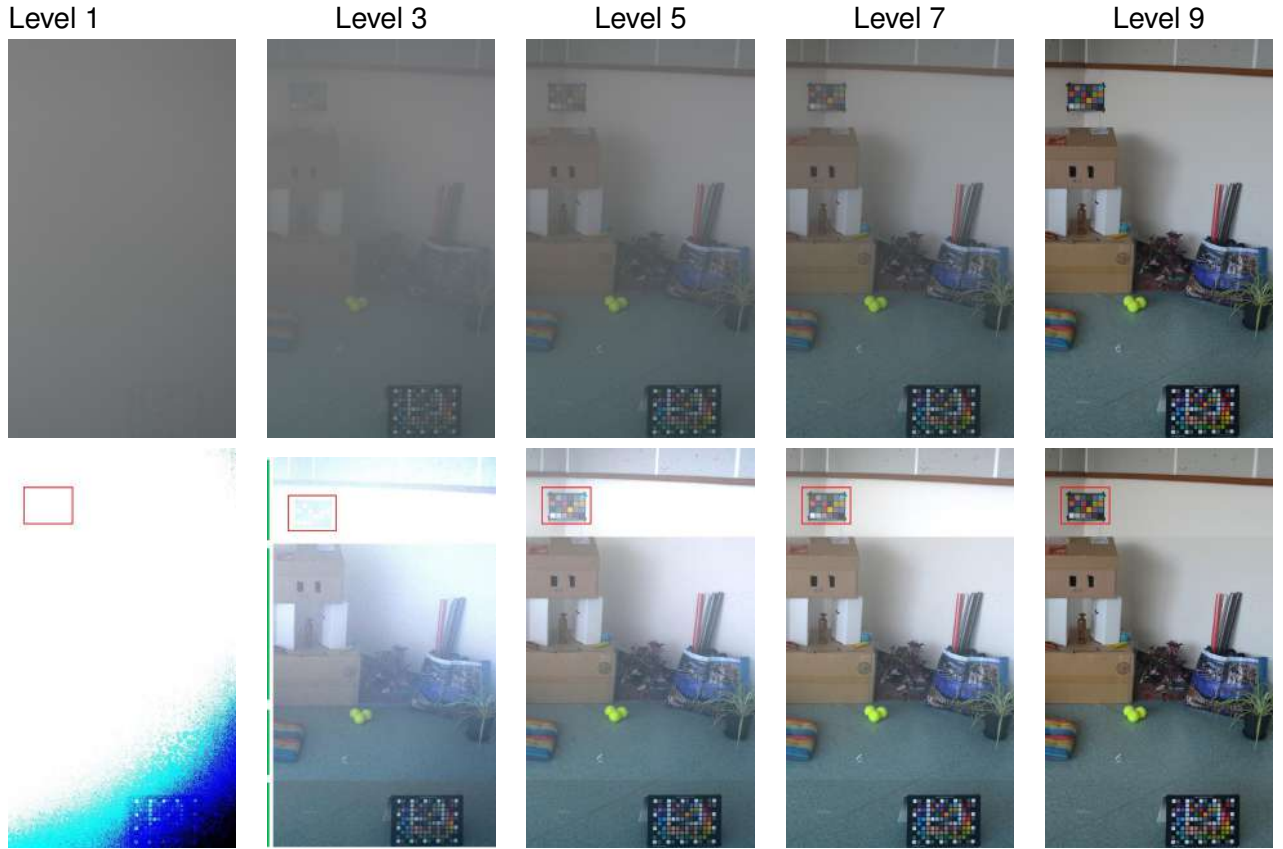


Figure 5.2: The original hazy (first row) and the reconstructed images of Scene B (second row).  $A$  and  $t$  are estimated on the surrounded red color patch. The distance between it and the camera is  $4.25m$ . First row: original hazy images, second row: reconstructed images. Cropped image size is  $1537 \times 3073$ .

Table 5.2: Atmospheric attenuation and visual range of the different fog levels of Scene B.

Fog level	Visual range	Attenuation coefficient ( $km^{-1}$ )
Level 1	$0 m$	$\infty$
Level 2	$< 12m$	306.12
Level 3	$< 16m$	235.29
Level 4	$< 16m$	236.32
Level 5	$< 30m$	126.49
Level 6	$< 37m$	105.06
Level 7	$< 49m$	79.35
Level 8	$< 108m$	36.09
Level 9	$< 300m$	13.06

respectively. Scattering at all of these levels is not dependent on the wavelength. This proves the consistency between our semi-indoor conditions and the outdoor model.



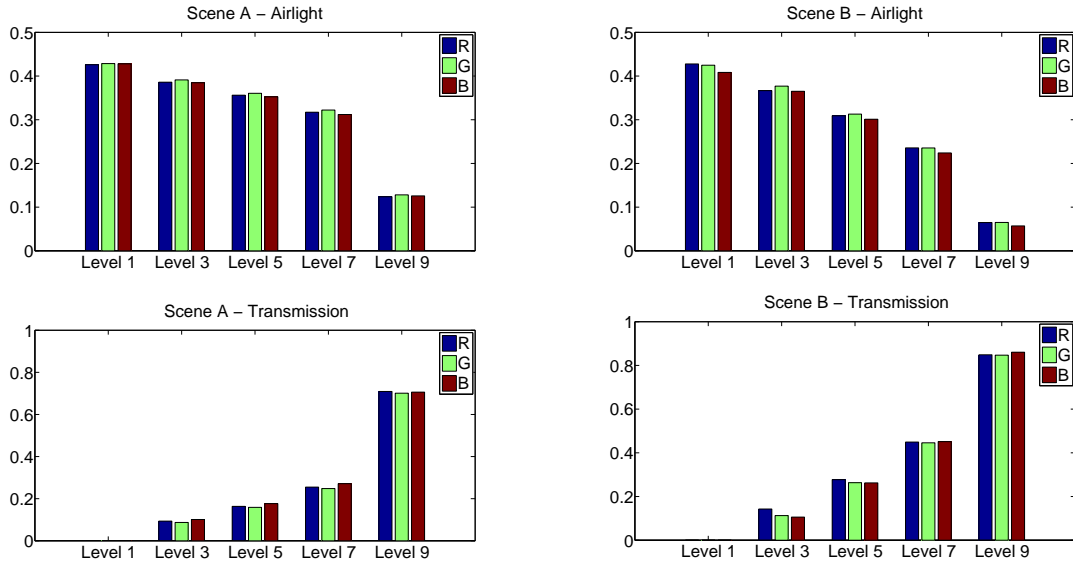


Figure 5.3: Estimated  $A$  and  $t$  obtained for each level of fog for a given distance of the MCC placed at the back of the scene. First row: airlight, second row: transmission. First column: scene A, second column: scene B.

### 5.2.1.2/ ANALYSIS

Referring to the previous sections (5.2.1 and 5.2.1.1), although Scene A and Scene B differ slightly from each other by depths and fog densities, corresponding images of both scenes of the same level provide close values of  $A$  and  $t$ . This gets reflected through reconstructed images (Figures 5.1 and 5.2), where the area within the red surrounding is poorly recovered in level 1 and level 3 from  $t_1 = 0.00$  to  $t_2 = 0.09$  in Scene A and from  $t_1 = 0.00$  to  $t_2 = 0.12$  in Scene B, respectively. From level 5 and on up, when  $t$  exceeds 0.17 in Scene A and 0.27 in Scene B, the inversion of the haze model (Equation 2.16) succeeds to recover recognizable features comparing to the haze-free image. This means that in dense fog when the visual range is lower than almost  $40m$ , an object placed within  $7m$  is most likely to be well recognized through haze model inversion.

Since unknown parameters of all fog levels are similarly estimated, this means that the induced error is the same. When the fog density is relatively high (in our case, below level 5), even if the estimation is reasonably accurate, it seems difficult, if not impossible, to compensate due to the lost transmitted light through scattering and absorption and getting a reconstructed image close to the haze-free image features. This is clearly shown on images of low levels of fog, where reconstructed images are noticeably noisy with perceptible saturation shift. This comes to confirm once more what has been pointed out by Narasimhan and Nayar [127], that this model is not valid for depths that are more than a few kilometers. Similarly, when the amount of fog greatly increases, even the radiance of near objects is no more well captured by the camera. Moreover, since the exponential attenuation comes quickly down to zero, the noise is greatly amplified for high fog densities.

## 5.2.2/ REAL WORLD VS SIMULATION

Exploiting CHIC (scene A), the spectra of Figures 4.4, 4.5 and 4.6 depict the transmittance of the white patch of each haze level. When the haze veil dominates the image, we can notice that transmittance curves represent the light scattered by haze particles adding to it the daylight reflected by the patch. The manner how the transmission intensity evolves through haze levels, we can notice that the luminance of haze density is exponentially evolving. From level 6 the transmittance intensity becomes to reach back and to be closer again to the transmittance spectrum of the clear image. This leads to deduce that the airlight causes the atmosphere to behave like a secondary light source of a different type than the outdoor global illumination. According to the definition of convergence model of transparency perception,  $b = (1 - \alpha)a + \alpha f$ ,  $b$  is the image that is covered by a given level of haze.  $a$  is the clear image, which is considered to be the one captured without embedding haze.  $f$  represents the tristimulus value of the captured target when it is covered by an opaque haze veil. Finally,  $\alpha$  is calculated by inverting the convergence model and choosing the value corresponding to the black patch. We assume that the darkest patch does not reflect the daylight, and that the airlight over this patch is only due to the haze veil. The camera noise is removed by subtracting the tristimulus values of the black patch in the clear image from the values of the same patch covered by different haze levels. Equiluminous veil embedded in simulated images where  $\alpha$  is constant, is unnatural, and it cannot be represented in a satisfactory manner by such physical veil.

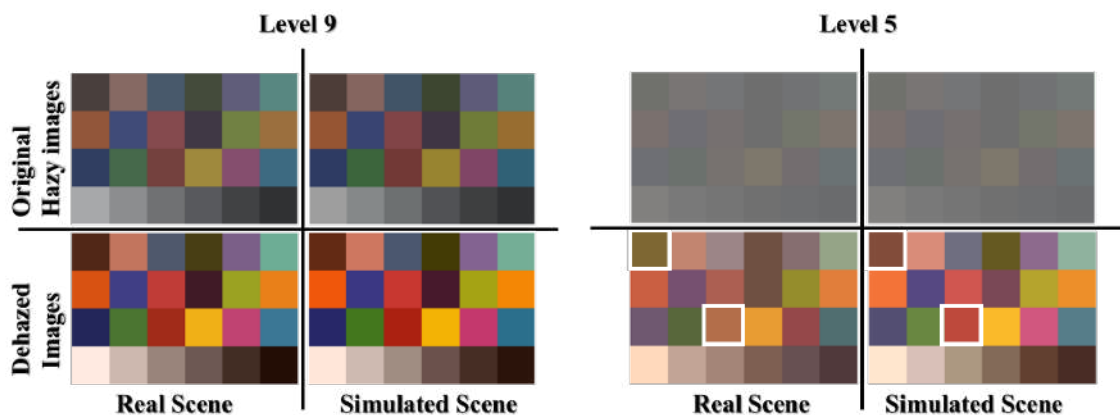


Figure 5.4: Images resulted through the haze model inversion from a real hazy image and the correspondent simulated one at fog level 9 and level 5. Unlike level 9 where there is a color matching between recovered patches of real and simulated scenes, the inversion of the haze model fails to recover accurately the same colors for both images of level 5 where the haze density is high. This is particularly clear at some patches such as the framed ones.

Haze that lies between the camera and the ColorChecker target modifies the light that emanates from it and reaches the camera. The light reflected from the target is added to the light scattered by the intervening particles. When the haze density greatly increases and the scattered light overcomes the light reflected by the target, the perceived colors components, hue and saturation, shift from their original values. This is clearly shown in Figure 5.4, where the simulation succeeds to represent the real scene of level 9 (with a little saturation difference related to the clear black patch) and fails for level 5. Referring to Figure 5.5, the distributions of points representing the red patch from level 5 to level 2

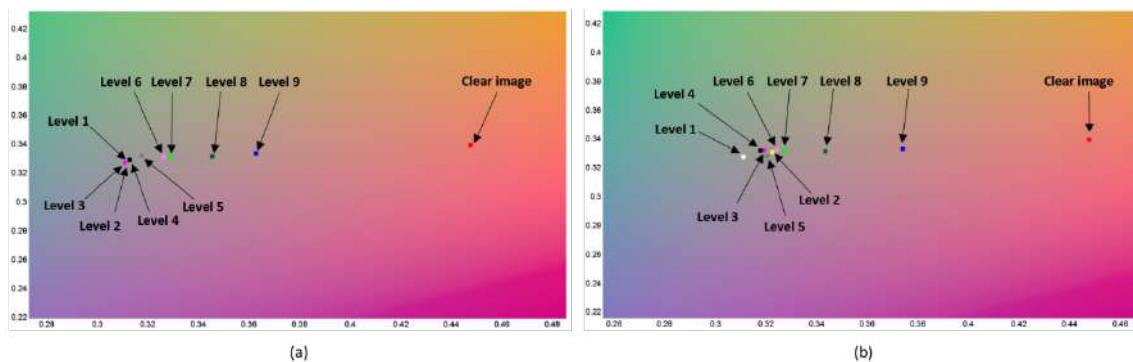


Figure 5.5: The chromaticities of different haze levels calculated in the color space CIE  $xyY$  and represented by the parameters  $x$  and  $y$ . They are placed on the chromaticity diagram of the red patch. (a) Real Scene, (b) Simulated Scene. Red: clear image white: Level 1 yellow: Level 2 magenta: Level 3 black: Level 4 - gray: Level 5 pink: Level 6 green: Level 7 dark green: Level 8 blue: Level 9. The distributions of points representing the red patch from level 5 to level 2 are different between (a) and (b), while other points keep the same relative place between the end points (red and white) with a little shift in saturation.

change between (a) and (b), while other points keep the same relative place between the end points (red and white) with a little shift in saturation (as shown in Figure 5.4 for scene with real fog level 9 and scene with simulated fog level 9).

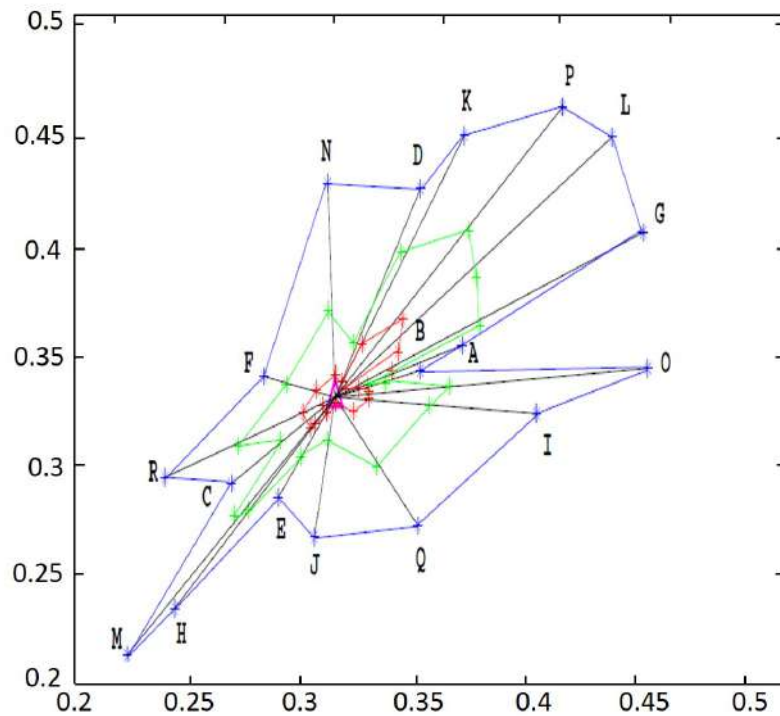
As it is defined above, the direct transmission is the light that reaches the camera without being scattered. Thus, the hue of this light is assumed to be independent of the reflected surface depth. The hue of airlight depends on the particle size distribution and tends to be gray or light blue in the case of haze and fog [132]. According to Figure 5.5, when the haze veil becomes great, the points placed on the chromaticity diagram of the patches, deviate from the line linking the haze veil color (white point) to the original unveiled color (red point), and they are biased toward blue/green area. Some points are also located outside the area between the red and the white points. The deviation rate depends on the patch color, the airlight and the sunlight interference. When the deviation in simulated scenes is smaller, all points representing a given patch at different haze levels remain between the red and the white point.

When the haze model inversion is applied to the scene of real fog level 5 (Figure 5.4), it accentuates the veiled colors by enhancing saturation. The recovered colors are very different from those recovered from the scene with the simulated fog level 5, where the target and the veil are colorimetrically independent. This work confirms the previous conclusions considering that the inversion of the haze model saturates colors. And the way it estimates the airlight and the transmission does not enable it to take into consideration the interference of different illuminants. As the retrieval of these parameters is limited to the pixels intensities estimation, its mission remains limited to saturation enhancement, and original hues are not accurately recovered (Figure 5.4). On the other side, when the density of haze is small and the original hue is not altered, an adjustment based on convergence model could reinstate original saturation.

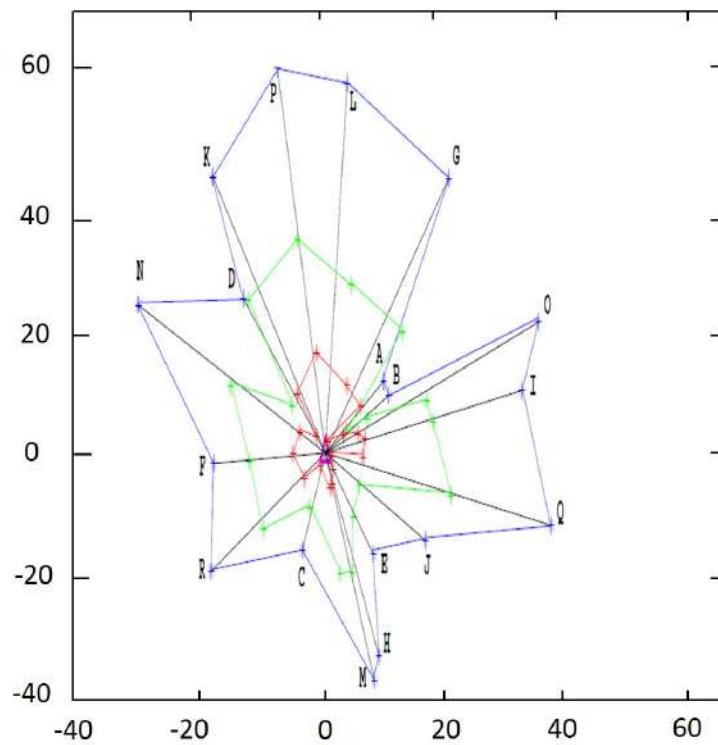
In this part, we study the similarities between a simulated hazy scene created by a convergence model and a real hazy scene. Physical luminous interaction modifies the perceived scene, while colors in the simulated image maintain their hue information and only their

saturation component shifts between the original color (saturated), and the haze color (unsaturated). Convergence model fails to stand for hazy image when the density of haze becomes considerably high. Dehazing methods like DCP, aim just to remove the covered veil and to recover the color as it is not completely hidden, without taking into consideration the interaction of different phenomenon. Thus, it is mandatory to have a pre-processing stage that aims to adjust the color's hue, and a post-processing stage based on convergence model for saturation adjustments.

The atmospheric light  $A_\infty$  has a particular relation with each of the ColorChecker colors placed at the back of the scenes A and B (7 and 4.25 m, respectively)(see Figures 5.6 and 5.7). A relative low or medium density of fog, through which we can distinguish the color of the object, converges proportionally to the haze-free colors all colors toward  $A_\infty$ . Thus, the convergence shape is preserved across medium and low levels (level 5 to level 6).

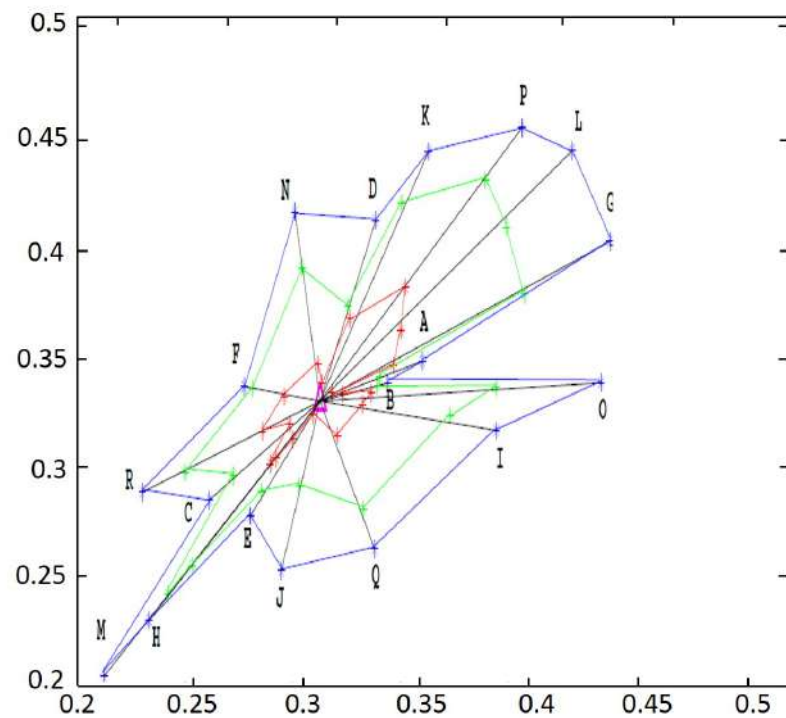


(a)

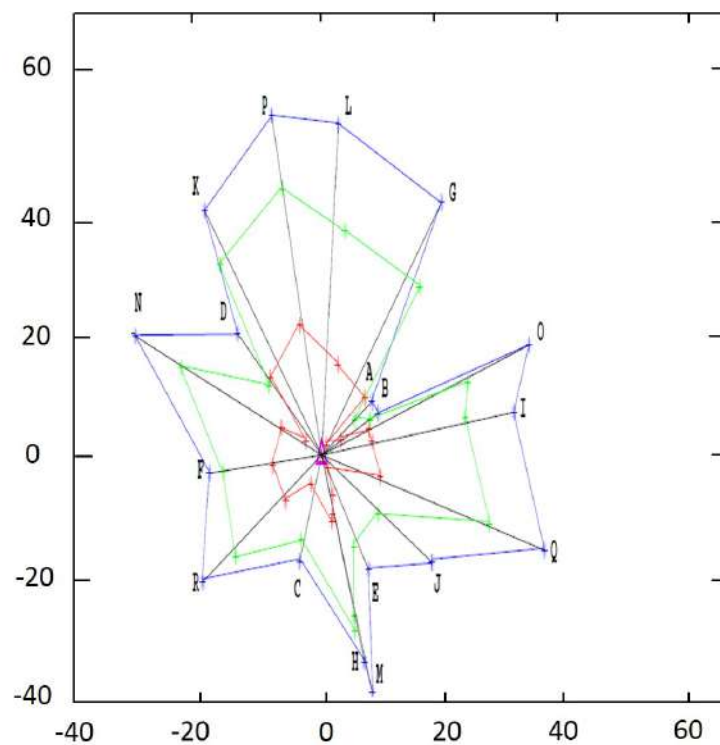


(b)

Figure 5.6: Chromaticities (a) and color appearance distribution (b) in CIE  $xyY$  and CIE Lab color spaces, respectively, of the ColorChecker patches (Figure 3.13) at fog level 7 (red), fog level 9 (green) and haze-free level (blue) of Scene A.  $A_\infty$  is placed at the center.



(a)



(b)

Figure 5.7: Chromaticities (a) and color appearance distribution (b) in CIE  $xyY$  and CIE Lab color spaces, respectively, of the ColorChecker patches (Figure 3.13) at fog level 7 (red), fog level 9 (green) and haze-free level (blue) of Scene B.  $A_\infty$  is placed at the center.

Beyond the density at level 5, colors become to be hardly distinguishable as indicate the  $\Delta E_{ab}^*$  values in Tables 5.3 and 5.4 ( $\Delta E_{ab}^* \ll 6$ ). Colors coordinates become very close to  $A_\infty$  and the convergence loses its shape. Thus, we are no more able to find back the color direction indices.

Considering the perceptual color difference represented by  $\Delta E_{ab}^*$  in Tables 5.3 and 5.4. When the density of fog is relatively high (level 1 to level 4) the values are around 2 (no distinction is perceived anymore) and the standard deviation is very small. At level 5 for both scenes,  $\Delta E_{ab}^*$  values are close to 6, thus the recovered colors at this level are similar to the haze-free images. However, unlike Scene A, at level 5 values being higher than 6 in Scene B, this is reflected by a better color recovery (see Figures 5.1 and 5.2).

In all of this, we distinguish between:

- A critical high density of fog (small transmission' values (Figure 5.3)) that brings all colors to look alike (from level 1 to level 4 in our CHIC database). The result does not depend on the objects colors.
- A low density (high transmission' values) that differently alters the perception of various colors. But since the values of  $\Delta E_{ab}^*$  are all very high, even if they are different, they are all easily distinguished from the airlight and they are therefore accurately recovered in hue but with a small bias in the saturation (level 7, level 8 and level 9 in our CHIC database).
- A medium density behavior that lies at the edge between the two others. In our database, we consider level 5 and level 6 as representative. In the presence of such densities, some colors such as patch B and patch F, unlike other patches, have low  $\Delta E_{ab}^*$  values ( $< 6$ ) (see Table 5.3). This is manifested by providing recovered colors not easily recognized with the naked eye (see the recovered patches B and F at level 5 in Figure 5.1).

**How can we generally represent this convergence behavior?** From the geometrical point of view, the perceptual convergence of a haze-free color towards the atmospheric light  $A_\infty$  is presented in the Figure 5.8, where we show three segments with a common point  $A_\infty$ , to which all colors should converge.  $J_1$ ,  $J_2$  and  $J_3$  are three different haze-free colors.  $I_1$ ,  $I_2$  and  $I_3$  are the hazy colors and they are connected to the segments extremities as given in Equation 5.1:

$$I_c = A_\infty + \gamma_c(J_c - A_\infty) \quad (5.1)$$

The blue circle marks the achromatic critical zone of center  $A_\infty$  and radius  $r$ .  $r$  is a constant value common to all colors. This geometrical distance denotes the smallest perceived dissimilarity between  $A_\infty$  and all hazy patches at level 4. For a given color  $c$ ,  $d_c$  is a constant value. It represents the distance between  $A_\infty$  and a given fully saturated (haze-free) color. We assume that  $\gamma_c = \frac{l_c}{d_c} \in [0,1]$ .  $l_c$  is the distance from the center  $A_\infty$  to the hazy color  $I_c$ . Depending on the color  $c$ , through fog levels,  $l_c$  varies from 0 (opaque layer of fog, level 1) to  $d_c$  (haze-free image).

We consider that a given physical value of  $t$  induces a geometrical value of  $\gamma_c$ . When the  $t$  value decreases,  $\gamma_c$  decreases also. This brings the hazy color closer to the critical area. When the hazy color falls into this critical zone ( $l_c < r$ ), the original color is no more accurately recovered. The direction of the color saturation levels is no more known. For

Table 5.3:  $\Delta E_{ab}^*$  between atmospheric light and the chromatic patches of the Macbeth ColorChecker at different fog levels of Scene A. For each level we calculate the standard deviation of  $\Delta E_{ab}^*$  of all patches.  $A_\infty$  is placed at the center.

Patch	L1	L2	L3	L4	L5	L6	L7	L8	L9	Haze-free
A	0	2.255	2.553	2.272	<b>4.890</b>	7.968	6.957	11.878	18.610	33.882
B	0	2.329	2.585	2.089	<b>3.817</b>	5.539	4.965	7.736	9.596	15.469
C	0	2.468	2.774	2.286	<b>4.294</b>	6.497	5.742	9.758	14.903	25.544
D	0	2.549	2.797	2.275	<b>4.715</b>	7.709	6.958	11.878	18.849	39.065
E	0	2.705	2.936	2.295	<b>3.878</b>	5.849	5.039	9.571	13.694	22.702
F	0	2.788	2.846	2.089	<b>3.318</b>	4.773	5.234	9.589	11.926	17.669
G	0	2.297	2.568	2.244	<b>4.773</b>	9.568	10.051	18.250	23.656	48.620
H	0	2.315	2.648	2.283	<b>4.844</b>	8.289	8.368	17.167	24.911	42.125
I	0	2.567	2.674	2.253	<b>4.554</b>	8.406	8.365	15.139	20.825	37.878
J	0	2.582	2.935	2.388	<b>5.056</b>	8.102	7.433	13.588	22.606	42.441
K	0	2.725	2.863	2.497	<b>4.971</b>	9.924	10.285	21.136	26.697	46.609
L	0	2.828	2.868	2.353	<b>5.191</b>	10.365	11.280	20.694	26.692	58.027
M	0	2.251	2.629	2.283	<b>4.848</b>	8.407	8.695	18.113	28.068	50.053
N	0	2.498	2.690	2.178	<b>4.807</b>	7.543	6.954	13.200	20.294	40.062
O	0	2.531	2.840	2.298	<b>4.747</b>	8.966	8.390	15.830	23.448	47.742
P	0	2.628	2.724	2.302	<b>5.615</b>	14.229	15.624	28.110	33.453	60.413
Q	0	2.679	2.971	2.353	<b>4.506</b>	8.003	7.528	16.813	22.993	41.051
R	0	2.774	2.986	2.399	<b>4.325</b>	6.700	6.760	12.785	17.825	30.181
STD	0	0.190	0.143	0.099	<b>0.542</b>	2.125	2.604	5.084	6.081	12.735

a given  $t$ , the induced  $\gamma_c$  depends strongly on  $d_c$ , the distance between the atmospheric light and the original haze-free color, and the proportion that  $r$  represents from it. Indeed, for the shortest distance  $d_1$  shown in Figure 5.8, not a very low value of  $t$  is able to bring  $I_1$  inside the achromatic area. In contrast, for  $d_2$  and  $d_3$ , a larger decreasing of  $t$  is needed to reach the achromatic crucial area.

Thus, referring to Figure 5.4, for the same  $t$  value, the recovered colors of some patches are close to the original ones and some are not. This proves our observations made upon Figures 5.3 and 5.4.

### 5.3/ GEOMETRIC MODEL

Here we present a geometric model to estimate the atmospheric light  $A_\infty$  for a given layer of fog. This can be verified using CHIC images, since the experimental  $A_\infty$  value is calculated from level 1 image.

In digital images, the fog converges the scene's colors to  $A_\infty$ . In geometry, this means that all the lines plotted through two points (\*: haze-free color,  $\Delta$ : hazy color) of all image pixels, intersect at one point  $A_\infty$  (in the best conditions), or to cross its surrounding area.

In the following sections, we explain how the  $A_\infty$  is simply calculated in the 2D space  $rg$ ,



Table 5.4:  $\Delta E_{ab}^*$  between atmospheric light and the chromatic patches of the Macbeth ColorChecker at different fog levels of Scene B. For each level we calculate the standard deviation of  $\Delta E_{ab}^*$  of all patches.

Patch	L1	L2	L3	L4	L5	L6	L7	L8	L9	Haze-free
A	0	0.818	3.377	2.573	<b>7.282</b>	9.989	11.830	19.811	25.023	32.411
B	0	0.569	2.445	1.886	<b>4.561</b>	6.094	6.615	9.860	11.237	12.839
C	0	1.029	3.144	2.770	<b>6.602</b>	8.990	10.214	17.084	20.865	25.462
D	0	1.115	3.266	2.760	<b>6.761</b>	9.791	11.367	19.988	25.568	35.743
E	0	1.064	3.081	2.562	<b>6.072</b>	8.208	10.059	16.524	19.415	23.745
F	0	1.068	2.721	2.466	<b>5.4616</b>	7.020	8.570	12.907	15.900	18.006
G	0	0.441	2.736	2.109	<b>7.177</b>	11.168	13.561	24.399	33.123	46.997
H	0	0.977	3.368	2.848	<b>8.475</b>	12.086	15.336	26.580	33.413	42.378
I	0	0.836	2.868	2.370	<b>6.889</b>	9.904	12.088	21.199	27.863	36.257
J	0	1.054	3.530	2.882	<b>7.560</b>	10.747	13.047	23.232	30.671	43.735
K	0	0.722	2.685	2.183	<b>6.717</b>	11.139	15.598	27.548	35.240	44.273
L	0	0.501	2.270	1.768	<b>6.992</b>	11.146	15.686	27.546	37.281	54.518
M	0	0.851	3.465	2.911	<b>8.552</b>	12.824	15.905	29.290	39.229	51.463
N	0	0.885	2.875	2.521	<b>7.063</b>	9.157	10.965	22.047	28.679	37.599
O	0	0.581	3.089	2.391	<b>7.109</b>	10.305	13.402	24.133	32.660	45.267
P	0	0.274	2.456	2.209	<b>9.739</b>	16.137	21.643	34.921	44.201	56.347
Q	0	0.711	2.819	2.204	<b>6.901</b>	9.756	12.784	24.000	31.641	41.773
R	0	1.002	3.042	2.793	<b>6.904</b>	9.443	11.951	19.387	24.325	31.320
STD	0	0.249	0.368	0.343	<b>1.137</b>	2.213	3.338	6.029	8.391	12.143

and how the accuracy of calculation changes over fog levels. We then investigate as well the change in its estimation exactness with the number of selected colors all over the image.

### 5.3.1/ ATMOSPHERIC LIGHT CALCULATION

As a first step, for the sake of simplicity, we selected manually 8 patches sized of  $20 \times 20$  pixels. They are different in colors, in the distance to the camera and therefore in the density of fog and the attenuation rate of the transmitted signal. The selected colors are shown on the Figure 5.9. We matched them to the colors of lines of the Figures 5.10 and 5.11.

For a given level of fog of scene A, to plot the lines shown in Figures 5.10 and 5.11, we considered 2 points: the haze-free color value (saturated color) and its hazy value (desaturated color). In Figures 5.10 and 5.11, we show the convergence behavior, in zoomed out and zoomed in views, of two different levels of fog, level 5 and level 9, which are away from each other.

Considering the coordinates  $r$  and  $g$  calculated from the RGB channels:  $r = \frac{R}{R+G+B}$ ,  $g = \frac{G}{R+G+B}$ , we plotted the lines. When we look at the zoomed out graphs, we notice a convergence towards the  $A_\infty$ . But when we look more closely, we realize that for level





Figure 5.9: Selected color patches. The patches colors are the same matched with the curves colors in the Figures 5.10 and 5.11.

better (cf. Section 5.2.1.2).

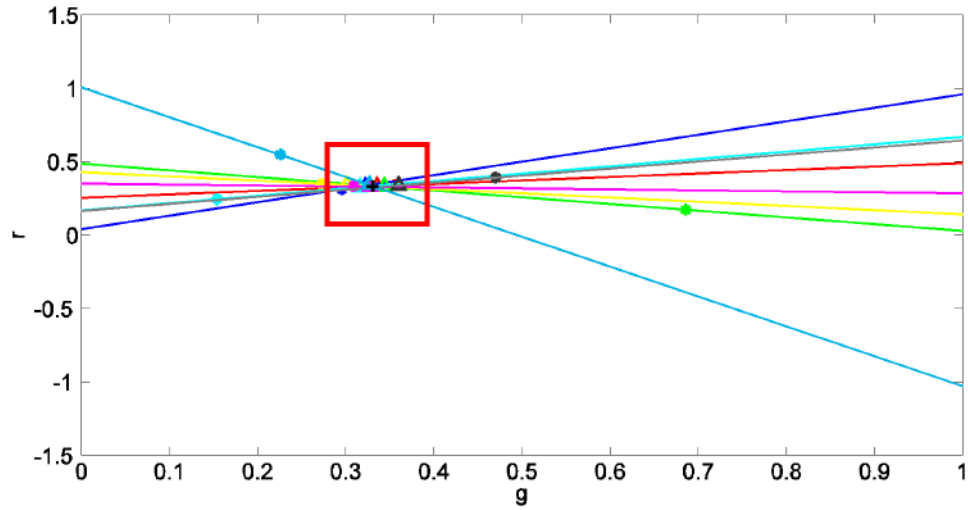
Table 5.5: The values of 2D distance between the real  $A_\infty$  and the calculated one as the centroid of the selected hazy colors at each fog level of the scene A.

Level 1	Level 2	Level 3	Level 4	Level 5	Level 6	Level 7	Level 8	Level 9	clear image
0.001	0.0021	0.003	0.0027	0.0033	0.0043	0.0046	0.0047	0.0052	0.0163

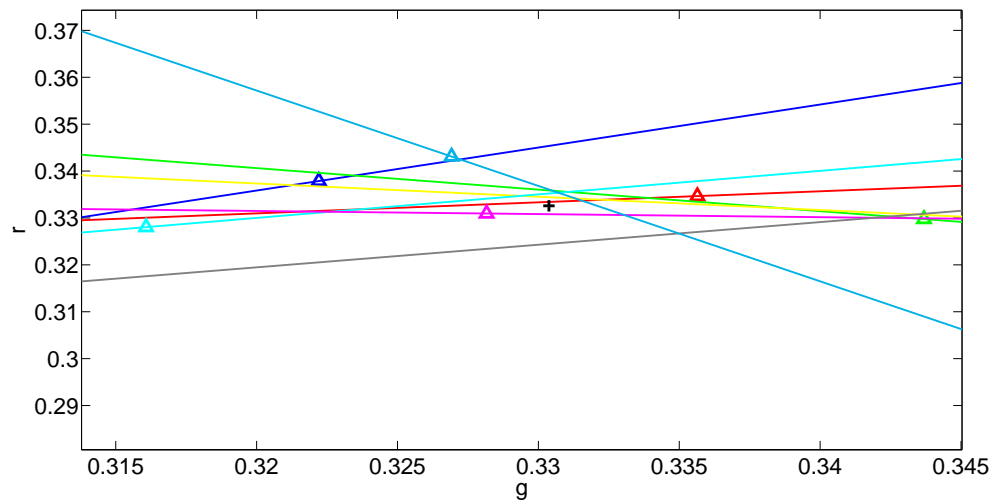
### 5.3.2/ IMPACT OF THE NUMBER OF SAMPLES

In a second step, we applied an automatic sampling of colors present in the image. The selected colors have been selected randomly respecting the precondition to be all different. For that, we transformed the RGB values into CIE Lab color space. At each selection iteration we calculated the values of the standard color difference metric  $\Delta E_{ab}$  between the pixel candidate and the previous selected pixels. According to the meaning of the  $\Delta E_{ab}$  value [21], we selected the pixels when all values are over than 6.

We randomly selected 10, 20, 70 and 100 patches sized of  $20 \times 20$  of different colors, respectively. We show in Table 5.6 the change of the computation precision depending on the number of the selected color samples. When it is a small number of selected colors (10 or 20 samples), according to the conditions of the selection algorithm, selected hazy colors do not necessarily surround the  $A_\infty$ . Thus, the euclidean distance across fog



(a)



(b)

Figure 5.10: (a) The lines constructed by the haze-free color and the hazy color  $\Delta$  at the same pixels of the level 5; (b) Zoom in of the red rectangle.

levels for such few samples seems to be greater than for the manual selection. When the number of samples relatively increases, the calculated value becomes closer to the real one. Since, when there is a high number of samples,  $A_\infty$  is perfectly surrounded, and the calculated value is therefore more accurate. According to the algorithm conditions, with more samples, the algorithm is no more practical. Consequently, the optimal number of samples would be all the image's pixels.

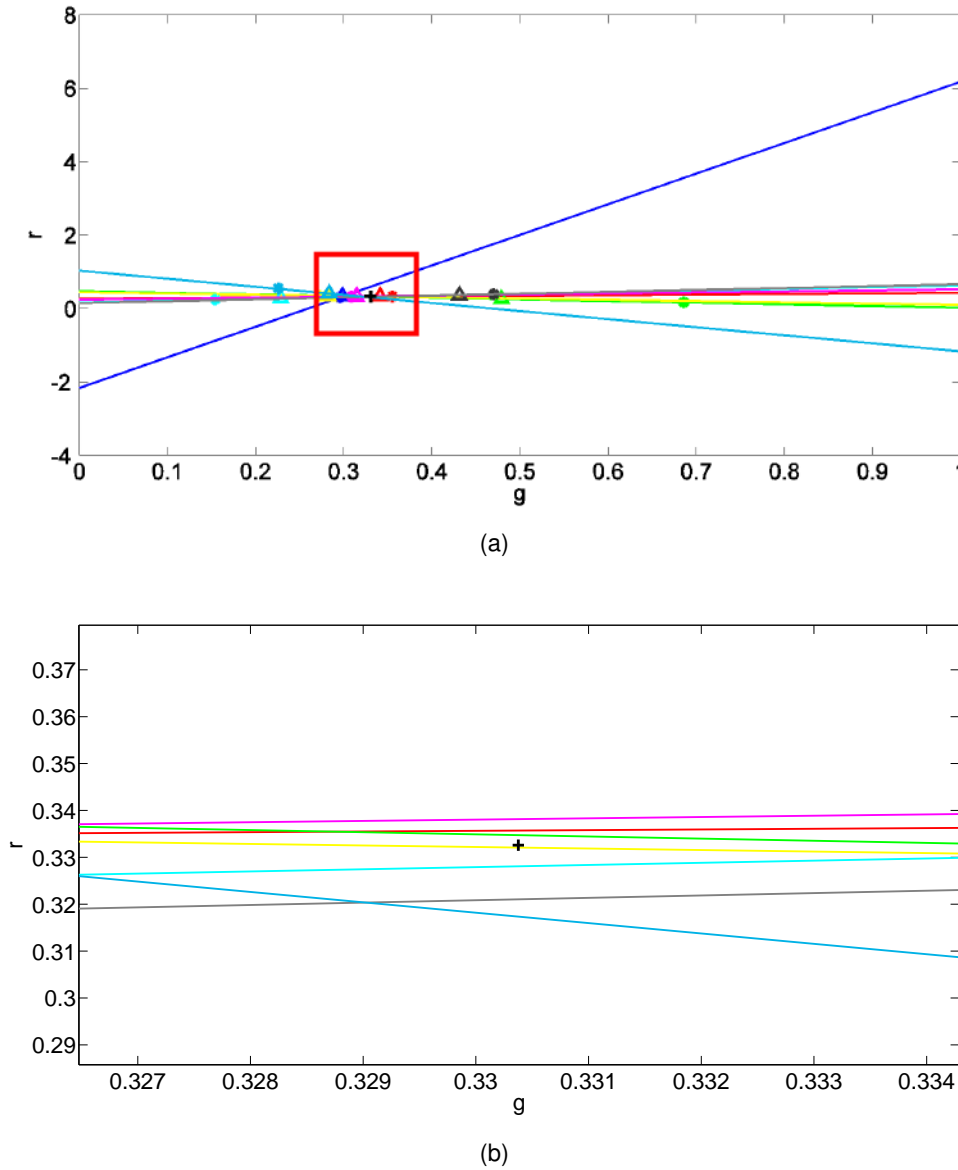


Figure 5.11: (a) The lines constructed by the haze-free color \* and the hazy color  $\Delta$  at the same pixels of the level 9; (b) Zoom in of the red rectangle.

## 5.4/ HAZE MODEL VS SPECTRAL DEPENDENCE

As we have stated previously, it is critical to verify whether the real situation of hazy scenes meets the physical haze model. Considering the fog levels of the database scenes (cf. Section 5.2.1.1) and the prevailing scattering type, we proceed to investigate the behavior of the haze model parameters across narrow wavelength bands in the VIS and the NIR ranges.

After performing the preprocessing steps (Dark Master and spectral calibration) described in Section 4.4.1.3, we have adopted the same method described in Section 5.2.1 to calculate  $A$  and  $t$  at visible and NIR wavelengths over the black patch of the MCC placed in the middle of the scene. A test of acquisition system linearity has been also performed

Table 5.6: The change in the accuracy of  $A_\infty$  estimation with the number of selected colors all over the image. The values below represent the 2D distance between the real atmospheric light and the calculated one as the centroid of the selected hazy colors at each fog level of the scene A.

	10 samples	20 samples	70 samples	100 samples
Level 1	0.0037	0.0030	$2.7 \times 10^{-4}$	$8.5 \times 10^{-5}$
Level 2	0.0060	0.0052	$5.2 \times 10^{-4}$	$9.1 \times 10^{-5}$
Level 3	0.0066	0.0090	$6.6 \times 10^{-4}$	$9.1 \times 10^{-5}$
Level 4	0.0110	0.0120	$6.4 \times 10^{-4}$	$1.3 \times 10^{-4}$
Level 5	0.013	0.0136	$6.8 \times 10^{-4}$	$1.5 \times 10^{-4}$
Level 6	0.0070	0.0205	$7.5 \times 10^{-4}$	$2 \times 10^{-4}$
Level 7	0.0235	0.0260	$7.4 \times 10^{-4}$	$2.2 \times 10^{-4}$
Level 8	0.0273	0.0204	$7.9 \times 10^{-4}$	$2.5 \times 10^{-4}$
Level 9	0.0245	0.0426	$8.8 \times 10^{-4}$	$3.5 \times 10^{-4}$

for a more accurate analysis of the measured data (Figure 5.12). Referring to Appendix B, Figures B.1, B.2, B.5, B.6, B.9 and B.10 show the evolution of  $A$  and  $t$  across fog levels of the scenes  $M1_V$ ,  $M2_V$  and  $M2_{NIR}$ , respectively. At a given wavelength,  $A$  and  $t$  have opposite behaviors across fog levels. When the fog density decreases (from level 1 to level  $n$ )  $A$  decreases and  $t$  increases. This is true for VIS and NIR. However, in NIR this variation is very subtle. This is due quantum efficiency of the sensor beyond 950 nm (see Figures 5.13, 5.14 and 5.15).

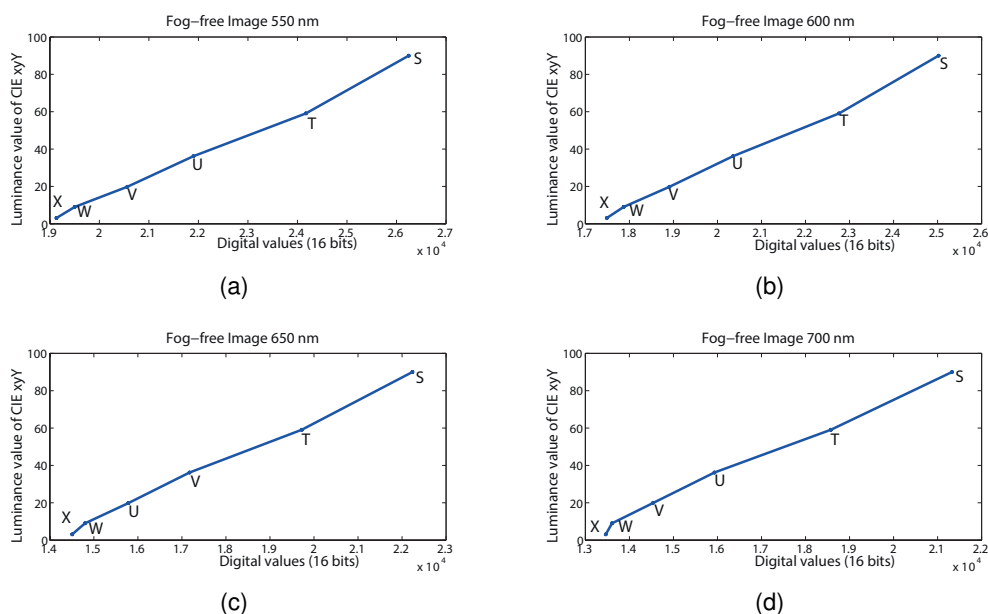


Figure 5.12: Linearity of the system composed of the sensor and the filter VIS. Considering the haze-free image, the luminance component of CIE xyY is plotted against the digital values (16 bits) calculated over the patches S, T, U, V, W and X (Figure 3.13). Being quasi-linear over 4 different wavelengths (550, 600, 650 and 700 nm), no correction such as Gamma correction is applied.

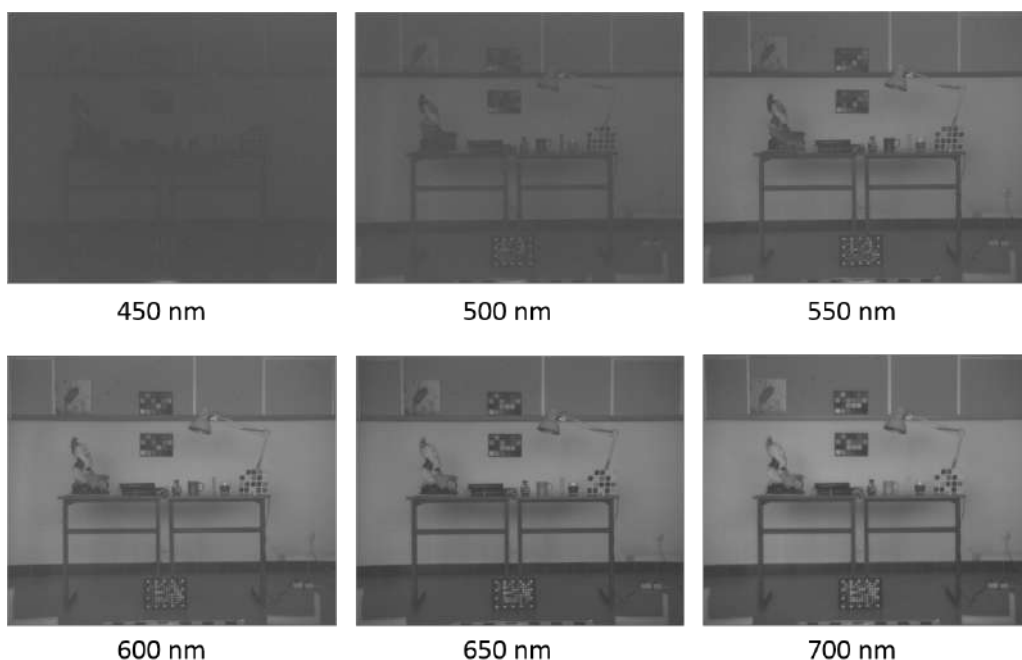


Figure 5.13:  $M1_V$  haze-free image. At low wavelengths (400-500 nm) the sensor noise prevails on the image. Thus, it avoids the accurate measurement of the airlight.

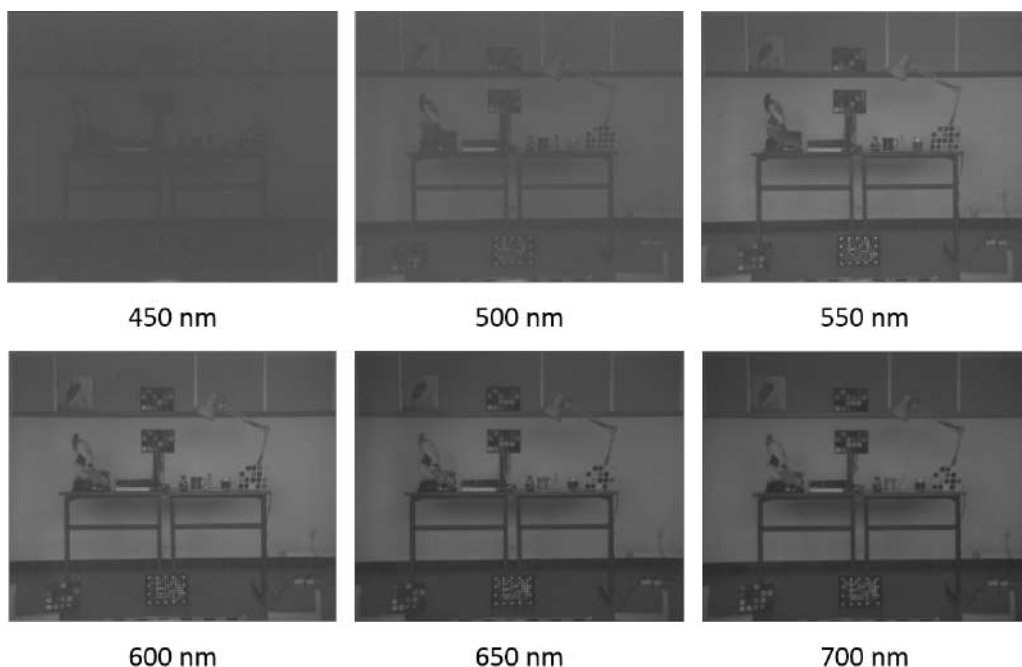


Figure 5.14:  $M2_V$  haze-free image. At low wavelengths (400-500 nm) the sensor noise prevails on the image. Thus, it avoids the accurate measurement of the airlight.

Figures B.3, B.4, B.7, B.8, B.11 and B.12 show the  $A$  values at the same level over the spectral channels of the VIS and the NIR filters. Referring to 2.3.5 and the fog levels characterization provided in Tables 5.1 and 5.2, the NIR ranges covered by our filters should not provide a remarkable enhancement over visible range. Thus, at the same

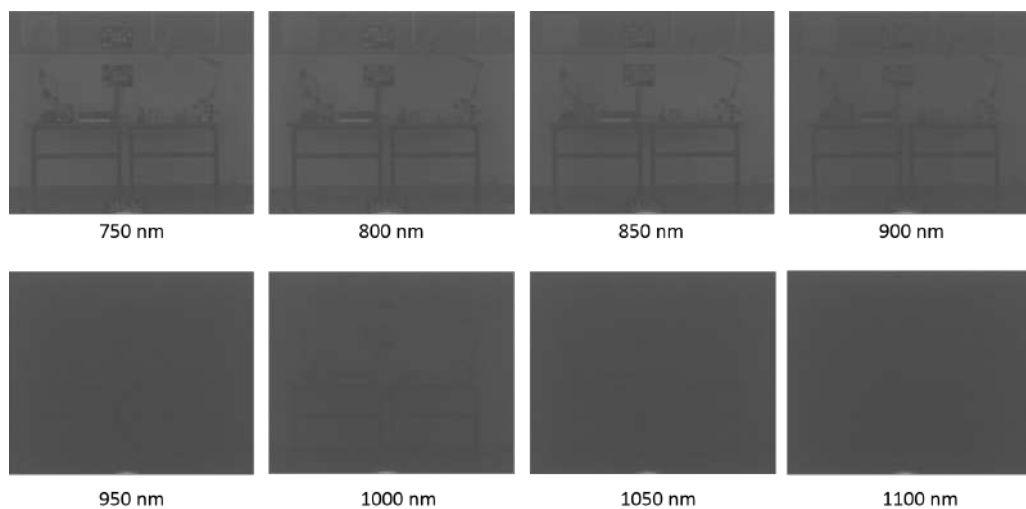


Figure 5.15:  $M2_{NIR}$  haze-free image. The energy beyond visible range seems to be extremely low. Thus, what we detect, especially from 900  $nm$  is just noise. Thus, airlight using these images is erroneously measured.

fog level, no difference is supposed to exist between the values of  $A$  at the considered visible and NIR wavelengths. Thus, there is a different reason lying between the values difference shown of the figures. Considering the airlight values across wavelength at haze-free level (see (f) in Figure B.4 and (c) in Figure B.8), they should be all set to zero as they are measured over the black patch. However, they have not negligible values. This bias widely the calculated values of  $A$  at other fog levels. Hence, this variation does not necessarily underline the dependence of the haze model parameters on the wavelengths.

In all of this, when the parameters are measured and extracted from an image, they are no more pure physical parameters. They undergo directly some transformations that make them strongly influenced and dependent on the acquisition system.

## 5.5/ CONCLUSION

Using our databases described in chapter 5, we sought to evaluate the haze model through two different vision systems properties: color system, which is characterized by wide sensitivity ranges and multispectral system characterized by narrow sensitivity ranges over a larger global range.

The haze model evaluation has been done according to two focuses: the amount of fog and the spectral dependence of estimated parameters. According to the first one, a critical saturation area is defined, where the perceptual difference between  $A_{\infty}$  and the desaturated hazy color is not that much. For a given color, it is hard to retrieve the hue line of the haze-free color. Since noise increases exponentially with  $t$ , it prevents the accurate color recovery with the high densities. As these limitations are imposed by the atmosphere, which represents a limiting factor for a color-based imaging system, the accurate estimation of the unknown parameters would not make an improvement. For the second focus, the sensor with its characteristics and precision play an active role in the estimation of the weather parameters and may bias the physical model validation.



## QUALITY ASSESSMENT OF SINGLE IMAGE DEHAZING

*"The quality of beauty lies on how beholder values an object."*

*-Jonathan Swift-*

*Quality assessment of enhanced images is inevitable. It guides us to select the most visually pleasing results and to develop automatic evaluating methods for computer vision. In this chapter we review the objective metrics that were developed to evaluate dehazing performance focusing on their pros and cons. Then, we describe the psychometric experiment that has been carried out using our hazy image database, to investigate fidelity quality attribute of a set of different approaches. A detailed discussion of a potential good evaluating metric is given.*

---

6.1	Introduction . . . . .	103
6.2	Quality of color dehazed images . . . . .	103
6.2.1	Background and motivation . . . . .	104
6.2.2	Subjective quality assessment . . . . .	108
6.2.3	Objective quality assessment . . . . .	109
6.2.3.1	General quality metrics . . . . .	111
6.2.3.2	Dehazing dedicated quality metrics . . . . .	115
6.3	Experiment . . . . .	118
6.3.1	Description . . . . .	121
6.3.2	Subjective evaluation of dehazing algorithms . . . . .	125
6.3.3	Subjective evaluation of image quality metrics . . . . .	125
6.3.4	Objective evaluation of dehazing algorithms . . . . .	129
6.3.5	Computational time . . . . .	131
6.3.6	Denoising . . . . .	132
6.3.7	Discussion . . . . .	135
6.4	Conclusion . . . . .	136

---

## 6.1/ INTRODUCTION

The physical properties of a given environment as well as the imaging systems introduce some amount of distortions that degrade the quality of captured images. The valuable information is no more properly extracted from such images to be used in further processing. Thus, we usually apply whether enhancement or restoration methods to improve the quality.

Evaluating the perceived quality of an image is usually done along two axes. On one hand, the subjective assessment through which we comprehend how the human visual system reacts effectively to the variations in features from a scene's image to another. On the other hand, observers' judgments are modeled as mathematical functions that correlate well with the subjective ratings, forming then a group of metrics used for the objective assessment.

In its turn, the quality of hazy and dehazed images represents an attractive research topic regarding the number of affected features and the lack of appropriate image databases.

In this chapter, we will first evaluate some dehazing methods using both dehazing-dedicated and non dehazing-dedicated metrics of different types. On the other hand, through a subjective evaluation, we will understand better to which extent observers succeed to judge image features recovery compared to the original image. It is not the first time that correlation between subjective and objective assessments provide useful information.

## 6.2/ QUALITY OF COLOR DEHAZED IMAGES

The quality evaluation of dehazed images forms an important part of this thesis. Dehazing is like other image processings, whose first goal is to optimize and to enhance an imperfect image in order to, either display it in a better way or to extract some useful information in order to be used in other post dehazing applications.

Throughout dehazing process, many modifications are introduced, affecting the image features. These modifications might lead to have a better or a worse rendering to the whole image, while knowing that image features are affected differently. The rendering level depends directly on the hypothesis of the method and the distortions introduced by viewing and capturing conditions.

There is a wide set of dehazing approaches and a variety of results (see Figure 6.1). The objective and subjective investigations of dehazed image quality are still relatively limited and miss some common data and tools. Thus, we dedicate this part to discuss the different aspects of dehazing quality using CHIC database images. It aims to:

- Outline the major challenges of such evaluation;
- Point out the performance of some representative dehazing methods through various haze densities;

- Emphasize as well the ability of metrics to quantify the perceived quality of dehazed images according to the haze-free image.

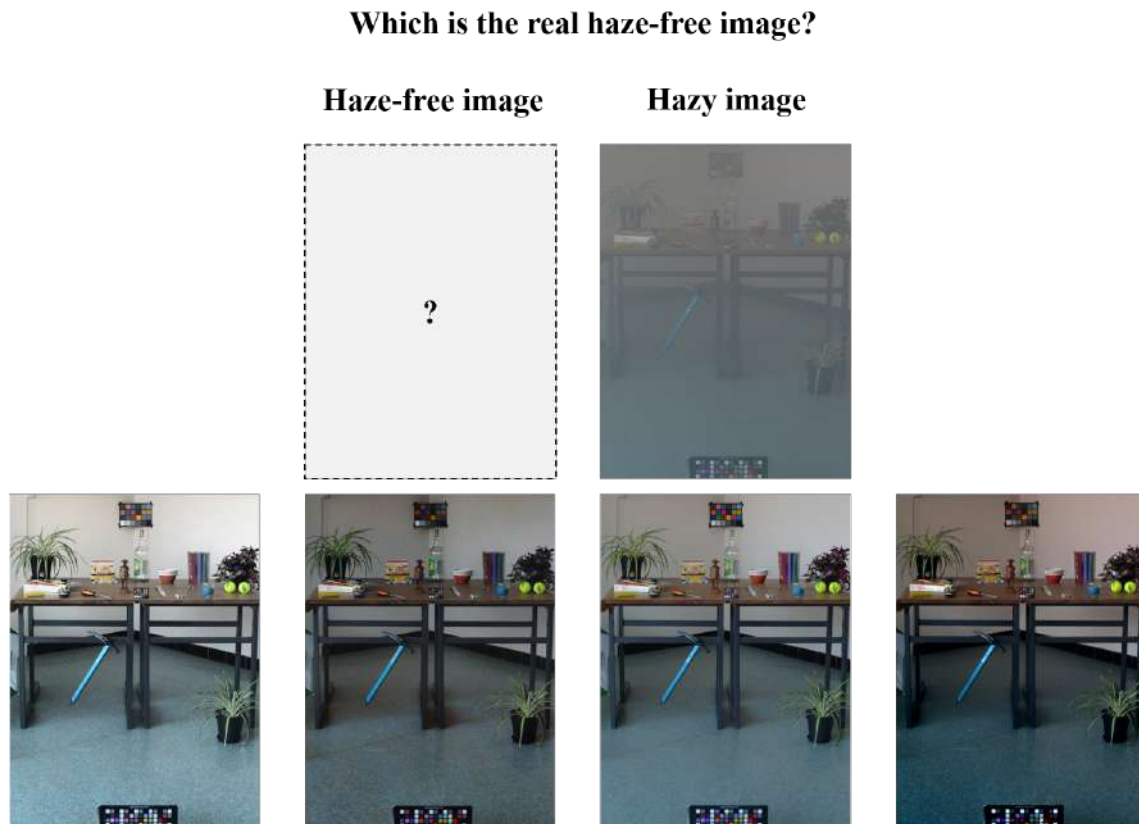


Figure 6.1: Case of confusion and disagreement between observers for the quality of recovered images that matches the best with the original haze-free image. scene A at haze level 9 taken from CHIC. In the second row, from left to right: image dehazed by CLAHE, image dehazed by VAR, haze-free image and dehazed image by Fusion (cf. Section 6.3).

The main difficulty in such evaluation is to specify the quality aspect we need to measure for dehazing. The selection of methods providing the best given type of quality depends strongly on the concerned application.

### 6.2.1/ BACKGROUND AND MOTIVATION

Image quality is an image characteristic that quantifies the perceived image degradation. Each step an image goes through, from the scene formation to the image storage, introduces some amounts of distortions or artifacts in the image. Image quality is affected by:

1. **Visibility conditions:** in bad mediums such as underwater environment, bad weather day, smoky place and outer space, the light emanating from an imaged objects scene undergoes attenuation caused by the particles of the substance lying along the path between the scene and the vision system. The degradation of the

visual quality worsens when, whether the particles become bigger or their concentration increases. The information loss is greater when the distance of the sensor to the scene increases and the viewing conditions become too bad, like a bad illuminant type or without light at all. All these conditions lead to a poor-quality image and may destroy drastically the original data.

- 2. Capture:** depending on the performance of the acquisition device, it is quite possible that noise is introduced while shooting, when the settings of the camera are not correctly adjusted. For example, noise is introduced into images when we shoot a long exposure image or shoot at a high ISO setting. In other cases, a relative motion between the object and the camera may produce blurry and noisy images.
- 3. Process:** when images are converted from one to another through processes such as enhancement and restoration techniques, the resulting output image is no more the same as the input image. While these processes are supposed to improve quality, it is likely to induce side effects. Some filtering processes may cause sharpness lost such as Mean filter. And other processes like dehazing may amplify noise (cf. Section 3.2.5).
- 4. Transmission:** when an image is transmitted over channels susceptible to noise and errors such as satellite communication channels [18], an adequate tradeoff should be established between the degradation of the received image quality caused by the loss of data and the added noise, and the adequate transmission delay imposed by the available bandwidth.
- 5. Display:** a considerable amount of processing is required between the image or signal source and the actual display device. All of this processing affects and modifies what each pixel winds up displaying, often adversely affecting image quality and accuracy and frequently introducing artifacts into the image. For example, a number of artifacts show up when we adjust image colors to be included in the color gamut of the display device to be finally reproduced by it. When the colors that can be reproduced by the device are less than the colors in the source image, we lose some color information. Likewise when we consider the features of the device like Gamma correction, dynamic range, color temperature, display contrast, etc.
- 6. Store:** digital images are usually compressed so that the files take up less storage space and can be transmitted more quickly. There is a tradeoff to make between the file size and the image quality. More the size is reduced, more compression artifacts are introduced into image. Depending on the type of lossy image compression, several types of artifacts can appear, like ringing, contouring, posterizing, aliasing, etc.

The distortions caused by each of the mentioned stages, induce distortions in one or more of these image quality features, such as sharpness, noise, contrast, color accuracy, vignetting, distortion, lens flare, etc.

After all that, the definition of image quality seems to be confusing. It is considered as a quantification of a preference accorded by an observer to an image over another one within the scope of a particular application. In this study, rather than considering the quality as a general concept, we differentiate between preference, usability and fidelity, which seem to be dependent on the fog densities (see Figure 6.2).

1. **Preference** When we favor an image over another one, either in a guided survey or to just evoke the aesthetic sense, this is known as image preference.

The human visual preference does not offer a stable behavior. It may be influenced by extrinsic and/or intrinsic factors. As extrinsic factors we may cite the purpose of the study and the visual conditions. Intrinsic factors could be the emotional state, the professional background, the individual gender and age, etc.

Human visual preference for some image features varies with learning experience and for some others it does not. The perception for the latter category relies on innate visual recognition mechanisms [149].

2. **Usability** Image usability refers to the level of processing efficiency from which an image becomes usable and provides useful information. Usability is defined by the target application domain.

If we consider, for example, driver assistance applications, what we consider of the best quality is an image that shows clearly the obstacles we have on the road. No matter if they appear in their real colors or not. Thus, we prioritize the methods that remove better the fog even if the recovered colors are completely different from the original ones. On the other hand, if we consider color-based segmentation, we prioritize the methods that maintain the original colors while the fog is removed to an extent, which is sufficient to recognize the colors (Figure 6.3).

3. **Fidelity** Image fidelity refers to the ability of a process to eliminate undesirable effects from a degraded image and to render it similar to the original image with no discriminable differences between them. The original image is considered as reference and it is assumed to have a perfect quality.

In this thesis, the dehazing matters are basically outlined by the image enhancement inside an oven. This represents an application where the fidelity of color is considered to be important for the color measurement of cooking meats in an oven. The funding that permitted this thesis work has been issued from the OFS project. Thus, only the Fidelity will be assessed in this thesis. The general integration of this thesis within the project is described in Appendix C.

In order to make best use of the CHIC characteristics, which are not provided for other sets of images, we deal only with the fidelity criterion through this study.

**Quality of dehazed images** Considering the different stages an image goes through, we match each of them to dehazing process. A hazy image is captured in a bad environment. Thus, besides the noise, which is due to the sensor, some amount of noise is due to the environment and particularly the haze and the induced bad visibility. The reversing of the haze model known by dehazing, increases exponentially (Equation 3.31) the noise added through the capture step. The remaining steps which are responsible for transfer and data communication, are common to different types of images.

Through all of these steps, a dehazed image loses its accurate features and ends up by having a lower quality comparing to the real raw haze-free scene.

IQA (Image Quality Assessment) of dehazed images is a challenging task, since the haze-free image is often not available and there is no easy way to have a proper reference image, as in the case of underwater and low light enhancement. Several factors make

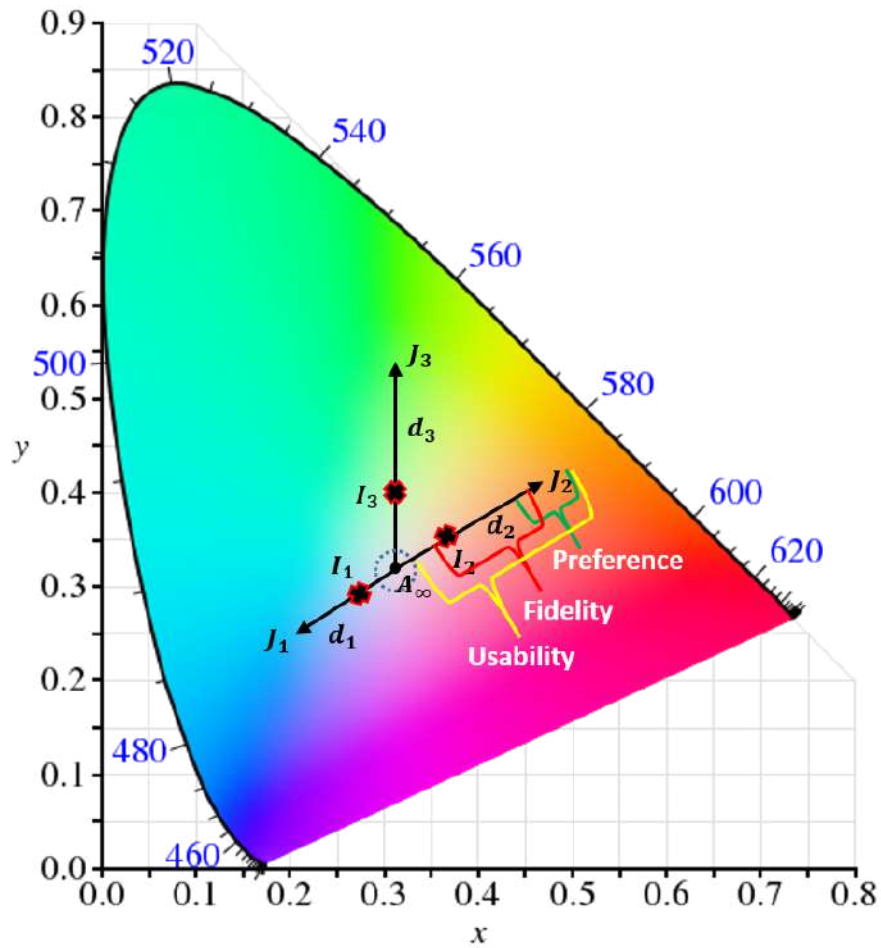


Figure 6.2: Preference, usability and fidelity have ranges of validation, which depend on the density of fog. When the density of fog is very high, we only consider the dehazing usability, which underlines the ability of dehazing to unveil some usable information. Usability can be considered for all fog densities. For intermediate densities, when the haze model is valid, we consider the fidelity of recovered features. When the fog is basically very light, the dehazed images are usually over-contrasted and therefore more preferred than the original haze-free images.

the evaluation of dehazing approaches not straightforward to be done. This is mainly due to the nature of the fog and the surrounding environment, and the way they influence the scene visibility (see Figure 2.4). Unlike classical image noise, fog is a continuous uniform/non-uniform layer across the image. It has depth effect: the chromatic effects of fog increase with depth, as the amount of fog intervening between surface and viewer increases. It leads to contrast reduction and color shift. Fog may have also different color casts depending on its density, the airlight and the surrounded medium ambient color. All of these factors turn dehazing IQA into a challenging task requiring an accurate evaluation of the altering features.

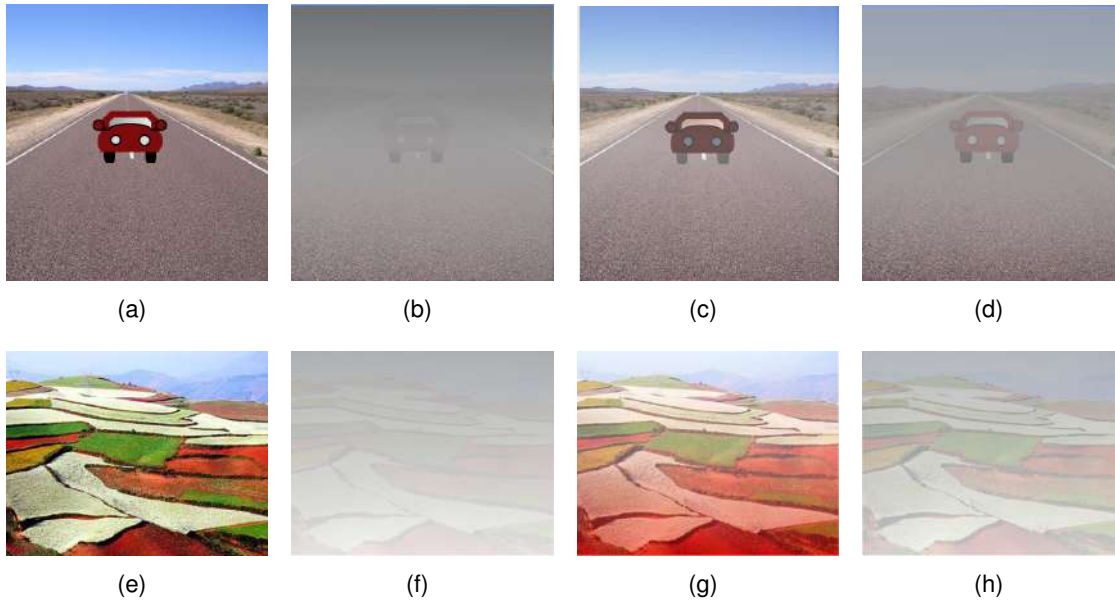


Figure 6.3: (a, e) Haze-free image; (b, f) Hazy image; (c, g) Dehazed image: efficient dehazing with color shift; (d, h) Dehazed image: inefficient dehazing with no color shift. In the case of obstacles detection for road safety, the result (c) is better than the result (d), since it provides a higher facility for objects detection. However, for applications consisting in segmentation based on color, the result (h) seems to be better than (g), since colors are recognized and similar to the original ones.

### 6.2.2/ SUBJECTIVE QUALITY ASSESSMENT

Image quality assessment is a crucial step for all processing and multimedia applications. It is mainly related to the humans' judgments. Only humans, who are the ultimate users of these applications, are able to judge accurately the perceptual quality. That is why, there are a number of subjective methods that define the way the humans should proceed to evaluate image quality in a controlled environment. We describe briefly the methods that are usually used for subjective quality evaluation [123].

**Single stimulus categorical rating** In this method, test images are shown randomly on a displaying device for a fixed period of time, then they will be disappeared and the observers will be asked to rank them according to five categories: excellent, good, fair, poor, or bad.

**Double stimulus categorical rating** This method is similar to the previous one. However, in addition to the test images, the reference image is also displayed.

**Ordering by force-choice pair-wise comparison** In this method, only two images are displayed for an indefinite time. Observers are asked to choose the one they prefer or the one they think it is of the best quality. Even, if they do not perceive any difference between them, they are required to choose one of them.



**Pair-wise similarity judgments** Unlike Ordering by force-choice pair-wise comparison method, observers are not forced to choose an image of two. However, they are asked to indicate the level of difference between both of them on a continuous scale.

**Difference mean opinion score (DMOS)** This method indicates the quality loss of the test image by calculating the difference between the raw scores assigned by observers to the test and the reference images.

**Z-score** In order to make easier the comparison between observers' opinions, we apply a linear transform to the DMOS. Equation 6.1 represents  $z_{m,n}$ , which is the Z-score of the observer  $m$  according to the reference image of the test image  $n$ .

$$z_{m,n} = \frac{DMOS_{m,n} - \overline{DMOS}_m}{\sigma_m} \quad (6.1)$$

$DMOS_{m,n}$  is the calculated DMOS for the observer  $m$  and the test image  $n$ ,  $\overline{DMOS}_m$  and  $\sigma_m$  are the mean DMOS and the standard deviation of the observer  $m$  computed for all test images.

Subjective quality assessment is a challenging task, since it is time consuming and expensive. Thus, it is not suitable for real-world applications. On the other hand, various factors make the subjective assessment complicated and not always reliable: lighting condition, display device, viewing distance, observer's mood, observer's ability [123]. Thus, mathematical models should complete the subjective evaluation, only on condition they provide the same predictions.



Figure 6.4: Scene 1. From left to right: Haze-free; Level A (highest fog level); Level B (medium fog level); Level C (lowest fog level). Image size is 1537×2049. These images are successively acquired within 5 minutes.

### 6.2.3/ OBJECTIVE QUALITY ASSESSMENT

Objective image quality assessment aims to measure and automatically evaluate the quality of a given image in agreement with the judgments of observers. Since the automatic evaluation should reflect the human judgment, the design process of a new metric



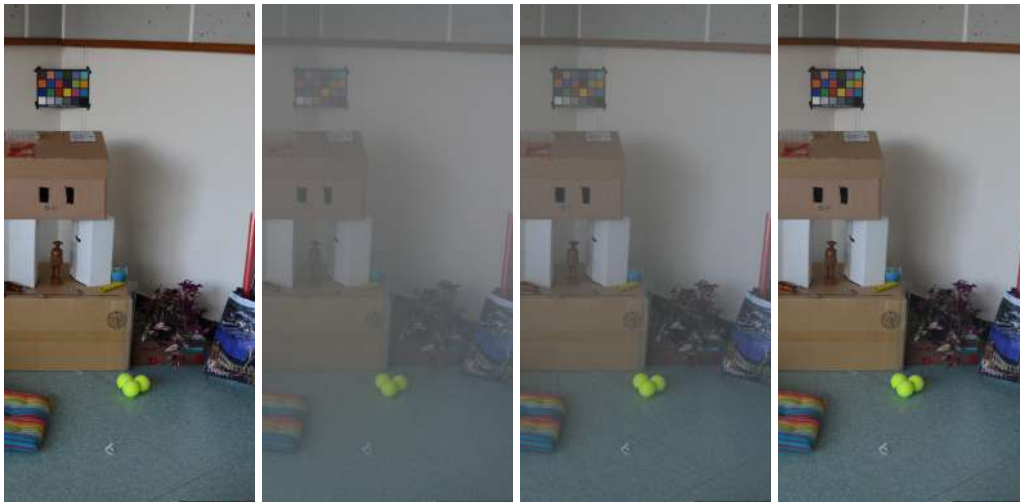


Figure 6.5: Scene 2. From left to right: Haze-free; Level A (highest fog level); Level B (medium fog level); Level C (lowest fog level). Image size is 1537×3073. These images are successively acquired within 5 minutes.

should go first through subjective testing. This is the most reliable method for assessing the quality of images. A good visual objective IQA metric is the one that can globally mimic human prediction.

Objective IQA metrics are divided into three categories: No-Reference Image Quality Assessment (NR-IQA), Reduced-Reference Image Quality Assessment (RR-IQA) and Full-Reference Image Quality Assessment (FR-IQA).

**NR-IQA** No-reference, referenceless and blind metrics, these nominations can all be used to designate the metrics that are applied when the reference image is not available. In many applications such as communication systems, radar systems, and dehazing applications, the reference image cannot be available. Then, the quality evaluation is only based on the test image. Such assessment is based on the fact that human being is able to evaluate the quality of a perceived image even if the reference image is not available. This can be done, since the human's brain knows how a good image should look like. Or, they are based on models that can learn to predict human judgments of image quality from databases of human-rated distorted images.

There are subcategories of NR-IQA metrics that have tighter conditions:

- Opinion aware NR-IQA (OA-NR-IQA): a model is OA if it has been trained on a set of distorted images that have been ranked by humans. In other words, when the classification is done based on a subjective opinion. Such metrics suffer from a common problem: they are limited to the distortion types that they have been trained on.
- Opinion unaware NR-IQA (OU-NR-IQA): since such collections of distorted images with recorded human opinions are not easily available, OU models do not require training on distorted images with the related judgments. However, they require specific information about the expected image distortions. For instance, the mean

value and the entropy of the phase congruency image, the entropy of the distorted image and the mean value of the gradient magnitude of the distorted image could be used as potential quality features [94].

- Distorsion aware NR-IQA (DA-NR-IQA): this model is derived from OU model. When a model is defined by training on specific distortions.
- Distorsion unaware NR-IQA (DU-NR-IQA): like DA, this model is also based on OU model. It relies instead only on exposure to naturalistic source images or image models to guide the QA process.

**RR-IQA** In this category, the reference image is not fully accessible, and only some features can be extracted from it. These features are therefore used to evaluate the image quality. According to [123], the selected features should satisfy some criteria. For instance, they should represent efficiently the reference image, and to be sensitive to a variety of distortion types and to have good perceptual relevance.

**FR-IQA** In this category, the original image that has a perfect quality is fully available. Among these three objective IQA metrics, FR-IQA was much more developed and used in a number of application domains like compression [44], [60], watermarking [35], printing workflows evaluation [138], medical imaging displays [82], and so on. It is likely easier and more reliable to evaluate an image after comparing it to a full real image that we see, than to expect how it would look like based on the human memory.

### 6.2.3.1/ GENERAL QUALITY METRICS

Let us talk about these metrics according to their evolution through time. The first image quality metrics are error-based metrics that measure quality between an original image that is assumed to be without defects and an image contaminated by noise and other distortions. The quality metric Mean Square Error (MSE) has been the basis of the generation of automatic quality prediction. It points out the weight of distortion that induces an important difference between the values of the same pixel of both images. Some metrics are based on the MSE, such as root mean square error (RMSE), peak signal to noise ratio (PSNR), mean absolute error (MAE), and signal to noise ratio (SNR). Despite their limitations that are detailed later, they have been used for a long time for image quality measuring.

Although they have been widely used, MSE and their relatives have many drawbacks:

- MSE-based measure ignores some image features such as textures, ordering, patterns that affect clearly the image perception quality.
- MSE-based measure is independent of temporal or spatial relationship between samples and the reference image. It overlooks the structural distortions effects such as additive Gaussian noise, blur and lossy compression (e.g. JPEG).
- MSE-based measure does not distinguish between a negative and a positive error. Therefore, all image signals are considered and treated equally with MSE.

After this generation of metrics, Wang *et al.* [177] explain widely the weak points error sensitivity pixel-based quality measurement. The earlier quality models are not correlated well with the perceived quality. This is due to the fact that these metrics are based on simplistic image features consideration and quasi-linear operations, while the HVS (Human Visual System) is a complex and non linear system.

Subsequently, the Structural SIMilarity (SSIM) [178] comes to subvert the concepts of quality metrics. The SSIM approach is based on the observation evoked in [177] that natural images have highly structured signals with strong neighborhood dependencies, and it is motivated by the fact that human visual system is highly adapted to extract structural information from scenes.

Thus, SSIM switches IQA from error sensitivity pixel-based quality measurement to structural distortion based image quality measurement, to which the human perception is more sensitive. Three attributes are considered to measure the structure similarity: the luminance  $l$  (Equation 6.2), which is given by the image mean  $\mu$ . The contrast  $c$  (Equation 6.3), which is given by the image variance  $\sigma$ . The structure  $s$  (Equation 6.4), which is calculated through the covariance  $\sigma_{XY}$  of the reference image  $X$  and test image  $Y$ .

$$l(X, Y) = \frac{2\mu_X\mu_Y + C_1}{\mu_X^2 + \mu_Y^2 + C_1} \quad (6.2)$$

$$c(X, Y) = \frac{2\sigma_X\sigma_Y + C_2}{\sigma_X^2 + \sigma_Y^2 + C_2} \quad (6.3)$$

$$s(X, Y) = \frac{\sigma_{XY} + C_3}{\sigma_X\sigma_Y + C_3} \quad (6.4)$$

$C_1$ ,  $C_2$  and  $C_3$  are small constant. They are used to avoid unstable measurement when the denominator is close to 0.

The global index is calculated as Equation 6.5:

$$SSIM(X, Y) = [l(X, Y)]^\alpha \cdot [c(X, Y)]^\beta \cdot [s(X, Y)]^\gamma \quad (6.5)$$

$\alpha$ ,  $\beta$  and  $\gamma$  define the relative importance of SSIM attributes. They are all usually set equal to 1.

**MS-SSIM [179]** SSIM gives the best performance when it is applied at an appropriate scale. The right scale depends on the viewing conditions like viewing distance and the resolution of the display. MS-SSIM (Multi-Scale SSIM) outperforms SSIM because the image details at different resolutions and different viewing conditions are integrated into the quality assessment.

**VIF [160]** VIF consists of measuring the mutual information between a perceived distorted image  $F$  and reference image with no distortions  $E$  (see Figure 6.6). A reference image  $E$  is modeled as an output of a natural image source and it passes through HVS channel before being processed by the brain.

The natural image source  $C$  is modeled by Gaussian scale mixture as being a product of two independent random fields,  $C = S.U = \{S_i \cdot \vec{U}_i : i \in I\}$ .  $I$  is the set of spatial

indices.  $S = \{S_i : i \in I\}$  is a random field of positive scalars.  $U = \{\vec{U}_i : i \in I\}$  is a Gaussian vector random field with zero mean and covariance  $C_U$ . The degraded image  $D$  is modeled as the sum of the signal attenuation and the additive noise in the wavelet domain,  $D = GC + V = \{g_i(\vec{C}_i + (\vec{V}_i : i \in I))\}$ .  $G = \{g_i : i \in I\}$  is a deterministic scalar gain field and  $V = \{\vec{V}_i : i \in I\}$  is a stationary, additive, zero-mean, white Gaussian noise RF with variance  $C_V = \sigma_2^2 I$ .

While flowing through the HSV channel, an amount of additive noise is added to the input information.  $E = C + N$  (reference image) and  $F = D + N'$  (degraded image). The HSV noise is modeled in the wavelet domain like  $V$ ,  $N = \{\vec{N}_i : i \in I\}$  and  $N' = \{\vec{N}'_i : i \in I\}$ , where  $\vec{N}_i$  and  $\vec{N}'_i$  are zero-mean uncorrelated multivariate Gaussian with the same dimensions as  $\vec{C}_i$ .

The change in visual quality between the reference and the degraded images can be related to the amount of mutual information that the brain can extract from both images. The mutual information is calculated by Equation 6.6:

$$VIF = \frac{\sum_{j \in \text{subbands}} I(\vec{C}^{N,j}, \vec{F}^{N,j} | S^{N,j})}{\sum_{j \in \text{subbands}} I(\vec{C}^{N,j}, \vec{E}^{N,j} | S^{N,j})} \quad (6.6)$$

$I(\vec{C}^{N,j}, \vec{E}^{N,j} | S^{N,j})$  and  $I(\vec{C}^{N,j}, \vec{F}^{N,j} | S^{N,j})$  are the information that the brain extracts from the reference and the degraded image, respectively. For more information about the computation of the extracted information, reader can refer to [160].

It was shown that VIF is quite able to predict the enhanced image quality by contrast enhancement operation.

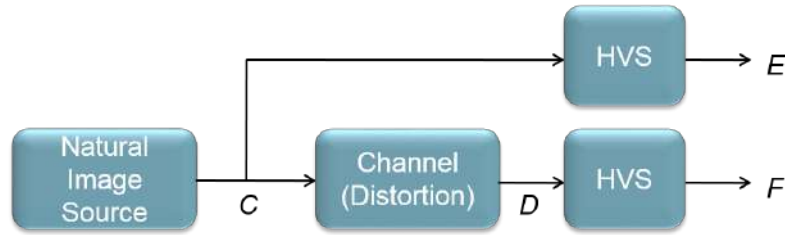


Figure 6.6: Modeling workflow of the reference and distorted images [160].

**MS-iCID [144]** The Multi-scale improved Color-Image-Difference has been proposed to rectify the shortcomings of the previous CID metric [101], which is a color version of the SSIM index. This means that, besides the lightness difference, contrast and structure, hue and chroma difference have been added. It is basically used for gamut mapping and tone mapping distortions evaluation.

It is sensitive to many distortions, including the expected color and lightness distortions generated by dehazing methods, such as lightness difference  $L$ , lightness-contrast  $L_C$ , lightness-structure  $L_S$ , chroma-difference  $C_L$ , hue-difference  $H$ , chroma-contrast  $C_C$  and chroma-structure  $C_S$ .

**VSI [195]** The human system has the ability to focus the attention to salient regions in the scene. To avoid the overload of visual information, our brain apprehend an image

content progressively, starting by the most eminent visual stimulus. Two main factors affect the order that a human adopts to perceive an image: bottom-up and top-down factors. In the first one, the objects that are different in the low-level features such as intensity, color and orientations attract the attention of the viewer. In the second one, the attention is guided by the requested task. In other words, the objects that are expected capture the observer's attention. A number of Visual Saliency (VS) models have been proposed to construct the VS map. For more information about computational VS models, the reader may refer to [78].

The perceived quality degradation of a given image induces perceptible change in the VS map. This map showed a weakness in the detection of the change of two features, contrast and saturation, which are strongly altered by the fog application and fog removal.

Due to the normalization operations involved in the VS map, it becomes no more sensitive to contrast change. Moreover, since it does not consider any chrominance information, it is not sensitive as well to color saturation change.

In order to handle the first issue, using the Scharr gradient operator, the gradient modulus maps of compared images are provided. The similarity score of both maps  $S_G$  is then provided. Gradient modulus map has a good potential to underline the local contrast loss of images.

To handle the saturation change, the RGB image is transformed into an opponent color space and the chrominance channels similarity score  $S_C$  is then calculated.

The global VSI (Equation 6.7) is calculated through the combination of the similarity scores across the image's pixels  $i$ :

$$VSI = S_{VS}(i) \cdot S_G(i)^\alpha \cdot S_C(i)^\beta \quad (6.7)$$

where  $\alpha$  and  $\beta$  define again the relative importance chrominance and contrast attributes.

**FSIMc [196]** Unlike SSIM, FSIM (Feature SIMilarity) is based on the fact that HVS is mainly adapted to perceive images degradation according to the change of its low-level features, such as edges and zero-crossings. It reproaches SSIM and MS-SSIM for the fact that pool a single quality score from the local quality map, thus, all positions are considered to have the same importance. In this metric two attributes are considered:

- Phase Congruency ( $PC$ ): this model postulates that sharp structural features in the image are perceived at points where the Fourier components are maximal in phase. For more information about the  $PC$  map computation, the reader can refer to [196].
- Gradient magnitude ( $GM$ ): since  $PC$  component is not sensitive to contrast variation, it was coupled to a  $GM$  expressed by convolution masks for edge detection such as Sobel, Prewitt and Scharr filters.

For each map position  $x$ , the similarity score between  $PC_1$  and  $PC_2$  maps extracted from haze-free and dehazed images, respectively, is calculated as follows:

$$S_{PC}(x) = \frac{2PC_1(x) \cdot PC_2(x) + T_1}{PC_1^2(x) + PC_2^2(x) + T_1} \quad (6.8)$$

Likewise, the similarity score between  $GM_1$  and  $GM_2$  maps extracted from haze-free and dehazed images, respectively, is calculated as follows:

$$S_{GM}(x) = \frac{2GM_1(x).GM_2(x) + T_2}{GM_1^2(x) + GM_2^2(x) + T_2} \quad (6.9)$$

where  $T_1$  and  $T_2$  are positive values. They are used to maintain the stability of  $S_{PC}(x)$  and  $S_{GM}(x)$  and they depend to the dynamic range of  $PC$  and  $GM$  maps, respectively.

The global achromatic FSIM index is given by Equation 6.10:

$$FSIM = \frac{\sum_{x \in \Omega} (S_L(x).PC_m(x))}{\sum_{x \in \Omega} PC_m(x)} \quad (6.10)$$

where  $S_L(x) = S_{PC}(x)^\alpha (S_{GM}(x))^\beta$ .  $\alpha$  and  $\beta$  denote the importance parameters of  $PC$  and  $GM$  features. Usually, they are both set to 1.  $PC_m(x) = \max(PC_1(x), PC_2(x))$ . It has been introduced to normalize the importance of  $PC$  and  $GM$  similarities all over the image.  $\Omega$  denotes the whole image.

FSIM is basically applied to graylevel images. However, it can be extended to color images by converting first the  $RGB$  to  $YIQ$  image, calculating the similarity of  $PC$  and  $GM$  of the luminance component  $Y$  (as explained before) and calculating likewise the similarity of the chromatic channels  $I$  and  $Q$ .

The global chromatic FSIMc index given in Equation 6.11 is calculated after incorporating the chrominance similarity  $S_C(x) = S_I(x).S_Q(x)$ , which is the product of the chromatic channels similarity scores:

$$FSIMc = \frac{\sum_{x \in \Omega} (S_C(x))^\lambda PC_m(x)}{\sum_{x \in \Omega} PC_m(x)} \quad (6.11)$$

where  $\lambda$  is a positive parameter used to define the importance degree of chromatic components.

**NIQE [121]** This OU-DU-NR-IQA is based on a number of quality features extracted from a large corpus of no distorted natural images. Thus, it is not limited to any specific distortions. The features of the NSS model [151] are extracted from patches of a given size and fitted in multivariate Gaussian (MVG) model. NIQE is expressed as the distance between two multivariate Gaussian models of NSS features extracted from natural images and the ones extracted from the patches of the test image. The less distortions are there, the distance difference value is low.

### 6.2.3.2/ DEHAZING DEDICATED QUALITY METRICS

IQA of dehazed images is a challenging task, since haze-free image is often not available and there is no easy way to have a proper reference image.

Several factors make the evaluation of dehazing approaches not straightforward to be done. This is mainly due to the nature of the fog, the surrounding environment and the way they influence the scene visibility.

In this part, we present the dehazing dedicated metrics in a chronological order.



Early works focused on showing off contrast enhancement. They overlooked in one way or the other the impact of color evolution on the global quality of restored images. The recently proposed indicators take into consideration this aspect, because we are aware of its ability to alter the perceived image quality.

There are two kinds of dehazing-dedicated metrics: full-reference metric, where the reference is the hazy image and no-reference metrics.

**Hautière *et al.*** As the hazy image is the only available input image, Hautière *et al.* [68] proposed to compute the ratio between the gradient of the visible edges between the image before and after contrast restoration.

Therefore, two indicators have been proposed. The rate of new visible edges:

$$e = \frac{n_r - n_0}{n_0} \quad (6.12)$$

$n_0$  and  $n_r$  are the cardinal numbers of the set of visible edges in the original hazy image and the restored image, respectively.

And the indicator of restoration quality:

$$\bar{r} = \exp\left[\frac{1}{n_r} \sum_{P_i \in P_r} \log r_i\right] \quad (6.13)$$

where  $P_r$  is the set of visible edges in the restored image. This indicator is the geometric mean of the ratios of the visibility level  $VL$  defined by:

$$r = \frac{VL_r}{VL_0} = \frac{\Delta L_r / \Delta L_{threshold}}{\Delta L_0 / \Delta L_{threshold}} \quad (6.14)$$

$VL_r$  and  $VL_0$  are the difference in luminance between the target and the background of the original hazy image and the restored image, respectively.  $\Delta L_{threshold}$  is the value at which a target becomes perceptible with a high probability. This is estimated using Adrians empirical target visibility model (Adrian, 1989).

In addition to  $\bar{r}$  and  $e$ , Hautière *et al.* proposed to calculate the percentage of the saturated pixels (black and white) generated by the restoration method, as an indicator of how a saturation degree may influence the restored image quality:

$$\sigma = \frac{n_s}{dim_x \times dim_y} \quad (6.15)$$

where  $n_s$  is the cardinal number of the saturated pixels.  $dim_x$  and  $dim_y$  are respectively the width and the height of the image. Good dehazing methods are supposed to increase contrast without saturating pixels. Otherwise, some visual information are lost. Therefore, a high image quality of dehazed images is described by high values of  $e$  (Equation 6.12) and  $\bar{r}$  (Equation 6.13) and low values of  $\sigma$  (Equation 6.15).

This methodology has been widely used to assess the performance of a method against others. The frequent use of these metrics might goes back to the lack of metrics rating such kind of treated images, and the faithful color restoration was usually overlooked. According to Guo *et al.* [63], the assessment based on these metrics is inconsistent with the human visual perception for color images. They do not take into consideration the apparent problems of over-enhancement and color distortion.

**Fang et al. [51]** The metric presented here, combines the increasing of contrast degree with the structural similarity. They are respectively computed based on the spatial frequency contrast and the edges consistency between the hazy and the dehazed image.

Based on the following characteristics, authors searched to highlight the contrast improvement and the structure similarity between the hazy and the dehazed image:

- Although the contrast of a hazy image is low, there is still gradient differences.
- The contrast of the dehazed image is higher than the contrast of the hazy image.
- The scene structure has strong correlation, thus, the pixels of image have similar property.

As the Michelson contrast [117] computes a global contrast for the whole image and it is sensitive for noise stimuli, based on the image spatial frequency characteristics, a local band-limited contrast gives the contrast of every pixel. The ascension of contrast degree (Equation 6.16) is calculated as follows:

$$C = \frac{\sum_{x=1}^H \sum_{y=1}^W (c_e(x, y) - c_o(x, y))}{\sum_{x=1}^H \sum_{y=1}^W c_o(x, y)} \quad (6.16)$$

$x$  and  $y$  are the pixels coordinates,  $H$  and  $W$  are respectively the height and width of the image.  $c_o$  and  $c_e$  are the contrast at the band of spatial frequencies of blurred and deblurred images, respectively.

When the ascension of the contrast degree is high, this means that the difference between  $c_o$  and  $c_e$  is greater, which reflects the difference of image quality between the original and the processed images.

Structural similarity (Equation 6.17) is measured by the consistency of edges of the original and the dehazed image:

$$S = \frac{\sum_{x=1}^H \sum_{y=1}^W (Edge_o(x, y) - Edge_r(x, y))}{E\_sum\_o} \quad (6.17)$$

$Edge_o(x, y)$  and  $Edge_r(x, y)$  are the edges of the original and dehazed image.  $E\_sum\_o$  is the sum of the edges in the original hazy image. In this formula, the difference of edge numbers has no influence. We just consider if the position of the edge of dehazed image is the same with the original edge. When  $S$  is low, this means that the structure is less similar. Then, the dehazing process has not inserted artificial edges, such as blocking effects.

The global CS index is given as follows:

$$CS = (C^\alpha) * (S^\beta) \quad (6.18)$$

$\alpha$  and  $\beta$  denote again the importance of  $C$  and  $S$  parameters. Here, they are both set to 1.

**Guo et al. [63]** They proposed a full-reference metric using synthetic hazy images simulated by image degradation. It consists on computing the absolute difference between the hazy image and the dehazed one.



They proposed as well, two no-reference metrics: the first one considers the fog density and the second one considers the human visual perception. The fog density  $f$  (Equation 6.19) is calculated focusing on the dark channel, which is computed using DCP method, and the refined fog veil  $v$  (Equation 6.21), which is calculated by the mean  $M$  (Equation 6.20) of the convolution of each color channel of the input image  $I$  with the Gaussian filter  $F(x, y)$  (cf. Appendix A):

$$f = \sum_{\Omega \in I} \frac{D_{c\Omega}(p)V_{\Omega}(p)}{HW} \quad (6.19)$$

$$M(x, y) = I(x, y) * F(x, y) \quad (6.20)$$

$$v = \frac{1}{HW} \sum_{x=1}^H \sum_{y=1}^W M(x, y) \quad (6.21)$$

For the hazy image,  $D_c$  is the dark channel,  $v$  is the estimated fog veil,  $H$  and  $W$  are the height and the width of the image. When  $D_c$  and  $V$  are high, the fog is dense. This is quite logical. The drawback of this indicator is that it is only consistent with human judgment for grey level images.

In order to settle this issue, the third indicator is based on the human visual perception that considers not only the contrast but also the color quality, by combining three components: contrast, naturalness and colorfulness.

The contrast component (Equation 6.22) is the ratio between the number of visible edges in the hazy image  $n_X$  and the number of visible edges in the dehazed image  $n_Y$ :

$$e = \frac{n_Y}{n_X} \quad (6.22)$$

The second component, Color Naturalness Index (CNI), has been introduced in [189]. This index shapes the degree of correspondence between human perception and reality world. After transforming the RGB image to CIELUV color space, three kinds of pixels according to the hue value are defined: skin pixels, grass pixels and sky pixels.

**Choi et al. [32]** Recently, a Fog Aware Density Evaluator (FADE) [32] was proposed to evaluate the performance of dehazing algorithms through the definition of the perceptual fog density of the image. This is a no-reference metric. Since hazy images are characterized by low contrast, faint color, and shifted luminance, this metric evaluates defogged image density by calculating by means of Mahalanobis distance the similarity with Natural Scene Statistics (NSS) and fog aware statistical features, including sharpness, contrast, image entropy, saturation in HSV color space and colorfulness. These features have been extracted from 500 images of hazy and 500 of haze-free images of different natural image databases such as LIVE IQA database [161], the Berkeley image segmentation database [112], and copy-right free web sources like Flickr.

### 6.3/ EXPERIMENT

In this experiment we evaluate, using images from CHIC database (cf. Section 4.3.2), five state-of-the-art dehazing algorithms (see Table 6.1) in terms of perceived quality for

visualization by means of subjective experiment. We also investigate the performances of eleven state-of-the-art image-difference metrics (full- and no-reference) (see Table 6.2).

For this study, which investigates the fidelity of dehazed image quality, we selected three images of different medium and light fog densities level 5, level 7 and level 9 to fulfill the fidelity requirements (see Figure 6.2). In this chapter, we use a different naming of levels than previous chapters. Level A, level B and level C denote the highest level (level 5), the medium level (level 7), and the lowest level (level 9) among the selected fog levels of scene 1 and scene 2, respectively (Figures 6.4, 6.5).

**Why did we select these methods and metrics?** A selection of representative dehazing methods and several quality metrics has been done to reduce the complexity of this study. These methods belong to different dehazing categories and they are based on different approaches (cf. Section dehazing model based, Table 6.1). For the metrics, we limited our selection to the most used and efficient metrics mentioned in literature, with obviously the dehazing-dedicated metrics that had been released before this study was done.

Table 6.1: Summary of selected dehazing methods. For each method, the default implementations' parameters proposed by the authors, have been used.

Dehazing method	Approach	Physics-based
DCP [136]	Statistics-based assumptions & filtering approach	✓
FAST [167]	Filtering approach	✓
FUSION [11]	White balance and contrast enhancement weights fusion	✓
VAR [57]	Variational approach & histogram equalization	×
CLAHE [187]	Histogram equalization	×

Table 6.2: Summary of selected metrics. Type can be Full-reference F and No-reference N. The reference image is in brackets.

Metric	Type	Haze-dedicated
MS-SSIM [179]	F (haze-free)	×
VIF [160]	F (haze-free)	×
MS-iCID [101]	F (haze-free)	×
FSIMc [196]	F (haze-free)	×
VSI [195]	F (haze-free)	×
NIQE [121]	N	×
FADE [32]	N	✓
Hautière's $r$ [68]	F (hazy)	✓
Hautière's $e$ [68]	F (hazy)	✓
CNC [63]	F (hazy)	✓
CS [51]	F (hazy)	✓

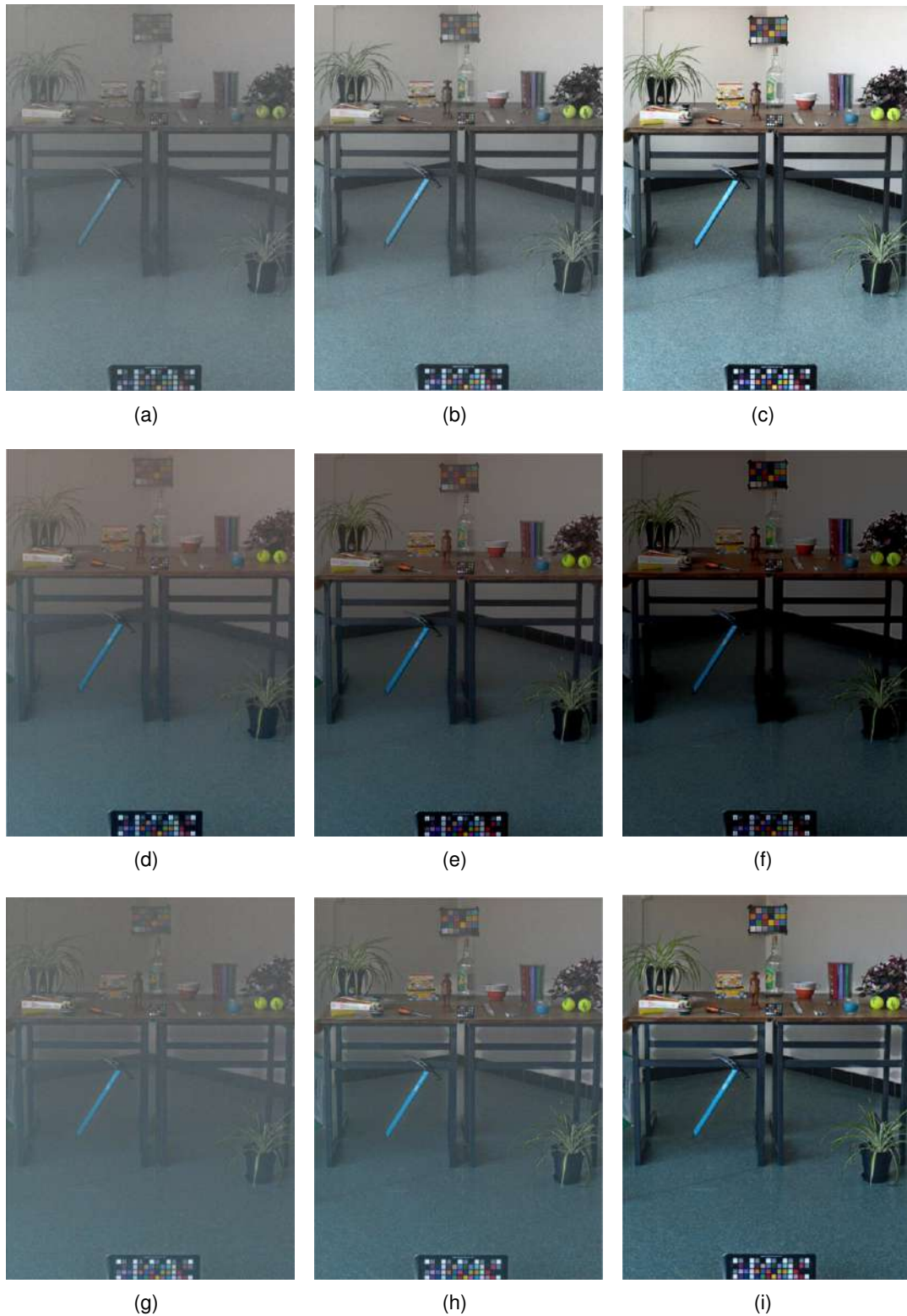


Figure 6.7: Dehazed images of Scene 1 of fog levels A, B and C. They have been processed by CLAHE, DCP and FAST algorithms. Rows: CLAHE, DCP, FAST. Columns: level A, level B, level C.

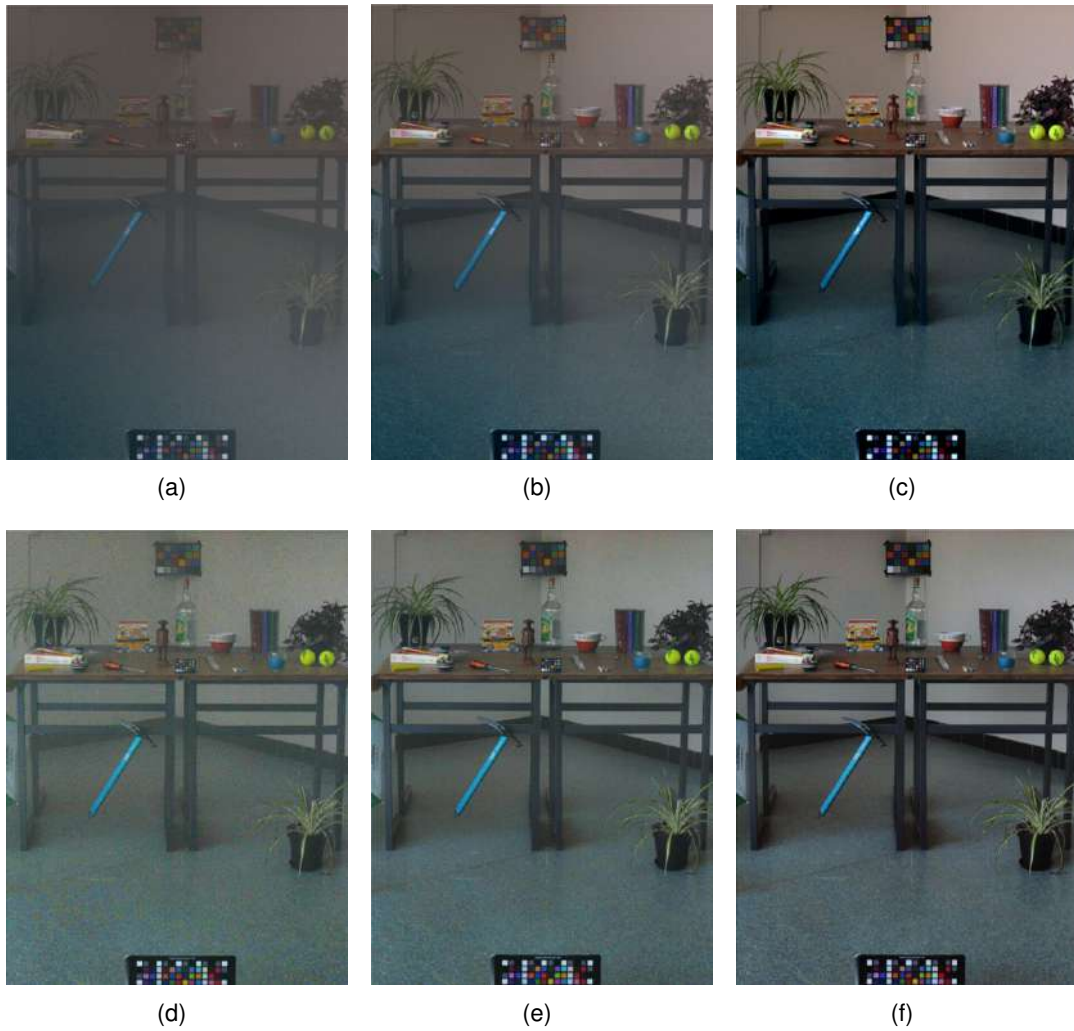


Figure 6.8: Dehazed images of Scene 1 of fog levels A, B and C. They have been processed by FUSION and VAR algorithms. Rows: FUSION and VAR. Columns: level A, level B, level C.

### 6.3.1/ DESCRIPTION

**Objective** We first want to pinpoint which algorithm would give the best results. The goal is to remove the haze while preserving color and sharpness fidelity comparing to the original haze-free image. We evaluate the selected algorithms with the selected metrics and with visual judgments. Then, we evaluate how metrics correlate with the visual judgments.

In this work, we consider the similarity between the haze-free and the processed images according to the most perceived criteria. The sharpness similarity that points at the same time to the ability to remove fog and the resulting amount of noise and artifacts. The color similarity that points to the ability to estimate accurately the airlight and the ability to find an acceptable compromise between the dehazing and the naturalness of images.



Figure 6.9: Dehazed images of Scene 2 of fog levels A, B and C. They have been processed by CLAHE and DCP algorithms. Rows: CLAHE and DCP. Columns: level A, level B, level C.

**Observers** A group of 20 subjects, men and women, has been asked to rank images. The judgments of only 14 observers have been retained (cf. paragraph 6.3.2). Their age



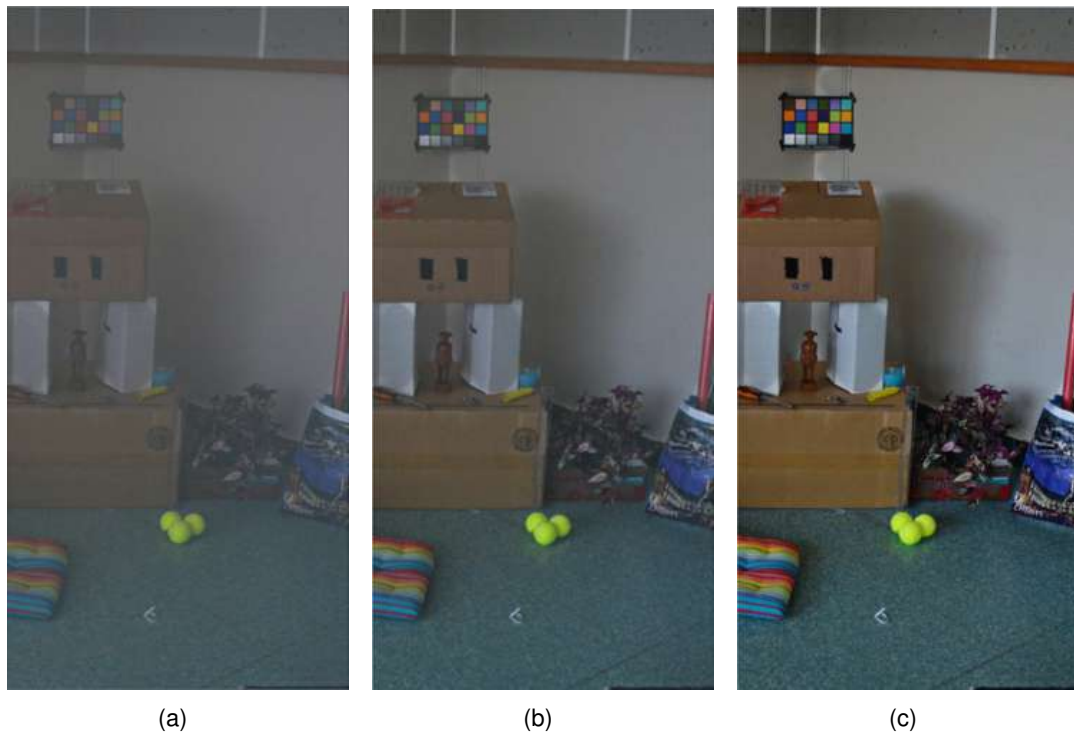


Figure 6.10: Dehazed images of Scene 2 of fog levels A, B and C. They have been processed by FAST algorithm. Columns: level A, level B, level C.

ranges from 20 to 40. They were students and researchers at Gjøvik University College. Most of them were familiar with images quality features.

**Stimuli** Scene 1 and scene 2 were used with fog level A, B and C. The five algorithms have been applied to each of these images (Figures 6.7, 6.8, 6.9, 6.10, 6.11). Thus, in the subjective evaluation, for each fog level of a scene, the five dehazed images are compared to the correspondent haze-free image in terms of color and in terms of sharpness similarities.

Thus, the observers examined 36 images for each feature. For the same fog level, 6 images (5 dehazed images and the haze-free image) of scene 1 were displayed followed by 6 images of scene 2.

**Procedure** The experiments were run in a dark room. Observers were seated approximately at 70 cm from the display. For each fog density, observers were asked to rank the dehazed images, considering the degree of matching with the haze-free image in terms of color and in terms of sharpness, respectively. For each feature, we displayed 6 sets grouping 6 images, starting by level A to level C of scene 1 and scene 2, respectively. This process has been done using the well-established Rank Order Correlation. *Quickeval* [174], a web-based tool for psychometric image evaluation, has been used. Observers were allowed to move the image to a zoomed-in view, and to focus only on a portion of the displayed scene at a time. In this experiment, we did not impose any constraints related to the time an observer could spend on the task, nor to the portion of



Figure 6.11: Dehazed images of Scene 2 of fog levels A, B and C. They have been processed by FUSION and VAR algorithms. Rows: FUSION and VAR. Columns: level A, level B, level C.

scene that was to be considered. Depending on the participants, the global analysis time of all stimuli varied from 35 to 45 minutes.

### 6.3.2/ SUBJECTIVE EVALUATION OF DEHAZING ALGORITHMS

We first performed a screening of the 20 participants according to [25] and found that 6 of them were not valid. Results from these outlying observers were discarded. Overall, we noted a relatively large inter-observer variability (see error bars on Figure 6.12), which we assume can be explained by several factors. First, the complexity of the task: even though we asked the observers to isolate the influence of color and that of sharpness, we believe that the extent to which they were able to do so varied greatly from one observer to another. Secondly, the software that we used allowed observers to focus on a portion of a scene. Although we did not record how each observer browsed the scenes, we argue that there might have been some variations in terms of what they considered as regions of interest. In other words, different observers chose to focus on different parts of the scene, and that behavior cannot be modeled by saliency only.

We computed the average ranks, over all 14 observers, given to each dehazing method in each sequence and obtained the results shown in Figure 6.12. Again, the large error bars suggest a large inter-observer variability. However in a few cases, observers tend to agree to a relatively large extent. For example, according to these results, the CLAHE method performs significantly worse than the other four in terms of recovering colors on the second scene, for the fog level A. Observers also agreed that this method performs poorly on the first scene for the fog level B and that the DCP method performs badly in terms of both color and sharpness recovery in scene 2 for the fog level C. We can also see that VAR performs best in terms of recovering color on the first scene and for the fog level A.

Overall, we found that inter-observer variability is larger for the sharpness recovery assessment (second row in Figure 6.12) than for that of color recovery. This is consistent with the feedback we obtained from most observers about the higher difficulty of the second part of the experiment.

Note that these results, *i.e.* large inter-observer variability and lack of consistency across scenes, have also been reported in [107]. Here we demonstrate in addition, and in a different framework when the observers had access to the original image, that:

- There seems to be no consistency across fog levels and between color and sharpness preservation. For instance, CLAHE is the best performing method of color recovery, while it fails to maintain a good sharpness at the same level B of scene 1.
- Not a single method performs the best nor the worst overall.

### 6.3.3/ SUBJECTIVE EVALUATION OF IMAGE QUALITY METRICS

We chose to use the **hit rate** to measure the agreement between subjective and objective data. It corresponds to the proportion of correct predictions made by the metric in a pairwise comparison setup and takes into account both intra- and inter-observer variability. A hit rate  $h$  has a value between 0 and 1, although it does have an upper bound in that it is impossible to obtain a perfect agreement with all observers. There is a maximal achievable hit rate  $h_{\max}$ , also referred to as **majority hit rate** [101], which is defined as the rate that would be obtained should the metric constantly agree with the majority of the observers. Additionally,  $h$  also has a pseudo lower bound in that a hit rate of 0.5 is



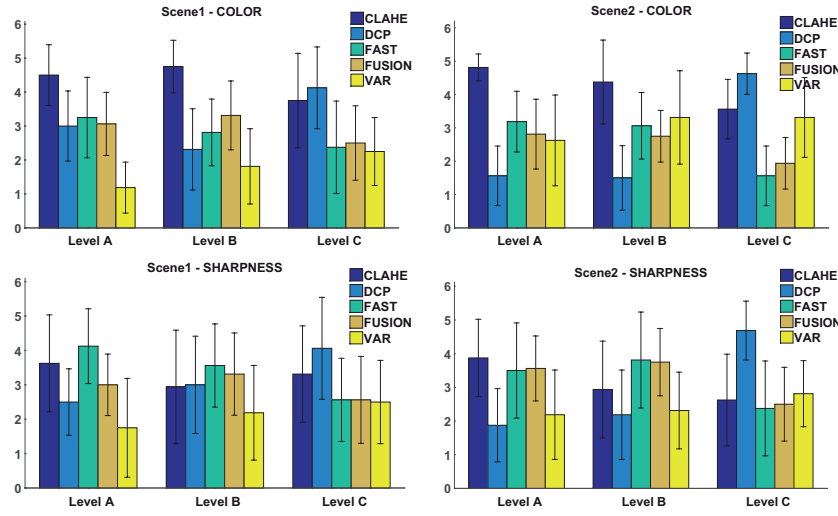


Figure 6.12: Average ranks obtained for each image sequence, and for each level of haze. First row: color, second row: sharpness. First column: scene 1, second column: scene 2.

considered as that of chance. Consequently, we also computed the *rescaled* hit rate  $\hat{h}$ , as follows:

$$\hat{h} = \frac{h - 0.5}{h_{\max} - 0.5} \quad (6.23)$$

and which ranges between -1 (worst) and +1 (best). Note that negative values can be considered as worse than chance (*i.e.* worse than a random predictor).

The subjective ranking data was therefore transformed in pairwise comparison preferences for each image sequence independently and objective preferences were computed with the benchmark metrics.

Table 6.3 gives the obtained hit rates for each metric of the benchmark, for each level of haze and overall. Additionally, we isolated individual features of the MS-iCID and CNC metrics in order to have a better insight in terms of which perceptual attributes contribute the most to a good dehazed image quality. Table 6.4 reports the results obtained. Note that, for the sake of readability, all values were rounded, which explains that some seemingly identical  $h$  lead to different  $\hat{h}$ . Note also that  $h_{\max}$  is different in each part of the experiment.

In order to evaluate if the difference between two hit rates is significant, we also performed a two-sample binomial test with Yule's confidence intervals [24]. We assumed that the metrics' predictions of observer choices can be modeled as binomial distributions. The test assesses whether or not two scores are likely to come from the same distribution. If yes, they are not significantly different. We found that, for color recovery assessment, MS-SSIM, VIF,  $r$  and MS-iCID perform significantly worse than CS, VSI,  $e$ , CNC, NIQE and FADE, while NIQE and FADE perform significantly better than CS and FSIMc. As for sharpness recovery assessment, VSI performs significantly better than  $r$ ,  $e$ , CNC, NIQE, FADE and MS-iCID.

Table 6.3: Hit rates obtained by each metric: (rescaled rates in brackets). The table is divided in four parts: metrics in reference with the haze-free greyscale image (**FG**), metrics in reference with the haze-free color image (**FC**), no-reference metrics (**N**), metrics in reference with the hazy greyscale image (**HG**) and metrics in reference with the hazy color image (**HC**).

		COLOR	SHARPNESS
FG	MS-SSIM	0.50 (0.00)	0.60 (0.50)
	VIF	0.48 (-0.08)	0.60 (0.49)
FC	MS-iCID	0.46 (-0.14)	0.52 (0.10)
	FSIMc	0.52 (0.07)	0.62 (0.63)
	VSI	0.58 (0.28)	0.63 ( <b>0.67</b> )
N	NIQE	0.63 (0.43)	0.58 (0.39)
	FADE	0.63 ( <b>0.45</b> )	0.55 (0.27)
HG	Hautière's $r$	0.48 (-0.06)	0.59 (0.44)
	Hautière's $e$	0.60 (0.36)	0.57 (0.38)
	CS	0.56 (0.22)	0.55 (0.26)
HC	CNC	0.60 (0.34)	0.57 (0.35)

These results suggest that:

- State-of-the-art image quality metrics demonstrate only a limited accuracy on de-hazing quality assessment (the maximal hit rate obtained with our benchmark is  $\hat{h} = 0.67$ ).
- Traditional metrics in reference with the haze-free image perform better at assessing sharpness than color recovery. Figure 6.13 shows a case of total disagreement between these metrics and observers, implying in particular that chromatic attributes such as chroma and hue are especially important in dehazing quality assessment, compared to more conventional quality assessment. Although we strove to isolate the influence of color and sharpness in our experiment, a recent study by Le Moan *et al.* [90] suggested that, given no particular instructions on which kind of distortions to focus on, observers tend to judge achromatic ones such as JPEG artifacts, less severely than chromatic ones such as hue shift. Consequently, the rankings obtained for color recovery assessment may be somewhat more meaningful than that of sharpness for the **overall** quality assessment case, thus emphasizing the need for traditional metrics in reference with the haze-free image to give more weight to chromatic distortions when used for dehazing quality assessment.
- Metrics that are proposed or used for dehazing evaluation (FADE,  $r$ ,  $e$ , CNC and CS) can be outperformed by metrics in reference with the haze-free image. In particular, VSI outperforms them all significantly when it comes to sharpness recovery assessment.
- NIQE and FADE, which are both based on natural scene statistics (NSS), perform particularly well at assessing color recovery assessment. This supports the conclusions obtained in [107]

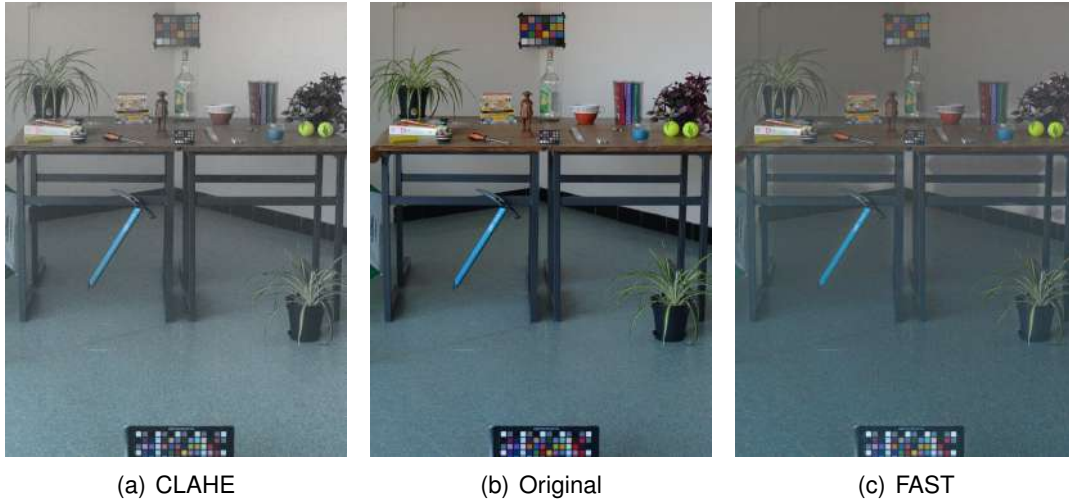


Figure 6.13: Case of total disagreement between metrics in reference with the haze-free image and observers for color recovery quality assessment (scene 1, level B). (a) Result from CLAHE, (b) original image and (c) result from FAST. While all metrics rate the CLAHE dehazed image as more fidel to the original, all observers agreed that FAST is better in terms of color. Indeed, the FAST image seems more vivid, although it clearly shows artifacts just under the tables and around the plants. When it comes to evaluating the structure however, a majority of observers (9 out of 14) find the CLAHE image more fidel. This suggests that these metrics in our benchmark do not perform well at balancing the importance of chromatic and achromatic attributes for dehazing quality assessment.

Table 6.4: Hit rates obtained by individual perceptual attributes: COLOR (rescaled rates in brackets). The MS-iCID attributes are as follows (refer to [89] for details):  $\mathbf{L}_L$ : lightness-difference,  $\mathbf{L}_C$ : lightness-contrast,  $\mathbf{L}_S$ : lightness-structure,  $\mathbf{C}_L$ : chroma-difference,  $\mathbf{H}_L$ : hue-difference,  $\mathbf{C}_C$ : chroma-contrast, and  $\mathbf{C}_S$ : chroma-structure.

	COLOR	SHARPNESS
MS-iCID: $\mathbf{L}_L$	0.46 (-0.14)	0.56 (0.31)
MS-iCID: $\mathbf{L}_C$	0.54 (0.12)	0.61 ( <b>0.57</b> )
MS-iCID: $\mathbf{L}_S$	0.52 (0.06)	0.49 (-0.02)
MS-iCID: $\mathbf{C}_L$	0.69 ( <b>0.64</b> )	0.57 (0.37)
MS-iCID: $\mathbf{H}_L$	0.42 (-0.28)	0.45 (-0.26)
MS-iCID: $\mathbf{C}_C$	0.64 (0.48)	0.51 (0.06)
MS-iCID: $\mathbf{C}_S$	0.41 (-0.33)	0.47 (-0.16)
CNC: contrast	0.60 (0.36)	0.57 (0.38)
CNC: colorfulness	0.57 (0.25)	0.52 (0.12)
CNC: naturalness	0.53 (0.09)	0.52 (0.12)

From the results in Table 6.4, we observe that the perceptual attributes that correlate the best with the subjective data are the MS-iCID  $\mathbf{C}_L$  (chroma-difference) and  $\mathbf{C}_C$  (chroma-contrast) terms for color, and  $\mathbf{L}_C$  (lightness-contrast) for sharpness. A significance analysis reveals that  $\mathbf{C}_L$  performs significantly better than all other attributes for color, whereas for sharpness,  $\mathbf{L}_C$  performs significantly better than all other attributes except  $\mathbf{C}_L$  and

CNC's contrast term. This implies that attributes such as hue and lightness-structure have a relatively small importance in dehazing quality assessment. Even chroma-structure seems to be irrelevant in this context. Finally, it is interesting to note that some of these features perform better individually than together: the MS-iCID  $C_L$  term performs significantly better than the metric itself, but also than FADE and NIQE, thus making  $C_L$  the best metric in our benchmark to estimate color restoration quality in dehazing.

#### 6.3.4/ OBJECTIVE EVALUATION OF DEHAZING ALGORITHMS

We first calculated the raw scores of all selected metrics for all dehazed images of scene 1 and scene 2 organized by fog levels (see Figures 6.14, 6.15 and 6.16). Overall, metrics that belong to the same category have monotonic trends across fog levels. Note that the metrics in reference with the haze-free image, which measure the similarity (fidelity) between test and reference images, show that the fidelity of an image's features is better maintained at low fog densities (see Figure 6.14). This means that dehazing methods are globally more efficient at these levels.

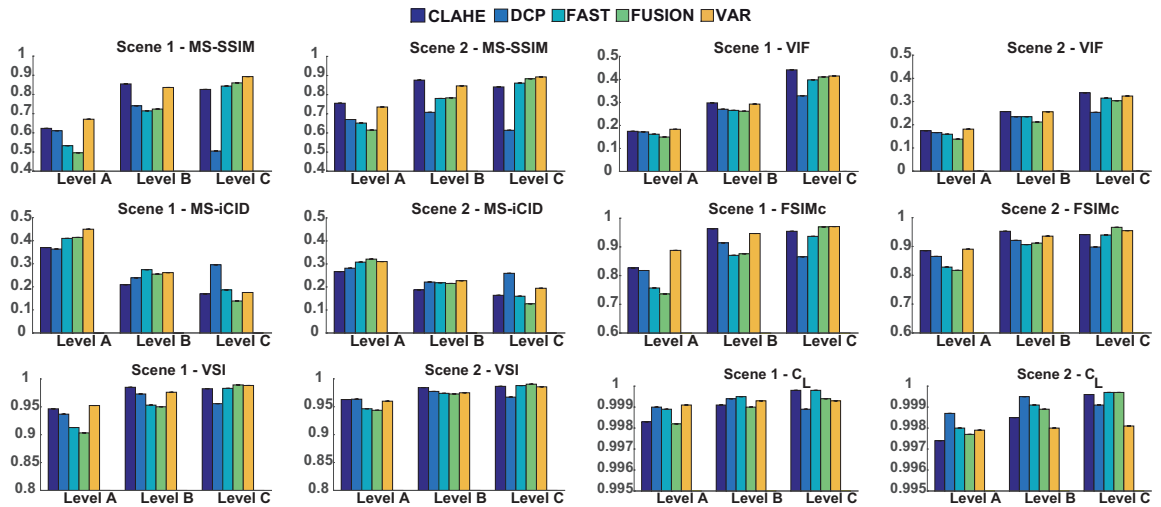


Figure 6.14: The scores of the metrics in reference with the haze-free image, which are obtained for each scene at each fog level. These five metrics (MS-SSIM, VIF, MS-iCID, FSIMc and VSI) evaluate the quality of the dehazed image as being the similarity rate of specified features between the hazy and the haze-free images. For light fog, all of these metrics show the high similarity rate compared to higher level of fog. Some of them such as MS-SSIM, FSIMc, VSI and NIQE show that DCP does not perform well in the lowest fog level. The subjective analysis shows that  $C_L$  and VSI are the most relevant metrics to evaluate color and sharpness. Both of these metrics' values of different methods are noticeably close to each other.

In order to evaluate methods by metrics in reference with the hazy image, we calculated the score of the haze-free image considered as the optimal one. Amongst these metrics, the scores of  $r$  and  $e$  which refer to the gain of visibility, are higher at high fog densities. This denotes that a good range of improvement is done at high fog densities, thus, the hazy and the recovered images are less similar. In other words, the less similarity would refer to a good improvement in quality. However, it is not always true. For the same fog level in Figure 6.15, the gain of visibility of corrected images is higher than the one of

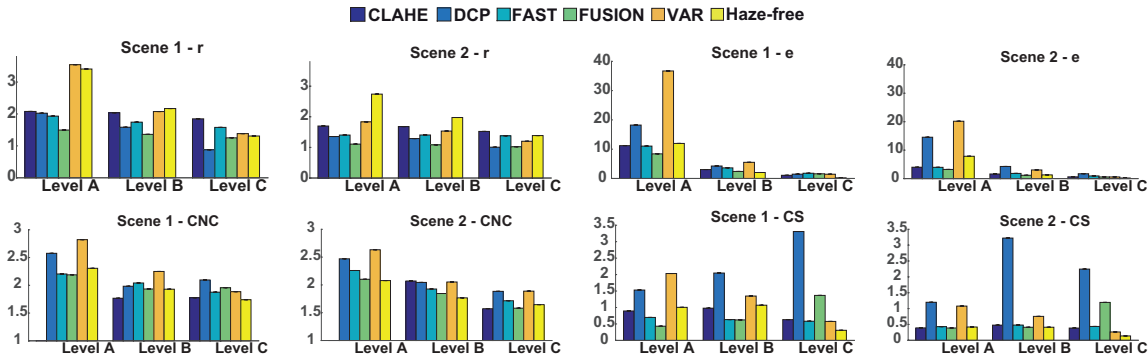


Figure 6.15: The scores of the metrics in reference with the hazy image, which are obtained for each scene at each fog level. These four metrics ( $r$ ,  $e$ , CNC, CS) compare the dehazed image to the hazy image. The dissimilarity is small for low levels of fog. The values of metrics on different dehazing methods are noticeably close to each other.  $e$ , CS and CNC scores exceed, across levels, the haze-free image scores. This is because appearing artifacts are accounted for edges in the resulting image.

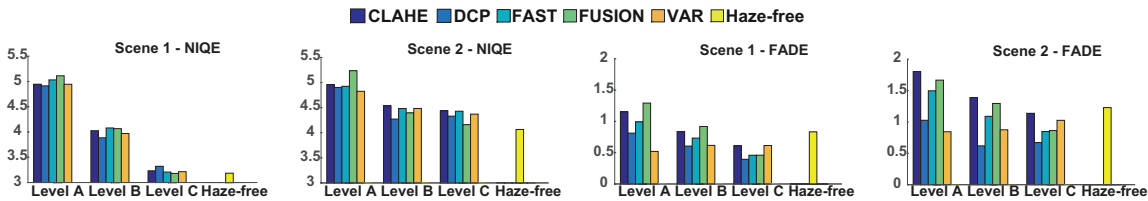


Figure 6.16: No-reference NSS-based metrics scores obtained for each scene at each fog level. NIQE is a non haze-dedicated metric. According to it, the image of the highest quality is the haze-free image. Dehazed images, which were basically covered by a light fog, have almost the same quality of the haze-free image. While for FADE, which is a haze-dedicated metric, some methods across the three fog levels beat the haze-free image's score. Indeed, it presents a weakness in evaluating the preservation of image's features comparing to the haze-free image.

haze-free image. This does not agree with the perceptual judgment. Thus, the highest dissimilarity does not necessarily mean the best quality. These indices that have been widely used to assess new proposed dehazing methods are inconsistent with the human visual evaluation of color, which was evoked in [63] and proved again in Table 6.3. Indeed, these indices ignore the apparent problems of over-enhancement and color distortion, and focuses on the recovered structures that may be an amplified noise and blocking artifacts [107]. The same issue is met when using CS metric.

CNC measures the dissimilarity between the test and the reference images. The dissimilarity decreases with the fog density. Across all fog densities, the haze-free image keeps globally the best score (lowest score).

Considering no-reference metrics, NIQE and FADE, they are both able to quantify the evolution of dehazed image quality. However, FADE seems to be more sensitive to over-saturated colors, which usually occur when the fog is very light (level C). At this level, the processed images seem to be of higher quality than the original haze-free image. Thus, such metric, which assesses better color than sharpness underlines the preference rather

than fidelity (see Table 6.3).

Now, we only consider CL and VSI that statistical analysis showed as the most adequate metrics to judge respectively color and sharpness restoration. These two metrics denote a good recovery of color and sharpness at low fog densities (see Figure 6.14). At the highest fog level of A, VAR followed by CLAHE and DCP perform the best in sharpness recovery. For color recovery, while VAR and DCP maintain a good performance in addition to FAST, CLAHE seems to be significantly bad. At the medium level of B, all methods show a similar performance in sharpness recovery, with a significant advancement of FAST and FUSION and a significant regress of DCP's performance comparing to others. In case of color, CLAHE remains the bad performing method and VAR seems to be bad in preserving color comparing to other methods. At the lowest fog level of C, all methods are globally efficient in sharpness recovery, except DCP, which fails as well in color recovery with VAR, while the other methods are more suitable.

In all of this, considering globally color and sharpness recovery, the physics based dehazing method DCP and the variational approach of contrast enhancement VAR are the most suitable for relatively high fog density. On the other hand, FAST and FUSION, perform well for thin layer of fog. CLAHE, which is a histogram equalization method, has a particular behavior. At all considered fog levels CLAHE has the ability to preserve sharpness. However, it widely fails to maintain color fidelity.

### 6.3.5/ COMPUTATIONAL TIME

In computer vision, the efficiency of an image processing method is not only measured by the perceived quality of processed images. It involves the determination of the amount of resources such as computational time and storage space a method requires for execution.

When it comes to real time applications the determination of such resources becomes strongly inevitable and becomes prior to any other evaluation factors. When they do not meet the real time execution conditions, the method is automatically discarded and there is no more need to investigate image quality.

We usually consider in such applications the efficiency of methods. A method's efficiency is the ability to provide images of high quality within an extremely brief time. Thus, the efficiency rate can be calculated as the ratio of the quality index over time. Regarding the real-time application, when this ratio is high, this means the considered method is properly adequate.

A high execution time is not suitable for real world applications. Different reasons can justify it such as non optimized code, lack of resources (*i.e.* CPU, memory) and size of input data. To deal with these issues, a number of optimization measures can be taken [180]. Regarding the values presented in Table 6.5, we allowed ourselves to make this time-based comparative study since methods share the same physical resources and the same input data. The related codes are supposed to be quite optimized since they were provided by the authors of methods.

Let us first analyze the performance of methods according to the time without any regard for the previous interpretation.

Globally, all methods have a relatively high processing time that makes them no suitable



Table 6.5: Computational time of dehazing methods applied on scene A and scene B. These algorithms were run using MATLAB R2010b on HP Intel(R) core (TM) i7 - 3687U CPU @ 2.10 GHZ 2.60 GHZ.

Dehazing method	Computational time	
	Scene A	Scene B
DCP	7.894 <i>s</i>	39.42 <i>s</i>
FAST	1398.943 <i>s</i>	7328.681 <i>s</i>
FUSION	18.845 <i>s</i>	31.202 <i>s</i>
VAR	35.456 <i>s</i>	57.392 <i>s</i>
CLAHE	4.128 <i>s</i>	4.978 <i>s</i>

for real time applications. An example would be if in a driver assistance application the dehazing process takes 4 *s* (which is the best time score in our set) to allow driver to distinguish better possible obstacles, the driver would be definitely exposed to a grave risk since a consequent accident can happen in a shorter time.

### 6.3.6/ DENOISING

An additional step to this experiment has been added later to deal with the noise, which is mainly amplified after the dehazing, especially when the haze density is relatively high (cf. Section 3.2.5).

Considering the same images that have been used for the quality assessment experiments, we have applied first the denoising method BM3D described in [36], respectively, as a pre-processing step to dehazing and then as a post-processing step to it. They are denoted as denoising + dehazing and dehazing + denoising, respectively.

In denoising + dehazing case, since the noise standard deviation is estimated and not accurately known, it could be over-estimated or under-estimated. In hazy images, the noise is considered to be uniform on the image and independently distributed of the fog level. Thus, we expect that any standard spatially-invariant denoising methods would have a proper performance. If the noise is over-estimated, this means that the hazy image is over-denoised and therefore smoother. The over-smoothing induces the lost of useful details such as edges and textures. However, it produces a better results than when the noise is under-estimated, because the remaining amount of noise is amplified after dehazing [113].

In dehazing + denoising case, the standard spatially-invariant denoising methods are not suitable and they produce erroneous results, since the noise is amplified depending on the haze level (Equation 3.31). Thus, a local denoising processing is required. The actions of both over-denoising and under-denoising are similar to those of denoising + dehazing case, but with a lower impact, since these inaccuracies will not be amplified by a post inversion process.

In the image processing, the imperfection of the environment and the instruments causes the noise in digital images. The noise degrades the overall quality of these images. Thus, there is a need to remove this noise to get back the original high quality. The selection of the denoising method depends upon the type of noise [83], which is characterized by

particular properties and a specific source [20]. For example, non-linear filter is suitable for salt and pepper noise and speckle noise. Wiener Filter reduces better the Gaussian noise than Mean filter and Median filter.

Three main reasons lie behind the selection of BM3D: this denoising method has been already used to reduce the noise in hazy images [113] and it showed good results. It is among the best denoising methods in terms of PSNR, MSE and subjective image quality. Finally, it takes only one tuning parameter, which is the estimating value of the standard deviation of noise.

Our selected denoising method BM3D consists of two steps: basic and final denoising. The first one aims at grouping similar 2D patches into 3D groups by calculating block-distance. Then, the noise is reduced through a hard-thresholding in a 3D transform domain (Discrete Cosine Transform). Estimates are calculated for each group of blocks and the estimates are placed at the original positions. Finally, an aggregation step is there to calculate a global estimate of the whole image by weighted averaging of all overlapping blocks estimates.

The second one consists in applying again a grouping of similar blocks but this time the groups are taken from the original noisy image and the image resulted from the first step. A Collaborative Wiener filtering 3D transform domain is applied to the new groups as an estimate of the resulted image energy spectrum. Finally, an aggregation step is also performed to compute the final result.

For RGB images, they are first transformed to a luminance-chrominance color space such as  $YCbCr$ . Since the Grouping step in BM3D is sensitive to noise, it is only performed on the luminance channel, which contains the most important image features such as high-frequency information, and it is reused for the chrominance channels. The rest of the algorithm is applied naively on each channel before to convert back the image to RGB image.

The images processed by BM3D have been compared to the images processed only by dehazing. Since the metrics show a similar behavior across fog densities (cf. Paragraph 6.3.4), we used only the metric MS-SSIM to make this comparison and to see the impact of denoising when it is considered before and after dehazing.

Table 6.6: MS-SSIM scores of the results of CLAHE dehazing method preceded by denoising, dehazing without denoising, dehazing followed by denoising and dehazing preceded and followed by denoising. Denoising is performed by BM3D. The highest scores are written in bold. The BM3D applied after CLAHE provides globally the best results.

CLAHE	Denoising + dehazing	Dehazing	Dehazing + denoising	Denoising + dehazing + denoising
Scene1-Level A	0.6336	0.6232	0.6484	<b>0.6539</b>
Scene2-Level A	0.7920	0.7552	0.7950	<b>0.8106</b>
Scene1-Level B	0.8763	0.855	<b>0.8909</b>	0.8829
Scene2-Level B	0.9173	0.8759	0.9166	<b>0.9198</b>
Scene1-Level C	0.8647	0.8263	0.8635	<b>0.8707</b>
Scene2-Level C	0.8607	0.8405	0.8654	<b>0.8689</b>

Referring to the scores shown in Tables 6.6, 6.7, 6.8, 6.9 and 6.10, MS-SSIM scores underline a better quality when BM3D is applied, no matter if it is done before or after



Table 6.7: MS-SSIM scores of the results of DCP dehazing method preceded by denoising, dehazing without denoising, dehazing followed by denoising and dehazing preceded and followed by denoising. Denoising is performed by BM3D. The highest scores are written in bold. The BM3D prior to DCP provides the best results.

DCP	Denoising + dehazing	Dehazing	Dehazing + denoising	Denoising + dehazing + denoising
Scene1-Level A	0.6339	0.611	0.6324	<b>0.6984</b>
Scene2-Level A	0.8200	0.6702	0.6982	<b>0.8565</b>
Scene1-Level B	0.7291	0.7411	0.7454	<b>0.8943</b>
Scene2-Level B	0.8190	0.7077	0.7333	<b>0.8956</b>
Scene1-Level C	0.5332	0.5051	0.4993	<b>0.7611</b>
Scene2-Level C	0.6556	0.6139	0.6290	<b>0.7520</b>

Table 6.8: MS-SSIM scores of the results of FAST dehazing method preceded by denoising, dehazing without denoising, dehazing followed by denoising and dehazing preceded and followed by denoising. Denoising is performed by BM3D. The highest scores are written in bold. The BM3D prior to DCP provides the best results.

FAST	Denoising + dehazing	Dehazing	Dehazing + denoising	Denoising + dehazing + denoising
Scene1-Level A	0.5342	0.533	0.5494	<b>0.5644</b>
Scene2-Level A	0.6968	0.6516	0.6810	<b>0.7012</b>
Scene1-Level B	0.7118	0.7147	0.7331	<b>0.7349</b>
Scene2-Level B	0.8161	0.7802	0.8125	<b>0.8191</b>
Scene1-Level C	0.8632	0.8438	<b>0.8710</b>	0.8640
Scene2-Level C	0.8850	0.8604	0.8854	<b>0.8855</b>

Table 6.9: MS-SSIM scores of the results of FUSION dehazing method preceded by denoising, dehazing without denoising, dehazing followed by denoising and dehazing preceded and followed by denoising. Denoising is performed by BM3D. The highest scores are written in bold. The BM3D prior to DCP provides the best results.

FUSION	Denoising + dehazing	Dehazing	Dehazing + denoising	Denoising + dehazing + denoising
Scene1-Level A	0.4957	<b>0.4959</b>	0.4953	0.4817
Scene2-Level A	0.6251	0.6149	<b>0.6382</b>	0.6232
Scene1-Level B	0.7244	0.7239	<b>0.7245</b>	0.7052
Scene2-Level B	0.7922	0.7834	<b>0.8097</b>	0.7789
Scene1-Level C	0.8689	0.8604	<b>0.8708</b>	0.8455
Scene2-Level C	0.8996	0.8831	<b>0.9060</b>	0.8822

dehazing (the scores are globally very close to each other) for a given noise variance  $\sigma = 0.25$ . This is mainly related to the accuracy in the noise variance estimation.

Thus, using BM3D, if  $\sigma$  is close to the real value, no matter if the denoising is performed before or after dehazing. The result of dehazing will be better when we deal with the

Table 6.10: MS-SSIM scores of the results of VAR dehazing method preceded by denoising, dehazing without denoising, dehazing followed by denoising and dehazing preceded and followed by denoising. Denoising is performed by BM3D. The highest scores are written in bold. The BM3D prior to DCP provides the best results.

VAR	Denoising + dehazing	Dehazing	Dehazing + denoising	Denoising + dehazing + denoising
Scene1-Level A	0.7498	0.6709	0.7489	<b>0.8236</b>
Scene2-Level A	0.7846	0.7355	0.7911	<b>0.8359</b>
Scene1-Level B	0.8701	0.8365	0.8798	<b>0.8961</b>
Scene2-Level B	0.8863	0.8459	<b>0.8926</b>	0.8856
Scene1-Level C	0.9203	0.8932	0.9180	<b>0.9205</b>
Scene2-Level C	0.9108	0.8928	0.9194	<b>0.9287</b>

noise.

One may wonder, what would provide a processing consisting of denoising process applied before and after dehazing. For the majority of dehazing methods, when a noise filtering is applied before and after dehazing, the quality of the resulted image is better. For FUSION method, which shows a decreasing in the quality after this process, this may be due to the over-denoising (over-smoothing) since the method basically includes a smoothing step. In all of this, only an adequate denoising increases the quality of dehazed images.

### 6.3.7/ DISCUSSION

The application of fog and fog removal induces several types of distortions, such as noise, color fade, contrast degradation and artifacts near the edges, which are spatially variant and spatially correlated to imaged objects: the accuracy of colors recovery depends largely on initial objects colors and on their distance to the camera [27]. Thus, an adequate full-scale metric is required.

According to the statistical significance, it seems that in color-based metrics, image structure evaluating features are more weighted than color evaluating features. The individual feature  $C_L$ , which calculates the chromatic difference in CIELAB color space [102], is significantly better than all other metrics in color preservation judgment. VSI, which was basically detecting perceptual quality distortions as changes in visual saliency map, was not sensitive to contrast change. It was then boosted through the insertion of the scharr gradient operator similarity map [195].

The clue for mastering the quality assessment of dehazed images is to specify the desired quality type to be assessed. Metrics, as we categorized, seem to be related to the identified quality types. As they calculate the similarity between the haze-free and the processed images, metrics in reference with the haze-free image are the most suitable for fidelity evaluation. However, they show a variable efficiency between evaluated features (see Table 6.3). Metrics in reference with the hazy image, as they emphasize the dissimilarity between the hazy and the processed images, they mainly fail to accurately judge the perceived quality at extreme fog densities. Such metrics can be rather used to characterize the extent from which a processed image becomes usable according to

a target application. For metrics without reference image, at extreme fog levels such as level C, it becomes clear that they rather judge preference, which is not always equivalent to the natural appearance.

## 6.4/ CONCLUSION

Quality assessment of single image dehazing is a challenging task. According to the target application, quality is differently considered. Although single image dehazing has been an active field for several years, not much work has been dedicated to subjective and objective quality assessment. This is mainly because original haze-free image, which is assumed to have the highest visual quality is not easily available.

Using a new hazy image database that contains scenes degraded with several levels of fog with their haze-free images, we conduct a composite study based on the agreement between subjective and objective evaluation. Accordingly, we evaluate the performance of three categories of quality metrics and five dehazing methods.

We single out the clear distinction between what people perceive as good quality in terms of color restoration and in terms of sharpness fidelity across the fog levels. Though, we deduce that metrics with reference to the haze-free perform the best at features fidelity assessment if the evaluated features are adequately weighted. Accordingly, the performance of dehazing methods changes across fog levels. Image enhancement techniques except variational approach, are only suitable for recovery at light fog. Otherwise, the colors are badly recovered.

Based on our observations, for natural hazy images with no reference image, metrics without reference image would be adequate for dehazing if they were designed to handle all types of distortions that may be introduced differently by dehazing processing, while respecting the improvement's boundaries.

In order to support the strong conclusions, some technical points should be addressed. Further research direction would be the validation of these contributions on other similar indoor scenes with reference images and natural hazy images. A complementary work would focus on the investigation of how regions of interest are defined in the image and how these change between observers and across fog levels.

## GENERAL CONCLUSION

*"A conclusion is simply the place where you got tired of thinking."*

*-Dan Chaon-*

*This general conclusion summarizes our contributions. It reports as well, the extent to which we have succeeded to answer to our research questions. Moreover, we highlight our study limitations and propose to extend our method toward a more extensive study. Then, we provide some directions and areas for future research.*

---

7.1 Summary . . . . .	137
7.2 Perspectives . . . . .	139
7.3 Closing . . . . .	141

---

### 7.1/ SUMMARY

In this thesis, we have addressed a number of problems that hamper normal functioning of computer vision applications by making the performance and the reliable evaluation of dehazing not straightforward. Through this project, we wanted to make clear how we can proceed and what kind of data we may need to make a step forward in optimizing the use of dehazing.

We started this dissertation by presenting in **Chapter 2**, the natural and unnatural phenomena and the different scenarios that cause the degradation of the visibility and the quality of images taken in these conditions. Since this study focused on the outdoor images taken in various weather conditions, we explained the strong relation between the properties of the atmospheric particles and the visual observation. On the other side, the vision system stands, which has a particular variable way to perceive the resulting effects.

We reviewed in **Chapter 3** the different categories of dehazing methods with shedding the light on those with significant impact on this active research field. Some of these methods have been used to perform a composite study of subjective and objective image quality evaluation to deal with the challenging issue of dehazed image quality. Having a continuous increasing number of dehazing methods, which tackle the haze removal differently

and providing therefore non consistent results, this creates new research ways. This led us to define what we should consider while developing a new method and evaluating it. All of this can be considered in the future potential methods.

Based on what was evoked in Part I, we pointed out in **Chapter 4** the lack of the ground truth haze-free image. This fundamental problem hampers the proper evaluation of dehazing methods, especially when it comes to evaluate the fidelity of original information, which represents the heart of this project. To tackle this problem, we have created a color hazy image database (CHIC) of semi-indoor scenes covered by real fog, which contains the haze-free image, images with different fog densities and a set of physical measured parameters. We proposed also a multispectral database (MHIA) associated to a depth map acquired by a Kinect sensor, which is not fully exploited. In addition to the haze-free image and the different fog levels that provides, it can be used to test the extended version dehazing methods from color to multispectral. It can be used also to optimize the filters characterization of a sensor conceived for acquisition in bad weather. Moreover, it can be used for many other research purposes.

Using CHIC database images, we addressed in **Chapter 5** the dissimilarities between simulated and real hazy images. The hazy images formed by the haze model, fail to simulate the real situation for objects located at very long distances or for high fog levels. This appears clearly through dehazing, when the haze model is no more properly inverted in these both situations. This failure is noticed in the context of the perceived recovered colors that deviate from the original ones and the amplification of noise after dehazing and the incomplete removal of haze, especially when it is abundant.

We close this dissertation in **Chapter 6** by addressing the challenging subject of quality evaluation of single color image dehazing algorithms. Through our inter-correlated subjective and objective experiments, we provided, for the first time, qualitative elements allowing to compare quality criteria such as color and sharpness. Besides the investigation that was done on various dehazing algorithms, we addressed also the evolution of the selected criteria according to the fog level. Considering the objective metric-based analysis, we concluded that not a single dehazing algorithm performs the best, nor the worst, for different fog densities. Likewise, there is a clear distinction between what people perceive as good quality in terms of color and sharpness restoration. Moreover, in processing such as dehazing, which do not have a linear behavior over fog densities, it is mandatory to specify the quality type that can be evaluated in regards to the fog densities.

Since this work falls within three main areas: physics, image processing and color science, it consisted to apprehend first the natural physical phenomena and to model them to whether reproduce real-world or to recover useful information, which are likely to be deteriorated. All of this should be done while keeping a closeness to the real situation and maintaining a high perceived quality. Therefore, we retain from this work the importance to model accurately the real situation and to consider methods, which deal with it. The accuracy of modeling depends mainly upon the data type. Color images, being limited in wavelength band, do not provide sufficient data to retrieve objects hidden with a thick fog layer.

## 7.2/ PERSPECTIVES

Not all issues of color and multispectral dehazing have been addressed in this thesis. Nevertheless, our contributions and our experience of this problem allows us to provide valuable suggestions and openings for further research.

- **Color image dehazing**

- **Image database and haze model**

1. CHIC database is a step forward in the migration from simulated to real hazy images with the haze-free image. However, it comprises a limited number of images. There is a need to have more real hazy images with various contexts. In addition to the images with uniform airlight and fog density which were used in this thesis, further efforts could be made to build images with different lights. Moreover, nighttime hazy scenes could be set up. Such scenes are often met in reality.

For more accurate measurements, it would be nice to quantify the amount of outdoor lighting. When the acquisition time of a frame increases with the number of fog layers and the sensors speed, the outdoor lighting remains no more constant. In this case, the lighting quantification using a light meter becomes mandatory.

2. Referring to Section 5.2.2, we can imagine to:
  - \* Refine a connection model between the physical transmission and the appearance of colors while considering the chromatic properties of the atmospheric light.
  - \* Refine a method to calculate the airlight at a given fog density based on the geometrical distribution of the airlight and the hazy colors within a color space.
3. The scope of this study was limited to the aerosols and water droplet particles presented in Table 2.2. Other conditions such as sandstorm causes chromatic airlight. In terms of scattering, large particles like sand (radius =  $25\ \mu m$ ) do not behave like small achromatic particles. They reflect light like big objects. Similar processing steps of the ones provided in this thesis could be adopted for database construction and methods and model evaluation. In such case of chromatic airlight, multispectral images can provide useful data for methods optimization.

- **Quality evaluation**

1. Although the quality criteria of dehazed images seem to be fuzzy and application-dependent, it would be interesting to keep on investigating the possibilities to design either a global metric that encompasses as much as possible the main different altered criteria, or a metric dedicated for each application profile. Since the haze-free image is not always available, it would be better to focus on no-reference metrics trained on clear images of the particular context in question.
2. In the light of the quality aspects identification (preference, usability and fidelity), it is worth considering in similar studies the ones that we did not consider in this work. Usability and preference are more likely to be considered in wider application fields such as photography, assistance applications, objects recognition, tracking, etc.

3. Further subjective evaluations are required to understand better the features that observers consider without being already specified and to extend this study in order to investigate more features with many more images. Considering fidelity, more features such as global contrast of the image and naturalness could be considered in similar experiments. This leads to more accurate and exhaustive metrics.

For the preference, it may be a global or a particular preference, which considers a specific feature. Depending on the evaluation purpose, the haze-free image will be or not among the images to compare.

When it comes to usability, regarding the target application, we favor, instead of subjective evaluation of dehazing, the hit rate of its post processing applications. A good associated metric should predict the achievement possibility. For instance, returning to the driving assistance example shown in Figure 6.3, a good metric must be able to point out the extent of the post recognition algorithm to which it is able to detect correctly the obstacles at different distances, in order to predict therefore the risk of accident. Thus, several preventive measures will be taken.

4. In terms of clearly determining how Regions of Interest (ROI) vary between observers and also with different levels of fog, we may consider in a future work the recording of the observers' interaction with hazy images.
5. As explained previously, the perceived quality within the same dehazed image is not constant. It varies from region to another, since it depends on the distance from the object to the camera, the scattering coefficient and the object color. In the subjective experiment 6.3.1, observers were free to focus on different parts of the scene and make therefore their raking. This was one of the main reason of that divergence in judgments. A better way could be to cut the scene into different parts with the same distance and the same fog density.

As directions for future work, it will be good in such fuzzy evaluation to have simple scenes and pointed question by precisising the zone to look at to make decision. It may be computationally expensive, but more exact.

6. Dehazing is time consuming process and it strongly depends on the size of the image. Some images like the one present in our database have huge sizes, it seems sensible to add a preliminary step to dehazing to detect areas of fog and define the density, to avoid unnecessary long process over clear areas that could have negative effect. The fog detection and estimation of density can be refined and tested through our database thanks to different densities of real fog, which are accurately measured.

Furthermore, a good dehazing method must hold a compromise between the efficiency of fog removal in regards to the application requirements and its processing time. In real-world applications, computational time is a limiting and critical factor. Thus, it must be considered prior to the quality. To this end, several options can be considered such as the use of images with as low as possible resolution, optimized algorithms and adequate hardware resources.

- **Multispectral image dehazing**

Since multispectral image dehazing has not been investigated as much as color



image dehazing, it would be of interest to develop a specific method for the reconstruction of dehazed images using the data contained in our multispectral images, and then to investigate the possibility to apply it in other domains such as satellite and underwater imaging.

In this context, two focal areas are defined. The first one seeks to construct multispectral outdoor hazy images. Other multispectral databases could be created also to simulate satellite images and the non-uniformities we find in such images. The second one aims at developing a specific method based on a variational approach to the reconstruction of the spectral information of the images by exploiting the elements identified in the first area. Indeed, the variational treatment was applied to color images and showed a good performance comparing to other approaches, when there is no uniformities within the hazy image, such as non-uniform illumination and a variable brightness and when the fog density is relatively high (cf. Section 6.3.4). The variational approach showed this superiority, however it was not directly attached to hazy images (haze model), but it can be applied to all types of images that present a contrast reduction problem. Thus, in a future work haze model parameters will be estimated through variational approaches in order to maintain as much as possible the haze model integrity.

In summary, haze model should be reviewed and refined through the spatial and the spectral dimensions. Furthermore, the criteria of usability must be revealed through the best quality metrics in order to optimize them in time and modeling.

### 7.3/ CLOSING

One may wonder about the consequences of such a study may have on the world, and especially on the dehazing research field. The choice of a dehazing method is critical and depends on the user needs. It changes with the fog densities and the scenes properties. Hence, it is important to prompt the use of common tools for different methods evaluation and global reliable quality metrics. Moreover, these tools are useful for the elaboration of other quality metrics.

Following the methodology presented in this thesis, there is a tendency to move toward the standardization of dehazing quality assessment in terms of evaluating tools. This can help researchers in two directions. First, one can use a reliable comparison method to judge different dehazing algorithms. Second, one can design a customized dehazing method dedicated to act on a specific image feature for a particular aim.

# BIBLIOGRAPHY

- [1] Causes of poor visibility. <http://www.hazecam.net/poor-vis.aspx>, 2012.
- [2] Konica minolta, cs-2000 spectroradiometer. <http://sensing.konicaminolta.us/products/cs-2000-spectroradiometer/>, 2015.
- [3] Users manual, nikon d7100. <http://cdn-10.nikoncdn.com/pdf/manuals/dslr/D7100EN.pdf>, 2015.
- [4] Fog. <http://education.nationalgeographic.org/encyclopedia/fog/>, 2016.
- [5] Image dehazing. [http://ivrl.epfl.ch/supplementary\\_material/SFS\\_ICIP09](http://ivrl.epfl.ch/supplementary_material/SFS_ICIP09), 2016.
- [6] Infrared. <https://en.wikipedia.org/wiki/Infrared>, 2016.
- [7] Photon focus. [http://www.photonfocus.com/products/camerafinder/camera/?no\\_cache=1&prid=16](http://www.photonfocus.com/products/camerafinder/camera/?no_cache=1&prid=16), 2016.
- [8] Waterloo ivc dehazed image database. <http://ivc.uwaterloo.ca/database/Dehaze/Dehaze-Database.php>, Accessed March 1, 2016.
- [9] Yousef Al Ohali. Computer vision based date fruit grading system: Design and implementation. *Journal of King Saud University-Computer and Information Sciences*, 23(1):29–36, 2011.
- [10] Émile Allard. *Mémoire sur l'intensité et la portée des phares... par MÉ Allard...* Impr. nationale, 1876.
- [11] Codruta O Ancuti and Cosmin Ancuti. Single image dehazing by multi-scale fusion. *Image Processing, IEEE Transactions on*, 22(8):3271–3282, 2013.
- [12] Codruta O Ancuti, Cosmin Ancuti, Chris Hermans, and Philippe Bekaert. A fast semi-inverse approach to detect and remove the haze from a single image. In *Computer Vision–ACCV 2010*, pages 501–514. Springer, 2010.
- [13] Codruta Orniana Ancuti, Cosmin Ancuti, and Philippe Bekaert. Effective single image dehazing by fusion. In *Image Processing (ICIP), 2010 17th IEEE International Conference on*, pages 3541–3544. IEEE, 2010.
- [14] M Anitharani. Haze removal of secure remote surveillance system. *IOSR Journal of Engineering*, 3:10–17, 2013.
- [15] J Floor Anthoni. Water and light in underwater photography. <http://www.seafriends.org.nz/phgraph/water.htm>, 2005.
- [16] S ARCHA and ALI ABDUL. A novel method for video dehazing by multi-scale fusion. 2014.

- [17] Volker Aurich and Jörg Weule. Non-linear gaussian filters performing edge preserving diffusion. In *Mustererkennung 1995*, pages 538–545. Springer, 1995.
- [18] HM Behairy and MS Khorsheed. Improving image quality in remote sensing satellites using channel coding. In *Proceedings of World Academy of Science, Engineering and Technology*, volume 9, pages 189–194, 2005.
- [19] Kurt Beier and Hans Gemperlein. Simulation of infrared detection range at fog conditions for enhanced vision systems in civil aviation. *Aerospace Science and Technology*, 8(1):63–71, 2004.
- [20] Ajay Kumar Boyat and Brijendra Kumar Joshi. A review paper: Noise models in digital image processing. *arXiv preprint arXiv:1505.03489*, 2015.
- [21] David H Brainard. Color appearance and color difference specification. *The science of color*, 2:191–216, 2003.
- [22] Johannes Brauers, Nils Schulte, and Til Aach. Multispectral filter-wheel cameras: Geometric distortion model and compensation algorithms. *IEEE Transactions on Image Processing*, 17(12):2368–2380, 2008.
- [23] X Briottet, Y Boucher, A Dimmeler, A Malaplate, A Cini, M Diani, HHPT Bekman, P Schwering, T Skauli, I Kasen, et al. Military applications of hyperspectral imagery. In *Defense and Security Symposium*, pages 62390B–62390B. International Society for Optics and Photonics, 2006.
- [24] Lawrence Brown and Xuefeng Li. Confidence intervals for two sample binomial distribution. *Journal of Statistical Planning and Inference*, 130(1):359–375, 2005.
- [25] ITU-R BT.500-12. Recommendation: Methodology for the subjective assessment of the quality of television pictures. November 1993.
- [26] Antoni Buades, Bartomeu Coll, and Jean-Michel Morel. A review of image denoising algorithms, with a new one. *Multiscale Modeling & Simulation*, 4(2):490–530, 2005.
- [27] Damon M Chandler. Seven challenges in image quality assessment: past, present, and future research. *ISRN Signal Processing*, 2013, 2013.
- [28] Pat S Chavez. An improved dark-object subtraction technique for atmospheric scattering correction of multispectral data. *Remote sensing of environment*, 24(3):459–479, 1988.
- [29] Chuan Cheng Chen. Attenuation of electromagnetic radiation by haze, fog, clouds, and rain. Technical report, DTIC Document, 1975.
- [30] Zhengying Chen, Tingting Jiang, and Yonghong Tian. Quality assessment for comparing image enhancement algorithms. In *Computer Vision and Pattern Recognition (CVPR), 2014 IEEE Conference on*, pages 3003–3010. IEEE, 2014.
- [31] Yi-Jui Cheng, Bo-Hao Chen, Shih-Chia Huang, Sy-Yen Kuo, Andrey Kopylov, Oleg Seredint, Leonid Mestetskiy, Boris Vishnyakov, Yury Vizilter, Oleg Vygolov, et al. Visibility enhancement of single hazy images using hybrid dark channel prior. In *Systems, Man, and Cybernetics (SMC), 2013 IEEE International Conference on*, pages 3627–3632. IEEE, 2013.

- [32] Lark Kwon Choi, Jaehee You, and Alan Conrad Bovik. Referenceless prediction of perceptual fog density and perceptual image defogging. *Image Processing, IEEE Transactions on*, 24(11):3888–3901, 2015.
- [33] CIE CIE. International lighting vocabulary. *Central Bureau of the Commission Internationale de l'Eclairage, Kegelgasse*, 27, 1989.
- [34] Philippe Colantoni, Ruven Pillay, Christian Lahanier, and Denis Pitzalis. Analysis of multispectral images of paintings. In *Signal Processing Conference, 2006 14th European*, pages 1–5. IEEE, 2006.
- [35] Ingemar Cox, Matthew Miller, Jeffrey Bloom, Jessica Fridrich, and Ton Kalker. *Digital watermarking and steganography*. Morgan Kaufmann, 2007.
- [36] Kostadin Dabov, Alessandro Foi, Vladimir Katkovnik, and Karen Egiazarian. Image denoising by sparse 3-d transform-domain collaborative filtering. *Image Processing, IEEE Transactions on*, 16(8):2080–2095, 2007.
- [37] David J Diner, Jewel C Beckert, Terrence H Reilly, Carol J Bruegge, James E Conel, Ralph A Kahn, John V Martonchik, Thomas P Ackerman, Roger Davies, Siegfried AW Gerstl, et al. Multi-angle imaging spectroradiometer (misr) instrument description and experiment overview. *Geoscience and Remote Sensing, IEEE Transactions on*, 36(4):1072–1087, 1998.
- [38] Maurice Dubin, N Sissenwine, and H Wexler. Us standard atmosphere. *NASA, Air*, 1962.
- [39] Seibert Q Duntley. The reduction of apparent contrast by the atmosphere. *JOSA*, 38(2):179–191, 1948.
- [40] Seibert Q Duntley. Light in the sea\*. *JOSA*, 53(2):214–233, 1963.
- [41] Michael D’Zmura, Philippe Colantoni, Kenneth Knoblauch, and Bernard Laget. Color transparency. *Perception*, 26(4):471–492, 1997.
- [42] Mariam Adawiah Dzulkifli and Muhammad Faiz Mustafar. The influence of colour on memory performance: A review. *The Malaysian journal of medical sciences: MJMS*, 20(2):3, 2013.
- [43] Fritz Ebner and Mark D Fairchild. Development and testing of a color space (ipt) with improved hue uniformity. In *Color and Imaging Conference*, volume 1998, pages 8–13. Society for Imaging Science and Technology, 1998.
- [44] Michael P Eckert and Andrew P Bradley. Perceptual quality metrics applied to still image compression. *Signal processing*, 70(3):177–200, 1998.
- [45] Jessica El Khoury, Steven Le Moan, Jean-Baptiste Thomas, and Alamin Mansouri. Quality assessment in single image dehazing. *Signal Processing: Image Communication*, 2016. Under review.
- [46] Jessica El Khoury, Jean-Baptiste Thomas, and Alamin Mansouri. Does dehazing model preserve color information? In *Signal-Image Technology and Internet-Based Systems (SITIS), 2014 Tenth International Conference on*, pages 606–613. IEEE, 2014.

- [47] Jessica El Khoury, Jean-Baptiste Thomas, and Alamin Mansouri. Haze and convergence models: Experimental comparison. In *AIC 2015*, 2015.
- [48] Jessica El Khoury, Jean-Baptiste Thomas, and Alamin Mansouri. A color image database for haze model and dehazing methods evaluation. In *Image and Signal Processing*, pages 109–117. Springer, 2016.
- [49] Jessica El Khoury, Jean-Baptiste Thomas, and Alamin Mansouri. A database with reference for image dehazing evaluation. *Machine Vision and Applications*, 2016. Under review.
- [50] Faming Fang, Fang Li, and Tieyong Zeng. Single image dehazing and denoising: a fast variational approach. *SIAM Journal on Imaging Sciences*, 7(2):969–996, 2014.
- [51] Shuai Fang, Jingrong Yang, Jiqing Zhan, Hongwu Yuan, and Ruizhong Rao. Image quality assessment on image haze removal. In *Control and Decision Conference (CCDC), 2011 Chinese*, pages 610–614. IEEE, 2011.
- [52] Raanan Fattal. Single image dehazing. In *ACM Transactions on Graphics (TOG)*, volume 27, page 72. ACM, 2008.
- [53] Chen Feng, Shaojie Zhuo, Xiaopeng Zhang, Liang Shen, and Sabine Susstrunk. Near-infrared guided color image dehazing. In *Image Processing (ICIP), 2013 20th IEEE International Conference on*, pages 2363–2367. IEEE, 2013.
- [54] Hasan Fleyeh and Mark Dougherty. Road and traffic sign detection and recognition. In *Proceedings of the 16th Mini-EURO Conference and 10th Meeting of EWGT*, pages 644–653, 2005.
- [55] WH Flygare and TD Gierke. Light scattering in noncrystalline solids and liquid crystals. *Annual Review of Materials Science*, 4(1):255–285, 1974.
- [56] Adrian Galdran, Javier Vazquez-Corral, David Pardo, and Marcelo Bertalmío. A variational framework for single image dehazing. In *Computer Vision-ECCV 2014 Workshops*, pages 259–270. Springer, 2014.
- [57] Adrian Galdran, Javier Vazquez-Corral, David Pardo, and Marcelo Bertalmío. Enhanced variational image dehazing. *Applied Optics*, 27:25, 2015.
- [58] Romain Gallen, Aurélien Cord, Nicolas Hautière, and Didier Aubert. Towards night fog detection through use of in-vehicle multipurpose cameras. In *Intelligent Vehicles Symposium (IV), 2011 IEEE*, pages 399–404. IEEE, 2011.
- [59] Elisa Drelie Gelasca, Danko Tomasic, and Touradj Ebrahimi. Which colors best catch your eyes: a subjective study of color saliency. In *Fisrt International Workshop on Video Processing and Quality Metrics for Consumer Electronics*. Citeseer, 2005.
- [60] Akshay Gore and Savita Gupta. Full reference image quality metrics for jpeg compressed images. *AEU-International Journal of Electronics and Communications*, 69(2):604–608, 2015.
- [61] D Gruyer, C Royere, N Du Lac, G Michel, and JM Blosseville. Sivic and rtm maps, interconnected platforms for the conception and the evaluation of driving assistance systems. In *Proceedings of the ITS world congress*, 2006.

- [62] Fan Guo, Jin Tang, and Zi-Xing Cai. Image dehazing based on haziness analysis. *International Journal of Automation and Computing*, 11(1):78–86, 2014.
- [63] Fan Guo, Jin Tang, and Zi-xing Cai. Objective measurement for image defogging algorithms. *Journal of Central South University*, 21:272–286, 2014.
- [64] John Hagedorn and Michael D’Zmura. Color appearance of surfaces viewed through fog. *PERCEPTION-LONDON-*, 29(10):1169–1184, 2000.
- [65] Houssam Halmaoui, Karine Joulan, Nicolas Hautière, Aurélien Cord, and Roland Brémond. Quantitative model of the driver’s reaction time during daytime fog—application to a head up display-based advanced driver assistance system. *Intelligent Transport Systems, IET*, 9(4):375–381, 2014.
- [66] Jon Hardeberg. *Acquisition and reproduction of color images: colorimetric and multispectral approaches*. Universal-Publishers, 2001.
- [67] Nicolas Hautière, Raphaël Labayrade, Clément Boussard, Jean-Philippe Tarel, and Didier Aubert. Perception through scattering media for autonomous vehicles. *Autonomous Robots Research Advances. Nova Science Publishers, Inc*, pages 223–267, 2008.
- [68] Nicolas Hautière, Jean-Philippe Tarel, Didier Aubert, Eric Dumont, et al. Blind contrast enhancement assessment by gradient ratioing at visible edges. *Image Analysis & Stereology Journal*, 27(2):87–95, 2008.
- [69] Nicolas Hautière, Jean-Philippe Tarel, Jean Lavenant, and Didier Aubert. Automatic fog detection and estimation of visibility distance through use of an onboard camera. *Machine Vision and Applications*, 17(1):8–20, 2006.
- [70] Kaiming He, Jian Sun, and Xiaoou Tang. Single image haze removal using dark channel prior. In *Computer Vision and Pattern Recognition, Proceedings of IEEE Computer Society Conference on*, pages 1956–1963. IEEE, 2009.
- [71] Kaiming He, Jian Sun, and Xiaoou Tang. Guided image filtering. In *Computer Vision—ECCV 2010*, pages 1–14. Springer, 2010.
- [72] Kaiming He, Jian Sun, and Xiaoou Tang. Single image haze removal using dark channel prior. *Pattern Analysis and Machine Intelligence, IEEE Transactions on*, 33(12):2341–2353, 2011.
- [73] H v Helmholtz. *Physiological optics*. english translation 1962 by jpc southall from the 3rd german edition of *handbuch der physiologischen optik*. vos, hamburg, 1909.
- [74] Shih-Chia Huang, Bo-Hao Chen, and Wei-Jheng Wang. Visibility restoration of single hazy images captured in real-world weather conditions. *Circuits and Systems for Video Technology, IEEE Transactions on*, 24(10):1814–1824, 2014.
- [75] EO Hulburt. Optics of atmospheric haze. *JOSA*, 31(7):467–472, 1941.
- [76] Aapo Hyvärinen and Erkki Oja. Independent component analysis: algorithms and applications. *Neural networks*, 13(4):411–430, 2000.
- [77] IFSTAR. *Frida (foggy road image database)*, 2010.

- [78] Laurent Itti and Ali Borji. Computational models: Bottom-up and top-down aspects. *arXiv preprint arXiv:1510.07748*, 2015.
- [79] Soowoong Jeong and Sangkeun Lee. The single image dehazing based on efficient transmission estimation. In *Consumer Electronics (ICCE), 2013 IEEE International Conference on*, pages 376–377. IEEE, 2013.
- [80] Jisha John and M Wilscy. Enhancement of weather degraded video sequences using wavelet fusion. In *Cybernetic Intelligent Systems, 2008. CIS 2008. 7th IEEE International Conference on*, pages 1–6. IEEE, 2008.
- [81] Ran Kaftory, Yoav Y Schechner, and Yehoshua Y Zeevi. Variational distance-dependent image restoration. In *Computer Vision and Pattern Recognition, 2007. CVPR'07. IEEE Conference on*, pages 1–8. IEEE, 2007.
- [82] George C Kagadis, Alisa Walz-Flannigan, Elizabeth A Krupinski, Paul G Nagy, Konstantinos Katsanos, Athanasios Diamantopoulos, and Steve G Langer. Medical imaging displays and their use in image interpretation. *RadioGraphics*, 33(1):275–290, 2013.
- [83] Rupinderpal Kaur and Rajneet Kaur. Survey of denoising methods using filters and fast wavelet transform. *International Journal of Advanced Research in Computer Science and Software Engineering*, 3(2), 2013.
- [84] Kumiko Kikuchi, Yuji Masuda, and Tetsuji Hirao. Imaging of hemoglobin oxygen saturation ratio in the face by spectral camera and its application to evaluate dark circles. *Skin research and technology*, 19(4):499–507, 2013.
- [85] ADITYA KONDALAMAHANTY. China air pollution: Smog blankets beijing, shanghai day after christmas. <http://www.ibtimes.com/china-air-pollution-smog-blankets-beijing-shanghai-day-after-christmas-2240081>, 2015.
- [86] Johannes Kopf, Boris Neubert, Billy Chen, Michael Cohen, Daniel Cohen-Or, Oliver Deussen, Matt Uyttendaele, and Dani Lischinski. Deep photo: Model-based photograph enhancement and viewing. In *ACM Transactions on Graphics (TOG)*, volume 27, page 116. ACM, 2008.
- [87] Harald Koschmieder. *Theorie der horizontalen Sichtweite: Kontrast und Sichtweite*. Keim & Nemnich, 1925.
- [88] Pierre-Jean Lapray, Xingbo Wang, Jean-Baptiste Thomas, and Pierre Gouton. Multispectral filter arrays: Recent advances and practical implementation. *Sensors*, 14(11):21626, 2014.
- [89] Steven Le Moan, Jens Preiss, and Philipp Urban. Evaluating the Multi-Scale iCID metric. In Mohamed-Chaker Larabi and Sophie Triantaphillidou, editors, *Image Quality and System Performance XII*, volume 9396, pages 9096–38, San Francisco, CA, February 2015. SPIE.
- [90] Steven Le Moan and Philipp Urban. Image-difference prediction: From color to spectral. *Image Processing, IEEE Transactions on*, 23(5):2058–2068, 2014.



- [91] Sungmin Lee, Seokmin Yun, Ju-Hun Nam, Chee Sun Won, and Seung-Won Jung. A review on dark channel prior based image dehazing algorithms. *EURASIP Journal on Image and Video Processing*, 2016(1):1–23, 2016.
- [92] Richard M Levenson and James R Mansfield. Multispectral imaging in biology and medicine: slices of life. *Cytometry part A*, 69(8):748–758, 2006.
- [93] Anat Levin, Dani Lischinski, and Yair Weiss. A closed-form solution to natural image matting. *Pattern Analysis and Machine Intelligence, IEEE Transactions on*, 30(2):228–242, 2008.
- [94] Chaofeng Li, Yiwen Ju, Alan C Bovik, Xiaojun Wu, and Qingbing Sang. No-training, no-reference image quality index using perceptual features. *Optical Engineering*, 52(5):057003–057003, 2013.
- [95] Yibing Li, Qiang Fu, Fang Ye, and Hayaru Shouno. Dark channel prior based blurred image restoration method using total variation and morphology. *Systems Engineering and Electronics, Journal of*, 26(2):359–366, 2015.
- [96] Yu Li and Michael Brown. Single image layer separation using relative smoothness. In *Proceedings of the IEEE Conference on Computer Vision and Pattern Recognition*, pages 2752–2759, 2014.
- [97] Yu Li, Robby T Tan, and Michael S Brown. Nighttime haze removal with glow and multiple light colors. In *Proceedings of the IEEE International Conference on Computer Vision*, pages 226–234, 2015.
- [98] Haida Liang. Advances in multispectral and hyperspectral imaging for archaeology and art conservation. *Applied Physics A*, 106(2):309–323, 2012.
- [99] Zheqi Lin and Xuansheng Wang. Dehazing for image and video using guided filter. *Open Journal of Applied Sciences*, 2(04):123, 2013.
- [100] Yu Linan, Piao Yan, and Yan Xiaoyuan. Video defogging based on adaptive tolerance. *TELKOMNIKA Indonesian Journal of Electrical Engineering*, 10(7):1644–1654, 2012.
- [101] Ingmar Lissner, Jens Preiss, Philipp Urban, Matthias Scheller Lichtenauer, and Peter Zolliker. Image-difference prediction: From grayscale to color. *Image Processing, IEEE Transactions on*, 22(2):435–446, 2013.
- [102] Ingmar Lissner, Jens Preiss, Philipp Urban, Matthias Scheller Lichtenauer, and Peter Zolliker. Image-difference prediction: From grayscale to color. *Image Processing, IEEE Transactions on*, 22(2):435–446, 2013.
- [103] Shilong Liu, MA Rahman, CY Wong, ScF Lin, G Jiang, and Ngaiming Kwok. Dark channel prior based image de-hazing: A review. In *Information Science and Technology (ICIST), 2015 5th International Conference on*, pages 345–350. IEEE, 2015.
- [104] Ximvei Liu and Jon Yngve Hardeberg. Fog removal algorithms: Survey and perceptual evaluation. In *Visual Information Processing (EUVIP), 2013 4th European Workshop on*, pages 118–123. IEEE, 2013.

- [105] Jiao Long, Zhenwei Shi, and Wei Tang. Fast haze removal for a single remote sensing image using dark channel prior. In *Computer Vision in Remote Sensing (CVRS), 2012 International Conference on*, pages 132–135. IEEE, 2012.
- [106] Xingyong Lv, Wenbin Chen, and I-fan Shen. Real-time dehazing for image and video. In *Computer Graphics and Applications (PG), 2010 18th Pacific Conference on*, pages 62–69. IEEE, 2010.
- [107] Kede Ma, Wentao Liu, and Zhou Wang. Perceptual evaluation of single image dehazing algorithms. In *IEEE International Conference on Image Processing*, 2015.
- [108] David L MacAdam. Perceptual significance of colorimetric data for colors of plumes and haze. *Atmospheric Environment (1967)*, 15(10):1797–1803, 1981.
- [109] Kenneth David Mankoff and Tess Alethea Russo. The kinect: A low-cost, high-resolution, short-range 3d camera. *Earth Surface Processes and Landforms*, 38(9):926–936, 2013.
- [110] H Charles Manning, Sheila D Shay, and Robert A Mericle. Multispectral molecular imaging of capillary endothelium to facilitate preoperative endovascular brain mapping: Laboratory investigation. *Journal of neurosurgery*, 110(5):975–980, 2009.
- [111] Alamin Mansouri, FS Marzani, and Pierre Gouton. Development of a protocol for ccd calibration: application to a multispectral imaging system. *International Journal of Robotics and Automation*, 20(2):94–100, 2005.
- [112] David Martin, Charless Fowlkes, Doron Tal, and Jitendra Malik. A database of human segmented natural images and its application to evaluating segmentation algorithms and measuring ecological statistics. In *Computer Vision, 2001. ICCV 2001. Proceedings. Eighth IEEE International Conference on*, volume 2, pages 416–423. IEEE, 2001.
- [113] Erik Matlin and Peyman Milanfar. Removal of haze and noise from a single image. In *IS&T/SPIE Electronic Imaging*, pages 82960T–82960T. International Society for Optics and Photonics, 2012.
- [114] Calvin S McCamy, H Marcus, and JG Davidson. A color-rendition chart. *J. App. Photog. Eng.*, 2(3):95–99, 1976.
- [115] Earl J McCartney. Optics of the atmosphere: scattering by molecules and particles. New York, John Wiley and Sons, Inc., 1976. 421 p., 1, 1976.
- [116] Fabio Metelli. The perception of transparency. *Scientific American*, 1974.
- [117] Albert Abraham Michelson. *Studies in optics*. Courier Corporation, 1995.
- [118] William Edgar Knowles Middleton. *Visibility in meteorology*. University of Toronto Press, 1935.
- [119] William Edgar Knowles Middleton. Vision through the atmosphere. In *Geophysik II/Geophysics II*, pages 254–287. Springer, 1957.
- [120] E Misimi, JR Mathiassen, and U Erikson. Computer vision-based sorting of atlantic salmon (*salmo salar*) fillets according to their color level. *Journal of food science*, 72(1):S030–S035, 2007.

- [121] A. Mittal, R. Soundararajan, and A. C. Bovik. Making a completely blind image quality analyser. *IEEE Signal Processing Letters*, 22:209–212, 2013.
- [122] G Mm. A contribution in the optics of turbid media, especially collidal metallic suspensions. *Ann. Phys*, 25:377–445, 1908.
- [123] Pedram Mohammadi, Abbas Ebrahimi-Moghadam, and Shahram Shirani. Subjective and objective quality assessment of image: A survey. *arXiv preprint arXiv:1406.7799*, 2014.
- [124] Dong Nan, Du-yan Bi, Chang Liu, Shi-ping Ma, and Lin-yuan He. A bayesian framework for single image dehazing considering noise. *The Scientific World Journal*, 2014, 2014.
- [125] Srinivasa G Narasimhan and Shree K Nayar. Chromatic framework for vision in bad weather. In *Computer Vision and Pattern Recognition, 2000. Proceedings. IEEE Conference on*, volume 1, pages 598–605. IEEE, 2000.
- [126] Srinivasa G Narasimhan and Shree K Nayar. Vision and the atmosphere. *International Journal of Computer Vision*, 48(3):233–254, 2002.
- [127] Srinivasa G Narasimhan and Shree K Nayar. Contrast restoration of weather degraded images. *Pattern Analysis and Machine Intelligence, IEEE Transactions on*, 25(6):713–724, 2003.
- [128] Srinivasa G Narasimhan and Shree K Nayar. Interactive (de) weathering of an image using physical models. In *IEEE Workshop on Color and Photometric Methods in Computer Vision*, volume 6, page 1. France, 2003.
- [129] Srinivasa G Narasimhan and Shree K Nayar. Shedding light on the weather. In *Computer Vision and Pattern Recognition, 2003. Proceedings. 2003 IEEE Computer Society Conference on*, volume 1, pages 1–665. IEEE, 2003.
- [130] Srinivasa G Narasimhan, Chi Wang, and Shree K Nayar. All the images of an outdoor scene. In *Computer Vision ECCV 2002*, pages 148–162. Springer, 2002.
- [131] Srinivasa G Narasimhan, Chi Wang, and Shree K Nayar. Wild: Weather and illumination database, 2002.
- [132] Shree K Nayar and Srinivasa G Narasimhan. Vision in bad weather. In *Computer Vision, 1999. The Proceedings of the Seventh IEEE International Conference on*, volume 2, pages 820–827. IEEE, 1999.
- [133] John P Oakley and Brenda L Satherley. Improving image quality in poor visibility conditions using a physical model for contrast degradation. *Image Processing, IEEE Transactions on*, 7(2):167–179, 1998.
- [134] Erik Ødegard. What do you see with a thermal imaging camera in foggy and rainy conditions? <https://www.linkedin.com/pulse/20140625165540-14073483--what-do-you-see-with-a-thermal-imaging-camera-in/-foggy-and-rainy-conditions-is-one-of-the-most-frequently-asked-questions-from-/our-clients>, 2014.

- [135] Anikender Kumar P. Goyal, Sumer Budhiraja. Impact of air pollutants on atmospheric visibility in delhi. *International Journal of Geology, Agriculture and Environmental Sciences*, 2(2):11–16, 2014.
- [136] Jiahao Pang, Oscar C Au, and Zheng Guo. Improved single image dehazing using guided filter. In *Asia-Pacific Signal and Information Processing Association Annual Summit and Conference 2011*, 2011.
- [137] Mario Pavlić, Heidrun Belzner, Gerhard Rigoll, and Slobodan Ilić. Image based fog detection in vehicles. In *Intelligent Vehicles Symposium (IV), 2012 IEEE*, pages 1132–1137. IEEE, 2012.
- [138] Marius Pedersen, Nicolas Bonnier, Jon Y Hardeberg, and Fritz Albregtsen. Image quality metrics for the evaluation of print quality. In *IS&T/SPIE Electronic Imaging*, pages 786702–786702. International Society for Optics and Photonics, 2011.
- [139] Soo-Chang Pei and Tzu-Yen Lee. Nighttime haze removal using color transfer pre-processing and dark channel prior. In *Image Processing (ICIP), 2012 19th IEEE International Conference on*, pages 957–960. IEEE, 2012.
- [140] Patrick Perez et al. *Markov random fields and images*. IRISA, 1998.
- [141] Niklas Pettersson. Gpu-accelerated real-time surveillance de-weathering. 2013.
- [142] Stephen M Pizer, E Philip Amburn, John D Austin, Robert Cromartie, Ari Geselowitz, Trey Greer, Bart ter Haar Romeny, John B Zimmerman, and Karel Zuiderveld. Adaptive histogram equalization and its variations. *Computer vision, graphics, and image processing*, 39(3):355–368, 1987.
- [143] Ulrich Platt, Klaus Pfeilsticker, and Michael Vollmer. Radiation and optics in the atmosphere. In *Springer Handbook of Lasers and Optics*, pages 1475–1517. Springer, 2012.
- [144] Jens Preiss, Felipe Fernandes, and Philipp Urban. Color-image quality assessment: From prediction to optimization. *IEEE Transactions on Image Processing*, 23(3):1366–1378, 2014.
- [145] Jianwei Qin, Kuanglin Chao, Moon S Kim, Renfu Lu, and Thomas F Burks. Hyper-spectral and multispectral imaging for evaluating food safety and quality. *Journal of Food Engineering*, 118(2):157–171, 2013.
- [146] C Ramya and S Subha Rani. A novel method for the contrast enhancement of fog degraded video sequences. *International Journal of Computer Applications*, 54(13), 2012.
- [147] Ramesh Raskar. Computational photography. In *Computational Optical Sensing and Imaging*, page CTuA1. Optical Society of America, 2009.
- [148] Erik Reinhard, Michael Ashikhmin, Bruce Gooch, and Peter Shirley. Color transfer between images. *IEEE Computer graphics and applications*, (5):34–41, 2001.
- [149] Ingo Rentschler, Martin Jüttner, Alexander Unzicker, and Theodor Landis. Innate and learned components of human visual preference. *Current Biology*, 9(13):665–671, 1999.

- [150] Robert A Rohde and Richard A Muller. Air pollution in china: Mapping of concentrations and sources. *PloS one*, 10(8):e0135749, 2015.
- [151] Daniel L Ruderman. The statistics of natural images. *Network: computation in neural systems*, 5(4):517–548, 1994.
- [152] C. Sahu and R. Sahu. Comparative study on fusion based image dehazing. *International Journal of Advanced Research in Computer and Communication Engineering*, 3, 2014.
- [153] MS Sandeep. Remote sensing image dehazing using guided filter. *IJRSCSE*, 1(3):44–49, 2014.
- [154] Lex Schaul, Clément Fredembach, and Sabine Süsstrunk. Color image dehazing using the near-infrared. In *Proc. IEEE International Conference on Image Processing (ICIP)*, number LCAV-CONF-2009-026, 2009.
- [155] Yoav Y Schechner and Nir Karpel. Clear underwater vision. In *Computer Vision and Pattern Recognition, 2004. CVPR 2004. Proceedings of the 2004 IEEE Computer Society Conference on*, volume 1, pages I–536. IEEE, 2004.
- [156] Yoav Y Schechner, Srinivasa G Narasimhan, and Shree K Nayar. Instant dehazing of images using polarization. In *Computer Vision and Pattern Recognition, 2001. CVPR 2001. Proceedings of the 2001 IEEE Computer Society Conference on*, volume 1, pages I–325. IEEE, 2001.
- [157] Yoav Y Schechner, Srinivasa G Narasimhan, and Shree K Nayar. Instant dehazing of images using polarization. In *Computer Vision and Pattern Recognition, 2001. CVPR 2001. Proceedings of the 2001 IEEE Computer Society Conference on*, volume 1, pages I–325. IEEE, 2001.
- [158] Yoav Y Schechner, Srinivasa G Narasimhan, and Shree K Nayar. Polarization-based vision through haze. *Applied Optics*, 42(3):511–525, 2003.
- [159] Raimondo Schettini, Francesca Gasparini, Silvia Corchs, Fabrizio Marini, Alessandro Capra, and Alfio Castorina. Contrast image correction method. *Journal of Electronic imaging*, 19(2):023005–023005, 2010.
- [160] Hamid Rahim Sheikh and Alan C Bovik. Image information and visual quality. *Image Processing, IEEE Transactions on*, 15(2):430–444, 2006.
- [161] Hamid Rahim Sheikh, Muhammad Farooq Sabir, and Alan Conrad Bovik. A statistical evaluation of recent full reference image quality assessment algorithms. *Image Processing, IEEE Transactions on*, 15(11):3440–3451, 2006.
- [162] Sarit Shwartz, Einav Namer, and Yoav Y Schechner. Blind haze separation. In *Computer Vision and Pattern Recognition, 2006 IEEE Computer Society Conference on*, volume 2, pages 1984–1991. IEEE, 2006.
- [163] Serdar Solak and Emine Dogru Bolat. Real time industrial application of single board computer based color detection system. In *Electrical and Electronics Engineering (ELECO), 2013 8th International Conference on*, pages 353–357. IEEE, 2013.

- [164] Wei Sun. A new single-image fog removal algorithm based on physical model. *Optik-International Journal for Light and Electron Optics*, 124(21):4770–4775, 2013.
- [165] Robby T Tan. Visibility in bad weather from a single image. In *Computer Vision and Pattern Recognition, 2008. CVPR 2008. IEEE Conference on*, pages 1–8. IEEE, 2008.
- [166] Zhiming Tan, Xianghui Bai, Bingrong Wang, and Akihiro Higashi. Fast single-image defogging. *FUJITSU Sci. Tech. J*, 50(1):60–65, 2014.
- [167] Jean-Philippe Tarel and Nicolas Hautière. Fast visibility restoration from a single color or gray level image. In *Computer Vision, 2009 IEEE 12th International Conference on*, pages 2201–2208. IEEE, 2009.
- [168] Jean-Philippe Tarel, Nicolas Hautière, Laurent Caraffa, Aurélien Cord, Houssam Halmaoui, and Dominique Gruyer. Vision enhancement in homogeneous and heterogeneous fog. *Intelligent Transportation Systems Magazine, IEEE*, 4(2):6–20, 2012.
- [169] Jean-Philippe Tarel, Nicolas Hautière, Aurélien Cord, Dominique Gruyer, and Housam Halmaoui. Improved visibility of road scene images under heterogeneous fog. In *Intelligent Vehicles Symposium (IV), 2010 IEEE*, pages 478–485. IEEE, 2010.
- [170] Jean-Baptiste Thomas, Pierre-Jean Lapray, Pierre Gouton, and Cdric Clerc. Spectral characterization of a prototype sfa camera for joint visible and nir acquisition. *Sensors*, 16(7):993, 2016.
- [171] William B Thompson, Peter Shirley, and James A Ferwerda. A spatial post-processing algorithm for images of night scenes. *Journal of Graphics Tools*, 7(1):1–12, 2002.
- [172] Carlo Tomasi and Roberto Manduchi. Bilateral filtering for gray and color images. In *Computer Vision, 1998. Sixth International Conference on*, pages 839–846. IEEE, 1998.
- [173] Fabrizio Vagni. Survey of hyperspectral and multispectral imaging technologies. 2007.
- [174] Khai Van Ngo, Jehans J Storvik, Christopher A Dokkeberg, Ivar Farup, and Marius Pedersen. Quickeval: a web application for psychometric scaling experiments. In *IS&T/SPIE Electronic Imaging*, pages 93960O–93960O. International Society for Optics and Photonics, 2015.
- [175] Paul Von Allmen, Seungwon Lee, Rachel Hodos, David Diner, John Martonchik, and Anthony Davis. De-hazing of multi-spectral images with evolutionary computing. In *Aerospace Conference, 2010 IEEE*, pages 1–4. IEEE, 2010.
- [176] Lixia Wang, Weixin Xie, and Jihong Pei. Patch-based dark channel prior dehazing for rs multi-spectral image. *Chinese Journal of Electronics*, 24(3):573–578, 2015.
- [177] Zhou Wang, Alan C Bovik, and Ligang Lu. Why is image quality assessment so difficult? In *Acoustics, Speech, and Signal Processing (ICASSP), 2002 IEEE International Conference on*, volume 4, pages IV–3313. IEEE, 2002.

- [178] Zhou Wang, Alan Conrad Bovik, Hamid Rahim Sheikh, and Eero P Simoncelli. Image quality assessment: from error visibility to structural similarity. *Image Processing, IEEE Transactions on*, 13(4):600–612, 2004.
- [179] Zhou Wang, Eero P Simoncelli, and Alan C Bovik. Multiscale structural similarity for image quality assessment. In *Signals, Systems and Computers, 2004. Conference Record of the Thirty-Seventh Asilomar Conference on*, volume 2, pages 1398–1402. Ieee, 2003.
- [180] Reinhard Wilhelm, Jakob Engblom, Andreas Ermedahl, Niklas Holsti, Stephan Thesing, David Whalley, Guillem Bernat, Christian Ferdinand, Reinhold Heckmann, Tulika Mitra, et al. The worst-case execution-time problem: overview of methods and survey of tools. *ACM Transactions on Embedded Computing Systems (TECS)*, 7(3):36, 2008.
- [181] Di Wu and Da-Wen Sun. Hyperspectral imaging technology: a nondestructive tool for food quality and safety evaluation and inspection. In *Advances in Food Process Engineering Research and Applications*, pages 581–606. Springer, 2013.
- [182] Chunxia Xiao and Jiajia Gan. Fast image dehazing using guided joint bilateral filter. *The Visual Computer*, 28(6-8):713–721, 2012.
- [183] Bin Xie, Fan Guo, and Zixing Cai. Universal strategy for surveillance video defogging. *Optical Engineering*, 51(10):101703–1, 2012.
- [184] Haoran Xu, Jianming Guo, Qing Liu, and Lingli Ye. Fast image dehazing using improved dark channel prior. In *Information Science and Technology (ICIST), 2012 International Conference on*, pages 663–667. IEEE, 2012.
- [185] Yong Xu, Jie Wen, Lunke Fei, and Zheng Zhang. Review of video and image defogging algorithms and related studies on image restoration and enhancement. 2015.
- [186] Zhiyuan Xu, Xiaoming Liu, and Xiaonan Chen. Fog removal from video sequences using contrast limited adaptive histogram equalization. In *Computational Intelligence and Software Engineering, 2009. CiSE 2009. International Conference on*, pages 1–4. IEEE, 2009.
- [187] Zhiyuan Xu, Xiaoming Liu, and Na Ji. Fog removal from color images using contrast limited adaptive histogram equalization. In *Image and Signal Processing, 2009. CISP'09. 2nd International Congress on*, pages 1–5. IEEE, 2009.
- [188] Hongbo Yang and Jiuhe Wang. Color image contrast enhancement by co-occurrence histogram equalization and dark channel prior. In *Image and Signal Processing (CISP), 2010 3rd International Congress on*, volume 2, pages 659–663. IEEE, 2010.
- [189] Sergej N Yendrikhovski, Frans JJ Blommaert, and Huib de Ridder. Perceptually optimal color reproduction. In *Photonics West'98 Electronic Imaging*, pages 274–281. International Society for Optics and Photonics, 1998.
- [190] Inhye Yoon, Seonyung Kim, Donggyun Kim, Monson H Hayes, and Joonki Paik. Adaptive defogging with color correction in the hsv color space for consumer surveillance system. *Consumer Electronics, IEEE Transactions on*, 58(1):111–116, 2012.



- [191] Jing Yu, Chuangbai Xiao, and Dapeng Li. Physics-based fast single image fog removal. In *Signal Processing (ICSP), 2010 IEEE 10th International Conference on*, pages 1048–1052. IEEE, 2010.
- [192] Xiaoliang Yu, Chuangbai Xiao, Mike Deng, and Li Peng. A classification algorithm to distinguish image as haze or non-haze. In *Image and Graphics (ICIG), 2011 Sixth International Conference on*, pages 286–289. IEEE, 2011.
- [193] Hongying Zhang, Qiaolin Liu, Yadong Wu, and Fan Yang. Single image dehazing combining physics model based and non-physics model based methods. *Journal of Computational Information Systems*, 9(4):1623–1631, 2013.
- [194] Jing Zhang, Yang Cao, and Zengfu Wang. Nighttime haze removal based on a new imaging model. In *Image Processing (ICIP), 2014 IEEE International Conference on*, pages 4557–4561. IEEE, 2014.
- [195] Lin Zhang, Ying Shen, and Hongyu Li. VSI: a visual saliency-induced index for perceptual image quality assessment. *Image Processing, IEEE Transactions on*, 23(10):4270–4281, 2014.
- [196] Lin Zhang, Lei Zhang, Xuanqin Mou, and David Zhang. FSIM: a feature similarity index for image quality assessment. *Image Processing, IEEE Transactions on*, 20(8):2378–2386, 2011.
- [197] Yong-Qin Zhang, Yu Ding, Jin-Sheng Xiao, Jiaying Liu, and Zongming Guo. Visibility enhancement using an image filtering approach. *EURASIP Journal on Advances in Signal Processing*, 2012(1):1–6, 2012.
- [198] Yuanyuan Zhang, Guangmin Sun, Qian Ren, and Dequn Zhao. Foggy images classification based on features extraction and svm. In *Proceeding of 2013 International Conference on Software Engineering and Computer Science. Yichang, China: Atlantis*, volume 145, 2013.
- [199] Qingsong Zhu, Jiaming Mai, and Ling Shao. Single image dehazing using color attenuation prior. In *Proceedings of the BMVC*, 2014.
- [200] Ximei Zhu, Ying Li, and Yu Qiao. Fast single image dehazing through edge-guided interpolated filter. In *Machine Vision Applications (MVA), 2015 14th IAPR International Conference on*, pages 443–446. IEEE, 2015.

# LIST OF FIGURES

2.1	Images captured in bad environments. (a) underwater image; (b) foggy road image; (c) landscape foggy image; (d) fog over snow image; (e) air pollution image; (f) satellite image; (g) nighttime foggy image; (h) indoor smoky image. . . . .	10
2.2	Hazy images with different haze types. (a) Uniform haze; (b) Layered haze; (c) ; (d) Plumes. . . . .	12
2.3	Foggy images with different fog types. (a) Uniform fog; (b) Radiation fog; (c) Advection fog. . . . .	13
2.4	The intensity of the forward scattered light by a single atmospheric particle. According to Rayleigh scattering, with the angular increase from $0^\circ$ (red) to $90^\circ$ (blue), the intensity decreases. . . . .	14
2.5	The variation of the scattering properties (intensity, type and form) with the ratio of the particle size to the incident light wavelength. Rayleigh scattering is applied when the size of the scattering particle is lower than $\frac{\lambda}{10}$ . For particles with a larger size than the light wavelength $\lambda$ , Mie scattering is applied. This figure is reproduced here from the Figure 1 of the paper of Nayar <i>et al.</i> [132] . . . . .	15
2.6	Atmospheric multiple scattering. This figure is reproduced here from the presentation of the paper of Nayar <i>et al.</i> [132]. . . . .	15
2.7	An illuminated unit volume observed at angle $\theta$ . . . . .	17
2.8	An atmospheric particle placed on the line of sight between the observer and the object with no defined geometrical shape plays the role of a light source by scattering the light coming either from other scattering particles or from the sun. . . . .	18
2.9	Imaging through haze. The apparent luminance $I$ of an object placed at distance $d$ is controlled by two processes that occur concurrently: the transmitted light denoted by $t$ , which emanates from the object and it is attenuated by scattering and absorption along the line of sight. The airlight $A$ , which comes from a light source ( <i>i.e.</i> Sun) and scattered by the haze particles toward the observer before reaching the object. This figure is reproduced here from the Figure 1 of the paper of Schechner <i>et al.</i> [156]. . . . .	18
3.1	Number of publications describing new dehazing approaches over 13 years. This figure has modified from Figure 1 of the paper of Liu <i>et al.</i> [103]. . . . .	25
3.2	The family of dehazing methods. . . . .	26

3.3	Flowchart of DCP showing its main steps. . . . .	28
3.4	(a) Hazy image. (b) Dark channel obtained by Equation 3.2 ( $3 \times 3$ ). (c) Dark channel obtained by Equation 3.4 ( $3 \times 3$ ). (d) Dark channel obtained by Equation 3.2 ( $15 \times 15$ ). (e) Dark channel obtained by Equation 3.4 ( $15 \times 15$ ). This figure is reproduced here from Figure 6 of the paper of Lee <i>et al.</i> [91]. . . . .	29
3.5	(a) Hazy image. (b) Tan's result. (c) DCP's result. Images are borrowed from the Figure 8 of the paper of He <i>et al.</i> [70]. . . . .	33
3.6	The estimated color coordinates of the same scene point taken under two different weather conditions $i$ and $j$ are plot on the same plane in the RGB color space. These coordinates differ from each other by the magnitudes of $\hat{A}$ and $\hat{B}$ . This figure has been modified from Figure 1 of the paper of Narasimhan <i>et al.</i> [128]. . . . .	36
3.7	The estimated color coordinates of two points $P^1$ and $P^2$ of the same scene are plot on two different planes in the RGB color space. . . . .	37
3.8	A hazy scene taken from CHIC database processed by five different dehazing methods: (a) CLAHE; (b) DCP; (c) FAST; (d) FUSION; (e) VAR. Dehazed colors are differently perceived across images. . . . .	48
3.9	The color recovery of a hazy image treated by Tan's dehazing method. These images have been borrowed and modified from the Figure 10 of the paper of Tan [165]. . . . .	49
3.10	Hazy input image and dehazed output image obtained by DCP. In order to investigate the influence of dehazing with depth on both saturation and hue, we select pixels at red and green points, which are supposed to have the same initial color, located at different depths and covered by a uniform haze veil. These images have been borrowed and modified from the Figure 7 of the paper of Tan [72]. . . . .	50
3.11	(a) Saturation difference and (b) IPT angle difference at red and green dots in hazy and dehazed images. When dehazing is applied, both points are saturated. The green point, which is covered with much haze is less saturated. The difference of hue angle at the green point is larger. This reflects the failure of dehazing to provide accurate recovery of colors hue at far objects and high haze density as well. . . . .	51
3.12	Flowchart of the synthetic formation of analyzed images . . . . .	52
3.13	Original and hazy images . . . . .	53
3.14	Original RGB image and corrected images. (b): $RGB_{XYZ}^D \alpha = 0.5$ , (c): $RGB_{XYZ}^D \alpha = 0.7$ , (d): $RGB_{XYZ}^D \alpha = 0.9$ , (e): $RGB_{RGB}^D \alpha = 0.9$ . . . . .	54
3.15	Saturation evolution curves of the patches recovered from hazy image when $\alpha = 0.5$ in comparison with original clear images and other rectified images (normalized images). . . . .	55
3.16	Saturation evolution with $\alpha$ ( $RGB_{XYZ}^D$ image) . . . . .	55

3.17 Hue evolution curves of the patches recovered from hazy image when $\alpha = 0.5$ in comparison with original clear images and other rectified images (normalized images). . . . .	56
4.1 The light reaching the camera is the sum of the light coming from the object and attenuated by the scattering and the light coming from outside and scattered by fog particles towards the camera. The airlight component scattered by the fog particles depends on the wavelength. . . . .	65
4.2 Scene A (a) and Scene B (b). The distances of different MCCs to the camera are shown. The resolution of the image is 6000×4000. . . . .	66
4.3 Dynamic scene. The left column shows images with haze, with distances between the window and the camera: 0, 3.5, and 5.6m. The right column shows the free-haze images of the same distances. . . . .	68
4.10 (a)Visible band, (b)NIR wavelength band. . . . .	71
4.11 Image of the setup. . . . .	72
4.12 Transmission curves of LCTFs: (a) VIS and (b) NIR. These graphs have been scanned from the technical documentations of VariSpec Liquid Crystal tunable filters. Note that the transmission values are within the interval of [0,1] in the graph (a) and within the interval of [0,100] in the graph (b). . . . .	74
4.13 Transmission curve of the sensor Photon focus MV1-D1280I-120-CL camera based on e2v EV76C661 CMOS. This graph is borrowed from the correspondent technical documentation [7]. . . . .	74
4.4 Scene A. Scene images taken under different fog levels and their correspondent transmission curves, which are measured over the farthest white patch from the camera. From top to bottom: level 1, level 2, level 3 and level 4. . . . .	76
4.5 Scene A. Scene images taken under different fog levels and their correspondent transmission curves, which are measured over the farthest white patch from the camera. From top to bottom: level 5, level 6, level 7 and level 8. . . . .	77
4.6 Scene A. Scene images taken under different fog levels and their correspondent transmission curves, which are measured over the farthest white patch from the camera. From top to bottom: level 9 and clear image. . . . .	78
4.7 Scene B. Scene images taken under different fog levels and their correspondent transmission curves, which are measured over the farthest white patch from the camera. From top to bottom: level 1, level 2, level 3 and level 4. . . . .	79
4.8 Scene B. Scene images taken under different fog levels and their correspondent transmission curves, which are measured over the farthest white patch from the camera. From top to bottom: level 5, level 6, level 7 and level 8. . . . .	80
4.9 Scene B. Scene images taken under different fog levels and their correspondent transmission curves, which are measured over the farthest white patch from the camera. From top to bottom: level 9 and clear image. . . . .	81

- 5.1 The original hazy (first row) and the reconstructed images of Scene A (second row).  $A$  and  $t$  are estimated on the surrounded red color patch. The distance between it and the camera is  $7m$ . First row: original hazy images, second row: reconstructed images. Cropped image size is  $1537 \times 2049$ . . . 84
- 5.2 The original hazy (first row) and the reconstructed images of Scene B (second row).  $A$  and  $t$  are estimated on the surrounded red color patch. The distance between it and the camera is  $4.25m$ . First row: original hazy images, second row: reconstructed images. Cropped image size is  $1537 \times 3073$ . 85
- 5.3 Estimated  $A$  and  $t$  obtained for each level of fog for a given distance of the MCC placed at the back of the scene. First row: airlight, second row: transmission. First column: scene A, second column: scene B. . . . . 86
- 5.4 Images resulted through the haze model inversion from a real hazy image and the correspondent simulated one at fog level 9 and level 5. Unlike level 9 where there is a color matching between recovered patches of real and simulated scenes, the inversion of the haze model fails to recover accurately the same colors for both images of level 5 where the haze density is high. This is particularly clear at some patches such as the framed ones. . 87
- 5.5 The chromaticities of different haze levels calculated in the color space CIE xyY and represented by the parameters  $x$  and  $y$ . They are placed on the chromaticity diagram of the red patch. (a) Real Scene, (b) Simulated Scene. Red: clear image white: Level 1 yellow: Level 2 magenta: Level 3 black: Level 4 - gray: Level 5 pink: Level 6 green: Level 7 dark green: Level 8 blue: Level 9. The distributions of points representing the red patch from level 5 to level 2 are different between (a) and (b), while other points keep the same relative place between the end points (red and white) with a little shift in saturation. . . . . 88
- 5.6 Chromaticities (a) and color appearance distribution (b) in CIE xyY and CIE Lab color spaces, respectively, of the ColorChecker patches (Figure 3.13) at fog level 7 (red), fog level 9 (green) and haze-free level (blue) of Scene A.  $A_\infty$  is placed at the center. . . . . 90
- 5.7 Chromaticities (a) and color appearance distribution (b) in CIE xyY and CIE Lab color spaces, respectively, of the ColorChecker patches (Figure 3.13) at fog level 7 (red), fog level 9 (green) and haze-free level (blue) of Scene B.  $A_\infty$  is placed at the center. . . . . 91
- 5.8 Representative graph showing the distribution of the original haze-free colors and the atmospheric light  $A_\infty$ .  $J_1$ ,  $J_2$  and  $J_3$  are three different haze-free colors.  $A_\infty$  is the center of the achromatic zone. Considering  $r$  as the radius of the achromatic zone. Depending on the distance between  $A_\infty$  and  $J$ , the transmission value from which the original color can be recovered. The shorter the distance  $d$ , not a very low  $t$  value is enough to put the color inside the blue achromatic area, and the accurate recovery is no more feasible. . . . . 95
- 5.9 Selected color patches. The patches colors are the same matched with the curves colors in the Figures 5.10 and 5.11. . . . . 96

5.10 (a) The lines constructed by the haze-free color and the hazy color $\Delta$ at the same pixels of the level 5; (b) Zoom in of the red rectangle. . . . .	97
5.11 (a) The lines constructed by the haze-free color $*$ and the hazy color $\Delta$ at the same pixels of the level 9; (b) Zoom in of the red rectangle. . . . .	98
5.12 Linearity of the system composed of the sensor and the filter VIS. Considering the haze-free image, the luminance component of CIE xyY is plotted against the digital values (16 bits) calculated over the patches S, T, U, V, W and X (Figure 3.13). Being quasi-linear over 4 different wavelengths (550, 600, 650 and 700 nm), no correction such as Gamma correction is applied. . . . .	99
5.13 $M1_V$ haze-free image. At low wavelengths (400-500 nm) the sensor noise prevails on the image. Thus, it avoids the accurate measurement of the airlight. . . . .	100
5.14 $M2_V$ haze-free image. At low wavelengths (400-500 nm) the sensor noise prevails on the image. Thus, it avoids the accurate measurement of the airlight. . . . .	100
5.15 $M2_{NIR}$ haze-free image. The energy beyond visible range seems to be extremely low. Thus, what we detect, especially from 900 nm is just noise. Thus, airlight using these images is erroneously measured. . . . .	101
6.1 Case of confusion and disagreement between observers for the quality of recovered images that matches the best with the original haze-free image. scene A at haze level 9 taken from CHIC. In the second row, from left to right: image dehazed by CLAHE, image dehazed by VAR, haze-free image and dehazed image by Fusion (cf. Section 6.3). . . . .	104
6.2 Preference, usability and fidelity have ranges of validation, which depend on the density of fog. When the density of fog is very high, we only consider the dehazing usability, which underlines the ability of dehazing to unveil some usable information. Usability can be considered for all fog densities. For intermediate densities, when the haze model is valid, we consider the fidelity of recovered features. When the fog is basically very light, the dehazed images are usually over-contrasted and therefore more preferred than the original haze-free images. . . . .	107
6.3 (a, e) Haze-free image; (b, f) Hazy image; (c, g) Dehazed image: efficient dehazing with color shift; (d, h) Dehazed image: inefficient dehazing with no color shift. In the case of obstacles detection for road safety, the result (c) is better than the result (d), since it provides a higher facility for objects detection. However, for applications consisting in segmentation based on color, the result (h) seems to be better than (g), since colors are recognized and similar to the original ones. . . . .	108
6.4 Scene 1. From left to right: Haze-free; Level A (highest fog level); Level B (medium fog level); Level C (lowest fog level). Image size is 1537×2049. These images are successively acquired within 5 minutes. . . . .	109
6.5 Scene 2. From left to right: Haze-free; Level A (highest fog level); Level B (medium fog level); Level C (lowest fog level). Image size is 1537×3073. These images are successively acquired within 5 minutes. . . . .	110

6.6	Modeling workflow of the reference and distorted images [160]. . . . .	113
6.7	Dehazed images of Scene 1 of fog levels A, B and C. They have been processed by CLAHE, DCP and FAST algorithms. Rows: CLAHE, DCP, FAST. Columns: level A, level B, level C. . . . .	120
6.8	Dehazed images of Scene 1 of fog levels A, B and C. They have been processed by FUSION and VAR algorithms. Rows: FUSION and VAR. Columns: level A, level B, level C. . . . .	121
6.9	Dehazed images of Scene 2 of fog levels A, B and C. They have been processed by CLAHE and DCP algorithms. Rows: CLAHE and DCP. Columns: level A, level B, level C. . . . .	122
6.10	Dehazed images of Scene 2 of fog levels A, B and C. They have been processed by FAST algorithm. Columns: level A, level B, level C. . . . .	123
6.11	Dehazed images of Scene 2 of fog levels A, B and C. They have been processed by FUSION and VAR algorithms. Rows: FUSION and VAR. Columns: level A, level B, level C. . . . .	124
6.12	Average ranks obtained for each image sequence, and for each level of haze. First row: color, second row: sharpness. First column: scene 1, second column: scene 2. . . . .	126
6.13	Case of total disagreement between metrics in reference with the haze-free image and observers for color recovery quality assessment (scene 1, level B). (a)Result from CLAHE, (b) original image and (c) result from FAST. While all metrics rate the CLAHE dehazed image as more fidel to the original, all observers agreed that FAST is better in terms of color. Indeed, the FAST image seems more vivid, although it clearly shows artifacts just under the tables and around the plants. When it comes to evaluating the structure however, a majority of observers (9 out of 14) find the CLAHE image more fidel. This suggests that these metrics in our benchmark do not perform well at balancing the importance of chromatic and achromatic attributes for dehazing quality assessment. . . . .	128
6.14	The scores of the metrics in reference with the haze-free image, which are obtained for each scene at each fog level. These five metrics (MS-SSIM, VIF, MS-iCID, FSIMc and VSI) evaluate the quality of the dehazed image as being the similarity rate of specified features between the hazy and the haze-free images. For light fog, all of these metrics show the high similarity rate compared to higher level of fog. Some of them such as MS-SSIM, FSIMc, VSI and NIQE show that DCP does not perform well in the lowest fog level. The subjective analysis shows that $C_L$ and VSI are the most relevant metrics to evaluate color and sharpness. Both of these metrics' values of different methods are noticeably close to each other. . . . .	129



- 6.15 The scores of the metrics in reference with the hazy image, which are obtained for each scene at each fog level. These four metrics ( $r$ ,  $e$ , CNC, CS) compare the dehazed image to the hazy image. The dissimilarity is small for low levels of fog. The values of metrics on different dehazing methods are noticeably close to each other.  $e$ , CS and CNC scores exceed, across levels, the haze-free image scores. This is because appearing artifacts are accounted for edges in the resulting image. . . . . 130
- 6.16 No-reference NSS-based metrics scores obtained for each scene at each fog level. NIQE is a non haze-dedicated metric. According to it, the image of the highest quality is the haze-free image. Dehazed images, which were basically covered by a light fog, have almost the same quality of the haze-free image. While for FADE, which is a haze-dedicated metric, some methods across the three fog levels beat the haze-free image's score. Indeed, it presents a weakness in evaluating the preservation of image's features comparing to the haze-free image. . . . . 130
- A.1 (a) U080 (640×480, taken from FRIDA database [169, 77]), (b) Scene A\_Level 7 (6000×4000). . . . . 166
- B.1 Exponential fit of  $A$  and  $T$  values across the fog levels of  $M2_V$ . Six wavelengths are considered with steps of 50 nm (450, 500 and 550 nm). The calculated values are clearly different across fog levels. . . . . 171
- B.2 Exponential fit of  $A$  and  $T$  values across the fog levels of  $M1_V$ . Six wavelengths are considered with steps of 50 nm (650 and 700 nm). The calculated values are clearly different across fog levels. . . . . 172
- B.3 Exponential fit of  $A$  values of  $M1_V$  across visible wavelengths of fog levels (level 1, level 2, level 3, level 4, level 5, level 6, level 7 and level 8). At each fog level the difference between  $A$  values at different wavelength is due to the lack in the sensor precision. . . . . 173
- B.4 Exponential fit of  $A$  values of  $M1_V$  across visible wavelengths of fog levels (level 9, level 10 and haze-free level). At each fog level the difference between  $A$  values at different wavelength is due to the lack in the sensor precision. . . . . 174
- B.5 Exponential fit of  $A$  and  $T$  values across the fog levels of  $M2_V$ . Six wavelengths are considered with steps of 50 nm (450, 500 and 550 nm). The calculated values are clearly different across fog levels. . . . . 175
- B.6 Exponential fit of  $A$  and  $T$  values across the fog levels of  $M2_V$ . Six wavelengths are considered with steps of 50 nm (450, 500 and 550 nm). The calculated values are clearly different across fog levels. . . . . 176
- B.7 Exponential fit of  $A$  values of  $M2_V$  across visible wavelengths of fog levels (level 1, level 2, level 3, level 4, level 5, level 6, level 7 and level 8). At each fog level the difference between  $A$  values at different wavelength is due to the lack in the sensor precision. . . . . 177

B.8	Exponential fit of $A$ values of $M2_V$ across visible wavelengths of fog levels (level 9, level 10 and haze-free level). At each fog level the difference between $A$ values at different wavelength is due to the lack in the sensor precision. . . . .	178
B.9	Exponential fit of $A$ and $T$ values across the fog levels of $M2_{NIR}$ . Four wavelengths are considered with steps of 50 nm (750, 800, 850, 900 and 950 nm). The calculated values show a subtle difference across fog levels comparing to VIS. . . . .	179
B.10	Exponential fit of $A$ and $T$ values across the fog levels of $M2_{NIR}$ . Four wavelengths are considered with steps of 50 nm (950, 1000, 1050 and 1100 nm). The calculated values show a subtle difference across fog levels comparing to VIS. . . . .	180
B.11	Exponential fit of $A$ values of $M2_{NIR}$ across visible wavelengths of fog levels (level 1, level 2, level 3, level 4, level 5, level 6, level 7 and level 8). $A$ value is constant across wavelengths. . . . .	181
B.12	Exponential fit of $A$ values of $M2_{NIR}$ across visible wavelengths of fog levels (level 9, level 10 and haze-free level). $A$ value is constant across wavelengths.	182
C.1	Cooking automation flowchart. . . . .	184
C.2	The oven Bartscher equipped with tools such as probe for temperature measure and oxygen sensor has been used for cooking measurements. The illustration shows the oven cavity components. Measurements were performed through the windows Hublot 1 and Hublot 2. . . . .	185
C.3	Evolution of condensation over time. From left to right: film condensation, water drops, water drops + seeps. . . . .	186
C.4	Light source transmission variation across condensation aspects. It is measured through the vertical window. . . . .	186
C.5	Spectral emission of the original oven light. . . . .	187
C.6	Reflectance variation across condensation aspects of the red ceramic tile (a) and the blue ceramic tile (b). The reflectance values across visible wavelengths converge towards the prevailing steam color. . . . .	187
C.7	Reflectance curves of a white patch at various locations within the oven. Since the position changes inside the oven, at position 3, the reflectance exceeds the calibration value 100. . . . .	187
C.8	Relative spectral power distribution of the white LED (a) and the blue LED (b). . . . .	189

# LIST OF TABLES

2.1	The constituents of the dry air [38]. . . . .	11
2.2	Weather conditions and associated particle types, sizes and concentrations [115]. . . . .	11
2.3	Atmospheric attenuation and visual range of atmospheric conditions [75]. .	12
2.4	The characteristics of Hazy/foggy image degradation. . . . .	19
3.1	Nighttime vs daytime hazy images . . . . .	42
4.1	Relative transmittance $t$ of fog in original hazy images of scene A and scene B. Level 1: highest fog density. Level 9: lowest fog density. . . . .	66
4.2	Requirements fulfilled by the hazy image databases: FRIDA, WILD and CHIC. . . . .	69
4.3	The characteristics of CHIC and MHIA databases. . . . .	73
5.1	Atmospheric attenuation and visual range of the different fog levels of Scene A. . . . .	84
5.2	Atmospheric attenuation and visual range of the different fog levels of Scene B. . . . .	85
5.3	$\Delta E_{ab}^*$ between atmospheric light and the chromatic patches of the Macbeth ColorChecker at different fog levels of Scene A. For each level we calculate the standard deviation of $\Delta E_{ab}^*$ of all patches. $A_\infty$ is placed at the center. . .	93
5.4	$\Delta E_{ab}^*$ between atmospheric light and the chromatic patches of the Macbeth ColorChecker at different fog levels of Scene B. For each level we calculate the standard deviation of $\Delta E_{ab}^*$ of all patches. . . . .	94
5.5	The values of 2D distance between the real $A_\infty$ and the calculated one as the centroid of the selected hazy colors at each fog level of the scene A. . .	96
5.6	The change in the accuracy of $A_\infty$ estimation with the number of selected colors all over the image. The values below represent the 2D distance between the real atmospheric light and the calculated one as the centroid of the selected hazy colors at each fog level of the scene A. . . . .	99
6.1	Summary of selected dehazing methods. For each method, the default implementations' parameters proposed by the authors, have been used. . .	119
6.2	Summary of selected metrics. Type can be Full-reference F and No-reference N. The reference image is in brackets. . . . .	119

6.3	Hit rates obtained by each metric: (rescaled rates in brackets). The table is divided in four parts: metrics in reference with the haze-free greyscale image ( <b>FG</b> ), metrics in reference with the haze-free color image ( <b>FC</b> ), no-reference metrics ( <b>N</b> ), metrics in reference with the hazy greyscale image ( <b>HG</b> ) and metrics in reference with the hazy color image ( <b>HC</b> ). . . . .	127
6.4	Hit rates obtained by individual perceptual attributes: COLOR (rescaled rates in brackets). The MS-iCID attributes are as follows (refer to [89] for details): $L_L$ : lightness-difference, $L_C$ : lightness-contrast, $L_S$ : lightness-structure, $C_L$ : chroma-difference, $H_L$ : hue-difference, $C_C$ : chroma-contrast, and $C_S$ : chroma-structure. . . . .	128
6.5	Computational time of dehazing methods applied on scene A and scene B. These algorithms were run using MATLAB R2010b on HP Intel(R) core (TM) i7 - 3687U CPU @ 2.10 GHZ 2.60 GHZ. . . . .	132
6.6	MS-SSIM scores of the results of CLAHE dehazing method preceded by denoising, dehazing without denoising, dehazing followed by denoising and dehazing preceded and followed by denoising. Denoising is performed by BM3D. The highest scores are written in bold. The BM3D applied after CLAHE provides globally the best results. . . . .	133
6.7	MS-SSIM scores of the results of DCP dehazing method preceded by denoising, dehazing without denoising, dehazing followed by denoising and dehazing preceded and followed by denoising. Denoising is performed by BM3D. The highest scores are written in bold. The BM3D prior to DCP provides the best results. . . . .	134
6.8	MS-SSIM scores of the results of FAST dehazing method preceded by denoising, dehazing without denoising, dehazing followed by denoising and dehazing preceded and followed by denoising. Denoising is performed by BM3D. The highest scores are written in bold. The BM3D prior to DCP provides the best results. . . . .	134
6.9	MS-SSIM scores of the results of FUSION dehazing method preceded by denoising, dehazing without denoising, dehazing followed by denoising and dehazing preceded and followed by denoising. Denoising is performed by BM3D. The highest scores are written in bold. The BM3D prior to DCP provides the best results. . . . .	134
6.10	MS-SSIM scores of the results of VAR dehazing method preceded by denoising, dehazing without denoising, dehazing followed by denoising and dehazing preceded and followed by denoising. Denoising is performed by BM3D. The highest scores are written in bold. The BM3D prior to DCP provides the best results. . . . .	135
A.1	Execution time of different refinement transmission methods using two RGB images of different sizes shown in Figure A.1. These algorithms were run using MATLAB R2010b on HP Intel(R) core (TM) i7 - 3687U CPU @ 2.10 GHZ 2.60 GHZ. . . . .	166

## TRANSMISSION REFINEMENT ALGORITHMS



Figure A.1: (a) U080 (640×480, taken from FRIDA database [169, 77]), (b) Scene A\_Level 7 (6000×4000).

Table A.1: Execution time of different refinement transmission methods using two RGB images of different sizes shown in Figure A.1. These algorithms were run using MATLAB R2010b on HP Intel(R) core (TM) i7 - 3687U CPU @ 2.10 GHZ 2.60 GHZ.

Method	U080		Scene A_Level 7	
	Time	MS-SSIM	Time	MS-SSIM
Soft matting	23400.316916 <i>s</i>	0.4496	$\infty$ <i>s</i>	—
Bilateral filter	7.150849 <i>s</i>	0.4553	341.545093 <i>s</i>	0.3555
Guided filter	0.358185 <i>s</i>	0.3551	19.384212 <i>s</i>	0.8364
Gaussian filter	0.197987 <i>s</i>	0.4550	0.265905 <i>s</i>	0.3553

It must be noted that a considerable margin of error is induced while estimating the transmission  $t$  of the hazy pixels. In a local patch,  $t$  is assumed to be constant. This is no more true when this patch contains an edge. This leads to obtain an irregular transmission map. In order to smooth it without losing the sharpness of edges, some methods are applied.

In this chapter, we want to compare the performances of four different filtering approaches

that have been widely used in the state of the art dehazing methods, in terms of computational complexity and global quality. For this aim, we have selected two hazy images of different resolutions. The first one is synthetic, taken from FRIDA database with the reference haze-free image and the second one is a real hazy image taken from our CHIC database with its reference image also.

As regards the computational complexity, which represents a crucial element in dehazing processing that are often used in real-world computer vision applications, the processing time should be as short as possible. While maintaining a short time, it is mandatory to reach a compromise which retains the good quality of the recovered image.

According to the scores given in Table A.1, in both images, the soft matting takes up an enormous amount of time, even if the image size is not very large. Such processing is not at all suitable for CHIC database images.

The processing time of the Bilateral filter increases significantly with the image size and the resulting image does not seem of good quality as the guided filter result (Scene A \_ Level 7).

The processing time of the Guided filter increases as well with the image size but not as much as the Bilateral filter. It provides an image among the highest qualities. Thus, comparing to the other refinement methods, it succeeds to achieve the compromise noted above. This is clear when considering the real hazy image Scene A \_ Level 7.

Even when the image size greatly increases, the computational time of the Gaussian filter remains small. Considering the calculated scores in Table A.1, this filter fails to provide a good quality comparing to the others.

All refinement methods show a similar performance for the synthetic scene U080. However, when considering the real scene, the Guided filter proves its efficiency since it considers, like the soft matting, not only the gray image of the transmission map like the Gaussian and the Bilateral filters but the color hazy image. Indeed, this reduces the erroneous textures removal and maintains a similar sharpness to the original color hazy image.

In what follows, we will see the main characteristics of the refining methods.

N.B. In this section  $t_r$  and  $t_0$  denote the refined transmission and the estimated transmission before refinement, respectively.

## A.1/ SOFT MATTING

We start by the method that was the first to be used to refine the transmission in DCP. This method is basically used for digital image matting. It requires a reduced user interaction and deals analytically with the separation of the foreground  $F$  and the background  $B$  colors based on the assumption that the variation of  $F$  and  $B$  colors is smooth in order to obtain a quadratic cost function in alpha. Since haze model is similar to the matting equation [93], transmission map is equivalent to the alpha map:

$$I_i = \alpha_i F_i + (1 - \alpha_i) B_i \quad (\text{A.1})$$

where  $I_i$  is the input image and  $\alpha_i$  is the foreground opacity at pixel  $i$ .

The first step is to minimize the following cost function:

$$E(t) = \arg \min \{ t^T L t + k(t_r - t_0)^T (t_r - t_0) \} \quad (\text{A.2})$$

where  $k$  is a weight parameter that defines the importance of the data term. The solution of Equation A.2 is given by [93]:

$$(L + kU)t_r = kt_0 \quad (\text{A.3})$$

where  $U$  is an identity matrix and it has the same size as  $L$ , which is the Laplacian matrix deduced from the hazy image.

## A.2/ GAUSSIAN FILTER

Gaussian filter is a linear filter. It is applied to smooth the image using a low pass filter. The refined transmission map is expressed as:

$$t_r(x) = \frac{1}{W} \sum_{\Omega(x)} G_{\sigma_s}(\|x - y\|) t_0(y) \quad (\text{A.4})$$

where  $W$  is:

$$W = \sum_{\Omega(x)} G_{\sigma_s}(\|x - y\|) \quad (\text{A.5})$$

$\Omega(x)$  is a local patch centered at pixel  $x$ .

$G_{\sigma_s}$  denotes the 2D Gaussian kernel:

$$G_{\sigma_s}(x) = \frac{1}{2\pi\sigma^2} e^{-\frac{\|x\|^2}{2\sigma^2}} \quad (\text{A.6})$$

$\sigma$  is the neighborhood size.

## A.3/ BILATERAL FILTER

Bilateral filter is an adaptive alternative filter that preserves better edges by calculating weighted average near of nearby pixels. Pixels are treated based on nearby location and similar values.

The refined transmission is calculated as:

$$t_r(x) = \frac{1}{W_1} \sum_{\Omega(x)} G_{\sigma_s}(\|x - y\|) G_{\sigma_r}(\|I(x) - I(y)\|) t_0(y) \quad (\text{A.7})$$

where  $W_1$  is:

$$W_1 = \sum_{\Omega(x)} G_{\sigma_s}(\|x - y\|) G_{\sigma_r}(\|I(x) - I(y)\|) \quad (\text{A.8})$$

$G_{\sigma_s}$  and  $G_{\sigma_r}$  denote a spatial Gaussian weighting that decreases the influence of distant pixels and a range Gaussian that decreases the influence of pixels  $y$  when their intensity values differ from  $I(x)$ , respectively.

Bilateral filter is used for denoising, texture and illumination separation, tone mapping, retinex and dehazing. It suffers from high computational time and gradient reversal artifacts.

## A.4/ GUIDED FILTER

Unlike Gaussian and Bilateral filters, Guided filter as the soft matting considers the hazy image as guidance. This helps to maintain similarities in intensity/color regarding the guidance hazy image. It has as well a better behavior near the edges than the bilateral filter. Its computational complexity is independent of the filtering kernel size. Thus, it guaranties the accurate smoothing and the reduced computational time even when the image size greatly increases.

$$t_r(y) = a_x I(y) + b_x \quad \forall y \in \Omega_x \quad (\text{A.9})$$

$a_x$  and  $b_x$  are linear coefficients assumed to be constant in  $\Omega_x$ . This model ensures that  $t_r$  has an edge only if  $I$  has an edge:

$$\nabla t_r = a \nabla I \quad (\text{A.10})$$

To determine  $a_x$  and  $b_x$ , we have to minimize the difference between  $t$  and the filter input  $I$ . Thus, the cost function should be minimized in the window:

$$E(a_x, b_x) = \sum_{y \in \Omega_x} ((a_x I(y) + b_x - t(y))^2 + \epsilon a_x^2) \quad (\text{A.11})$$

where  $\epsilon$  is a regularization parameter penalizing large  $a_x$ .  $a_x$  and  $b_x$  are calculated as:

$$a_x = \frac{\frac{1}{|\Omega|} \sum_{y \in \Omega_x} I(y)t(y) - \mu_x \bar{P}_x}{\sigma_x^2 + \epsilon} \quad (\text{A.12})$$

$$b_x = \bar{P}_x - a_x \mu_x \quad (\text{A.13})$$

$\mu_x$  and  $\sigma_x$  are the mean and variance of the hazy image  $I$  in the local patch  $\Omega_x$ . After calculating  $a_x$  and  $b_x$  and  $t_r$  for each window, we calculate their averages along the image.



# B

## AIRLIGHT AND TRANSMISSION CURVES OF MHIA IMAGES

This appendix contains the curves of the haze model parameters, airlight  $A$  and transmission  $t$ , calculated for each of the VIS and NIR images of the MHIA scenes. They are calculated, for a given wavelength across different fog levels and for each fog level across all wavelengths bands (cf. Section 5.4).

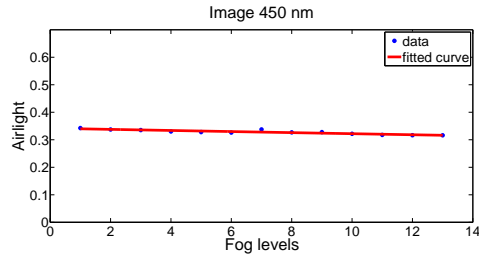
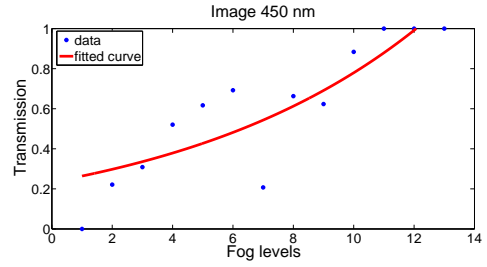
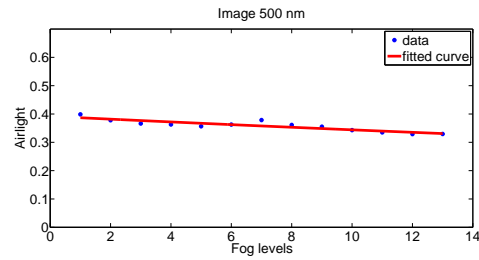
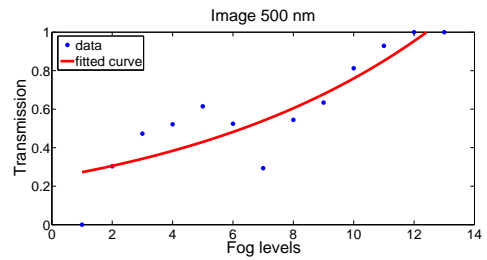
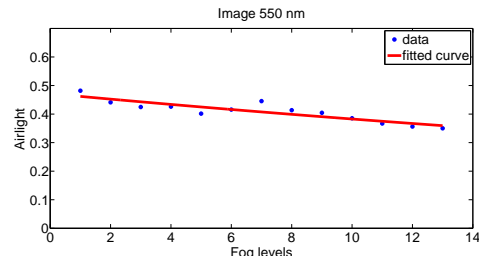
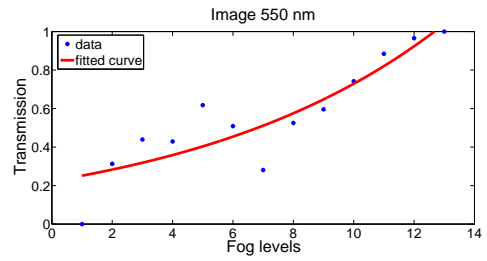
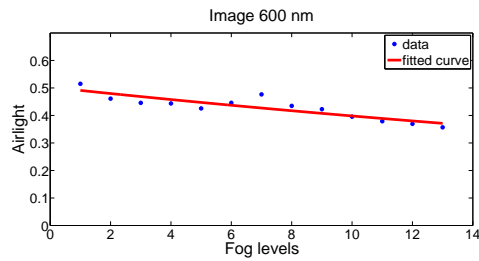
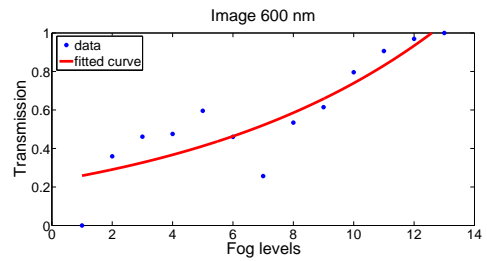
(a)  $M2_V - A - 450nm$ (b)  $M1_V - T - 450nm$ (c)  $M1_V - A - 500nm$ (d)  $M1_V - T - 500nm$ (e)  $M1_V - A - 550nm$ (f)  $M1_V - T - 550nm$ (g)  $M1_V - A - 600nm$ (h)  $M1_V - T - 600nm$ 

Figure B.1: Exponential fit of  $A$  and  $T$  values across the fog levels of  $M2_V$ . Six wavelengths are considered with steps of  $50\text{ nm}$  ( $450$ ,  $500$  and  $550\text{ nm}$ ). The calculated values are clearly different across fog levels.

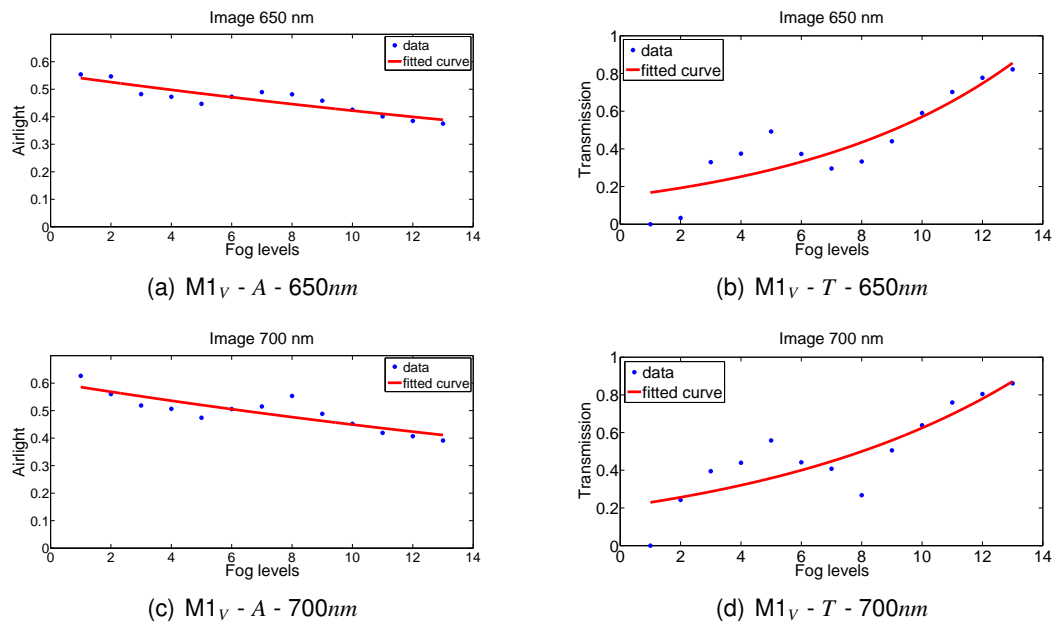


Figure B.2: Exponential fit of  $A$  and  $T$  values across the fog levels of  $M1_V$ . Six wavelengths are considered with steps of  $50\text{ nm}$  ( $650$  and  $700\text{ nm}$ ). The calculated values are clearly different across fog levels.

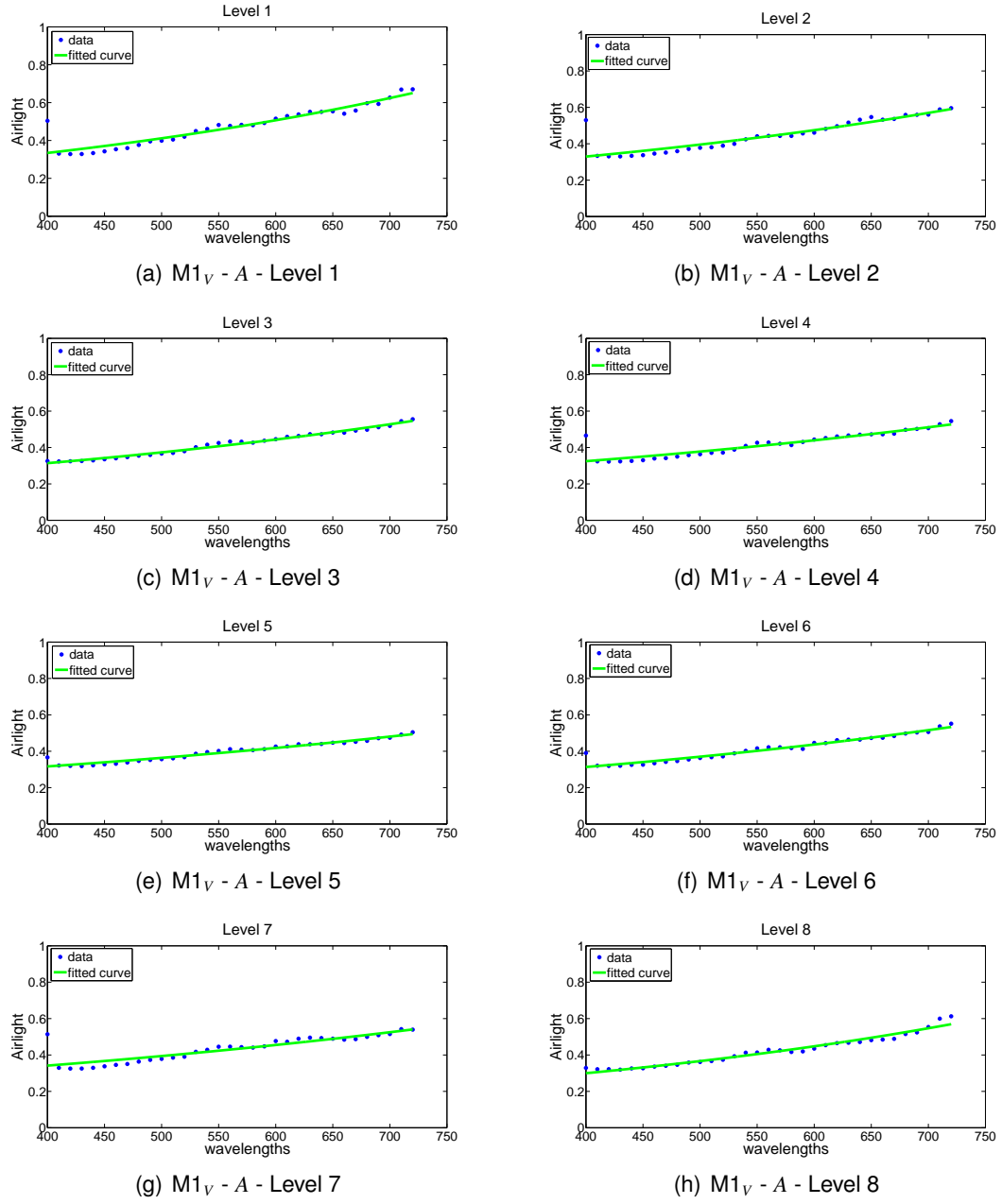


Figure B.3: Exponential fit of  $A$  values of  $M1_V$  across visible wavelengths of fog levels (level 1, level 2, level 3, level 4, level 5, level 6, level 7 and level 8). At each fog level the difference between  $A$  values at different wavelength is due to the lack in the sensor precision.

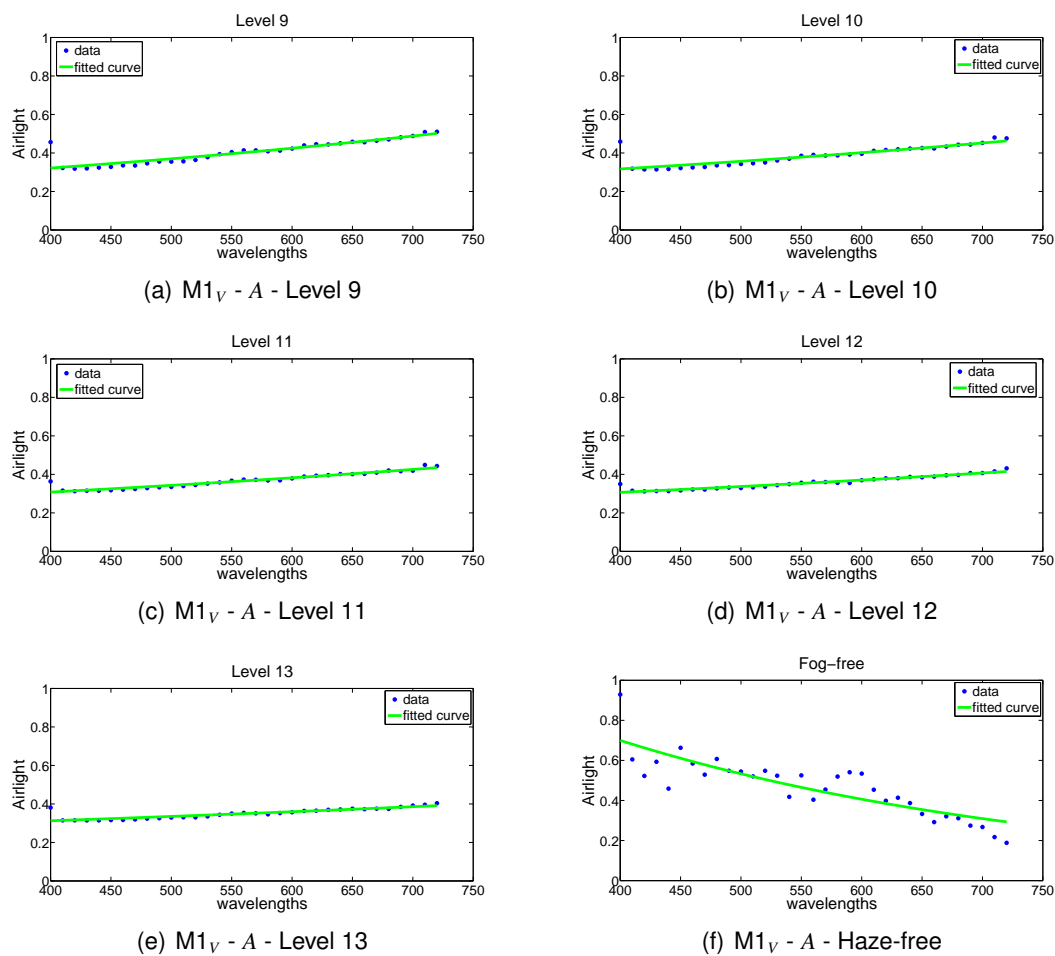


Figure B.4: Exponential fit of  $A$  values of  $M1_V$  across visible wavelengths of fog levels (level 9, level 10 and haze-free level). At each fog level the difference between  $A$  values at different wavelength is due to the lack in the sensor precision.

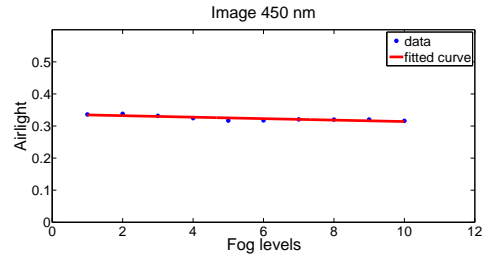
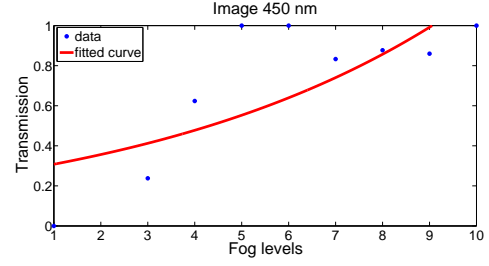
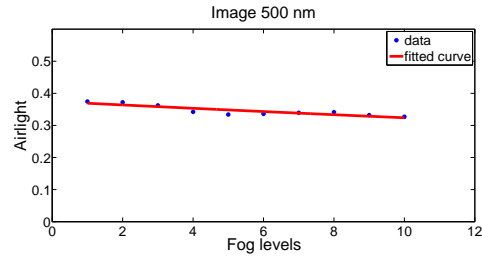
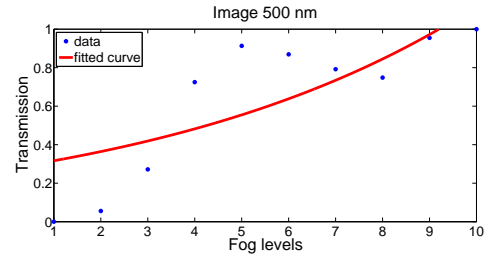
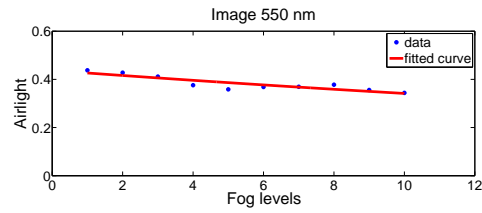
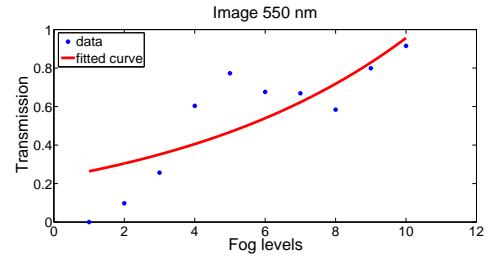
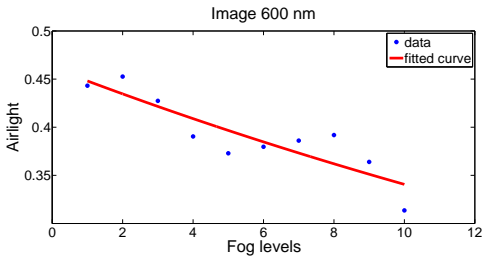
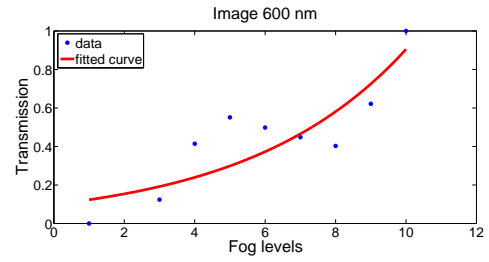
(a)  $M2_V - A - 450nm$ (b)  $M2_V - T - 450nm$ (c)  $M2_V - A - 500nm$ (d)  $M2_V - T - 500nm$ (e)  $M2_V - A - 550nm$ (f)  $M2_V - T - 550nm$ (g)  $M2_V - A - 600nm$ (h)  $M2_V - T - 600nm$ 

Figure B.5: Exponential fit of  $A$  and  $T$  values across the fog levels of  $M2_V$ . Six wavelengths are considered with steps of  $50\text{ nm}$  ( $450$ ,  $500$  and  $550\text{ nm}$ ). The calculated values are clearly different across fog levels.

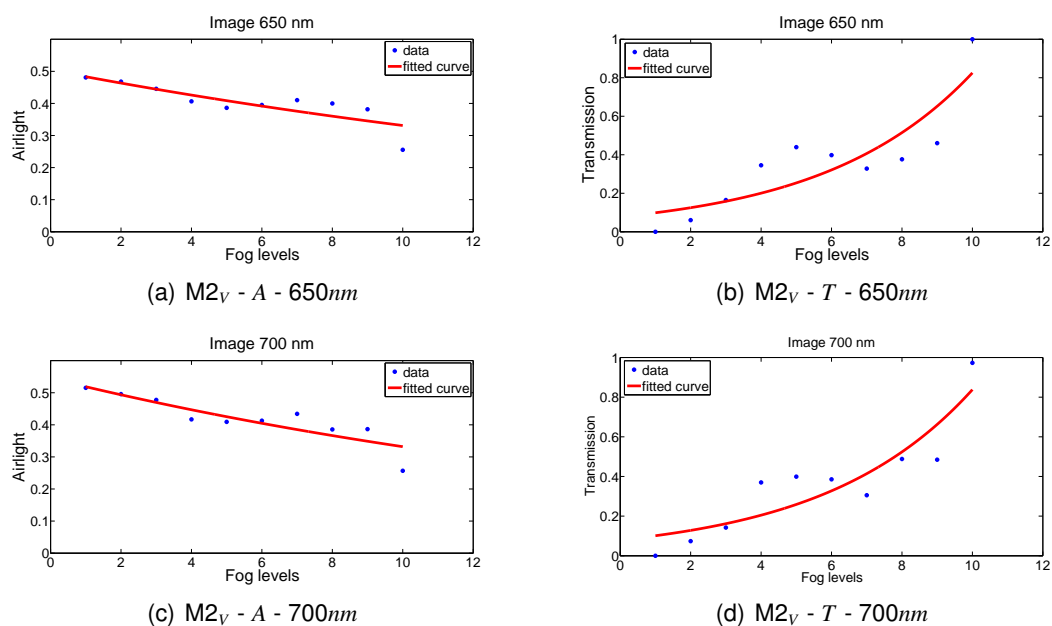


Figure B.6: Exponential fit of  $A$  and  $T$  values across the fog levels of  $M2_V$ . Six wavelengths are considered with steps of  $50\text{ nm}$  ( $450$ ,  $500$  and  $550\text{ nm}$ ). The calculated values are clearly different across fog levels.

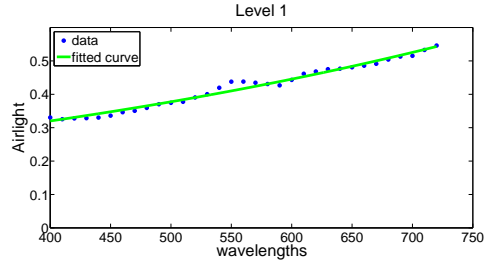
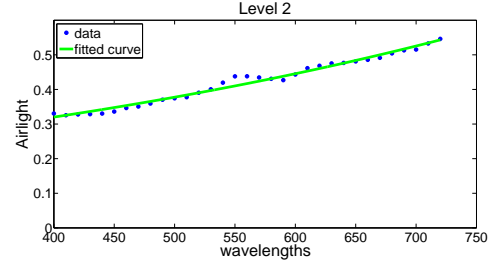
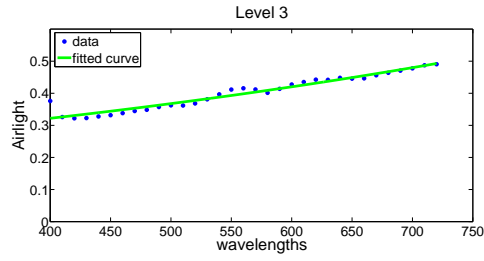
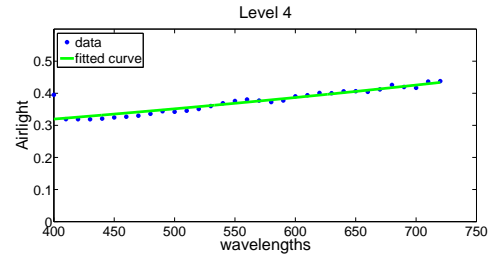
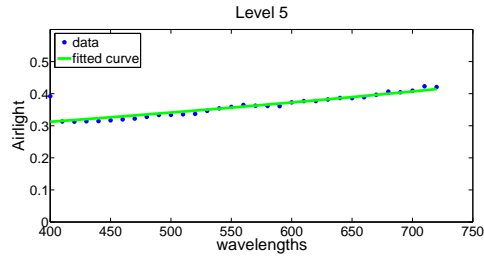
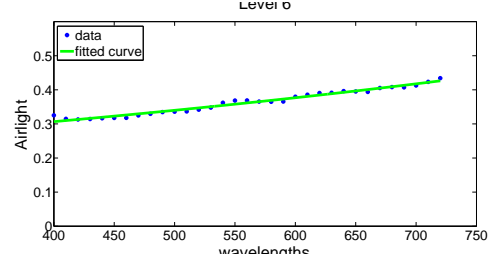
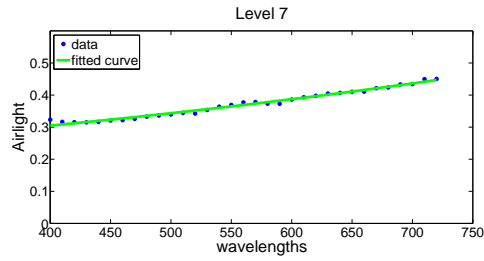
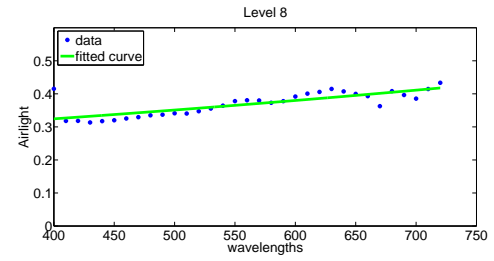
(a)  $M2_V - A$  - Level 1(b)  $M2_V - A$  - Level 2(c)  $M2_V - A$  - Level 3(d)  $M2_V - A$  - Level 4(e)  $M2_V - A$  - Level 5(f)  $M2_V - A$  - Level 6(g)  $M2_V - A$  - Level 7(h)  $M2_V - A$  - Level 8

Figure B.7: Exponential fit of  $A$  values of  $M2_V$  across visible wavelengths of fog levels (level 1, level 2, level 3, level 4, level 5, level 6, level 7 and level 8). At each fog level the difference between  $A$  values at different wavelength is due to the lack in the sensor precision.



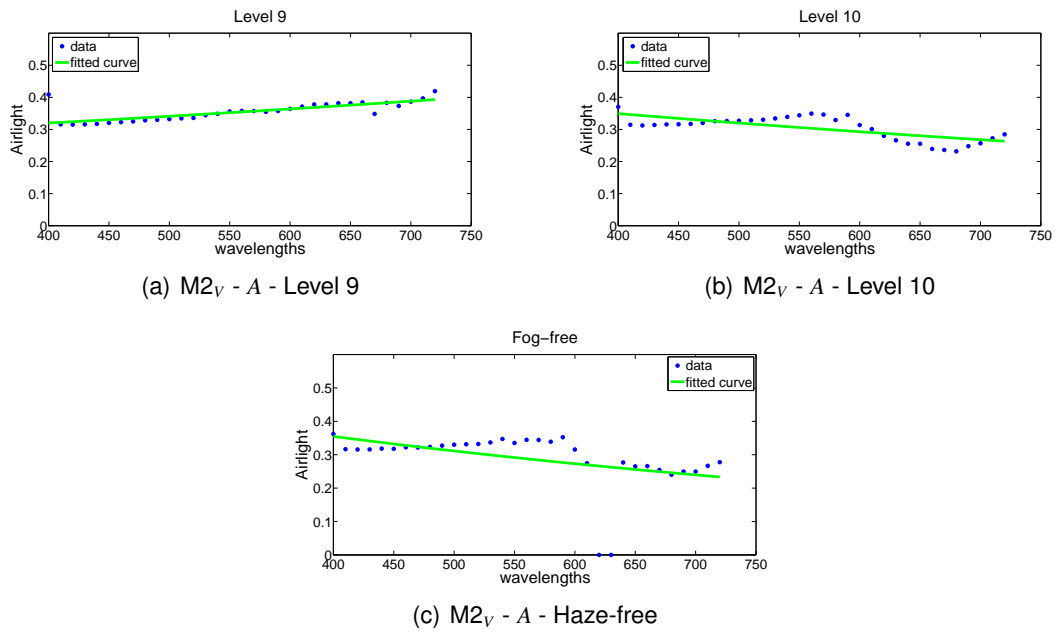


Figure B.8: Exponential fit of  $A$  values of  $M2_V$  across visible wavelengths of fog levels (level 9, level 10 and haze-free level). At each fog level the difference between  $A$  values at different wavelength is due to the lack in the sensor precision.

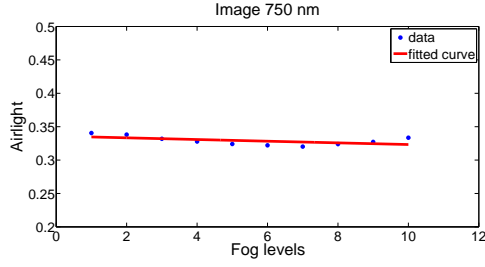
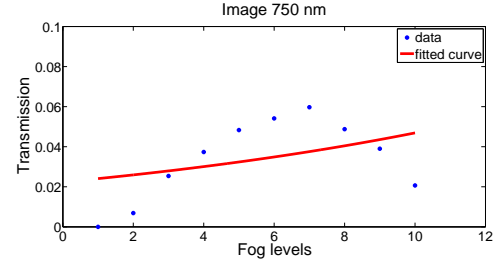
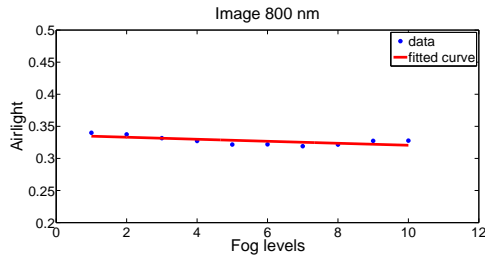
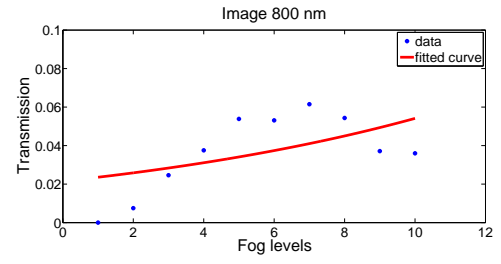
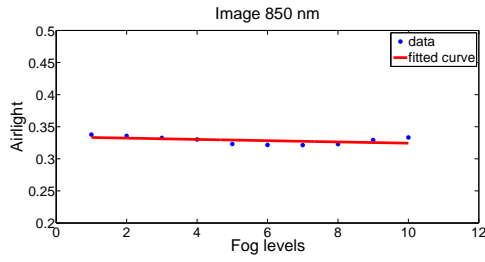
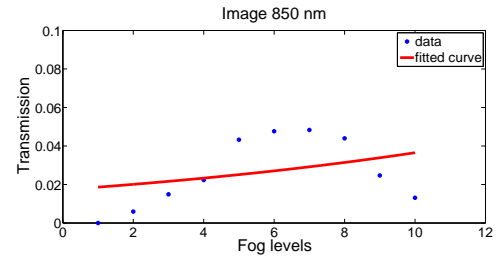
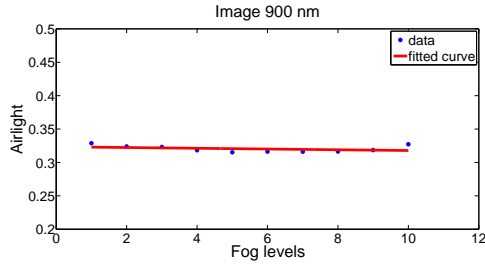
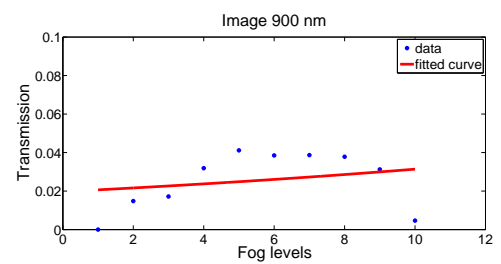
(a)  $M2_{NIR} - A - 750nm$ (b)  $M2_{NIR} - T - 750nm$ (c)  $M2_{NIR} - A - 800nm$ (d)  $M2_{NIR} - T - 800nm$ (e)  $M2_{NIR} - A - 850nm$ (f)  $M2_{NIR} - T - 850nm$ (g)  $M2_{NIR} - A - 900nm$ (h)  $M2_{NIR} - T - 900nm$ 

Figure B.9: Exponential fit of  $A$  and  $T$  values across the fog levels of  $M2_{NIR}$ . Four wave-lengths are considered with steps of  $50\text{ nm}$  ( $750, 800, 850, 900$  and  $950\text{ nm}$ ). The calculated values show a subtle difference across fog levels comparing to VIS.

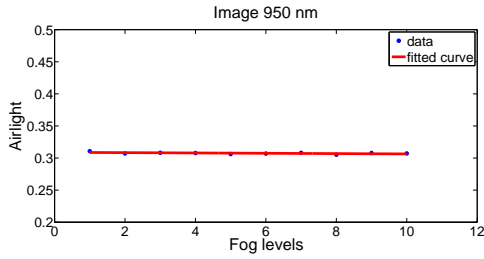
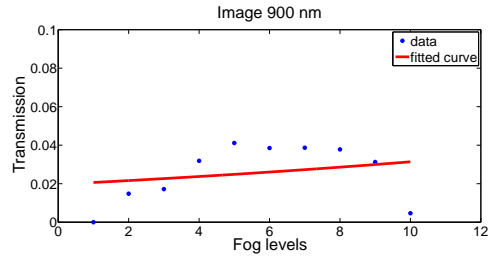
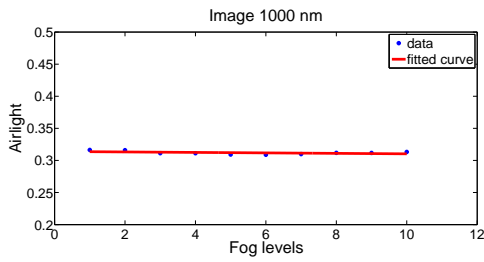
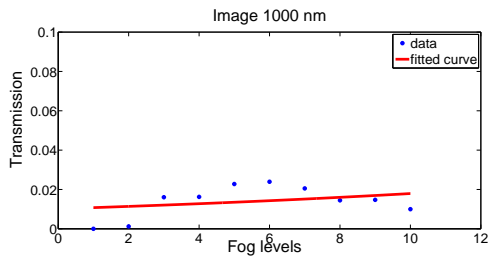
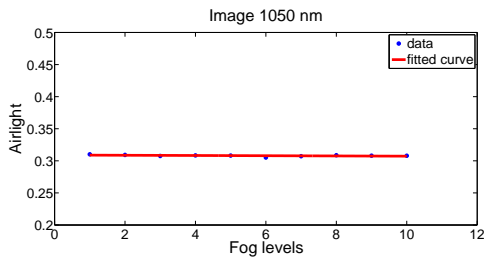
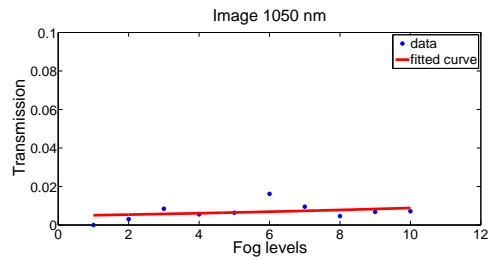
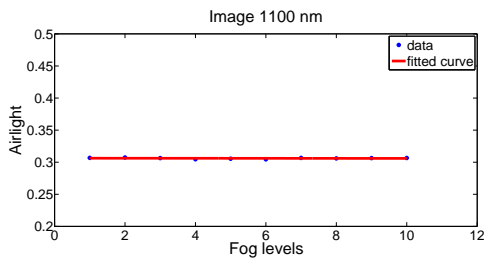
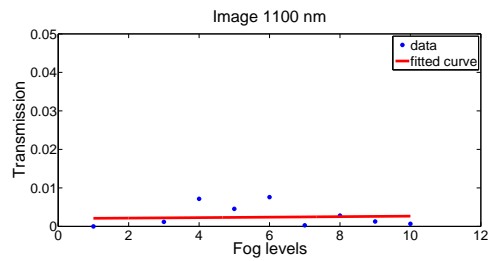
(a)  $M2_{NIR} - A - 950nm$ (b)  $M2_{NIR} - T - 950nm$ (c)  $M2_{NIR} - A - 1000nm$ (d)  $M2_{NIR} - T - 1000nm$ (e)  $M2_{NIR} - A - 1050nm$ (f)  $M2_{NIR} - T - 1050nm$ (g)  $M2_{NIR} - A - 1100nm$ (h)  $M2_{NIR} - T - 1100nm$ 

Figure B.10: Exponential fit of  $A$  and  $T$  values across the fog levels of  $M2_{NIR}$ . Four wavelengths are considered with steps of  $50\text{ nm}$  ( $950$ ,  $1000$ ,  $1050$  and  $1100\text{ nm}$ ). The calculated values show a subtle difference across fog levels comparing to VIS.

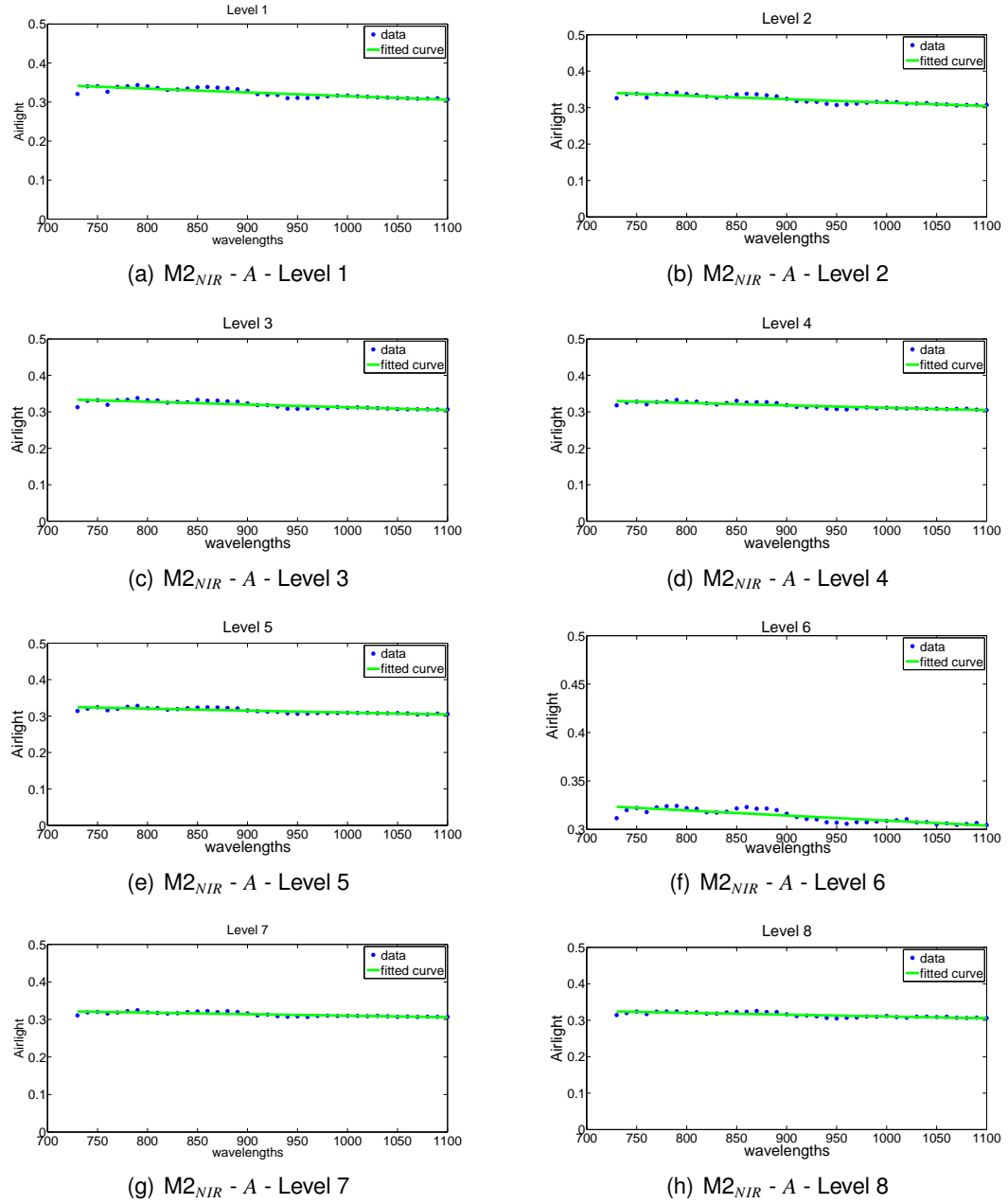


Figure B.11: Exponential fit of  $A$  values of  $M2_{NIR}$  across visible wavelengths of fog levels (level 1, level 2, level 3, level 4, level 5, level 6, level 7 and level 8).  $A$  value is constant across wavelengths.

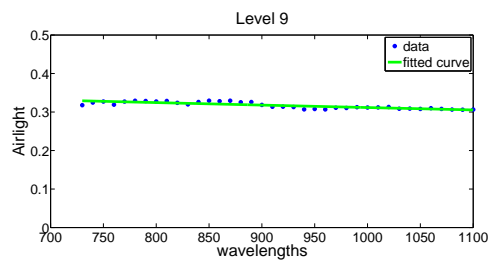
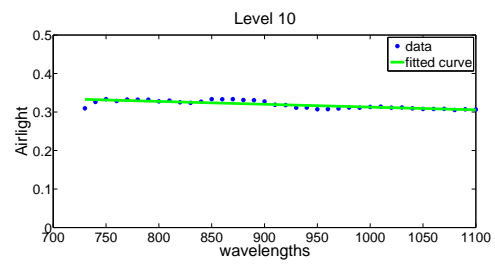
(a)  $M2_{NIR} - A$  - Level 9(b)  $M2_{NIR} - A$  - Level 10

Figure B.12: Exponential fit of  $A$  values of  $M2_{NIR}$  across visible wavelengths of fog levels (level 9, level 10 and haze-free level).  $A$  value is constant across wavelengths.

## LINK BETWEEN IMAGE ENHANCEMENT INSIDE OVEN AND THIS THESIS

People of today seek ways to make their lives easier, at work, in education and especially at home. The house is our refuge, where we spend the most of time and we do some tasks that we cannot do elsewhere. When these tasks are done automatically, we will be freer for outdoor activities. Cooking is a daily time consuming task. It requires three steps: food purchase, food preparation (washing, slicing, mixing, etc.) and food cooking. In its turn, the last step requires the most time and some basic knowledge to pinpoint the doneness stage and ability to deal with such dangerous cooking materials. For example, a young person cannot achieve successfully such operation. For all these reasons and many more, the manufacturers of ovens have been moved towards intelligent cooking appliances. The new generation of such ovens is not limited to automate cooking in order to reduce time and user interaction, but to provide also a well cooked food meeting the standards of a healthy food empty of harmful bacteria.

The properties of food change under the action of heat and the high temperature. One of these properties is the color that seems to be strongly dependent on the food. Color and spectral measurements require specific calibrated conditions, which are difficult to achieve in the cooking conditions. The steam releasing from the oven (steam mode) and the food creates a veil that deposits on the windows glasses (Figure C.3). This prevents from getting a clear image and accurate spectral measurements data. Hence the need to incorporate a process to get rid of this veil and to recover accurately the hidden colors. Two hardware and software solutions can be considered (see Section C.2).

Considering the color issue, we find a bridge between the oven and the outdoor environment. The images taken in a hazy/foggy day do not show clearly scenes. The existent veil reduces contrast and fades colors according to its properties. Although the variety of existent dehazing methods that aim to remove the undesired veil and enhance image visibility, the accurate color restoration is still not achieved. Thus, it seems important to characterize and describe how colors are biased and shifted with the illuminant type, the particles size and the density of the covered veil.

The oven may be defined as a controlled atmosphere with finite dimensions (see Figure C.2). The conditions that generate events and disturb others, are from climatic and natural changes that can never be controlled due to human intervention. By contrast, for ovens, any component included in their construction is designed by the manufacturer, thus, each element contributing to the performance of the cooking operation is adjustable.

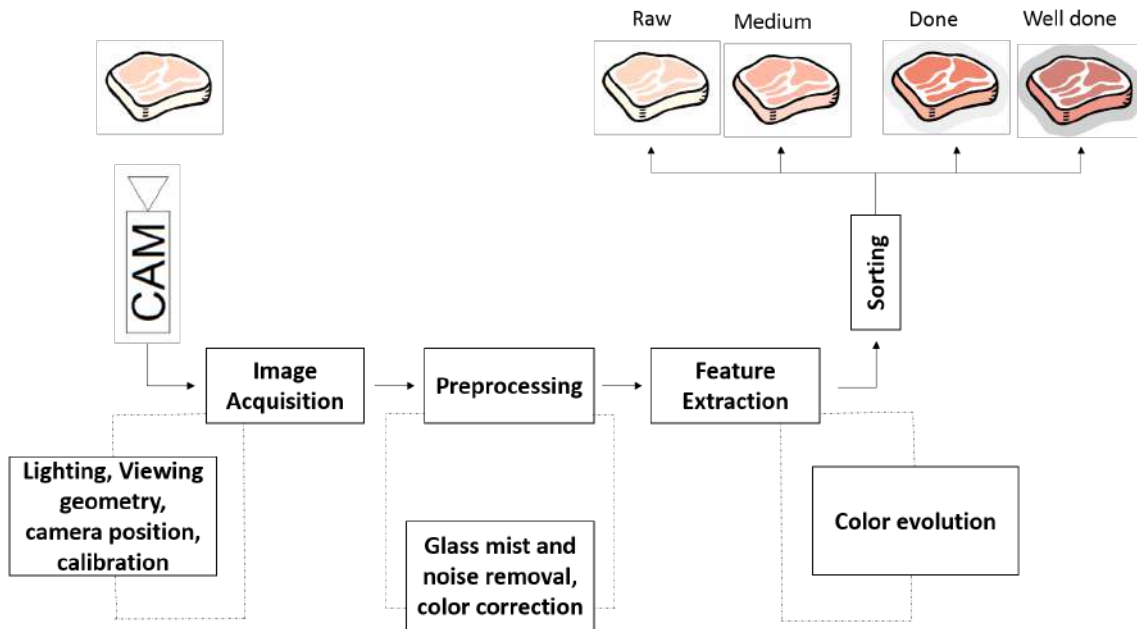


Figure C.1: Cooking automation flowchart.

Figure C.1 shows the main steps of cooking automation, from data acquisition to data processing. The user is usually judging cooking based on the global appearance: the preprocessing of images acquired in good conditions may be used to extract appearance parameters, which correlate with the cooking stage.

In order to capture spectral data in a proper way, and to maintain reliability between various measurements, some pre-conditions should be met. The light source and the camera should be positioned in a manner to cover a largely sufficient part of the food to represent well the entire portion. The light should emit an energy over the whole visible spectrum. This ensures to have sufficient information no matter what the color of the cooked food is. Acquisition should be also preceded by a calibration session.

In the preprocessing step, the acquired data are processed in such a way to be enhanced after being altered by external factors, such as steam condensation that causes also color shift and the noise caused basically by the sensor noise and amplified by the inverse enhancement processes (*i.e.* dehazing).

Once the collected data are adjusted, we move to features investigation, such as spectral indices to classify the cooking states.

### C.1/ VISIBILITY DISTURBANCE

Two types of steam can be identified inside the oven: the vapor deposited on the glass due to the variation between inside and outside temperatures. We call it *steady steam (SS)*. And the *moving steam (MS)* which is evaporated from the food under the action of high temperature. Both types are mathematically modeled as follows:

- Steady steam

$$AS_{SS} = S \alpha e^{-d} \quad (C.1)$$

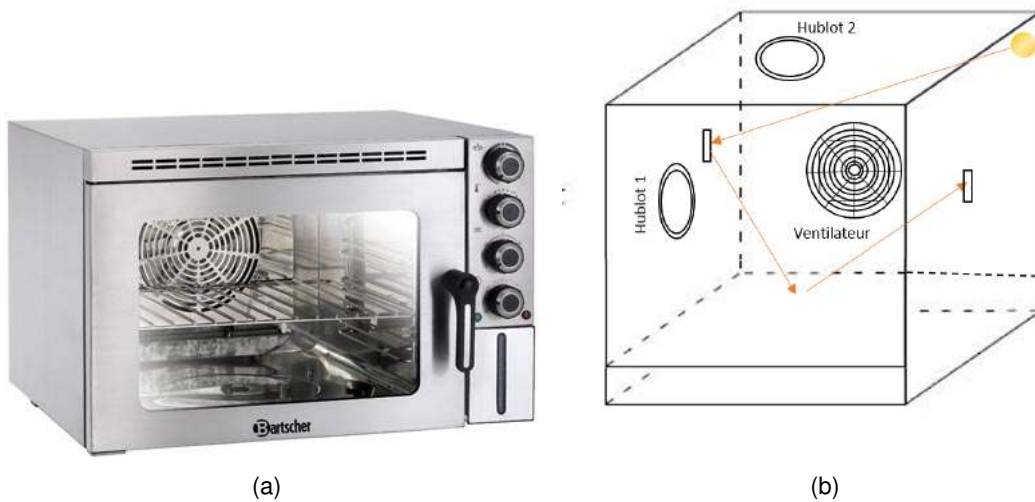


Figure C.2: The oven Bartscher equipped with tools such as probe for temperature measure and oxygen sensor has been used for cooking measurements. The illustration shows the oven cavity components. Measurements were performed through the windows Hublot 1 and Hublot 2.

- Moving steam

$$AS_{MS} = S e^{-\alpha d} \quad (C.2)$$

where  $AS$  is the abbreviation of “Attenuated Signal”,  $S$  is the real signal value,  $\alpha$  is the attenuation coefficient (it is considered to be:  $0 \leq \alpha \leq 1$ ),  $d$  is the distance between the sensor and the object.

Condensation is the opposite phenomenon of evaporation. This phenomenon is observed on the glass of the oven and which is due to the fact that the air in the oven containing steam and mixed modes, contains water vapor in suspension. When water vapor is greater than the saturation limit, there is condensation. This condensation is carried out in priority over the cooler walls: the temperature difference between the temperature inside the oven and the inner wall (cooled by the outer temperature) of the glass will cause condensation. The observation of condensation shows the existence of three distinct phenomena that could be attributed to three consecutive time following the launch of the oven steam and mixed modes (Figure C.3):

- **Film condensation:** this type of condensation occurs just after turning the oven on. Water vapor forms first a thin film that turns then thick.
- **Water drops:** this aspect of condensation happens after the film condensation, and it does not stay long. It is an intermediate phase between the two other stages. The droplets become heavy, and under the influence of gravity, a flow phenomenon appears on the glass.
- **Water drops and seeps:** when water droplets get larger and heavier, they fall down, forming flows. This phenomenon is observed on horizontal windows (Hublot 1) of the oven. In contrast, on the vertical glass (Hublot 2) in the oven ceiling, drops expand and keep their positions.



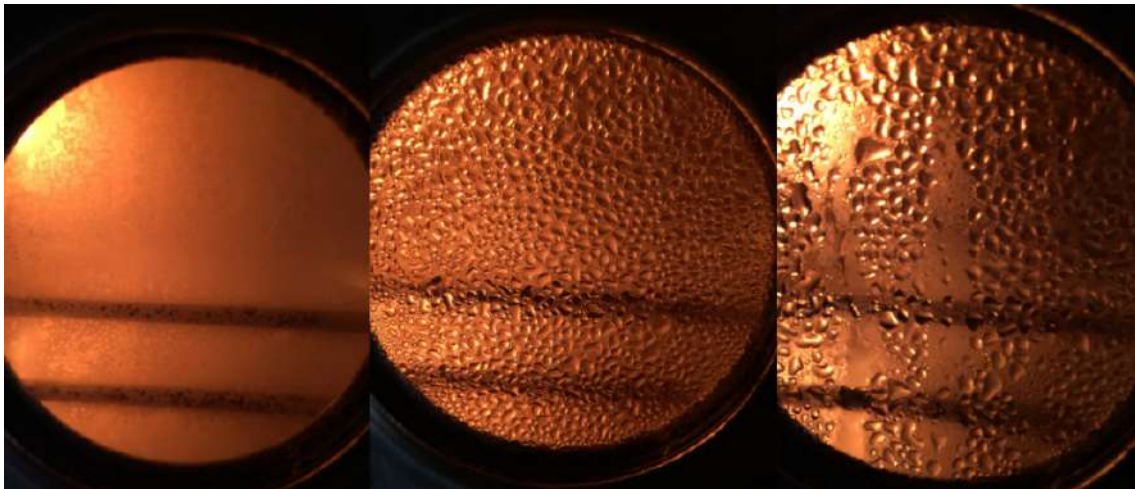


Figure C.3: Evolution of condensation over time. From left to right: film condensation, water drops, water drops + seeps.

Considering these three phenomena, we suggest different ways to process the data: dehazing can be applied in case of film condensation. Inpainting and/or drop models can be used in case of water drops and seeps.

In order to understand how light is influenced by the condensation types previously described, in presence of each of them we measured the transmittance of the oven light through the window. Figure C.4 shows transmittance spectra corresponding to different condensation aspects.

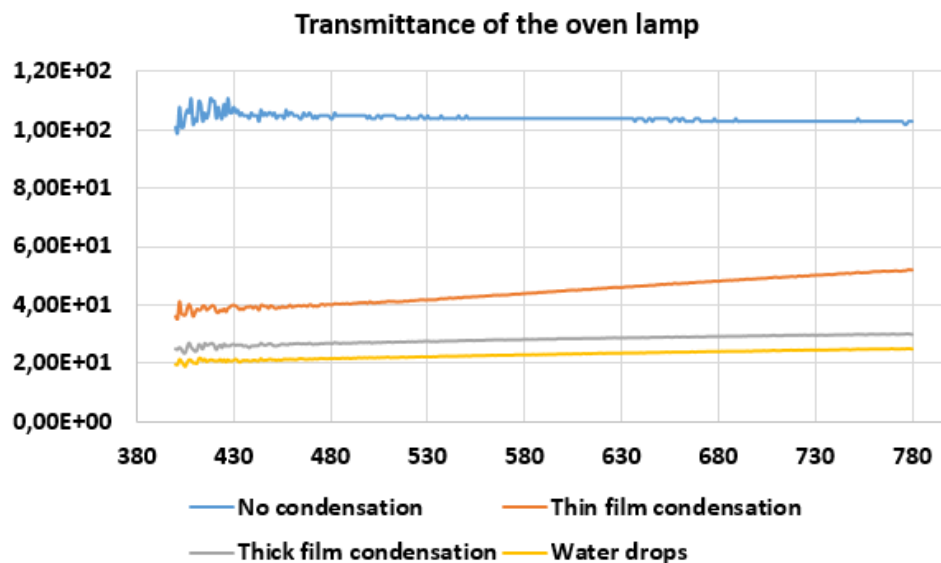


Figure C.4: Light source transmission variation across condensation aspects. It is measured through the vertical window.

The reflectance of several ceramic tiles with and without condensation, was similarly measured. As the color of the tile remains constant under the influence of the oven tempera-

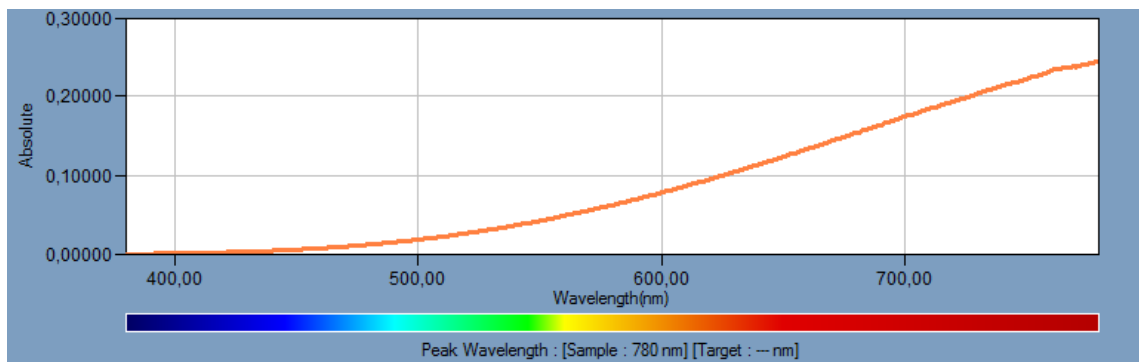


Figure C.5: Spectral emission of the original oven light.

ture for a limited time, unlike food, it helps to monitor the steam effect. These measures aim to characterize the steam effect across visible wavelengths. The calibration of Konica Minolta Spectro-radiometer CS-2000 is a white patch whose measurement is done through the window without steam. Figure C.6 shows the reflectance pieces of red and blue tiles acquired with the different types of condensation.

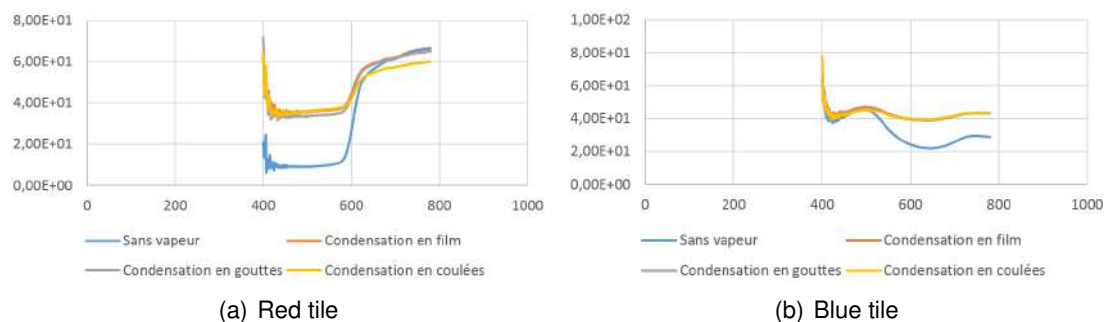


Figure C.6: Reflectance variation across condensation aspects of the red ceramic tile (a) and the blue ceramic tile (b). The reflectance values across visible wavelengths converge towards the prevailing steam color.

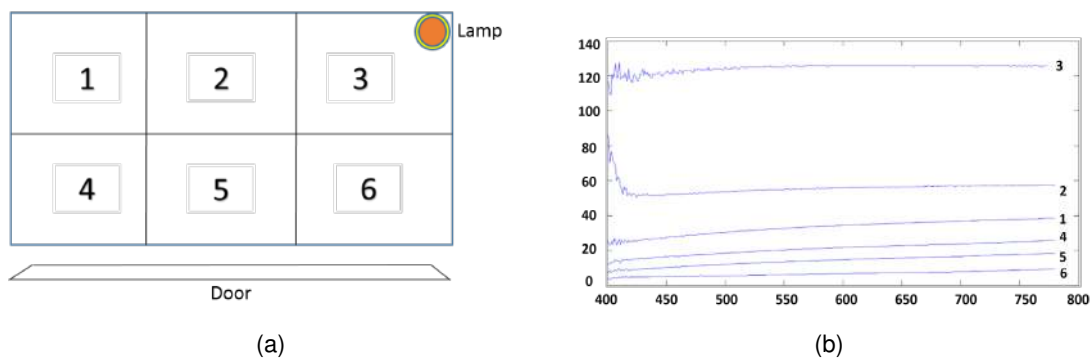


Figure C.7: Reflectance curves of a white patch at various locations within the oven. Since the position changes inside the oven, at position 3, the reflectance exceeds the calibration value 100.

**Replacing light** Concerning the lamp with which the oven is originally equipped, two related issues are popped up. The first is due to the lamp position (Figure C.7) and the second one is due to the spectral emission of the lamp (Figure C.5).

Referring to Figure C.7, there is no spatial uniformity of the lamp radiation at various positions on the horizontal tray.

As it is shown in Figure C.5, the energy emitted from the original oven light is not evenly distributed across the visible spectrum. This may induce erroneous perceived colors of the food across cooking steps. What is actually needed is to have a uniform distribution over all wavelengths.

According to [66], we usually underestimate the importance of the illumination in image acquisition systems. Many requirements should be met:

- **Geometry** – the light source should be placed in a manner to ensure a spatial uniformity. If the camera is to be used for spectrophotometric or colorimetric measurements, a lighting/viewing geometry recommended by the CIE should be used (typically  $45^\circ/0^\circ$  geometry). Specular reflection should be avoided in many acquisitions, otherwise measurements will be erroneous.
- **Power** – the light source power should be sufficiently high through the spectral band of the filter. Long integration time can be a solution to compensate low intensity. However, this may generate additional problems such as amplifying acquisition noise and slowing down the acquisition.
- **Spectral properties** – sufficient spectral power is also needed in each part of the visible spectrum. It is preferred that the spectral power be smoothly distributed all over the spectrum.
- **Stability and repeatability** – of the irradiance from the light source is of great importance for reliable and accurate measuring results.

Referring to the weaknesses, noted earlier and the previous requirements, of the light type placed originally in the oven, we changed the original light to a new one that lights up well the food. We have agreed that a combination of two LEDs, white LED and blue LED (Figure C.8) would provide a good performance because they provide together a high and well distributed energy over the visible range.

In addition to water vapor, volatile particles are suspended in the oven during cooking and they are then glued on the internal walls. During cooking, a large amount of heat is evolved. Under the action of high temperature, other substances than water release from the food such as oil and fat. The particles which are due to fat have completely different characteristics than water vapor: the rate of absorption, the extent of persistence, maintaining the physical condition, size, opacity.

Hence cleaning is an essential process after each cooking. Otherwise, the spots accumulate baking at another preventing the net acquisition of photos and spectral values. During one firing, the probability that the door is widely spotted is minimal. As the spots are relatively small, we are simply applying an interpolation method to rebuild the part obscured by the stain.

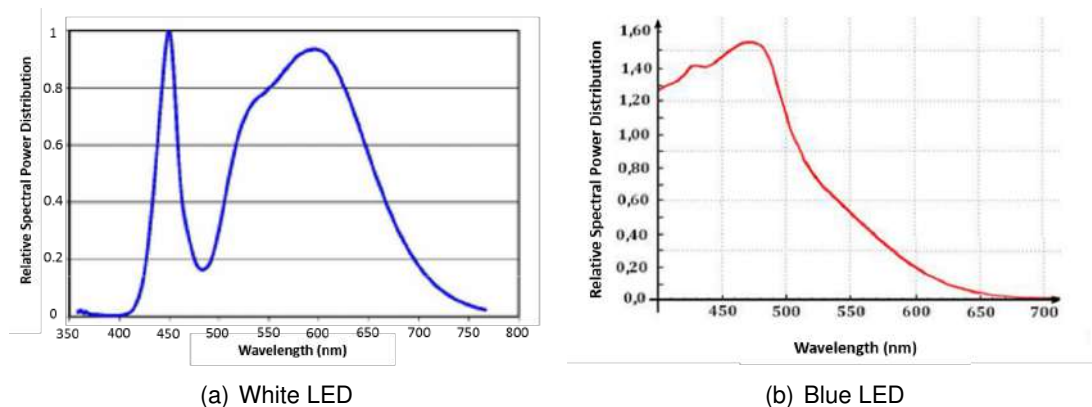


Figure C.8: Relative spectral power distribution of the white LED (a) and the blue LED (b).

## C.2/ PROPOSED SOLUTIONS

In order to reduce the negative effects caused by the steam, especially the steady steam, two approaches have been proposed.

### C.2.1/ HARDWARE SOLUTION

This solution has been proposed by the Open Food System consortium. It consists of replacing the original window's glass by a heating glass to avoid the steam condensation. In this way we succeeded to prevent it. However, the accurate adjustment remains an open problem unless a software processing is performed.

It is of crucial importance to measure the real color of the food during cooking. From a certain threshold of inaccuracy, the color that could define a cooking stage may be confused with another color and the cooking is therefore misled. Such problems are there even if the glass is clean. This is mainly due to the light of source and the glass itself. The modeling and the quantification of this is explained in the next section.

### C.2.2/ SOFTWARE SOLUTION

Referring to Figure C.1, the link between all what has been addressed in this thesis is located at the pre-processing step. At this step we correct and enhance the acquired radiometric and photometric data in order to be properly exploited in the subsequent steps.

This algorithm may be used when a camera is placed inside the oven. Image data may be considered in two different ways: the extraction of information on surface properties and the transmission of images to a tablet or smartphone of the user.

Let us show the link between this project and each of the above chapters.

- Chapter 2:** The oven cavity when the oven is running, and all the resulting interacted phenomena can be assimilated to the atmosphere. In bad weather, atmosphere

represents a bad environment like the oven, which both of them degrade the clear visibility. Therefore, humans activities become risky and inefficient. Hence there is a need to increase the visibility level, while considering the fidelity of the original data and the overall quality.

In dehazing, we consider color images and not reflectance measurements.

**2. Chapter 3:** Referring to Section 3.1, dehazing is considered as a pre-processing tool that aims at enhancing outdoor visibility. Since several elements that come into the frame remain the same in the clear and the degraded images, no additional data or strong assumptions are needed.

Considering Equation 2.16, the parameters are defined as follows:

- $I$  is the captured degraded image containing the cooked food and the surrounding frame.
- The glass through which the image capturing is done, should be first characterized. According to [41], a surface seen through a transparent filter (we consider here the window glass) leads to color translation or convergence.  $A_\infty$  is a constant value. It represents the color coordinates of the glass.
- The transmission factor  $t$  should be measured by using a surface with known reflectance. It is calculated as the ratio between the emitted intensities in the absence and the presence of the glass, respectively.  $t$  is no more a function of distance  $d$  and scattering coefficient  $\alpha$ . In our case,  $d$  is negligible in comparison to the outdoor images and it is accurately known as well.  $\alpha$  does not stand for suspended particles.  $d$  and  $\alpha$  represent together the glass properties that lead to transmission reduction.
- $J$  is the corrected image that will be considered for the classification process. In order to simplify this task and reduce the computational complexity, which is a crucial factor in such real-world application, only a part of the image showing a representative part of the food is considered.

Since the dehazing is done through the haze model inversion, an amplification of the noise is highly likely to occur (cf. Section 3.2.5). Noise elimination should be applied. As the noise is known, it is better to be eliminated before dehazing. Thus, a simple no consuming space-invariant denoising method can be used.

**3. Chapter 4:** In outdoor situations, the original clear image is often not available. To investigate quality and haze model validation, a color image database has been created including the haze-free image. Indeed, there is a key difference between the outdoor environment and the oven cavity. Inside the oven, the environment and its elements do not change. Only the food changes in the image. Thus, an important part of the problem met in outdoor situations is already solved. There is only a need to define how much a color shift under the action of the light and the glass.

**4. Chapter 5:** One may wonder if it is possible to recover the original color regardless of the thickness of vapor and its condensation type. Using the images of different fog levels, we showed that the color-based haze model has some limits. Outside of these limits, the recovery of original data is no more feasible. With color-based technical capabilities, it is impossible to go across an opaque layer of steam and clear it out. However, thanks to the heating glass, it is nearly impossible to face such problem.

**5. Chapter 6:** Automatic quality judgment is part of the game. The fidelity criterion is critical and it must be met. Since the cooking characterization is done based on the color variation of the food, this variation should be only caused by the cooking evolution. Otherwise, we will not be able anymore to identify where the color shift comes from: if it is a cooking indicator changing over cooking time, or it is generated by the image enhancement algorithms.

Thus, a given dehazing method is considered to be usable for this purpose, if and only if it maintains a high fidelity of image features.





## Abstract:

This thesis is mainly related to color imaging science, involving many disciplines, such as color image enhancement, image formation, color reproduction, optical physics, radiometry, colorimetry, image quality and psychophysics.

*Dehazing* aims at recovering the image information degraded by light scattering, e.g. bad weather. This process is an ill-posed and a challenging problem. Although a variety of approaches have been proposed, there is still room for further improvement and standardization. In this work, we investigate the limitations of haze model in terms of accuracy of color image recovery. We address also the link between the visibility deterioration and the spectral content of the images. Moreover, with the multiple existing dehazing algorithms, it is mandatory to evaluate and compare their performance. Indeed, only limited investigations have been performed on the quality of dehazing in particular on the fidelity of the recovered material. Thus, we propose to evaluate the quality of dehazed images. To this aim, a color and a multispectral hazy image databases have been conceived. These databases represent with their ground truth clear image, an adequate tool to deal with dehazing quality in terms of objective and subjective assessment.

**Keywords:** Dehazing, Image quality, Hazy image database, Psychometric experiment

## Résumé :

Cette thèse s'intègre dans le cadre de la science de l'imagerie couleur, impliquant de nombreuses disciplines, telles que l'amélioration des images couleur, la formation de l'image, la reproduction des couleurs, la physique optique, la radiométrie, la colorimétrie, la qualité d'image et la psychophysique. Le *Dehazing* permet d'améliorer les images dégradées par la diffusion de la lumière. Il représente un problème difficile et mal-posé. Malgré la diversité des approches qui ont été proposées, la marge d'amélioration et la standardisation reste encore considérable. Dans ce travail, nous étudions, d'une part, les limites de la manipulation du modèle de dégradation de la visibilité en termes de précision de la reconstruction des images couleur. D'autre part, nous examinons le lien probable entre la détérioration de la visibilité et le contenu spectral des images. En outre, avec la multiplication des algorithmes de dehazing, il est nécessaire d'évaluer et de comparer leur performance.

En effet, il y a peu d'études qui ont été effectuées sur la qualité de dehazing, en particulier sur la fidélité des données restituées. Donc, nous proposons d'évaluer la qualité des images traitées par le dehazing. À cette fin, nous avons élaboré deux bases de données des images couleurs et multispectrales. Ces bases de données avec l'image originale qu'elles contiennent, représentent des outils adéquats pour étudier la qualité d'images en termes d'évaluation objective et subjective.

**Mots-clés :** Dehazing, Qualité de l'image, Base de données des images de brume, Test psychométrique

